MINISTÉRIO DA EDUCAÇÃO
UNIVERSIDADE FEDERAL DO RIO GRANDE DO SUL
Escola de Engenharia
Programa de Pós-Graduação em Engenharia de Minas, Metalúrgica e de Materiais – PPGE3M

SIMULAÇÃO E OTIMIZAÇÃO DE PROCESSOS E MATERIAIS APLICADOS À PRODUÇÃO DE HIDROGÊNIO E A CÉLULAS A COMBUSTÍVEL DO TIPO ÓXIDO SÓLIDO (SOFC) E MEMBRANA POLIMÉRICA (PEMFC)

ALINE LIMA DA SILVA

Tese para obtenção do Título de Doutor em Engenharia

Porto Alegre
2012

Aline Lima da Silva
Mestre em Engenharia

SIMULAÇÃO E OTIMIZAÇÃO DE PROCESSOS E MATERIAIS APLICADOS À PRODUÇÃO DE HIDROGÊNIO E A CÉLULAS A COMBUSTÍVEL DO TIPO ÓXIDO SÓLIDO (SOFC) E MEMBRANA POLIMÉRICA (PEMFC)

Trabalho realizado no Laboratório de Pesquisa em Corrosão da Escola de Engenharia da UFRGS, dentro do Programa de Pós-Graduação em Engenharia de Minas, Metalúrgica e de Materiais – PPGE3M, como parte dos requisitos para a obtenção do Título de Doutor em Engenharia.

Área de Concentração: Ciência e Tecnologia dos Materiais

Orientador: Profª.Drª.Iduvirges Lourdes Müller

Porto Alegre
2012

Esta Tese foi julgada adequada para obtenção do título de Doutor em Engenharia – área de concentração Ciência e Tecnologia dos Materiais e aprovada em sua forma final, pelo Orientador e pela Banca Examinadora do Curso de Pós-Graduação.

Orientador: Profª. Drª. Iduvirges Lourdes Müller

Banca Examinadora:

Profª Drª. Lúcia Allebrandt da Silva Ries – UERGS

Profª. Drª. Tania Denise Miskinis Salgado – Instituto de Química – UFRGS

Prof. Dr. Nestor Cezar Heck – Programa de Pós Graduação em Engenharia de Minas, Metalúrgica e de Materiais – UFRGS

Prof. Dr. Telmo Roberto Strohaecker
Coordenador do PPGE3M

Dedico esta humilde contribuição a todas as pessoas honestas e justas que há neste mundo....

AGRADECIMENTOS

À Profª Drª Iduvirges Lourdes Müller, por acreditar no meu trabalho, haver aceitado ser minha orientadora ao longo destes quatro anos, e por ter contribuído na minha formação, desde a época em que eu era aluna de graduação em Engenharia Metalúrgica.

Ao Mr. José Walter Farfan Valverde, pela contribuição na produção dos artigos publicados nos periódicos.

Aos diversos docentes dos diferentes Programas de Pós-graduação da Universidade Federal do Rio Grande do Sul (PPGE3M, PPGEQ, PROMEC, PPGMAT, PGCIMAT, PPGQ) que contribuíram na minha formação multidisciplinar, o que ampliou a minha capacidade de análise.

A todos os entusiastas da termodinâmica, da simulação de processos e da pesquisa na área de geração de energia sustentável que incentivam a realização deste tipo de estudo. A todas as pessoas que fazem ciência de forma honesta e transparente, mesmo que com poucos recursos.

Aos meus pais Elisabete e Osvaldo Luiz da Silva.

Ao Conselho Nacional de Desenvolvimento Científico e Tecnológico (CNPq), pelo auxílio financeiro para a realização desta Tese de Doutorado.

SUMÁRIO

LISTA DE FIGURAS

LISTA DE TABELAS

RESUMO

A presente Tese, elaborada pela integração de seis artigos científicos publicados em periódicos internacionais, tem por objetivo geral a realização de simulações termodinâmicas aplicadas à produção de hidrogênio e geração de eletricidade a partir de células a combustível de baixa temperatura (*Proton Exchange Membrane Fuel Cell* - PEMFC) e alta temperatura (*Solid Oxide Fuel Cell* - SOFC). Foram simuladas diferentes rotas termoquímicas para a produção de hidrogênio (reforma a vapor, autotérmica, oxidação parcial, reforma com captura *in situ* de CO_2, *unmixed reforming* e *chemical looping*), empregando-se diversos combustíveis (etanol, glicerol, metanol, *n*-butanol, biogás e metano). Além disso, foi analisada a utilização direta de combustível (glicerol) no ânodo de uma célula SOFC. Com a realização desta Tese, as seguintes metas gerais foram alcançadas: (1) A partir de dados experimentais da literatura, foi possível propor explicações, com base na termodinâmica, capazes de justificar tais valores e tendências reportados; (2) Elaboração de diagramas práticos em que são mostradas as condições otimizadas para a realização de experimentos, o que é de utilidade para pesquisadores experimentalistas; (3) Proposição de novas rotas eficientes e limpas para produção de H_2 e geração de eletricidade com o uso de células a combustível; (4) Demonstração da aplicabilidade e robustez de uma ferramenta de fácil entendimento e acesso para uso em simulações termodinâmicas envolvendo problemas convexos.

ABSTRACT

The present Thesis, whose elaboration is based on the integration of six scientific papers published in refereed international journals, is focused on carrying out thermodynamic simulations applied to hydrogen production and electricity generation from fuel cells operating at low temperatures (*Proton Exchange Membrane Fuel Cell* – PEMFC) and high temperatures (*Solid Oxide Fuel Cell* – SOFC). Different thermochemical routes for hydrogen production were simulated (steam reforming, auto-thermal reforming, partial oxidation, sorption enhanced steam reforming, unmixed reforming and chemical looping), considering the use of a wide variety of fuels (ethanol, glycerol, *n*-butanol, methanol, biogas and methane). In addition, the direct utilization of a fuel (glycerol) in the SOFC anode is evaluated. The following general goals were achieved with this Thesis: (1) From experimental data obtained from literature, it was possible to propose explanations, based on thermodynamics, which were able to justify these reported values and trends; (2) Elaboration of practical diagrams, in which the optimized conditions for carrying out experiments are indicated. This is particularly useful for experimental researchers; (3) Proposal for new clean and efficient routes for hydrogen production and electricity generation from fuel cells; (4) Demonstration of applicability and robustness of a tool, which is easy to understand and apply, for thermodynamic simulations comprising convex problems.

CAPÍTULO 1: INTRODUÇÃO

1.1. Relevância da Pesquisa

As questões ambientais e energéticas, em particular, a geração de energia sustentável e o controle das emissões de carbono a partir de combustíveis fósseis, estão entre os maiores desafios que o mundo está enfrentando atualmente [1]. Assim sendo, é importante a utilização de fontes renováveis de energia, como os biocombustíveis, além do desenvolvimento de tecnologias que apresentem maior eficiência energética. No caso da utilização de combustíveis fósseis, tecnologias eficientes, com capacidade de sequestrar CO_2, devem ser desenvolvidas [2].

Vale mencionar também o grande incentivo que vem sendo dado à instalação da Geração Distribuída. Em âmbito nacional, convém citar que, em 2009, a Agência Nacional de Energia Elétrica (ANEEL) reformulou o Procedimento de Distribuição (PRODIST) e publicou o Decreto Lei 5163/04, que institui a Geração Distribuída no Brasil [3]. Geração Distribuída é aquela em que a produção de energia ocorre de forma descentralizada no próprio local, ou próximo de onde essa energia é utilizada. Possui como vantagens a redução de custos de transmissão e distribuição, o aproveitamento de recursos renováveis locais e o aumento da eficiência pela cogeração (geração de energia elétrica combinada com aproveitamento de calor). Além desses aspectos, salienta-se que o excedente de energia produzida pode ser vendido, utilizando-se, portanto, das redes de distribuição. Neste contexto, células a combustível para a Geração Distribuída têm sido consideradas de grande valor, devido à alta eficiência teórica e ao fato de que, em caso o ânodo da célula seja abastecido por hidrogênio puro, o único co-produto é vapor de água. Desse modo, as células a combustível apresentam-se como uma tecnologia capaz

de satisfazer os pré-requisitos mencionados no início deste texto: alta eficiência com compromisso ambiental.

Contudo, a geração de poluentes durante a produção de hidrogênio deve ser avaliada no processo global, considerando não somente a célula a combustível, mas também o processador de combustível. Além disso, o processo de produção de H_2 deve ter uma alta seletividade em relação ao H_2, minimizando a formação de produtos indesejáveis, além de ter o custo minimizado. Afinal, busca-se desenvolver uma tecnologia que tenha a capacidade de ser empregada em larga escala. A produção de hidrogênio, por meio da utilização das tecnologias atualmente disponíveis, envolve um grande consumo de gás natural (combustível fóssil), que, por sua vez, emite mais gases do efeito estufa. Para mitigar este efeito ambientalmente nocivo, unidades de sequestro de CO_2 devem ser instaladas no local de produção. Aliado a isto, há o problema da escassez dos combustíveis fósseis. Em contrapartida, a produção de H_2 a partir de fontes renováveis derivadas da agricultura ou de outros tipos de resíduos é sustentável, devido a menor (ou nula) emissão líquida de CO_2. Portanto, custos com infraestrutura de captura de CO_2 são evitados, aumentando a flexibilidade e melhorando a economia de um processo de reforma distribuído ou semicentralizado [1]. Além disso, existe grande disponibilidade de biomassa, o que facilita a instalação da Geração Distribuída. Biomassa é produto da fotossíntese. Desse modo, o hidrogênio produzido a partir da biomassa pode ser classificado como "CO_2-neutro", pois o CO_2 que é liberado durante a produção de hidrogênio é consumido para a geração da biomassa.

Atualmente, 95% da produção de hidrogênio provém da reforma a vapor do gás natural [4]. O aumento esperado da demanda por hidrogênio para aplicação em células a combustível dita, contudo, o desenvolvimento de novos métodos para a produção de hidrogênio. O uso de biocombustíveis – etanol, glicerol, *n*-butanol e biometanol – para a

produção de hidrogênio através de diferentes processos (reforma a vapor, oxidação parcial, reforma a seco ou reforma autotérmica) tem a vantagem de ser "CO_2-neutro". Dentre os biocombustíveis líquidos, etanol e glicerol são considerados como candidatos promissores para a produção de H_2. O etanol pode ser produzido de forma renovável a partir da fermentação de diversas fontes de biomassa, incluindo resíduos da agroindústria, fração orgânica do resíduo sólido municipal, etc. [5]. O glicerol é produzido como co-produto durante a produção de biodiesel pela transesterificação de óleos vegetais. Obtêm-se 100 toneladas de glicerol a cada 1000 toneladas de biodiesel que são produzidos. Desse modo, a produção de H_2 parece ser uma alternativa capaz de valorizar grandes quantidades de glicerol [6]. Além do etanol e glicerol, *n*-butanol e biometanol são também considerados como biocombustíveis apropriados para a produção de H_2. Recentemente, Nahar e Madhani [7] investigaram, por meio de uma análise termodinâmica, a produção de H_2 através da reforma a vapor de *n*-butanol. *n*-butanol, também conhecido por biobutanol, pode ser produzido pelo processo clássico de fermentação e suas matérias-primas incluem cana de açúcar, milho, trigo e biomassa lignocelulósica [8]. Entretanto, biobutanol também pode ser produzido de uma maneira nova e mais significativa, através da manipulação de sistemas biológicos ou da engenharia metabólica [9]. Mais recentemente, a produção de *n*-butanol a partir de macroalgas tem atraído atenção considerável, porque as algas marinhas constituem uma fonte potencialmente sustentável de biomassa que não requer terra arável ou água potável [10]. Com respeito ao biometanol, este termo se refere ao metanol renovável preparado a partir do gás de síntese (*syngas*, composto principalmente por CO e H_2) proveniente da pirólise da biomassa ou do processamento do biogás (CO_2 + CH_4) [11]. Todos estes biocombustíveis mencionados anteriormente podem ser previamente convertidos em H_2, por meio de reações de reforma em um reformador para uso

posterior em células a combustível de baixa temperatura, ou ser diretamente convertidos no ânodo de uma célula a combustível de alta temperatura, onde ocorrem tanto reações de reforma como eletroquímicas. A utilização direta do combustível no ânodo simplifica enormemente a planta, aumentando sua flexibilidade para aplicação em instalações de Geração Distribuída.

Além dos biocombustíveis mencionados anteriormente (etanol, glicerol, *n*-butanol e metanol), ressalta-se a importância do biogás como biocombustível na produção de H_2. O biogás, que até pouco tempo era visto apenas como um subproduto indesejado, obtido a partir da decomposição anaeróbica da matéria orgânica contida nos resíduos de atividades agroindustriais e agropecuárias, resíduos sólidos urbanos e nos efluentes domésticos e industriais, é atualmente reconhecido como um biocombustível, cujo aproveitamento na geração de eletricidade significa uma expressiva redução de gastos com energia e até mesmo fonte de receita nos setores de agronegócio e de saneamento básico. No Brasil, a Instrução Normativa 390/09 da ANEEL regulamenta a Geração Distribuída com biogás e saneamento ambiental [12]. Em países desenvolvidos, a estratégia de produção de eletricidade a partir do biogás baseia-se tanto na conversão do biogás em H_2 para posterior abastecimento do ânodo de uma célula a combustível, ou, alternativamente, na utilização direta de biogás no ânodo de uma célula a combustível de alta temperatura [13]. No Brasil, contudo, a realidade ainda é bem distinta. Enquanto, em alguns casos, o biogás é utilizado em turbinas a gás ou motores de combustão – o que corresponde à obtenção de uma eficiência muito menor daquela que seria obtida com a célula a combustível [14] –, em outras situações, o biogás é simplesmente queimado em '*flares*', sem nenhum aproveitamento energético. Convém salientar que muita pesquisa ainda é feita, conforme se verifica na literatura internacional, buscando condições experimentais otimizadas para a reação de reforma,

bem como o desenvolvimento de catalisadores que sejam resistentes ao H_2S presente no biogás e à deposição de carbono que ocorre durante a conversão [15-17].

Para o desenvolvimento de tecnologias eficientes para a produção de H_2 e geração de eletricidade através de células a combustível, necessita-se de muita pesquisa referente ao mapeamento das condições otimizadas de operação, ao planejamento de rotas alternativas para a conversão de diferentes tipos de combustíveis bem como à elaboração de materiais com propriedades adequadas para uso em reformadores e células a combustível.

O presente trabalho visa contribuir para o desenvolvimento do processo de reforma de diferentes combustíveis, sejam de origem renovável (etanol, glicerol, metanol, *n*-butanol, biogás), ou fóssil (gás natural). Do mesmo modo, esta pesquisa fornece informações úteis para a operação de células a combustível com biocombustíveis. Esta Tese tem como objetivos específicos:

a) Analisar a reforma a vapor do etanol em um reformador convencional, investigando as condições mais adequadas para a maximização de H_2 (combustível para a célula a combustível), minimização de CH_4, CO e prevenção da deposição de carbono (associada à desativação do catalisador); verificar a tendência à deposição de carbono em diferentes sistemas (estável e metaestável) e propor explicações para desvios entre resultados experimentais e previsões da termodinâmica. Os resultados desta análise são encontrados no artigo da seção 4.1.1, página 95: *Thermodynamic analysis of ethanol steam reforming using Gibbs energy minimization method: A detailed study of the conditions of carbon deposition.*

b) Avaliar o efeito que tem a adição de CaO no reformador na qualidade do produto gasoso, ou seja, verificar a possibilidade de obtenção de um gás rico em H_2, com quantidades mínimas de CO, CO_2 e CH_4; avaliar a possibilidade de obtenção de um reformato rico em H_2 (>95 mol%), com CO em concentrações na faixa de 10ppm, em um único passo, isto é, sem a necessidade de reatores de purificação, como o reator do tipo '*water-gas shift*' (WGS), onde ocorre a reação de deslocamento da água ($CO+H_2O=CO_2+H_2$), e reatores do tipo COPROX (*CO Preferential Oxidation*), onde ocorre a oxidação preferencial do CO; avaliar a eficiência térmica do processo na presença de CaO. Espera-se que o CaO que é colocado juntamente ao catalisador no reformador capture o CO_2, deslocando o equilíbrio em favor da produção de H_2. Isto contribui para o desenvolvimento de um processador de combustível mais compacto e eficiente. Os resultados desta análise são encontrados no artigo da seção 4.1.2, página 106: *Hydrogen production by sorption enhanced steam reforming of oxygenated hydrocarbons (ethanol, glycerol, n-butanol and methanol): Thermodynamic modelling.*

c) Analisar a utilização direta do glicerol em células a combustível do tipo óxido sólido operando em temperaturas intermediárias (IT-SOFC, *Intermediate Temperature Solid Oxide Fuel Cell*); apresentar a relação entre deposição de carbono no ânodo (indesejável, pois leva à perda de desempenho da célula, devido à desativação do eletrocatalisador) e densidade de corrente; apresentar as quantidades mínimas de H_2O, CO_2 e ar que devem ser adicionados juntamente ao glicerol no ânodo para a prevenção da deposição de carbono a potencial de circuito aberto; verificar o efeito da condução mista iônica-eletrônica na formação de carbono no ânodo. Os resultados desta análise são encontrados no artigo da seção 4.1.3, página 126: *Operation of solid oxide fuel cells*

on glycerol fuel: a thermodynamic analysis using the Gibbs free energy minimization approach.

d) Apresentar as condições mais adequadas de operação de células a combustível do tipo óxido sólido de temperatura intermediária (IT-SOFCs), com diferentes tipos de eletrólitos (condutores de íons de oxigênio e hidrogênio), abastecidas com glicerol no ânodo. Neste caso, é investigada a reforma direta do glicerol no ânodo da SOFC e o efeito que o tipo de eletrólito usado na SOFC tem na eficiência e na tendência à deposição de carbono no ânodo. Os resultados desta análise são encontrados no artigo da seção 4.1.4, página 135: *Thermodynamic study on glycerol-fuelled intermediate-temperature solid oxide fuel cells (IT-SOFCs) with different electrolytes*

e) Modelar termodinamicamente o processo de '*unmixed reforming*' usando metano como combustível em um reator de leito fixo; identificar as condições otimizadas de operação (processo autotérmico com a produção de um gás rico em H_2). A reforma convencional exige energia, devido ao caráter endotérmico da reação de conversão do combustível em H_2. Deste modo, o combustível deve ser queimado em um combustor catalítico que está acoplado às paredes do reformador para fornecimento de energia. Para as reações de reforma que ocorrem na presença de CaO, energia é necessária para a regeneração (durante a reforma, $CaCO_3$ é formado devido à reação do CaO com CO_2). Com a tecnologia '*unmixed reforming*', o calor necessário para as reações é fornecido no próprio processo, mediante a oxidação de um metal com o ar (etapa exotérmica). Na etapa seguinte, o óxido que foi formado é reduzido pela reação com o combustível (etapa endotérmica). Este metal em sua forma reduzida funciona, então, como catalisador para as reações de reforma. Na presença de CaO, o carbonato, que foi formado na etapa de alimentação com combustível, é regenerado a CaO quando

ar é injetado no reator. A oxidação do metal libera grande quantidade de calor que é suficiente para a decomposição do $CaCO_3$. Os resultados desta análise são encontrados no artigo da seção 4.1.5, página 150: *Towards H_2-rich gas production from unmixed steam reforming of methane: Thermodynamic modeling*

f) Avaliar o desempenho do sistema constituído pela integração da célula a combustível de baixa temperatura do tipo PEMFC (*Proton Exchange Membrane Fuel Cell*) com diferentes processadores de combustível (reformador convencional – onde ocorre a reforma a vapor, oxidação parcial ou reforma autotérmica – ou reformadores operando com a tecnologia de *chemical looping*). A simulação considera que os reformadores operam com biogás purificado. A tecnologia de *chemical looping* é muito similar a de *unmixed reforming*; no entanto, no caso do *chemical looping*, o processo ocorre em dois reatores de leito fluidizado que estão interconectados: um reator alimentado por ar e um reator alimentado por combustível. Na tecnologia de *chemical looping*, há circulação de sólidos entre os reatores. O calor gerado no reator de ar deve ser suficientemente alto para satisfazer o balanço de energia do sistema. Os resultados desta análise são encontrados no artigo da seção 4.1.6, página 166: *Performance of a PEMFC system integrated with a biogas chemical looping reforming processor: a theoretical analysis and comparison with other fuel processors (steam reforming, partial oxidation and auto-thermal reforming)*.

Como objetivo comum a todos os estudos realizados, está a validação dos resultados teóricos com resultados experimentais da literatura. Valores ou tendências reportados em trabalhos experimentais são considerados para avaliar a consistência das simulações. Do mesmo modo, o acompanhamento das citações das publicações, em periódicos

reconhecidos da literatura, é realizado, com o intuito de avaliar como os resultados teóricos deste trabalho são utilizados na pesquisa experimental de outros autores, bem como na realização de outros trabalhos teóricos.

Para a realização das simulações envolvendo a determinação de equilíbrios termodinâmicos, emprega-se o método da minimização da energia de Gibbs total do sistema. Trata-se de um problema de programação não linear que consiste em minimizar a função objetivo (descrição da energia de Gibbs total do sistema), sujeita às restrições do balanço de massa elementar. Para a implementação do modelo termodinâmico, propõe-se, neste trabalho, o uso de ferramentas computacionais de fácil entendimento e maior acessibilidade por parte do usuário. Apresenta-se, em detalhe, como a ferramenta *Solver* do Excel do pacote Office da Microsoft pode ser empregada no cálculo de equilíbrios termodinâmicos, para um sistema multicomponente e multifásico composto por uma fase gasosa (constituída por várias espécies) e por fases condensadas estequiométricas. A ferramenta *Solver* usa um algoritmo de otimização não-linear, conhecido como *Método dos Gradientes Reduzidos Generalizados (GRG)*, na resolução de problemas de minimização/maximização da função objetivo sujeita a restrições. Do mesmo modo, simulações envolvendo balanços de massa e de energia são conduzidas em ambiente Excel para análise do desempenho da planta. O modelo eletroquímico, utilizado para descrever a curva de polarização de uma célula do tipo PEMFC, também é implementado em planilhas do Excel.

1.2. Estrutura da Tese por Integração de Artigos Científicos

A estrutura desta Tese de Doutoramento segue a modalidade 'Tese por Integração de artigos'. De acordo com as normas do Regimento Interno do Programa de Pós-Graduação em Engenharia de Minas, Metalúrgica e de Materiais (PPGE3M), a Tese pode ser constituída por, no mínimo, três artigos científicos publicados em periódicos internacionais reconhecidos pela CAPES. Além dos artigos, a Tese inclui Resumo, Abstract, Introdução, Revisão da Literatura, Integração dos artigos e referências bibliográficas. Durante a realização desta Tese, foram publicados seis artigos em periódicos internacionais reconhecidos com *Qualis* Capes A1 na área de Engenharias II, que é a área de concentração do PPGE3M.

Desse modo, a presente Tese, elaborada nos moldes acima descritos, está estruturada da seguinte forma:

Capítulo* 1: *Introdução: Nesta seção, o leitor é informado a respeito do contexto envolvendo a utilização de biocombustíveis para produção de H_2 e geração de eletricidade a partir de células a combustível. Além disso, são apresentados os objetivos e a metodologia de trabalho.

Capítulo 2: Estado da Arte: Nesta seção, é feita uma revisão da literatura, buscando familiarizar o leitor com as diferentes tecnologias existentes para a produção de H_2 e com os diferentes tipos de células a combustível. Da mesma forma, os fundamentos de otimização são apresentados e é explicado como técnicas de otimização são úteis na termodinâmica para a determinação de equilíbrios em sistemas multicomponentes. Uma abordagem detalhada com respeito a modelos convexos é apresentada.

Capítulo 3: Metodologia: Nesta seção, estão descritos os métodos que foram empregados para a realização das simulações e publicação dos artigos. Informações adicionais, que não são encontradas na metodologia apresentada nos artigos, estão incluídas neste capítulo.

Capítulo 4: Resultados: Nesta seção, estão incluídos os artigos que foram publicados, em sua forma final, tal como são encontrados no periódico. Neste capítulo, também é feita a discussão integrando os artigos, mostrando ao leitor a relação existente entre os diferentes artigos, e como os resultados dos diferentes trabalhos se complementam. Além disso, é mencionado como a metodologia e os resultados teóricos do presente trabalho vêm sendo utilizados por outros autores na literatura.

Capítulo 5: Conclusões: São apresentadas conclusões gerais referentes aos trabalhos publicados.

Capítulo 6: Referências: As referências bibliográficas utilizadas no texto de integração desta Tese estão mencionadas neste capítulo.

CAPÍTULO 2: ESTADO DA ARTE

2.1. Rotas para a geração de hidrogênio

O hidrogênio não é encontrado em sua forma molecular (H_2) na Terra. Contudo, compostos de hidrogênio são abundantes na natureza, e, por meio de rotas químicas e eletroquímicas, é possível obter H_2 molecular. [18, 19]. Dentre estas rotas, podem ser citadas: eletrólise da água, gaseificação do carvão, reforma a vapor, reforma autotérmica e oxidação parcial. Além dessas, outros processos inovadores podem ser mencionados: reforma a vapor com captura *in situ* de CO_2, *chemical looping*, *unmixed reforming*, dissociação fotocatalítica da água.

Este trabalho está focado nas tecnologias mencionadas acima, excetuando-se a gaseificação do carvão, eletrólise da água e dissociação fotocatalítica.

2.1.1. Reforma a vapor

O processo de reforma a vapor é a rota mais conhecida para a produção de hidrogênio e de gás de síntese (mistura de CO e H_2), o qual é utilizado em processos de larga escala como a síntese do metanol e da amônia. O processo mais utilizado mundialmente é a reforma a vapor do gás natural. As principais reações envolvidas neste processo são:

Reforma a vapor do metano:

$$CH_4 + H_2O = CO + 3H_2; \qquad \Delta H = +206{:}1 \text{ kJ mol}^{-1} \qquad \text{(R1)}$$

Reação deslocamento da água (WGS, *water-gas shift*):

$$CO + H_2O = CO_2 + H_2; \qquad \Delta H = -41 \text{ kJ mol}^{-1} \qquad \text{(R2)}$$

Metanação reversa:

$$CH_4 + 2H_2O = CO_2 + 4H_2; \quad \Delta H = +164 \text{ kJ mol}^{-1} \qquad (R3)$$

Das reações acima, é fácil perceber que a reforma a vapor é um processo altamente endotérmico. A energia necessária provém da reação de combustão do combustível. Um reformador é constituído por tubos, em que o canal onde ocorre a reação de reforma é aquecido pelo calor proveniente do canal de combustão (Fig.1). No canal de reforma, o catalisador comumente utilizado é Ni/Al_2O_3; já no canal de combustão, os catalisadores são a base de metais nobres, como Pt e Pd, por exemplo. [20].

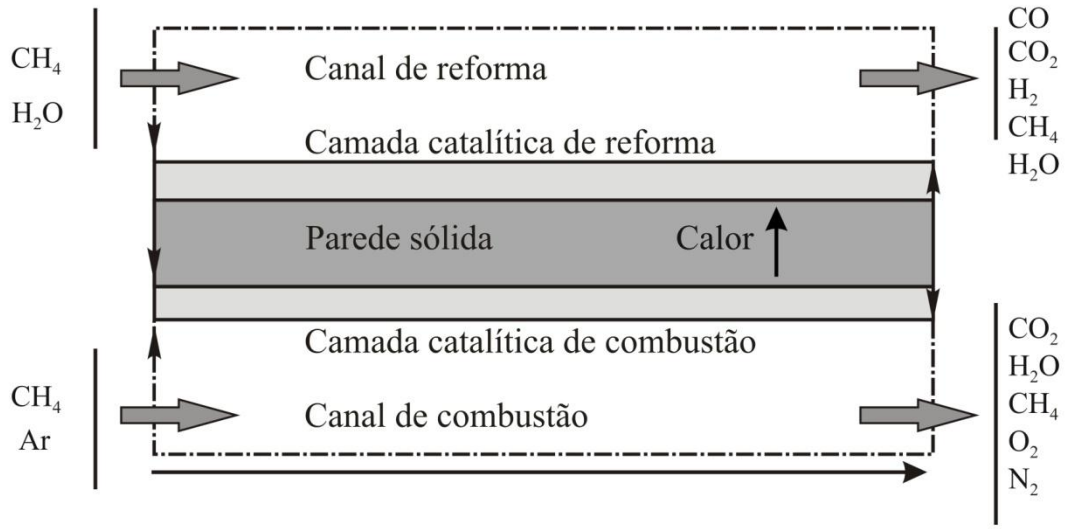

Fig.1. Geometria de um reformador em que o canal de reforma está acoplado ao canal de combustão, adaptado de [20].

2.1.2. Oxidação parcial

A oxidação parcial catalítica é uma tecnologia que consiste na oxidação sub-estequiométrica de metano ($CH_4 + 0.5O_2 \rightarrow CO + 2H_2$). Neste processo, utiliza-se uma razão de ar/combustível menor em comparação à combustão completa. Desta forma, os produtos obtidos são CO e H_2 ao invés de CO_2 e H_2O. Trata-se de um processo exotérmico ($\Delta H_{298} = -36000$ J mol^{-1}) que permite uma rápida ignição dos reagentes e o uso de um reator menor. Vários trabalhos têm sido desenvolvidos usando esta rota de conversão. Convém salientar que, durante a operação, ar é preferencialmente utilizado, uma vez que o uso de oxigênio puro não é economicamente viável. Como reportado em [21], até 40% dos gastos de uma planta de reforma baseada na oxidação parcial catalítica é atribuído à planta de oxigênio. O uso de O_2 puro requer uma unidade de separação de ar (do inglês, *Air Separation Unit*, ASU), a qual encarece muito uma planta de produção de hidrogênio e, no caso da produção de grandes quantidades de O_2, a demanda de energia aumenta grandemente [22]. Deste modo, a desvantagem de qualquer operação de oxidação parcial com adição de ar é a diluição do reformato com N_2. Como discutido em trabalhos anteriores [23-24], a diluição é prejudicial à operação da célula a combustível porque reduz o potencial de circuito aberto e, em altas densidades de corrente, sobrepotenciais maiores devido ao transporte de massa são observados experimentalmente.

Este processo é bem estabelecido como não-catalítico, mas, nos últimos anos, o processo de oxidação parcial catalítica tem recebido uma atenção considerável, como um dos modos mais econômicos de se produzir hidrogênio, em comparação com o processo de reforma a vapor. No processo de oxidação parcial, assim como no processo de reforma a vapor, um dos maiores problemas tecnológicos é constituído pelo fenômeno da desativação do catalisador, principalmente pela deposição de carbono nos

sítios ativos. A pesquisa referente ao processo de oxidação parcial catalítica tem sido focada no metano com a utilização do catalisador de Ni, já que se constitui no combustível mais empregado na produção de H_2. Sistemas com base em catalisadores de Ni resultam em alta produção do gás de síntese (CO e H_2), mas requerem operação em temperaturas menores para redução da perda metálica, enquanto catalisadores a base de Pt mostram um desempenho muito estável, mas com menor seletividade de H_2. [25].

Conforme a quantidade de oxigênio é aumentada, o combustível tende à formação de CO_2 e H_2O, e a quantidade de calor liberado também aumenta. Considere, por exemplo, o processo de oxidação parcial do etanol, em que a reação se torna cada vez mais exotérmica, à medida que aumenta a quantidade de oxigênio.

$CH_3CH_2OH + 0.5O_2 \rightarrow 2CO + 3H_2$, $\Delta Hr = +57\ kJ\ mol^{-1}$
$CH_3CH_2OH + O_2 \rightarrow CO_2 + CO + 3H_2$, $\Delta Hr = -226\ kJ\ mol^{-1}$
$CH_3CH_2OH + 1.5O_2 \rightarrow 2CO_2 + 3H_2$, $\Delta Hr = -509\ kJ\ mol^{-1}$
$CH_3CH_2OH + 3O_2 \rightarrow 2CO_2 + 3H_2O$, $\Delta Hr = -1368\ kJ\ mol^{-1}$

Existem diferentes tipos de reatores para a utilização na oxidação parcial. A mistura gasosa pré-aquecida entra no reator e passa pelo catalisador monolítico, havendo a conversão em H_2 e CO, como indica a Fig. 2.

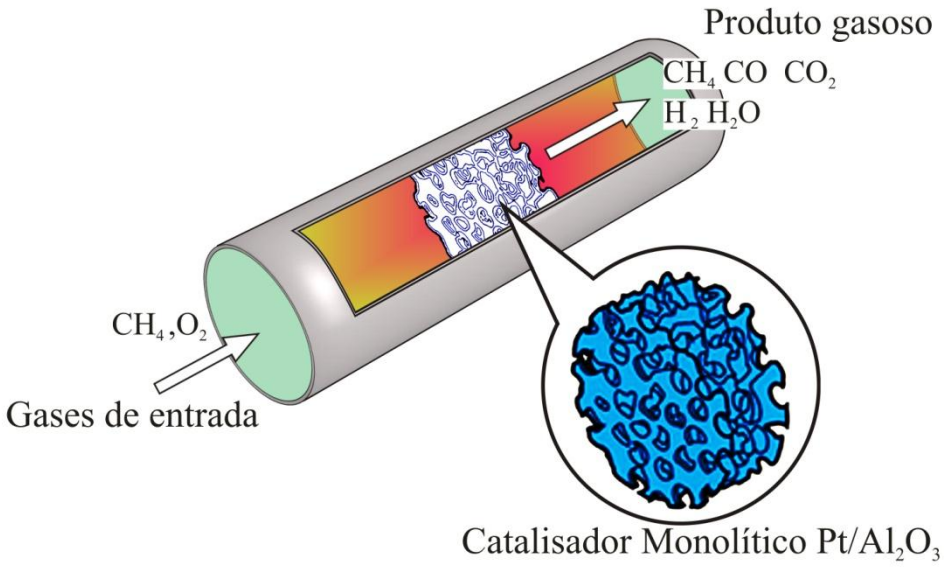

Fig. 2. Reator, com design compacto, para oxidação parcial catalítica, usando CH_4 e O_2 como reagentes, adaptado de [26].

Nemann e colaboradores [27] propõem um reator (Fig. 3) baseado em um catalisador monolítico inserido entre duas camadas monolíticas, inertes, feitas por extrusão, que servem como reservatório de calor. Assim, os reagentes, que estão à temperatura ambiente, entram na camada de catalisador, onde a reação ocorre. O calor de reação aumenta a temperatura do catalisador, do produto gasoso e, consequentemente, da zona inerte por onde passa o produto gasoso antes de deixar o reator. No modo reverso de operação, os gases de alimentação, que estão à temperatura ambiente, são, então, aquecidos ao trocar calor com a zona inerte que teve sua temperatura aumentada pela passagem dos produtos gasosos da etapa anterior. Os reagentes já chegam, assim, até o catalisador com uma temperatura elevada, e, com a reação de oxidação, têm a sua temperatura aumentada ainda mais. Ao sair da zona do catalisador, os produtos gasosos a altas temperaturas trocam calor com a 'nova' zona inerte por onde passam, resfriando os gases de saída e aquecendo a zona inerte. O ciclo é repetido, desta vez na direção oposta. Se esta reversão no sentido da alimentação dos gases é repetida em uma

frequência apropriada, ao longo dos ciclos, este processo resulta em temperaturas muito elevadas na zona de reação e, comparativamente, em temperaturas menores na zona de saída do reator.

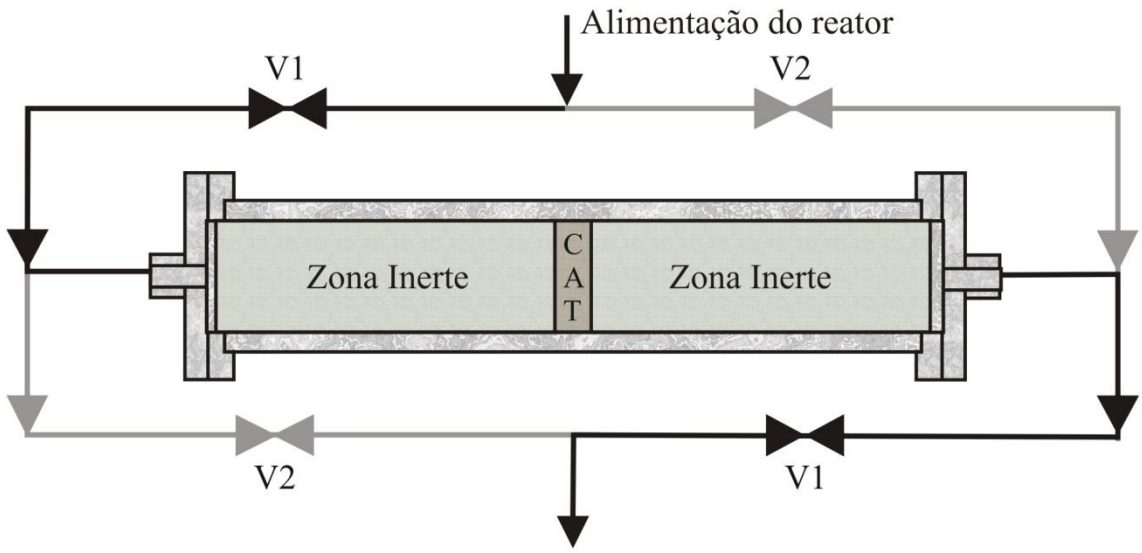

Fig. 3. Esquema de um reator para oxidação parcial catalítica. O catalisador (cat) encontra-se na parte central do reator, entre as zonas inertes. 4 válvulas , que são operadas aos pares (V1 e V2), permitem reverter a direção do fluxo no reator, adaptado de [27].

2.1.3. Reforma autotérmica

A reforma autotérmica é muito similar à oxidação parcial catalítica. A principal diferença diz respeito à utilização de água no reformador. Assim, para valores adequados da razão ar/combustível, em que ocorre a oxidação parcial do metano, a produção de H_2 no reator de reforma autotérmica é aumentada, devido ao efeito do vapor de água na reação do tipo *water-gas shift* ($CO + H_2O \rightarrow CO_2 + H_2$). A Fig. 4 mostra o esquema de um reator de reforma autotérmica abastecido por gás natural. Nesta representação, está indicada a adição de oxigênio, embora já tenha sido mencionado na

seção anterior que a adição de oxigênio puro não é economicamente viável, devido aos altos custos envolvidos em uma planta de separação de oxigênio. O processo de reforma autotérmica combina a oxidação parcial e a reforma a vapor em um único processo. Antes de entrar no reator, a mistura gasosa é pré-aquecida. No reator, há, então, a combustão do combustível com o oxigênio, e a mistura passa pelo catalisador, o que permite que a reação de reforma seja levada até o equilíbrio termodinâmico.

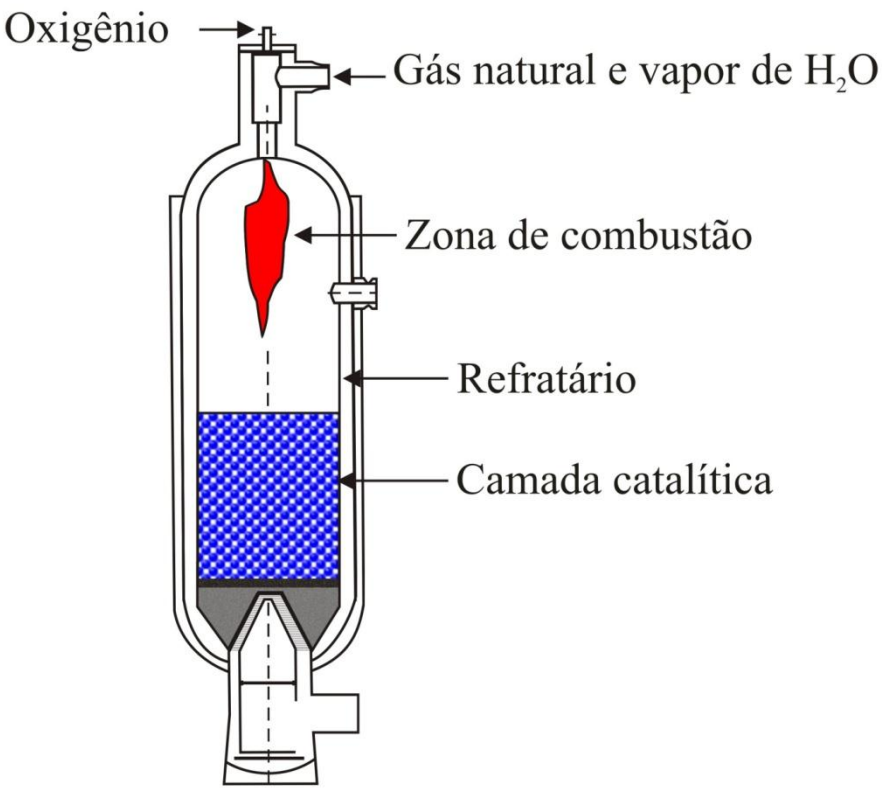

Fig. 4. Esquema de um reator de reforma autotérmica abastecido com gás natural, vapor de água e oxigênio, adaptado de [28].

2.1.4. Reforma a vapor com captura in situ de CO_2

Apesar da simplicidade aparente da reação estequiométrica para a produção de hidrogênio,

$$C_xH_yO_z + (2x\text{-}z)H_2O = (2x\text{-}z+0.5y)H_2 + xCO_2 \quad \text{(R8)},$$

a reforma a vapor de um hidrocarboneto oxigenado envolve um sistema de reação complexo, com caminhos indesejáveis de reação. Deste modo, a seletividade do H_2 é afetada e sua produção é limitada pelo equilíbrio termodinâmico. A fim de se obter a produção máxima de H_2, o processo convencional de reforma a vapor tem de ser conduzido em três passos, para que se possa abastecer o ânodo de uma célula PEMFC (*Polymer Electrolyte Membrane Fuel Cells*). O primeiro passo envolve a conversão do hidrocarboneto oxigenado em H_2, CH_4, CO e CO_2, seguido por um passo realizado a uma temperatura menor, onde CO é convertido em CO_2 e H_2 pela reação *water-gas shift* (WGS).

$$CO+H_2O=CO_2+H_2 \quad \Delta H(298) = -41.2 \text{ kJ mol}^{-1} \quad \text{(R9)}$$

Como a reação de deslocamento é limitada pelo equilíbrio termodinâmico, e o ânodo da PEMFC deve ser abastecido por H_2 de alta pureza, contendo CO em uma concentração menor do que 20ppm para evitar a desativação da Pt, um passo adicional tem que ser conduzido para remover o CO pela oxidação preferencial. Assim, no processo de reforma convencional, além do reformador e do reator WGS, um terceiro reator – COPROX, onde o CO residual é totalmente convertido em CO_2 através da reação preferencial de oxidação do CO – é necessário. No entanto, a comercialização em larga escala de geradores empregando a tecnologia de células a combustível requer um sistema de geração de H_2 compacto e eficiente. Portanto, componentes desnecessários devem ser eliminados da planta. Neste contexto, o processo de reforma

com captura *in situ* de CO_2 (da literatura, conhecido como *Sorption Enhanced Steam Reforming*) apresenta-se como uma alternativa promissora para a produção de H_2 de alta pureza em um único passo (*single step*). O conceito de reforma com captura *in situ* de CO_2 está baseado no princípio de *Le Chatelier*, em que a reação de equilíbrio é deslocada em favor da produção de H_2 com a remoção de CO_2 (ver reação (R9)). Assim, se o CO_2 gerado durante a reação de reforma é separado da fase gasosa, usando-se um aceptor sólido como CaO, a produção de H_2 pode ser favorecida até seu máximo valor. Neste caso, o reator contém tanto o catalisador para o processo de reforma como CaO para remoção do CO_2. A captura de CO_2 e a reação global da reação de reforma com a captura *in situ* de CO_2 são descritas nas reações (R10) e (R11), respectivamente:

$$CaO(s) + CO_2 = CaCO_3(s) \qquad \Delta H(298) = -179.8 kJ\ mol^{-1} \qquad (R10)$$

$$C_xH_yO_z + (2x\text{-}z)H_2O + xCaO = xCaCO_3 + (2x\text{-}z\text{+}0.5y)H_2 \qquad (R11)$$

A constante de equilíbrio da reação (R10) é favorecida com o decréscimo da temperatura, variando de 0,25 (a 1273) até 9271 (a 773K). Para a reação (R11), os correspondentes valores de entalpia para o etanol (C_2H_6O), glicerol ($C_3H_8O_3$), *n*-butanol ($C_4H_{10}O$) e metanol (CH_4O) são −186, −411, −325 e −92 kJ mol^{-1}. Estes biocombustíveis foram considerados na presente pesquisa. Note que, no processo de reforma com captura *in situ* de CO_2, a exotermicidade da reação global poderia levar a um processo auto-térmico durante a reforma.

Para que o processo seja economicamente viável, o material aceptor de CO_2 deve ser regenerado através dos ciclos. A reação de regeneração, que é a inversão da reação (R10), é altamente endotérmica. Assim sendo, a energia necessária na regeneração deve ser avaliada na análise da eficiência e de viabilidade do processo.

A Fig. 5 mostra o esquema de uma planta envolvendo o processo de reforma de um combustível (nesta ilustração, butanol). Primeiramente, o combustível líquido é vaporizado, misturado com vapor de água e aquecido até a temperatura de entrada do reformador. Então, a mistura gasosa é alimentada no reformador, que contém, além do catalisador (*e.g.* Ni/Al_2O_3), o material para a captura do CO_2 (e.g. CaO). O gás rico em H_2 que deixa o reformador é alimentado diretamente em um reator onde ocorre a oxidação preferencial de CO, para reduzir o teor de CO a teores tão pequenos quanto 10ppm. Neste caso, não se necessita um reator do tipo WGS (*water-gas shift*, $CO+H_2O=CO_2+H_2$), pois o gás que sai do reformador, já contém teores muito baixos de CO. Conforme a reforma vai procedendo no reformador, a maior parte do CaO vai se convertendo em carbonato sólido ($CaCO_3$). O carbonato é, então, introduzido em um regenerador, onde ocorre o desprendimento de CO_2 do $CaCO_3$, através da reação endotérmica de decomposição. A energia para o regenerador provém da combustão do combustível ($C_4H_{10}O$). O CO_2 que sai do regenerador é resfriado em um trocador de calor e armazenado em um tanque.

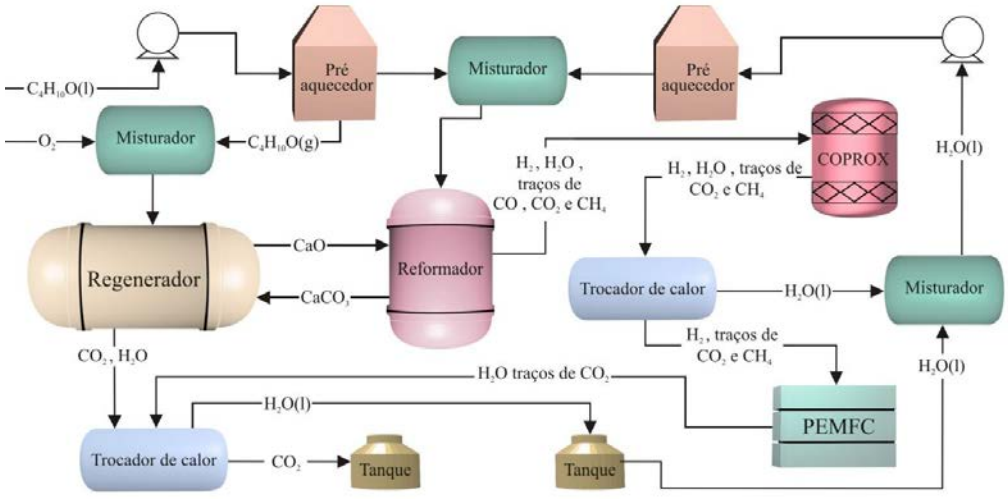

Fig. 5. Diagrama esquemático mostrando a planta que engloba a rota de produção do H_2 em um processo que utiliza a captura *in situ* de CO_2,adaptado de [29].

2.1.5. 'Unmixed reforming'

O processo conhecido como *unmixed reforming* é um processo alternativo à reforma a vapor. Esta rota alternativa baseia-se no uso de sopros alternados de ar e combustível para criar um processo cíclico. Portanto, os sopros de ar e de combustível não se misturam, diferentemente das técnicas descritas nas seções anteriores, como a reforma autotérmica e oxidação parcial. O processo *unmixed reforming* utiliza um material de transferência de oxigênio, um óxido metálico, por exemplo, que, em sua forma reduzida, funciona como catalisador de reforma a vapor. Óxido de níquel (NiO) é normalmente escolhido como o carreador de oxigênio (*oxygen carrier*), já que, após a redução, o níquel metálico (Ni) formado funciona como um excelente catalisador para as reações de reforma. Além disso, o níquel tem a facilidade de ser rapidamente oxidado e reduzido [30-37]. Durante o processo de *unmixed reforming*, um sopro de ar (primeira metade do ciclo, em que Ni é convertido em NiO) é seguido por um sopro de combustível/vapor de água (segunda metade do ciclo, em que NiO é regenerado a sua forma metálica, Ni, ocorrendo a reação de reforma). A oxidação do metal, que ocorre na primeira metade do ciclo, é altamente exotérmica, gerando, assim, o calor necessário para as reações de reforma endotérmicas que ocorrem na etapa subsequente. Desse modo, o processo pode ocorrer de forma autotérmica. Além disso, note que há separação do N_2, gás inerte, do produto gasoso contendo H_2. A tecnologia *unmixed reforming* pode ainda ser otimizada ao introduzir um material para captura *in situ* de CO_2, como o CaO. De fato, a calcita ($CaCO_3$) pode ser introduzida no reator juntamente com Ni. Durante o sopro de ar, parte do calor liberada durante a oxidação do Ni é utilizada na decomposição térmica da calcita em CaO (calcinação). Dessa forma, as reações de reforma a vapor ocorrem juntamente com a captura de CO_2 da fase gasosa durante a segunda metade do ciclo. O óxido de cálcio (CaO) reage com CO_2 formando

novamente a calcita. Consequentemente, a reação de deslocamento da água (WGS, $CO+H_2O=CO_2+H_2$) é favorecida devido à captura de CO_2, resultando em um decréscimo da produção de CO, que facilita a produção de H_2 de alta pureza. Na seção 2.1.4, mencionou-se a importância da regeneração do material empregado na captura de CO_2 para a obtenção de um processo economicamente viável. Contudo, regeneração demanda energia. Com o processo *unmixed reforming*, há uma possível solução para este problema. Enquanto Ni é oxidado durante o sopro de ar, parte do calor liberado é usado para decompor a calcita em óxido de cálcio, regenerando o material para o próximo ciclo. Deste modo, o gás que sai do reator durante o sopro de ar é uma mistura de CO_2 e N_2 (quando se utiliza $CaCO_3$ no processo); caso contrário, é fundamentalmente N_2. Durante o sopro de combustível/vapor de água, o produto gasoso é uma mistura rica em H_2. O processo *unmixed reforming* com adição de calcita está representado na Fig. 6. Esta rota foi originalmente proposta por Kumar [38] e Lyon e Cole [32]. Como pode ser observado, enquanto Ni passa por ciclos do tipo $NiO\leftrightarrow Ni$, CaO passa por ciclos do tipo $CaO\leftrightarrow CaCO_3$. A cor branca refere-se às regiões mais quentes devido à reação exotérmica durante o sopro de ar ou refere-se às regiões de armazenamento de calor, durante o sopro de combustível.

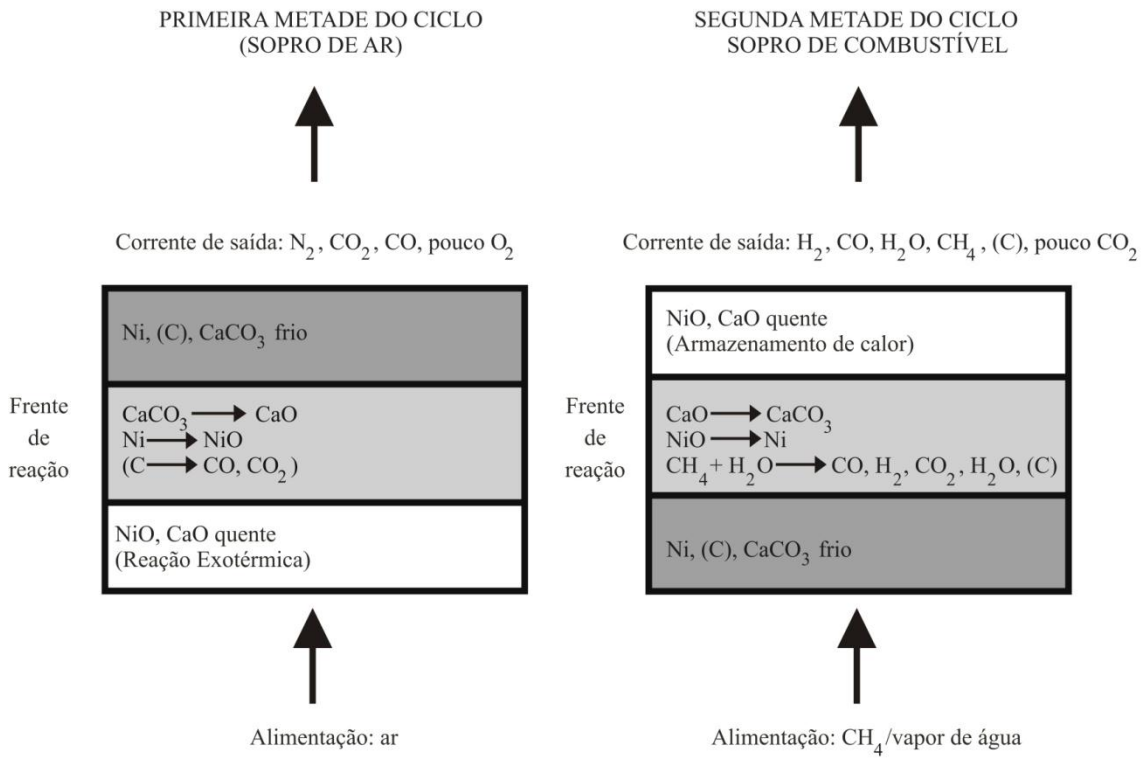

Fig. 6. Processo conhecido como *unmixed steam reforming*, adaptado de [33].

Mais recentemente, Dupont e colaboradores têm avaliado experimentalmente a produção de hidrogênio através do processo de unmixed reforming, usando uma variedade de combustíveis, incluindo metano [33,34], óleo de girassol [34], e resto de óleo de cozinha [36,37]. Os resultados experimentais reportados nestes trabalhos indicam que o processo de *unmixed reforming* é uma tecnologia flexível com respeito à utilização do combustível e com capacidade de geração de H_2 de alta pureza em um único reator. O aparato experimental usado por Dupont e colaboradores [39] está representado na Fig. 7. O catalisador fresco que estes pesquisadores usaram (NiO suportado em Al_2O_3) foi inicialmente ativado com uma mistura de H_2/N_2, até que se obtivesse Ni. A partir de então, experimentos, em que se alternam sopros de ar e sopros

de combustível/vapor de água, foram realizados. Note que entre o sopro de ar e o sopro de combustível, N_2 foi alimentado no reator, a fim de evitar explosões.

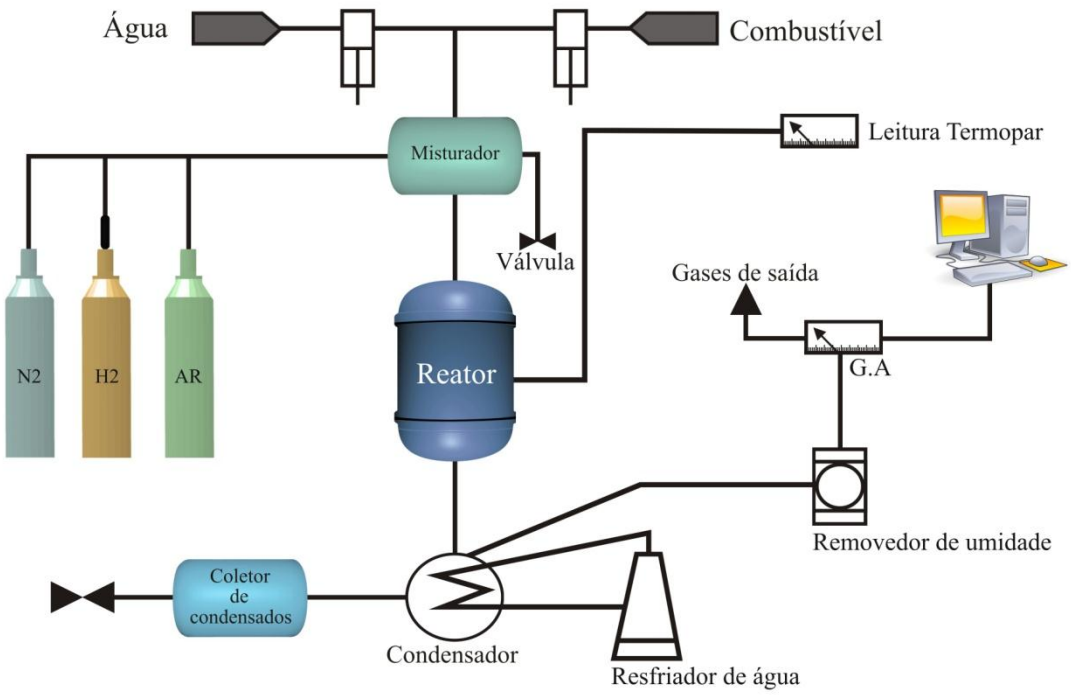

Fig. 7. Configuração do aparato experimental para investigação da rota *unmixed reforming*. GA= análise da composição do gás, adaptado de [39].

2.1.6. 'Chemical looping combustion' (CLC) e 'Chemical Looping auto-thermal reforming' (CLRa)

Recentemente, o processo conhecido como *chemical looping auto-thermal reforming* (CLRa) foi proposto como uma nova rota para produção auto-térmica de hidrogênio a partir do gás natural, sem o efeito indesejável da diluição do hidrogênio pelo N_2 do ar, como ocorre nas rotas de oxidação parcial e reforma auto-térmica. CLRa usa o mesmo princípio que o processo de *chemical looping combustion* (CLC) – uma tecnologia limpa de combustão que envolve o uso de um óxido metálico (carreador de oxigênio)

capaz de transferir o oxigênio do ar para o combustível, evitando o contato direto entre eles, o que garante a separação inerente do CO_2. [40]. Um sistema CLC é composto por dois reatores interconectados de leito fluidizado, designados como reator de ar e reator de combustível. No reator de combustível, o combustível (C_nH_{2m}) é oxidado a CO_2 e H_2O pelo óxido metálico (MeO), o qual, por sua vez, é reduzido a sua forma metálica (Me) ou a uma forma reduzida de MeO. O metal ou o óxido reduzido é transferido para o reator de ar, onde é oxidado pelo O_2 do ar, e o material regenerado está pronto para começar um novo ciclo. Se a conversão é completa no reator de ar, o gás que deixa o reator é composto por N_2 puro. O gás de saída do reator de combustível contém CO_2 e H_2O. Após a condensação de água, CO_2 praticamente puro pode ser obtido, gastando-se o mínimo de energia para separação do componente. O processo de CLC está representado na Fig. 8:

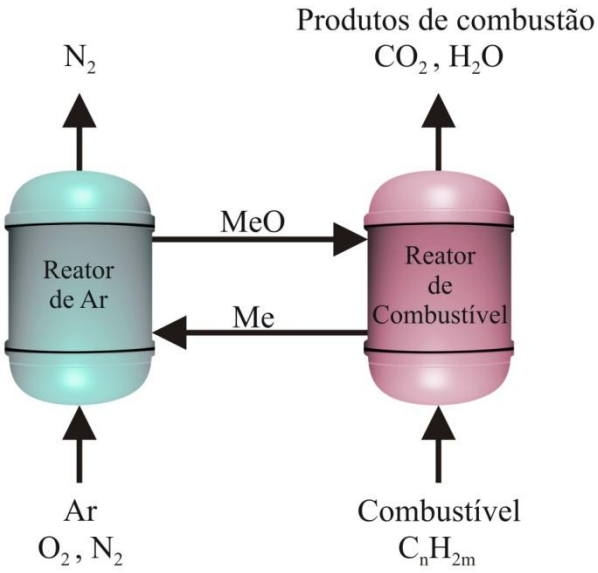

Fig. 8. *Chemical looping combustion* (CLC). A abreviação Me refere-se à forma metálica (forma reduzida), enquanto que MeO é usada para o óxido do metal Me, adaptado de [40].

Para a geração de eletricidade com a tecnologia CLC, é possível abastecer o reator de combustível com o produto da gaseificação do carvão (gás de síntese, $CO+H_2$), como

ilustra a Fig. 9. O produto do reator 1 (reator de combustível) é o gás constituído por CO_2 e H_2O, a alta pressão, capaz de ser expandido em uma turbina a gás. O gás a uma pressão menor passa pelo condensador, obtendo-se CO_2 puro, pronto para sequestro. Desse modo, pode-se ter uma tecnologia limpa para geração de energia a partir do carvão.

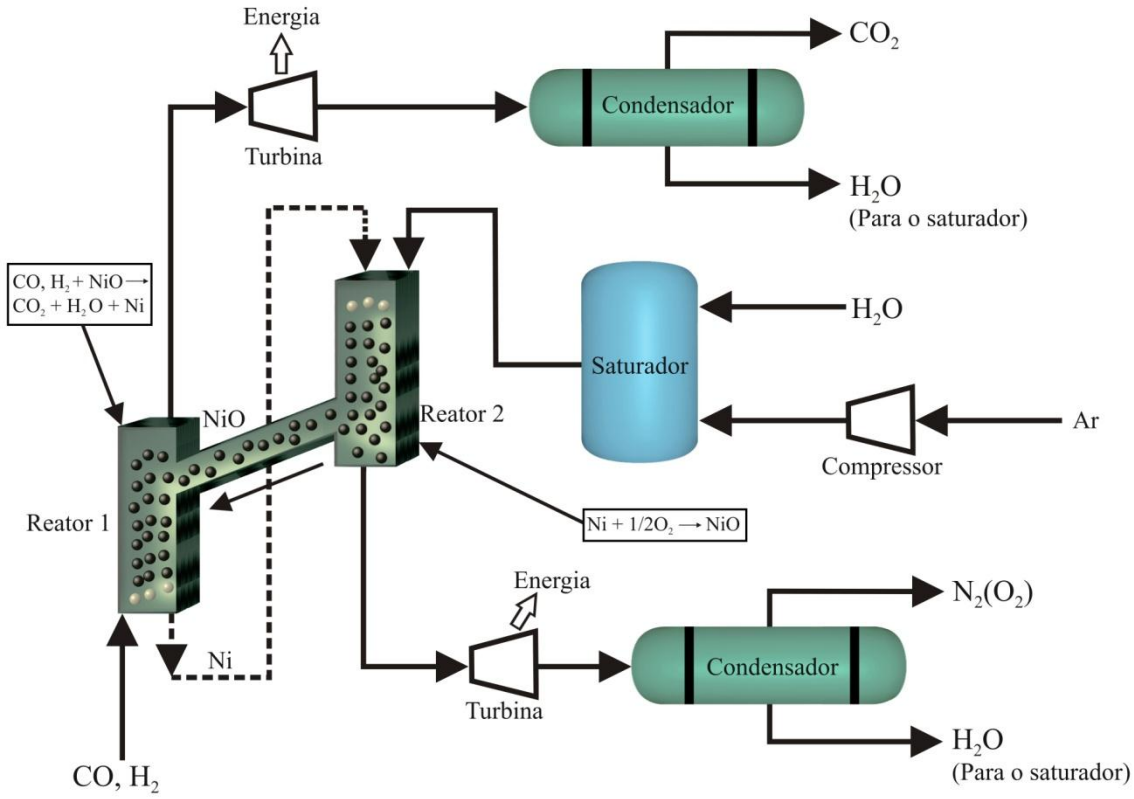

Fig. 9. Diagrama mostrando a planta de operação com *chemical looping combustion (CLC)*. Reator 1 é o reator de combustível e Reator 2 é o reator de ar. As partículas de NiO são carreadoras de oxigênio, adaptado de [41].

O processo de CLRa, como descrito na Fig. 10, foi proposto por Mattisson e Lyngfelt [42]. Este novo processo também utiliza um óxido metálico para transferir oxigênio para o combustível. Contudo, a principal diferença em relação ao CLC diz respeito ao produto gasoso obtido no reator de combustível, que, no caso do CLRa, é um reformato

rico em H_2. No processo do CLRa, a razão empregada de ar/combustível é mantida baixa para prevenir a oxidação completa do combustível, que formaria CO_2 e H_2O. A maior vantagem deste processo é que a reforma auto-térmica pode proceder sem a necessidade de uma produção custosa de O_2 e sem que ocorra a mistura do reformato com N_2.

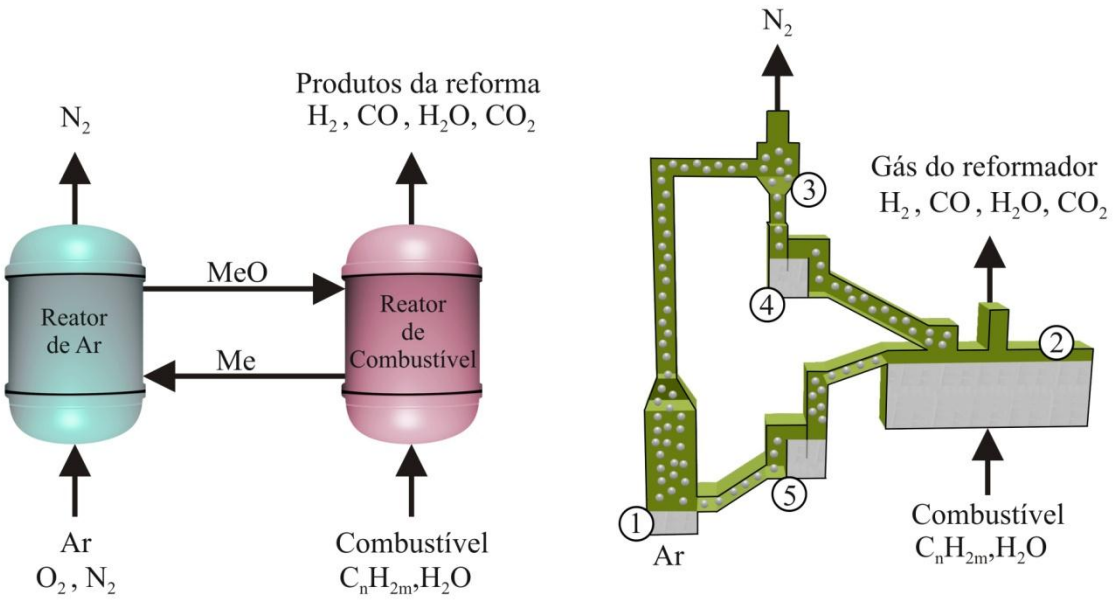

Fig. 10. Esquema representando o processo de CLRa (esquerda). Esquema do reator usado no processo de CLRa: (1) reator de ar, (2) reator de combustível, (3) ciclone para separação de partículas, (4) e (5) *loop seal* fluidizado com vapor de água (direita), adaptado de [43].

Rydén e colaboradores [44] realizaram análises termodinâmicas investigando o desempenho de plantas de produção de H_2 e geração de eletricidade a partir da tecnologia de CLRa. Estes autores demonstram que, para que o processo possa ter viabilidade econômica, é preciso operar em pressões elevadas, pois a energia gasta para a posterior compressão do H_2 é reduzida, visto que ele é obtido em uma pressão elevada (15 bar). Além disso, ao operar em pressão elevada a altas temperaturas, é possível a geração de eletricidade usando uma turbina a gás, conforme ilustra a Fig. 11.

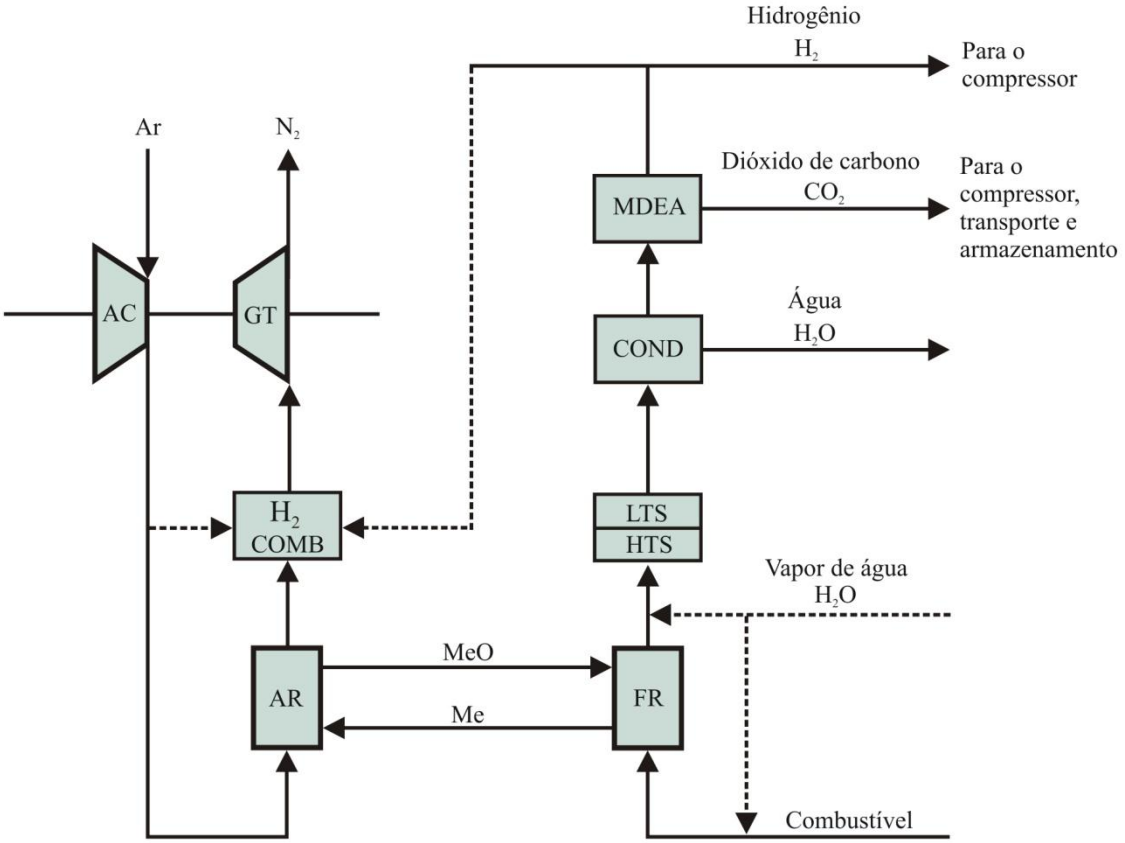

Fig. 11. Descrição esquemática de uma planta operando com CLRa pressurizado, com geração de energia pela turbina a gás (GT) e produção de H_2 pressurizado. COMB (combustor), COND (condensador), AR (reator de ar), FR (reator de combustível), AC (compressor de ar), HTS (‘*high temperature shift reactor*’, primeiro reator, a uma temperatura maior, onde ocorre a reação de deslocamento da água, WGS), LTS (‘*low temperature shift reactor*’, segundo reator, a uma temperatura menor, onde ocorre a reação de deslocamento da água), MDEA (solvente utilizado para separar CO_2 do H_2), adaptado de [44].

O sucesso da tecnologia de CLRa depende da seleção adequada do material capaz de transferir oxigênio para o combustível. Este material deve apresentar propriedades adequadas, tais como: alta reatividade através dos ciclos, elevada resistência ao atrito, alta seletividade para conversão do combustível em H_2 e CO, inibição de deposição de carbono (se depósitos de carbono são formados, estes são oxidados no reator de ar, liberando CO_2 misturado com N_2, o que contradiz os propósitos da tecnologia de *chemical looping*). Além disso, a seleção deste material depende do custo, características ambientais e de outros aspectos, como a toxicidade. Vários óxidos

metálicos suportados em diferentes tipos de materiais inertes têm sido propostos na literatura. Zafar et al. [45,46] prepararam e testaram diferentes materiais baseados nos óxidos de Fe, Mn, Ni e Cu suportados em SiO_2 e $MgAl_2O_4$. Os óxidos de Ni (NiO) mostraram a maior seletividade em relação ao H_2 e CO, enquanto os óxidos baseados em Fe, Cu e Mn exibiram uma seletividade baixa e produziram, principalmente, CO_2, H_2O e CH_4 (não reagido). Já que NiO parece ser o óxido mais adequado para a aplicação em CLRa, devido às suas propriedades catalíticas, este material tem sido o mais estudado. Partículas preparadas por diversos métodos, com tipos diferentes de suporte (Al_2O_3, $MgAl_2O_4$, Mg-ZrO_2) e teores de NiO, têm sido testadas [47-49]. A operação de uma unidade de CLRa usando NiO como material para transferência de oxigênio foi demonstrada, em pequena escala, por Rydén et al. [50-52] e por de Diego et al. [30], e, em uma unidade de 140kW, por Pröll et al. [53]. Se o óxido de níquel é usado em sistemas do tipo CLRa, as principais reações que ocorrem, no reator de combustível, são:

$$CH_4 + NiO \rightarrow CO + 2H_2 + Ni \quad \text{(R12)}$$

$$CH_4 + H_2O \rightarrow CO + 3H_2 \quad \text{(R13)}$$

$$CH_4 + 2H_2O \rightarrow CO_2 + 4H_2 \quad \text{(R14)}$$

$$CH_4 \rightarrow C + 2H_2 \quad \text{(R15)}$$

$$C + H_2O \rightarrow CO + H_2 \quad \text{(R16)}$$

As reações (R13)-(R16) são catalisadas por Ni metálico que se forma devido à reação (R12). Se um excesso de oxigênio é transferido para o reator de combustível, CO_2 e H_2O aparecem como produto de combustão:

$$CH_4 + 4NiO \rightarrow CO_2 + 2H_2O + 4Ni \quad \text{(R17)}$$

$$CO + NiO \rightarrow CO_2 + Ni \quad \text{(R18)}$$

$$H_2 + NiO \rightarrow H_2O + Ni \quad \text{(R19)}$$

No reator de ar, Ni é oxidado a NiO, regenerando o material com capacidade de transferir oxigênio:

$$Ni + 0.5O_2 + 1.881N_2 \rightarrow NiO + 1.881N_2 \quad \text{(R20)}$$

Um aspecto importante a ser considerado é o balanço de energia. A reação de oxidação (R20) é muito exotérmica, enquanto que as reações de redução (R12) e (R17), e a reforma a vapor (R13), são muito endotérmicas. Assim, o calor para as reações endotérmicas que ocorrem no reator de combustível é fornecido através da circulação dos sólidos provenientes do reator de ar que opera em alta temperatura. O calor gerado no reator de ar deve ser capaz de satisfazer o balanço térmico no sistema, sem haver a necessidade de uma fonte externa.

Note que o processo de '*unmixed reforming*' é o mesmo que o processo de '*chemical looping*'; contudo, no caso do '*unmixed reforming'*, somente um reator de leito fixo é empregado, em que sopros de ar e de combustível se alternam. Na tecnologia de '*chemical looping'*, dois reatores interconectados estão envolvidos no processo, havendo circulação de sólidos.

2.2. Biocombustíveis como matéria-prima para produção de H_2

2.2.1. Etanol

O etanol é uma fonte renovável que possui baixa toxicidade quando comparado a outros combustíveis líquidos como metanol e gasolina. Tipicamente, produzido a partir da cana-de-açúcar, o etanol é pouco poluente, e a emissão líquida de CO_2 é, em teoria, nula, pois o CO_2 formado tanto na produção do etanol, a partir da cana-de-

açúcar, como na reação de reforma, é consumido durante o processo de renovação da safra, fechando o ciclo global do carbono [54].

O esquema para a geração de eletricidade usando célula a combustível de baixa temperatura abastecida por H_2 produzido a partir do etanol, elaborado por Fatsikostas e colaboradores [55] e adaptado em [54], está indicado na Fig. 12.

O etanol é produzido a partir da cana-de-açúcar (1), usando-se o processo de sacarificação/fermentação (2). O produto aquoso deste produto é destilado, obtendo-se 45-55% de etanol (3). O resíduo sólido formado na fermentação é utilizado como matéria-prima para a digestão anaeróbica (4), onde biogás é produzido. A reforma do biogás (6) e do etanol (5) produz uma mistura rica em H_2. Um reator do tipo *water-gas shift* (WGS, $CO+H_2O=CO_2+H_2$), onde ocorre a reação deslocamento da água, é utilizado para aumentar a concentração de H_2 e diminuir a concentração do CO (7). Como o ânodo de Pt de uma célula de baixa temperatura, de membrana polimérica, tolera CO em um teor máximo de 10 ppm, a mistura gasosa ainda passa por um reator de oxidação seletiva de CO (COPROX, *CO Preferential Oxidation*) (8). A mistura gasosa, então, rica em H_2, contendo algum teor de CO_2 e CO em uma concentração < 10 ppm, alimenta o ânodo da célula a combustível, produzindo eletricidade e calor (9). Note que o processo pode ser integrado termicamente, em que as reações exotérmicas fornecem a energia para as endotérmicas.

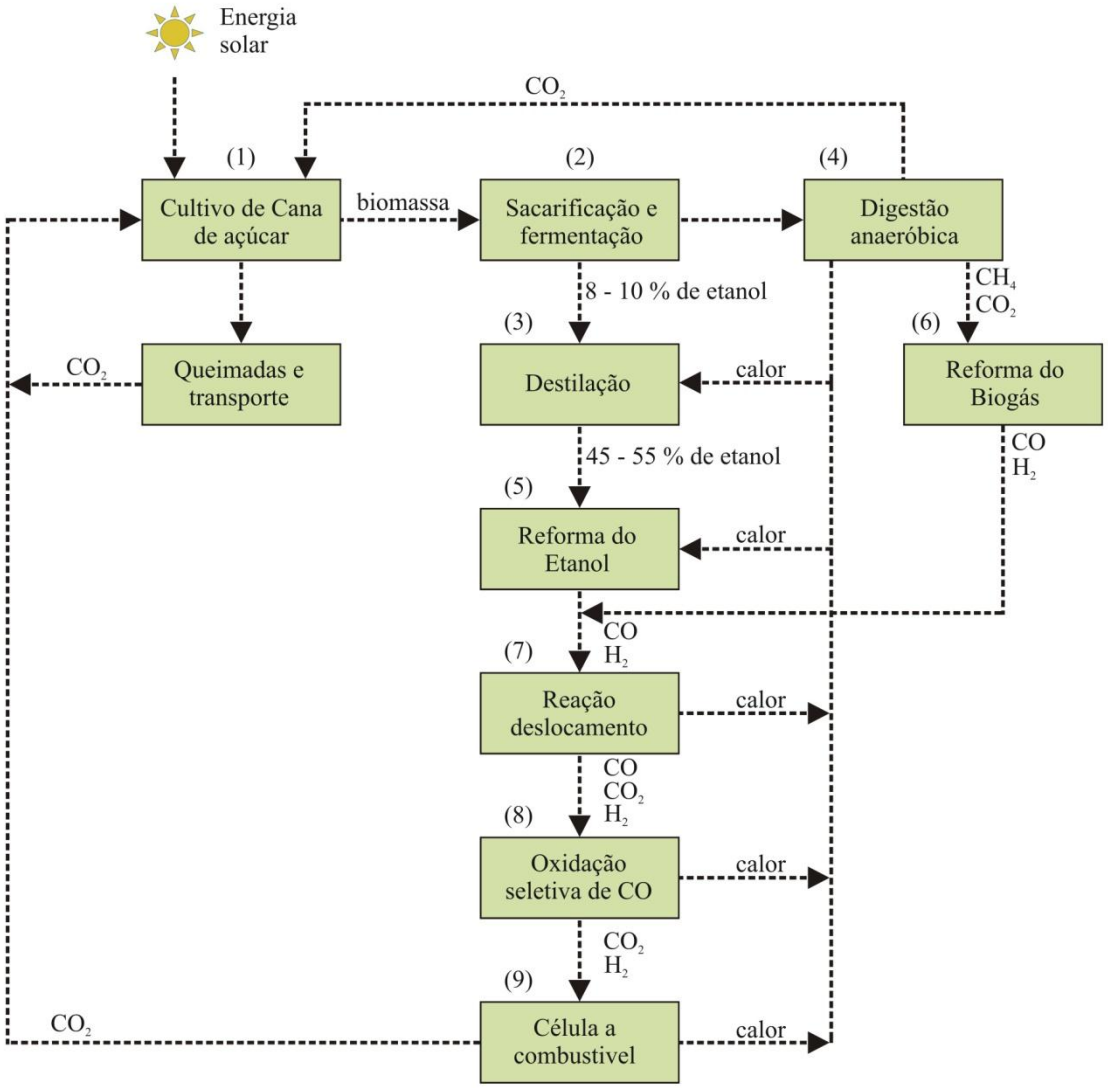

Fig. 12 Processo de geração de energia a partir da cana-de-açúcar, adaptado de [54].

Inúmeros trabalhos envolvendo o desenvolvimento de catalisadores para a reforma do etanol são encontrados na literatura. Na verdade, a reforma a vapor do etanol é um processo complexo, em que muitas reações ocorrem simultaneamente e consecutivamente, *i.e*, reforma a vapor, desidrogenação, desidratação, decomposição, Boudouard e reação deslocamento da água (WGS). Nestas reações, o catalisador desempenha um papel crucial na conversão completa do etanol. Catalisadores ativos

deveriam maximizar a seletividade do H_2 e inibir a deposição de carbono, bem como a produção de CO. Para isso, a escolha do metal e do suporte do catalisador é de extrema importância para satisfazer estes requerimentos. Catalisadores a base de metais (Ni e Co) [56,57] e de metais nobres (Pt, Pd, Rh) [58,59] demonstraram ser ativos na reação de reforma do etanol. Como regra geral, Rh é geralmente mais efetivo do que outros metais nobres. CeO_2, MgO e La_2O_3 são suportes eficientes para a reforma do etanol com metais nobres. O uso de Al_2O_3 mostra desativação do catalisador depois de longo tempo de operação. Em termos de estabilidade, MgO exibe o melhor desempenho [2].

2.2.2. Glicerol

Para entender o papel do glicerol na produção de hidrogênio e na geração de eletricidade através de sua utilização em células a combustível, primeiramente é preciso abordar o biodiesel. Biodiesel é um combustível biodegradável derivado de fontes renováveis como óleos vegetais e gordura animal que, em presença de um catalisador, reagem com o álcool ou metanol (Fig. 13). O óleo vegetal é um triglicerídeo, ou seja, um tri éster derivado do glicerol. Sob a ação de um catalisador básico, ou mesmo ácido, e na presença de metanol ou etanol, o óleo sofre uma reação de transesterificação formando três moléculas de ésteres metílicos ou etílicos dos ácidos graxos, liberando, como co-produto glicerol [60,61].

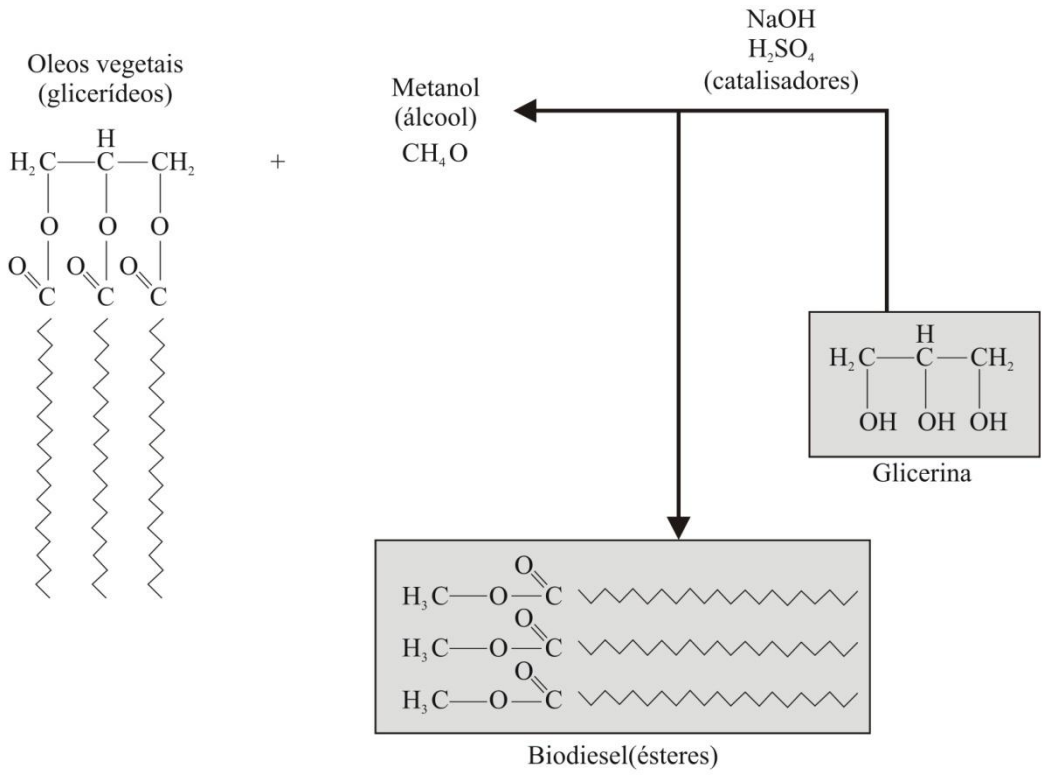

Fig. 13. Esquema da produção de biodiesel a partir da transesterificação do óleo vegetal, adaptado de [62].

Convém mencionar que somente uma pequena quantidade do glicerol oriundo da produção do biodiesel é purificada para uso na alimentação e na indústria de cosméticos, farmacêutica e de tabaco. Assim, boa parte é simplesmente desperdiçada. Consequentemente, com o aumento da produção de biodiesel, um excesso de glicerol é esperado no mercado mundial, lembrando que a cada 1000 toneladas de biodiesel, 100 toneladas de glicerol são produzidas; necessita-se, portanto, de aplicações rentáveis para este subproduto [6].

O glicerol não é tóxico, nem volátil, nem inflamável, o que o torna ideal para uma grande variedade de usos energéticos. Possui também uma alta densidade de energia (6,260 kWh L^{-1} para o líquido puro) tornando-o energeticamente um combustível muito atrativo [63]. Além disso, o glicerol é oxigenado, como o metanol e etanol. Assim, a

oxidação direta do glicerol em células a combustível de altas temperaturas para produzir eletricidade é de significante interesse, devido à sua grande disponibilidade e seu caráter renovável. Da mesma forma, o processo de reforma do glicerol, para produção de H_2 para o abastecimento de células a combustível de baixa temperatura, também tem atraído a atenção de muitos pesquisadores [5, 64].

2.2.3 Butanol

Recentemente, algumas Companhias têm proposto a utilização do *n*-butanol como combustível [65]. Esta nova aplicação está associada com algumas propriedades interessantes, entre as quais o elevado valor energético do *n*-butanol (29,2 MJ/L), quando comparado com o etanol (19,6 MJ/L) e o glicerol (22,5 MJ/L). Assim, há trabalhos, como o de Carvalho e colaboradores [65], que propõem a produção de *n*-butanol a partir do etanol, utilizando óxidos mistos de Mg-Al como catalisadores. Estes pesquisadores sugerem que o *n*-butanol pode ser empregado puro ou combinado com gasolina ou diesel em motores de combustão.

O *n*-butanol também pode ser obtido a partir de outras rotas, como mencionado no capítulo 1 deste trabalho. Pode ser produzido pelo processo clássico de fermentação e suas matérias-primas incluem cana de açúcar, milho, trigo e biomassa lignocelulósica [8]. Alternativamente, também pode ser produzido de uma maneira nova e mais significativa, através da manipulação de sistemas biológicos ou de engenharia metabólica [9]. Mais recentemente, a produção de *n*-butanol a partir de macroalgas tem atraído atenção considerável porque as algas marinhas constituem uma fonte potencialmente sustentável de biomassa que não requer terra arável ou água potável [10].

Trabalhos recentes vêm propondo a utilização do *n*-butanol como matéria-prima na produção de hidrogênio. Roy e colaboradores [66] produziram H_2 a partir da reforma em fase aquosa, utilizando Ni/Al_2O_3 e Ni/CeO_2 como catalisadores.

Cai e colaboradores [67] obtiveram uma produção eficiente de H_2 (~60 mol%, base seca) a partir da mistura (*n*-butanol, acetona e etanol), que é representativa do processo de fermentação na obtenção do *n*-butanol. Os pesquisadores conduziram a reação de reforma na presença de vapor de água e de oxigênio, utilizando catalisadores bimetálicos Co-Ir suportados em ZnO.

2.2.4. Biogás

O biogás é obtido a partir da decomposição anaeróbica da matéria orgânica contida nos resíduos de atividades agroindustriais e agropecuárias, resíduos sólidos urbanos e nos efluentes domésticos e industriais. Tipicamente, o biogás tem uma composição de 60-80% CH_4, 40-20% CO_2, além de gás sulfídrico (H_2S) e amônia (NH_3). É importante enfatizar que a composição do biogás é dependente significativamente do substrato digerido e das condições de operação da fonte. Na reforma, CH_4 é convertido tanto pelo CO_2 da própria composição do biogás, como pelo vapor de água que pode ser adicionado ao biogás, produzindo H_2, CO, CO_2, H_2O, além da possível deposição de carbono (sob as fases grafite, amorfa ou nanofilamentos). Devido às altas temperaturas de reforma, a amônia (NH_3) que está presente no biogás não representa um problema durante a operação, como demonstrado em trabalhos experimentais [68], já que NH_3 é decomposto em N_2 e H_2 no reformador. Quando se refere ao processo de reforma, entende-se que o processo também possa ocorrer no ânodo de uma célula do tipo óxido sólido (SOFC, *Solid Oxide Fuel Cell*), em um processo conhecido por reforma interna direta. Para que seja possível converter o

biogás, é preciso realizar a dessulfuração previamente. Ni, que é o catalisador comumente empregado nas reações de reforma, é envenenado por H_2S, mesmo quando esta espécie encontra-se presente em concentrações na faixa de ppm. Sabe-se, da literatura, que ocorre uma forte interação por adsorção do H_2S na superfície do níquel [15]. Desse modo, o enxofre adsorvido na superfície do catalisador não permite que os reagentes acessem a superfície do níquel, inibindo as reações de reforma do combustível. No caso do ânodo da SOFC, a adsorção de H_2S no Ni também impede o acesso dos reagentes para a reação eletroquímica. Em concentrações maiores do que 100ppm pode haver a formação de novas fases, de sulfeto de níquel, do tipo NiS, Ni_3S_2, que possuem um baixo ponto de fusão, comprometendo severamente a operação da célula. Portanto, a dessulfuração do biogás é de extrema importância para a operação da célula com biogás. No entanto, já que mesmo em concentrações muito reduzidas o H_2S inviabiliza a operação da célula, é necessário o desenvolvimento e otimização de materiais para os catalisadores (tanto do reformador quanto do ânodo da SOFC) operante com biogás.

2.3. Células a Combustível

Células a combustível são dispositivos eletroquímicos na qual a energia química de um combustível é convertida diretamente em energia elétrica (e térmica). Diferentemente de um motor, não há envolvimento do processo de combustão. Células a combustível podem ser consideradas como um híbrido entre bateria e motor. A energia química é diretamente convertida em energia elétrica, similar a uma bateria, enquanto ar e combustível são continuamente fornecidos ao dispositivo, como ocorre em um motor. Há vários tipos de células a combustível que são classificadas de acordo com o tipo de eletrólito e temperatura de operação. O eletrólito pode ser sólido (cerâmico ou

polimérico) ou líquido (aquoso ou sal fundido) e deve ter alta condutividade iônica e baixa condutividade eletrônica para a operação eficiente. O eletrólito em uma célula do tipo SOFC é geralmente um condutor de íons O^{2-}; contudo, o eletrólito também pode ser um condutor de prótons (H^+), íons carbonato (CO_3^{2-}), íons hidróxido (OH^-), dependendo o tipo de célula. A Fig. 14 sumariza os principais tipos de células a combustível. Cada célula recebe o nome de acordo com o seu tipo de eletrólito que determina o intervalo da temperatura de operação. A tecnologia de células a combustível de 'baixas' temperaturas, isto é, células a combustível alcalinas (AFC, *Alcaline Fuel Cell*), células de membrana polimérica (PEMFC, *Proton Exchange Membrane Fuel Cells* ou *Polymer Electrolyte Membrane Fuel Cells*) e células de ácido fosfórico (PAFC, *Phosforic Acid Fuel Cells*), requerem hidrogênio relativamente puro para manter um desempenho estável. Isto se deve ao fato que, em baixas temperaturas de operação, há a necessidade de eletrocatalisadores com base em metais preciosos (*i.e.* platina) para garantir uma cinética de reação adequada do eletrodo; estes catalisadores são desativados por monóxido de carbono, que é um produto da reforma do hidrocarboneto para a produção de hidrogênio.

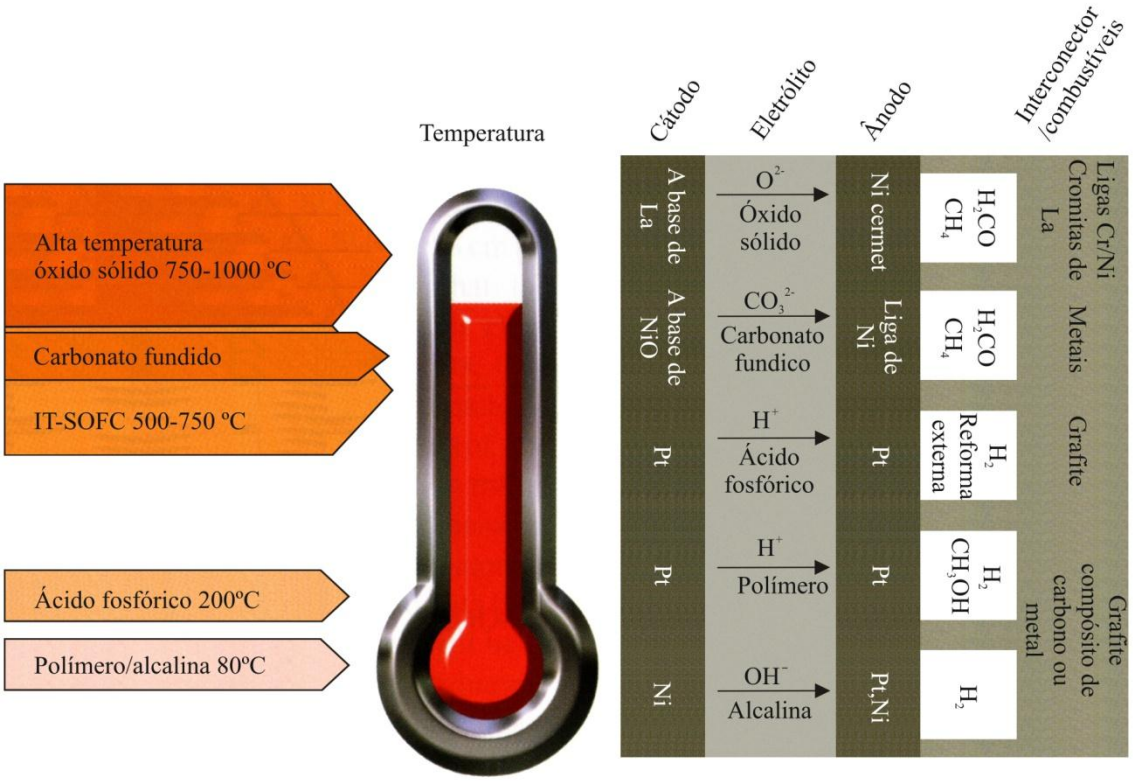

Fig. 14. Ilustração do tipo de células a combustível, e exemplos de materiais típicos de construção e suas temperaturas de operação, adaptado de [69].

2.3.1. Célula a combustível do tipo óxido sólido (SOFC)

Células a combustível do tipo óxido sólido (*Solid Oxide Fuel Cell*, SOFC) são tipicamente células de temperatura elevada (600-1000ºC) que utilizam um eletrólito condutor iônico sólido. As SOFCs são as mais eficientes entre todas as células a combustível [70], e operam de acordo com o princípio mostrado na Fig. 15. Note que neste tipo de célula o eletrólito conduz íons O^{2-}. Os componentes básicos de uma SOFC são: eletrólito, ânodo, cátodo, interconectores e um circuito elétrico conectado à carga externa. O eletrólito denso está em contato com os eletrodos porosos onde as reações eletroquímicas são conduzidas. No cátodo, íons oxigênio são formados pela redução do O_2. Os íons oxigênio migram através do eletrólito em direção ao ânodo onde oxidam as moléculas do combustível (H_2), produzindo elétrons, os quais, por sua vez, fluem em

direção ao cátodo pelo circuito externo. Os eletrodos são porosos para permitir o transporte do gás aos sítios de reação, enquanto o eletrólito e interconectores são densos para separar o ar (O_2) do combustível.

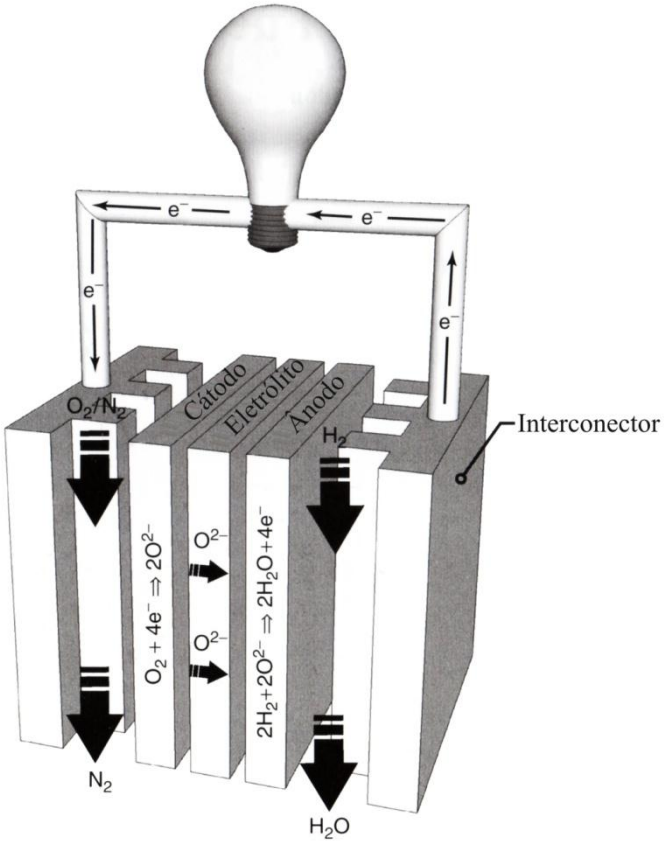

Fig. 15. Esquema de uma SOFC com arquitetura planar operando com hidrogênio puro como combustível, adaptado de [69].

A Fig. 16 mostra uma imagem em Microscopia Eletrônica de Varredura (MEV) em que se podem observar o eletrólito de zircônia estabilizada com ítria (YSZ, de 200 μm), o ânodo (cermet de Ni-YSZ, de 40 μm) e o cátodo (manganita de lantânio dopada com Sr, de 50 μm). Trata-se de uma célula em que o eletrólito é o suporte.

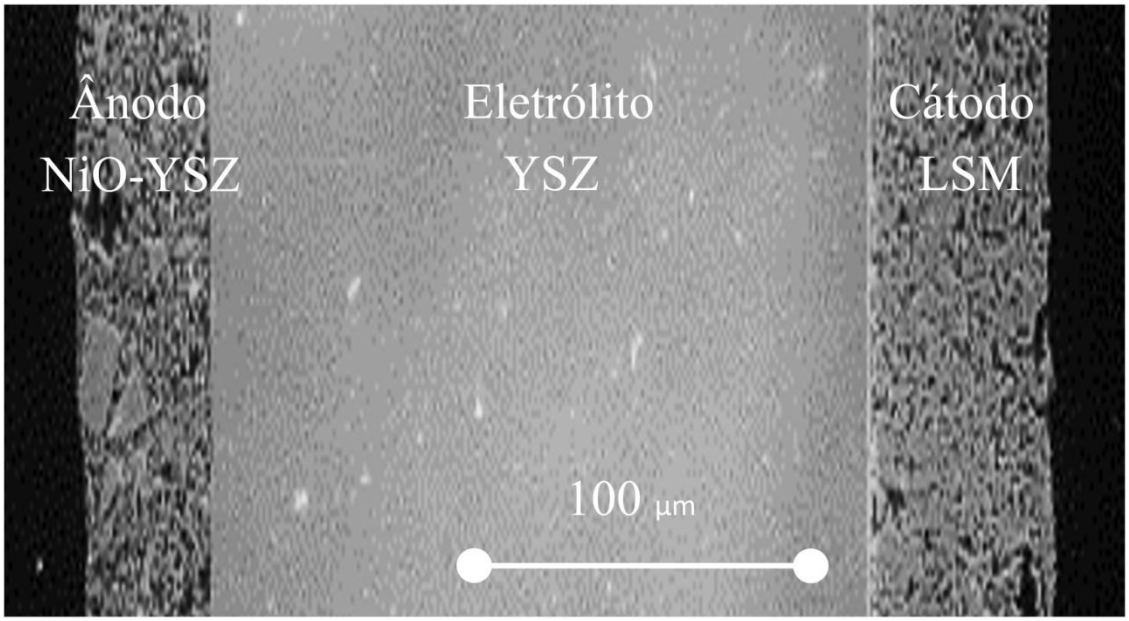

Fig. 16. Imagem em MEV de seção transversal de uma célula, adaptado de [71].

Na prática, para que se possa obter uma voltagem elevada, é preciso conectar diversas células, como mostra a Fig.17. Os interconectores (placa bipolar) são os responsáveis por fazer a união do cátodo de uma célula com o ânodo da célula adjacente. Além disso, os interconectores são responsáveis por fazer a distribuição dos gases reagentes nos canais. A Fig. 18 ilustra como o *stack* pode ser construído.

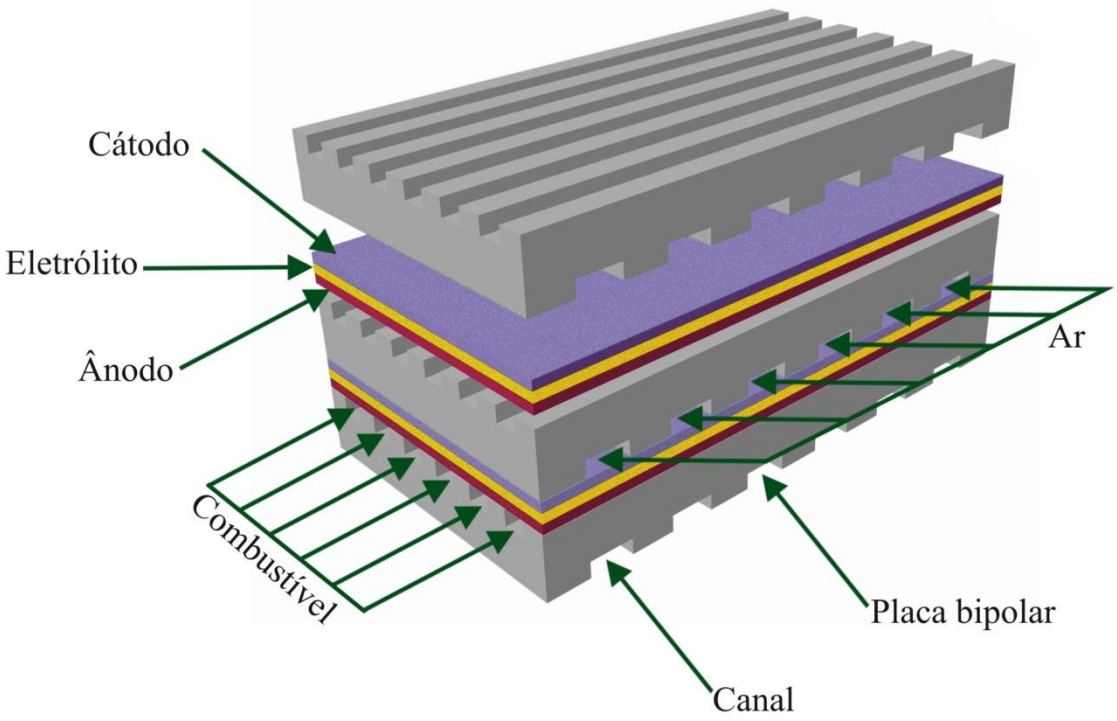

Fig. 17. Esquema de células SOFC com arquitetura planar, adaptado de [72].

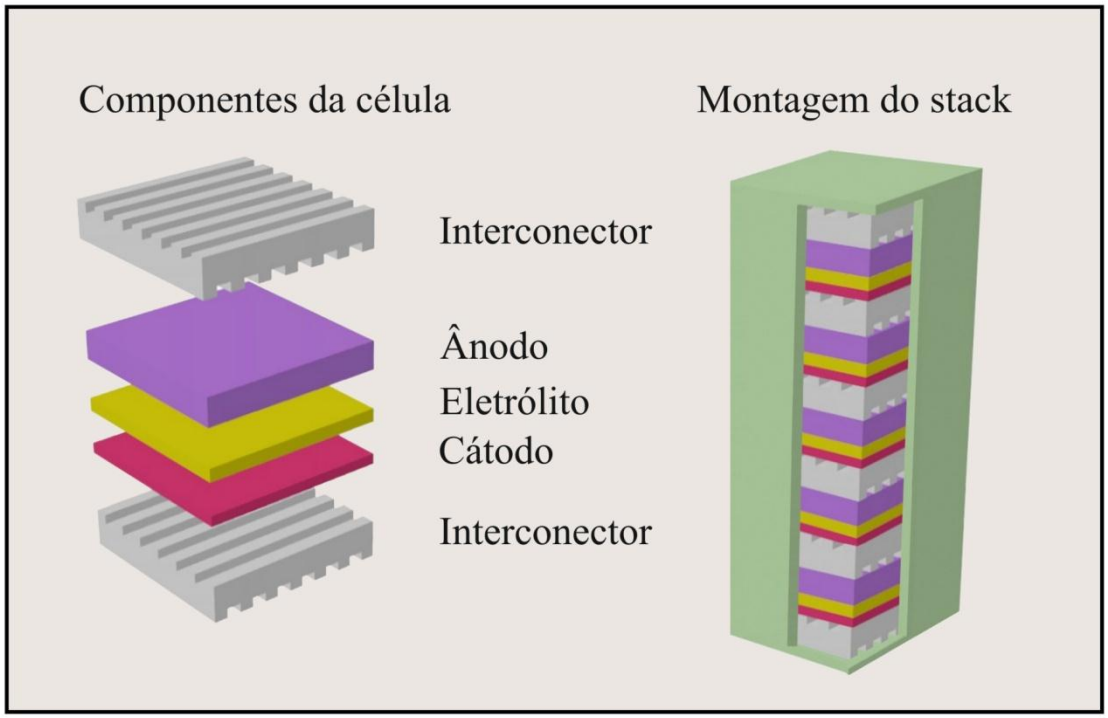

Fig. 18. Ilustração da montagem de um *stack*, adaptado de [73].

Os processos que ocorrem em uma célula a combustível estão distribuídos em diferentes escalas, como ilustrado na Fig. 19. Na escala do '*stack*', fatores como controle da geração de calor pela célula (resfriamento adequado e a remoção efetiva de calor para usos práticos), forças mecânicas nos componentes dos *stacks*, selagem, design para a redução de massa e volume são de grande relevância. No nível da célula, resistência de contato elétrico, distribuição de reagentes e temperatura, compatibilidade química de materiais sob condições operacionais são as principais preocupações. Já na escala correspondente à estrutura interna da célula, referente ao ânodo, eletrólito e cátodo, processos ocorrendo em escala micro e nanométrica são de relevância, e incluem o transporte de carga iônica, condução eletrônica, microporosidade e eletrocatálise. Dentro dos eletrodos, a reação ocorre na tripla camada (*triple phase boundary*, TPB), que é a interface entre os poros do ânodo (fase gasosa), e as fases condutoras eletrônica (fase metálica no ânodo, catalisador de Ni, por exemplo) e iônica (eletrólito condutor de íons O^{2-}). A TPB precisa formar um caminho contínuo de poros até a fonte de reagentes, bem como um caminho eletrônico contínuo até o interconector, e um caminho iônico contínuo até o eletrólito. Isto é, a extensão da estrutura completamente percolada da TPB, juntamente com a habilidade dos materiais de catalisar a reação do eletrodo, determina a atividade eletroquímica do eletrodo.

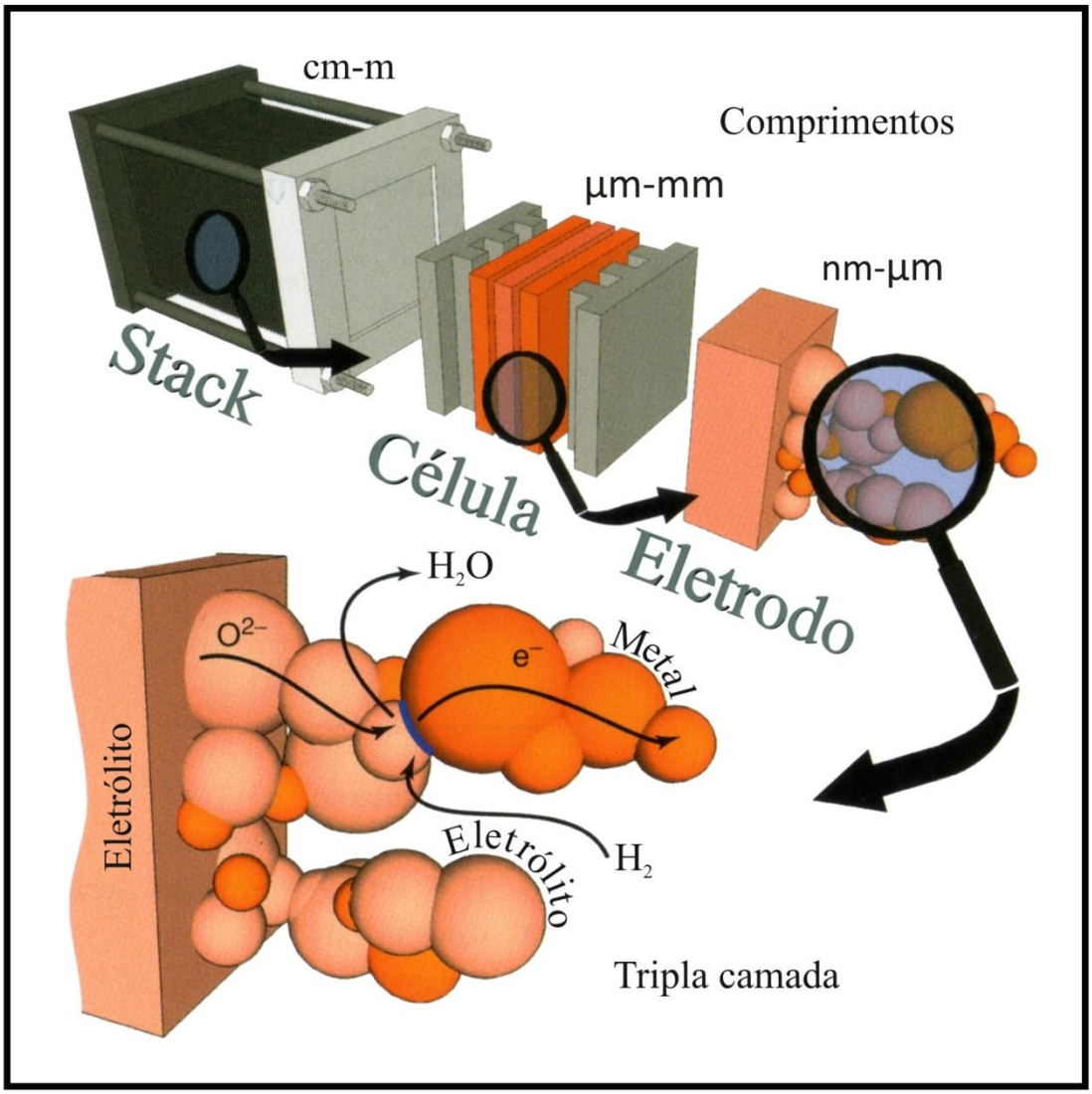

Fig. 19. Escalas de operação em uma célula a combustível e ilustração de uma tripla camada ativa de um ânodo, indicando onde a reação eletroquímica acontece, adaptado de [69].

Células SOFC de alta temperatura (HT-SOFC, *High Temperature* SOFC), produzidas por fabricantes como a *Siemens Westinghouse* e *Rolls-Royce*, operam em temperaturas até 1000ºC. Para tais sistemas, altas eficiências podem ser alcançadas a partir da integração com turbinas a gás para aplicações estacionárias de larga escala. Em células do tipo HT-SOFC, os componentes do *stack* necessitam ser principalmente cerâmicos. Para aplicações em uma escala menor, como *micro-CHP* (unidades de geração combinada de energia e calor, para aplicações residenciais, por exemplo), *APUs*

(*Auxiliary Power Unity*, para fornecimento de energia em caminhões, veículos recreacionais), e pequenos geradores elétricos, há uma tendência em direção ao desenvolvimento de células SOFC que operam em temperaturas menores, as chamadas células SOFC de temperatura intermediária (IT-SOFC, *Intermediate Temperature* SOFC), que operam no intervalo de temperatura de 500-750ºC, como definido por Steele [74]. Convém mencionar que, para a geração distribuída, as *micro-CHPs* são vistas com grande potencial de penetração no mercado. Em muitos locais, em que há produção de combustíveis renováveis, como biogás, etanol, biodiesel e glicerol, a utilização destes combustíveis na alimentação do ânodo de células do tipo IT-SOFC permite a geração sustentável de energia no próprio local de produção, para suprir as próprias necessidades do produtor, ou, ainda, ser fonte de receita com a venda do excedente de energia. Ao reduzir-se a temperatura de operação da célula SOFC, uma maior gama de materiais que permitem um menor custo na fabricação pode ser empregada, como os interconectores, que originalmente eram feitos de cerâmicas com alta condutividade eletrônica ($LaCrO_3$ dopada com Sr) e podem ser produzidos a partir de aços inoxidáveis ferríticos. A menor temperatura de operação permite que o *start up* e o *shutdown* das células sejam mais rápidos, além de redução na taxa de corrosão dos componentes metálicos, durabilidade melhorada (sinterização e interdifusão dos componentes são aceleradas em altas temperaturas), além de simplificação da planta (menos componentes são utilizados na planta).

Conforme pode ser observado na Fig. 20, existem várias configurações para a célula, cada uma sendo classificada de acordo com a camada que suporta mecanicamente a célula. Como indicador geral da escala da espessura destas montagens, o componente que suporta a estrutura tem, tipicamente, uma espessura maior do que 150 μm, e as camadas suportadas terão uma espessura de algumas dezenas

de mícrons. A possibilidade de fabricar eletrólitos com espessuras menores facilita a operação em temperaturas intermediárias.

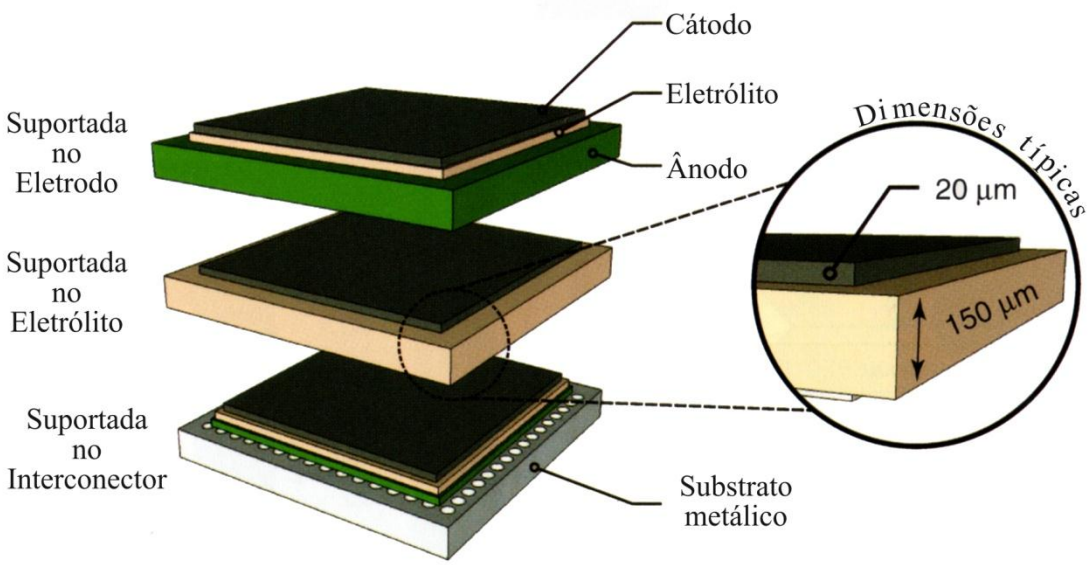

Fig. 20. Ilustração de diferentes tipos de arquiteturas para SOFCs, adaptado de [69].

A aplicação da célula SOFC é o que determina a seleção do tipo (HT ou IT-SOFC). Para aplicações em que é necessária a geração de energia na faixa de centenas de kW até MW, células HT-SOFC, com temperatura de operação de ~1000ºC, são preferíveis, e, neste caso, usa-se a HT-SOFC em combinação com uma turbina a gás, obtendo-se altos valores de eficiência. Para usos em que se necessita energia na faixa dos kW (até algumas dezenas), as células IT-SOFC são as mais adequadas.

2.3.1.1. Cerâmica condutora de íons oxigênio

O mecanismo de transporte de íons oxigênio em eletrólitos cerâmicos é termicamente ativado e a condutividade é, portanto, uma função fortemente dependente da temperatura. Temperaturas elevadas (>500ºC) são tipicamente necessárias para que

as SOFCs tenham um desempenho tecnologicamente útil; isto se deve ao fato que o íon oxigênio é grande e energia térmica é necessária para superar as barreiras para a migração nas vacâncias. Vale salientar que a condução iônica de íons O^{2-} no eletrólito depende da existência de vacâncias, por onde se dá a migração dos íons O^{2-} e, portanto, a condução iônica. A fim de introduzir vacâncias móveis na zircônia (ZrO_2), e estabilizar a estrutura cúbica, são adicionados dopantes trivalentes ou divalentes. A reação de incorporação de um dopante típico trivalente, como a ítria (Y_2O_3), é assim representada:

$$Y_2O_3 \xrightarrow[ZrO2]{} 2Y'_{Zr} + 3O_o^x + V_o^{\bullet\bullet}$$

Ao substituir Zr^{+4} pelo cátion trivalente Y^{+3}, vacâncias são introduzidas, para satisfazer o balanço de cargas. Uma vacância de oxigênio é criada para cada dois átomos de metal incorporados. A adição de ~8 mol% de ítria, i.e., $(ZrO_2)_{0.92}$ $(Y_2O_3)_{0.08}$ resulta na maior condutividade iônica, apesar de níveis maiores (10 mol% de ítria) produzirem uma melhor estabilização da fase cúbica. Embora o eletrólito de zircônia estabilizada com ítria tenha uma condutividade iônica menor do que a de muitos materiais que estão sendo desenvolvidos para IT-SOFCs, uma condução iônica adequada pode ser alcançada quando o eletrólito é fabricado com uma espessura de 10 μm ou menos. Soluções sólidas de céria (CeO_2) são consideradas promissoras para aplicação como eletrólitos de células IT-SOFC. Céria, assim como a zircônia, tem a estrutura cúbica de face centrada, e vacâncias de oxigênio são introduzidas ao substituir Ce^{+4} por cátions divalentes alcalino-terrosos ou íons trivalentes de terras-raras. Céria dopada com gadolínio (Gd^{+3}) é o eletrólito a base de céria mais estudado atualmente. Eletrólitos a base de céria apresentam redução parcial de Ce^{+4} para Ce^{+3} quando expostos a uma combinação de atmosfera redutora (baixa p_{O2}, tão pequena quanto 10^{-19} atm) e temperaturas elevadas (>600ºC), com o processo de redução acontecendo no lado do

ânodo da célula a combustível, afetando uma fração significativa do volume do eletrólito. A consequência desta reação química é que (i) há expansão do volume da rede, que resulta em falha mecânica do eletrólito; (ii) a condução eletrônica (tipo-n) é introduzida no eletrólito, o que reduz o desempenho da célula. O mecanismo de redução e condução mista iônica-eletrônica (MIEC, *Mixed Ionic Electronic Conduction*) tem sido estudada em diferentes trabalhos [75]. A condução MIEC ocasiona a diminuição do valor do potencial de circuito aberto (OCV). Quando a célula está operando, há um fluxo de íons O^{2-} em direção ao ânodo, o que inibe a redução do Ce^{+4}, já que a atmosfera do ânodo vai se tornando cada vez mais oxidante. O eletrólito CGO (céria dopada com Gd) é mais efetivo na faixa de temperatura de 500-600ºC, em que a temperatura é suficientemente alta para garantir a condução iônica do O^{2-} através do eletrólito, mas é suficientemente baixa para minimizar os efeitos da condução mista quando a célula opera em uma voltagem de ~ 0.65V.

2.3.1.2. Cerâmica condutora de íons hidrogênio

Até o momento, os eletrólitos de SOFCs mais empregados têm sido do tipo óxidos condutores de íons O^{2-}, incluindo zircônia estabilizada com ítria ou escândia. Devido ao grande tamanho do íon, a energia de ativação (E_a) para a difusão do íon oxigênio atinge aproximadamente 0.8 eV [76]. Consequentemente, uma queda rápida na condutividade com a redução da temperatura é normalmente observada para muitos condutores O^{2-}. Iwahara et al. [77] demonstraram que alguns óxidos do tipo perovskita exibiam condutividade protônica em temperaturas elevadas sob uma atmosfera umidificada. Um próton se move muito mais facilmente do que o íon oxigênio; consequentemente, um valor de E_a de 0.3–0.6 eV é tipicamente observado [76]. Assim, óxidos condutores protônicos são superiores aos condutores iônicos (O^{2-}), pensando-se em uma

temperatura reduzida na operação da SOFC, que é a meta para comercialização deste tipo de célula.

Quando óxidos com estrutura perovskita, de fórmula geral ABO_3, são dopados com cátions de valência menor, estes substituem parcialmente os cátions do sítio B, formando vacâncias de oxigênio. Por exemplo, o cerato de bário é uma cerâmica do tipo perovskita, ABO_3 com A=Ba e B=Ce. Quando dopado com ítria, Y_2O_3, o cátion Y^{3+} substitui parcialmente os sítios do Ce^{4+} e com isso produz vacâncias de oxigênio na rede cristalina. [78]. A produção destas vacâncias se dá de acordo com o princípio da eletroneutralidade. A reação de defeitos da incorporação da ítria na rede do cerato de bário pode ser escrita utilizando a notação de Kröger e Vink da seguinte forma:

$$Y_2O_3 \rightarrow 2Y'_{Ce} + V_O^{\bullet\bullet} + 3O_O^x$$

A cada dois íons ítrio incorporados na rede cristalina forma-se uma vacância de oxigênio. Assim, a concentração de vacâncias de oxigênio é diretamente proporcional à concentração de dopante. Quando o cerato de bário dopado com ítria (BCY) é submetido a uma atmosfera em presença de umidade, o óxido dissolve os prótons que ocupam as vacâncias:

$$H_2O(gas) + V_O^{\bullet\bullet} + O_O^x \rightarrow 2OH_O^{\bullet}$$

Estes prótons realizam a condução 'pulando' de um oxigênio para o vizinho mais próximo na rede cristalina [77]. O próton na notação Kröger-Vink denota-se $H^{\bullet}$, mas como o próton sempre se situa na nuvem eletrônica de um íon oxigênio, denota-se $OH_O^{\bullet}$ [79]. O eletrólito pode sustentar uma corrente protônica, onde o H_2 do ânodo pode se dissolver como um próton na estrutura do óxido da seguinte forma:

$$H_2 + 2\,O_O^x \rightarrow 2OH_O^{\bullet} + 2e'$$

Os elétrons percorrem o circuito externo. No cátodo, os prótons que percorreram o eletrólito são removidos pela seguinte reação:

$$2OH_o^{\bullet} + 0.5O_2 + 2e' \rightarrow H_2O + 2O_o^x$$

O funcionamento de uma SOFC com condução protônica pode ser visto na Fig. 21.

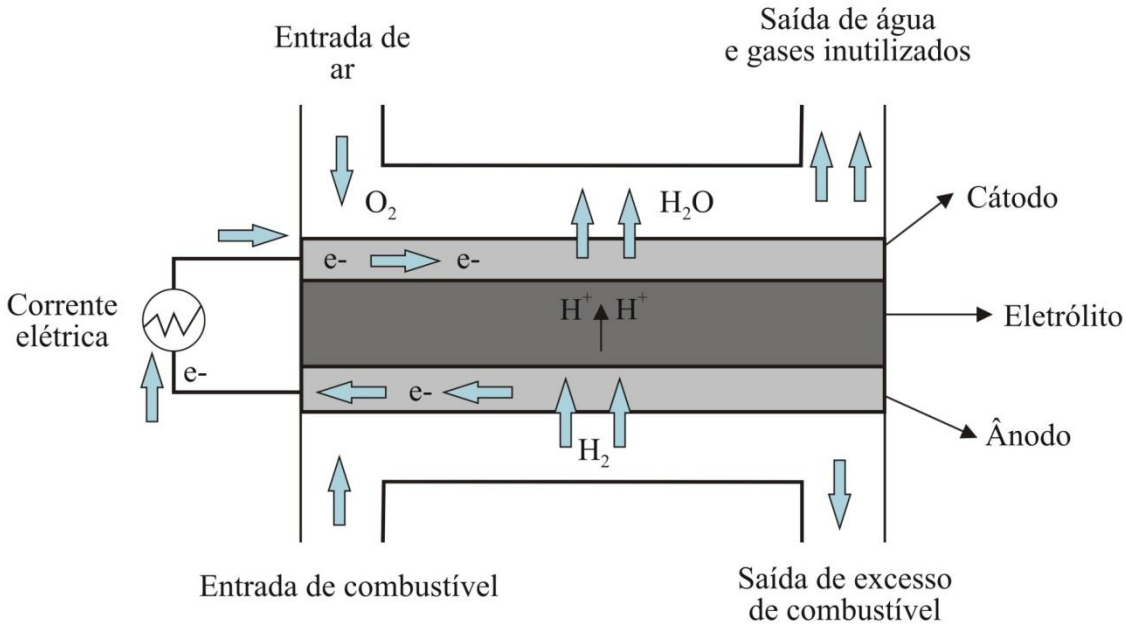

Fig. 21. Diagrama esquemático do funcionamento de uma célula a combustível com eletrólito sólido condutor protônico, adaptado de [80].

2.3.1.3. Modo de operação: Utilização direta

A aplicação final para a SOFC é o que determina o design do sistema, o combustível a ser utilizado, e, consequentemente, o modo de operação. A reforma externa do gás natural, por exemplo, é a opção mais conveniente para aplicações estacionárias, onde o volume do sistema, tempo de *start-up*, e flutuação de potência não são cruciais. A

oxidação parcial e a utilização direta de um combustível são modos de operação adequados para aplicações que requerem máxima densidade de potência, que é típica para aplicações portáteis [81].

No modo de operação conhecido por utilização direta, o combustível líquido é alimentado diretamente no ânodo da célula SOFC. Devido às altas temperaturas de operação da célula SOFC, há a possibilidade de realizar a conversão do combustível no canal e no próprio ânodo dá célula. A reação anódica envolve tanto a oxidação eletroquímica dos produtos formados pela pirólise do combustível como a oxidação eletroquímica das próprias moléculas do combustível. A oxidação eletroquímica global de um hidrocarboneto genérico pode ser representada pela seguinte reação global:

$$C_nH_{2n+2} + (3n + 1) \cdot O^{2-} \rightarrow n \cdot CO_2 + (n + 1) \cdot H_2O + (6n + 2) \cdot e^-$$

As reações de reforma a vapor e reforma a seco no ânodo da SOFC permanecem importantes para o caso da utilização direta de hidrocarbonetos, já que as pressões parciais de H_2O e CO_2 aumentam à medida que o combustível vai sendo consumido. É bem possível que em altas densidades de corrente as moléculas de combustível sejam reformadas no ânodo em vez de serem oxidadas eletroquimicamente.

O problema primário na utilização direta de hidrocarbonetos é a desativação do ânodo, rápida e irreversível, causada pela deposição do carbono. Em teoria, o carbono pode ser removido pela reação com os íons oxigênio de acordo com a reação:

$$C_{(s)} + 2O^{2-} \rightarrow CO_2 + 4e^-$$

De fato, o carbono depositado próximo à tripla camada (*triple phase boundary*, TPB) é removido a partir de certo valor de corrente, onde sua formação não é possível, indicando que a oxidação eletroquímica do carbono sólido é possível. Horita e

colaboradores [82] demonstraram este processo de remoção do carbono pela reação com O^{2-} usando a técnica SIMS (*Secondary Ion Mass Spetrometry*).

Alguns dos possíveis caminhos de reação para um hidrocarboneto genérico ou molécula de álcool no compartimento do ânodo são ilustrados na Fig. 22.

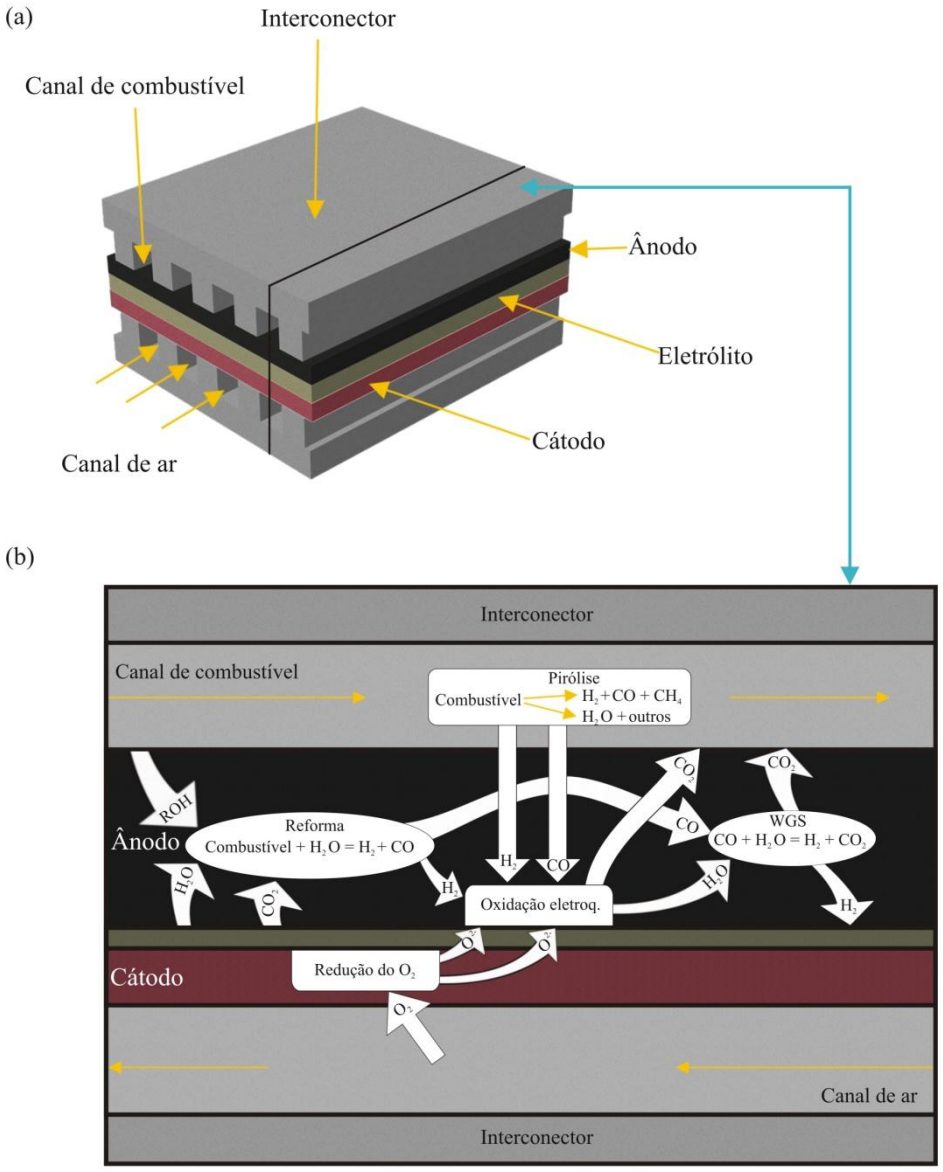

Fig. 22. Esquema de uma célula SOFC de arquitetura planar (a) seção transversal (b) incluindo os processos envolvidos na utilização direta do combustível na SOFC. WGS é a reação *water-gas shift* (reação deslocamento da água), adaptado de [81].

2.3.1.4. Modo de operação: Reforma interna direta e indireta

Quando as reações de reforma são conduzidas em um reformador externo, e o reformato (produto da reforma), composto por H_2, CO, CO_2, CH_4, H_2O, é conduzido ao ânodo da SOFC, onde ocorre a reação eletroquímica do H_2 (e do CO possivelmente), diz-se que se trata de um processo com reforma externa. Esta forma de operação é indicada para sistemas estacionários de larga escala com geração combinada de eletricidade e calor (Fig. 23 (a)). Por outro lado, para aplicações em pequena escala e, particularmente, para sistemas portáteis, a complexidade e o tamanho do sistema global devem ser reduzidos, eliminando o reformador externo e unidades anexas [83], e o combustível deve ser reformado no interior do próprio *stack*. Este tipo de design é conhecido como reforma interna e usa o calor gerado pela oxidação eletroquímica e outros processos não reversíveis para satisfazer os requerimentos térmicos das reações de reforma. A reforma interna pode ser feita indiretamente (Fig. 23 (b)), ou diretamente no ânodo Ni/YSZ (Fig. 23 (c)). Na reforma interna direta, a reação de reforma do combustível e a reação eletroquímica acontecem no próprio ânodo da célula. Isto é possível devido às altas temperaturas de operação da célula, que permitem flexibilidade em relação à utilização do combustível. Contudo, é preciso operar em condições nas quais a deposição de carbono seja evitada ou minimizada, já que o carbono depositado recobre os sítios ativos do ânodo, resultando em uma desativação rápida e irreversível da célula. Além disso, quando ocorre o crescimento de filamentos de carbono, aderidos aos cristalitos do ânodo, surgem tensões no estrutura do eletrodo, promovendo sua degradação [84].

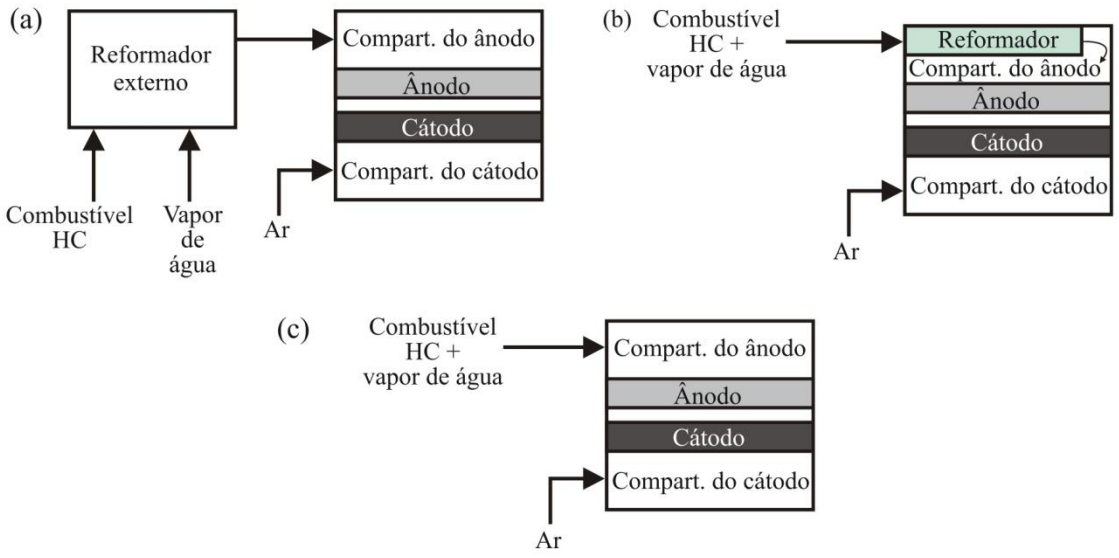

Fig. 23. Esquema de (a) reforma externa à célula SOFC, (b) reforma interna indireta, e (c) reforma interna direta, adaptado de [81].

2.3.2. Célula a combustível de membrana polimérica (PEMFC)

As células a combustível de membrana polimérica, que operam em temperaturas menores (~85ºC), conhecidas como células *PEMFC* (do inglês, *Proton Exchange Membrane Fuel Cells* ou *Polymer Electrolyte Membrane Fuel Cells*) são células preferíveis para aplicações em transporte e em sistemas portáteis, já que possuem rápido '*start-up*' e '*start-stop*', são compactas e possuem alta densidade de energia. As células PEMFC podem operar com H_2, metanol, etanol (neste caso, são chamadas de *Direct Etanol Fuel Cells*) ou ácido fórmico. Quando operam com H_2, os únicos co-produtos são água e vapor. A tecnologia PEMFC tem sido utilizada no provimento de energia em laptops, carros, ônibus, barcos, submarinos, e aeronaves [85]. A Fig. 24 mostra o esquema de uma célula PEMFC operando com H_2. Cada eletrodo consiste em uma camada eletrocatalítica, a qual é constituída, tipicamente, por catalisador de Pt suportado em carbono, e uma camada de difusão gasosa (do inglês, *Gas Diffusion Layer*, GDL). A camada GDL é porosa para permitir a permeação dos gases e o

escoamento de água, enquanto permite, ao mesmo tempo, a condução da corrente elétrica. É importante ressaltar que, para a reação eletroquímica acontecer, deve haver a tripla camada em que os gases reagentes, eletrólito (Nafion) e catalisador estão em íntimo contato. O contato entre as três fases é facilitado pela adição do ionômero Nafion na camada catalítica [86]. O combustível (lado do ânodo) e oxigênio (lado do cátodo) escoam ao longo dos canais nas placas bipolares que também servem de condutores elétricos.

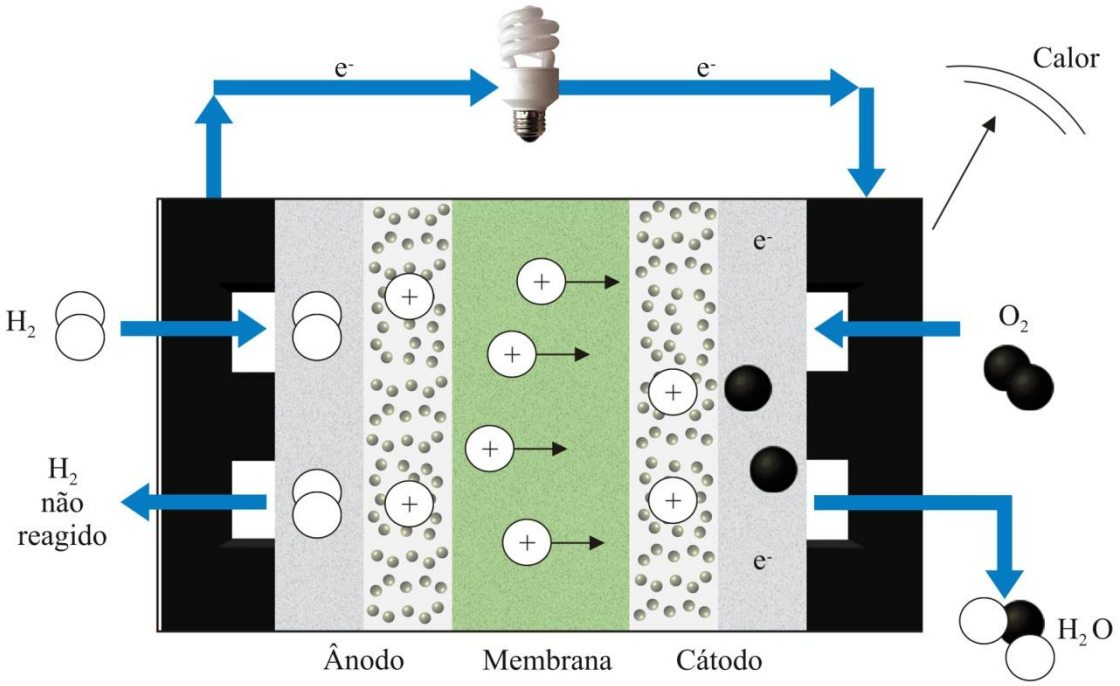

Fig. 24. Representação esquemática de uma célula PEMFC mostrando a placa bipolar, com reagentes nos canais, as camadas de difusão gasosa, camadas catalíticas nos eletrodos, e a membrana no centro, adaptada de [85].

A camada de difusão gasosa é composta por papel de fibra de carbono, Papel Toray®, com adição de material hidrofóbico, como Teflon (PTFE). A Fig. 25 mostra imagens de Microscopia Eletrônica de Varredura (MEV) do Papel Toray-TPGH-120, com (a) 0% PTFE, baixo aumento e (b) 60% PTFE, alto aumento.

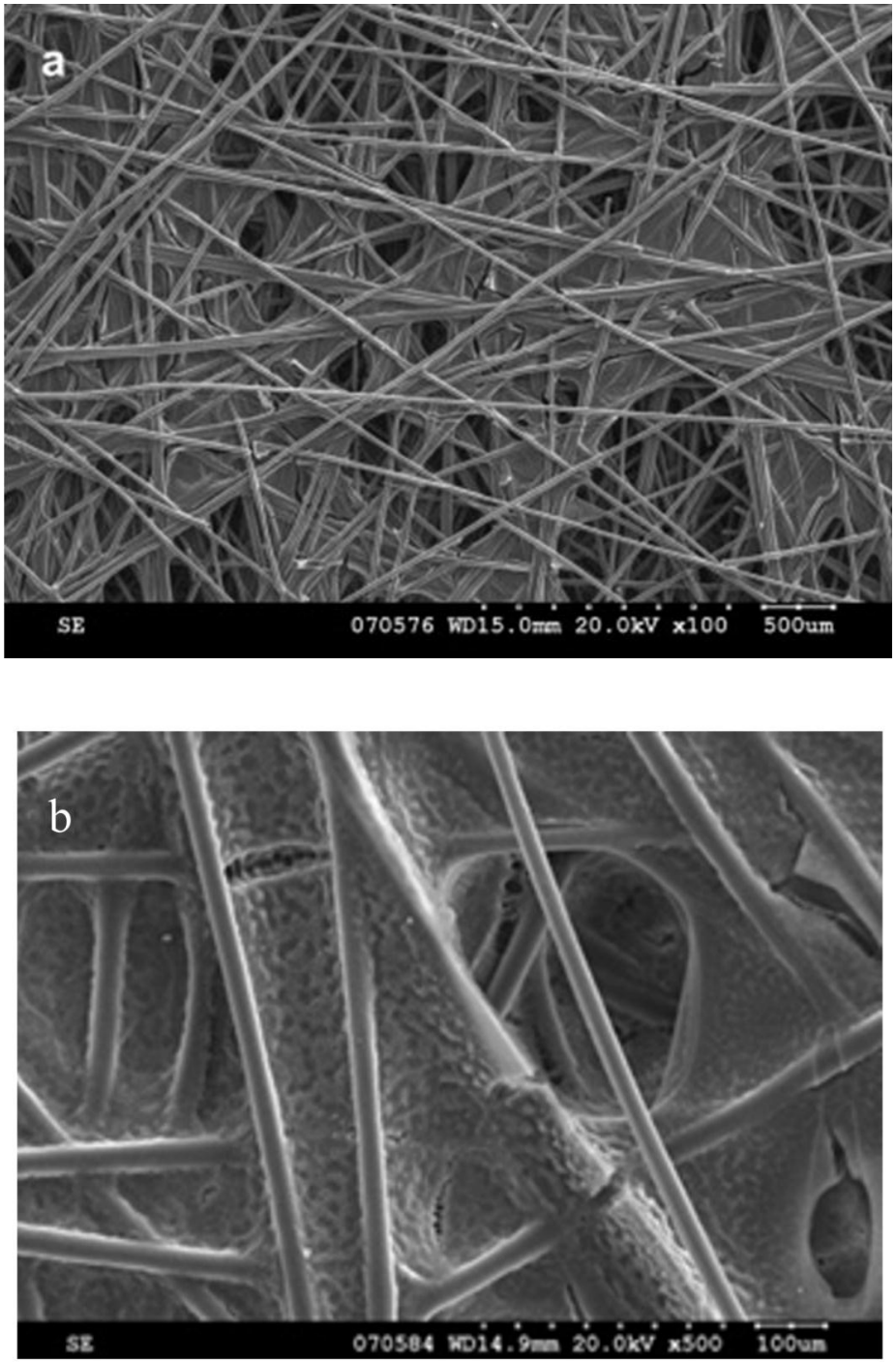

Fig. 25. Imagem MEV do Papel Toray-TPGH-120 (a) 0%PTFE - baixo aumento e (b) 60% PTFE – alto aumento, adaptado de [87].

A Fig. 26 mostra a imagem, em Microscopia Eletrônica de Transmissão (TEM), da nanopartículas de Pt suportadas em carbono Vulcan.

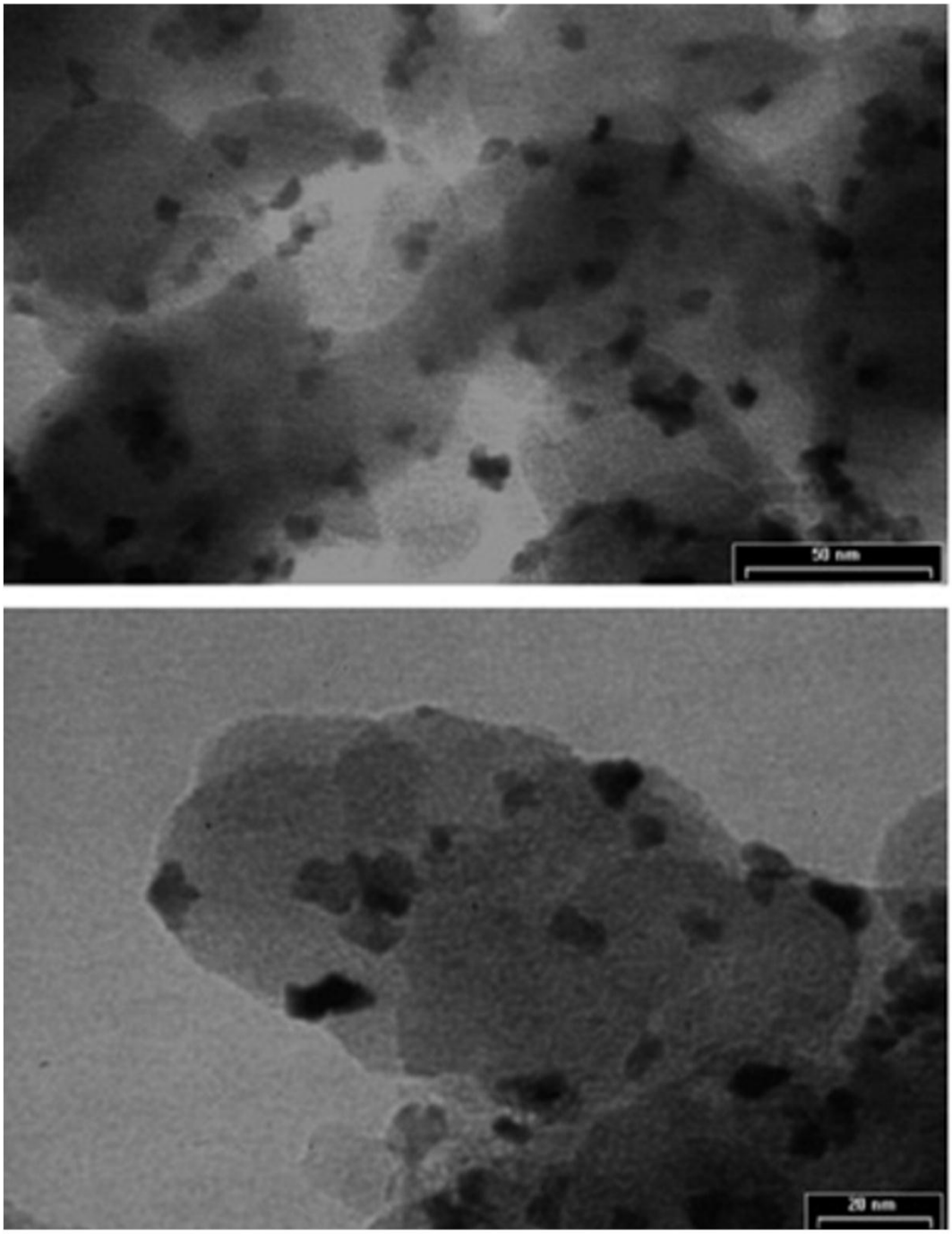

Fig. 26. Imagem TEM (em diferentes aumentos) de catalisador de Pt suportado em carbono Vulcan preparado pelo método do ácido fórmico (Pt/VF), adaptado de [88].

Várias destas células são conectadas em série para produzir um *stack*. O conjunto envolvendo eletrodo e membrana é conhecido como *Membrane-Electrode Assembly* (MEA) e constitui um elemento chave da PEMFC que possui maior influência no custo

e durabilidade. Hidrogênio se dissocia em prótons e elétrons no lado do ânodo. Os prótons viajam através da membrana polimérica, enquanto os elétrons são conduzidos por um circuito externo para produzir a corrente de saída da célula a combustível. No lado do cátodo, ocorre a redução do oxigênio. As reações de meia-célula são assim descritas:

Ânodo:

$2H_2 = 4H^+ + 4e^-$ $E^o_a=0.0$

Cátodo:

$4H^+ + 4e^- + O_2 = 2H_2O$ $E^o_c=1,229$ V

A reação global é:

$2H_2+ O_2 = 2H_2O$

Aqui, E^o_a e E^o_c são os potenciais padrões do ânodo e do cátodo, respectivamente. O potencial de circuito aberto, também conhecido como potencial de *Nernst*, é 1,229V. Uma célula PEMFC produz aproximadamente 0,6-0,7V sob operação, com a voltagem decrescendo à medida que a corrente aumenta, devido às perdas por ativação na camada catalítica, perdas por queda ôhmica, e ineficiências devido ao transporte de massa.

A membrana da célula tem que ter desempenho adequado em uma temperatura relativamente elevada (~85ºC), em um ambiente altamente ácido, com características oxidantes de um lado e condições altamente redutoras de outro lado. Idealmente, a membrana polimérica deve ter uma excelente condutividade protônica, mas uma condutividade elétrica muito baixa. Além disso, deve atuar como barreira para os gases reagentes, e impedir o '*crossover*' do combustível de um lado para o outro da célula. A membrana deve ainda ser compatível com os outros materiais e manter estabilidade

dimensional durante a operação, sem sofrer alterações pelas mudanças no nível de umidade. A membrana Nafion® , desenvolvida pela DuPont Inc., é um excelente condutor protônico a 75ºC e 100 % de umidade relativa (RH), e tem boa estabilidade química e mecânica. Para haver a condução protônica, necessita-se de uma solução aquosa. Contudo, a membrana Nafion® é de alto custo, além do problema da degradação física e química, que é um fator limitante no desempenho de membranas de ácido perfluorsulfônico (PFSA), principalmente em altas correntes de operação e condições de baixa umidade. A Fig. 27 mostra a estrutura química da membrana Nafion.

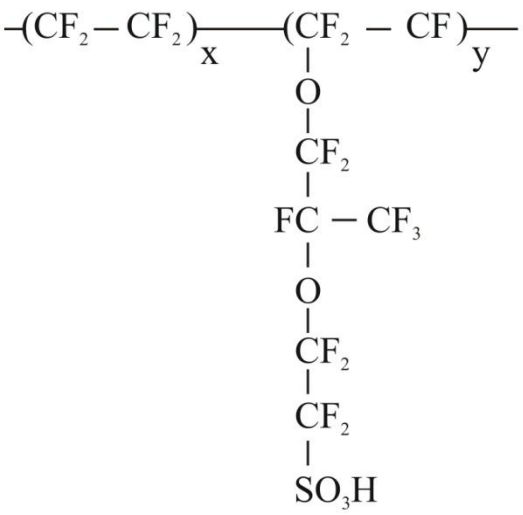

Fig. 27. Estrutura do polímero Nafion [85].

2.4. Fundamentos de otimização

Segundo Foulds [89], otimização é o processo pelo qual a solução ótima de um problema é produzida. As técnicas de otimização, que buscam a melhor solução para um problema (máximos ou mínimos de grandezas mensuráveis em seus domínios de definição), são necessárias em muitas áreas de engenharia, tais como:

(a) Pesquisa operacional: otimização de sistemas técnico-econômicos, controle de estoques, planejamento de produção, etc.;

(b) Engenharia de processos: dimensionamento e otimização de processos, integração mássica e energética de processos, estimação de parâmetros, reconciliação de dados, análise de flexibilidade, etc.;

(c) Controle de processos: identificação de sistemas, controle ótimo, controle adaptativo, controle preditivo, estimadores de estados, etc.;

(d) Análise numérica: aproximações, regressão, solução de sistemas lineares e não-lineares, etc [90].

Os componentes chaves da formulação de um problema de otimização são:

(a) A função objetivo

(b) O modelo do processo

(c) As restrições

A função objetivo representa lucro, custo, energia, produção, distância, etc., em termos de variáveis de decisão do processo ou sistema em análise. O modelo do processo e as restrições descrevem as inter-relações entre estas variáveis. No contexto de otimização, os problemas são tratados dentro das seguintes definições:

Função objetivo: É a função matemática cujo máximo ou mínimo deseja-se determinar. Nesta Tese, a função objetivo é a energia de Gibbs total do sistema.

Variáveis de decisão: São as variáveis independentes que aparecem na função objetivo. Correspondem, em número, ao excesso de variáveis em relação ao número de equações (restrições de igualdade), isto é, o grau de liberdade do sistema.

Restrições: São os limites impostos ao sistema ou estabelecidos por leis naturais que governam o comportamento do sistema, a que estão sujeitas as variáveis de decisão. As

restrições podem ser de igualdade (equações) ou de desigualdade (inequações). Nesta Tese, as restrições são equações que representam o balanço de massa elementar.

Região de Busca: Também é denominada de região viável. É a região do espaço definido pelas variáveis de decisão, delimitada pelas restrições, em cujo interior ou em cuja fronteira se localiza o ótimo da função objetivo.

Para compreender melhor estas definições, considere o seguinte exemplo apresentado no livro de Foulds [89]:

Maximizar $$x_o = f(X) = f(x_1, x_2) \quad (1)$$

Sujeito às seguintes restrições: $$h_1(X) \leq 0 \quad (2)$$

$$x_1 \geq 0 \quad (3)$$

$$x_2 \geq 0 \quad (4)$$

Este é um típico problema na teoria de otimização – a maximização (ou minimização) de uma função de valores reais de um número de variáveis reais sujeita a restrições. A função $f(X)$ é chamada de função objetivo. O problema consiste em achar valores reais para x_1 e x_2, satisfazendo as restrições dadas pelas equações (2), (3) e (4), de forma que a função tenha o maior valor possível dentro da região viável (não deve violar as restrições). As variáveis x_1 e x_2 são denominadas de variáveis independentes (variáveis de decisão).

Na Fig. 28, podem ser observados três contornos da função objetivo. A função objetivo tem o mesmo valor em todos os pontos ao longo de cada uma das três linhas. Observando-se a Fig. 28, é fácil ver que a solução do problema é:

$$X^* = (x_1^*, x_2^*) = (1,0)$$

Isto significa que

$$f(X^*) \geq f(X) \text{ para todo X que pertence à região viável } S \qquad (5)$$

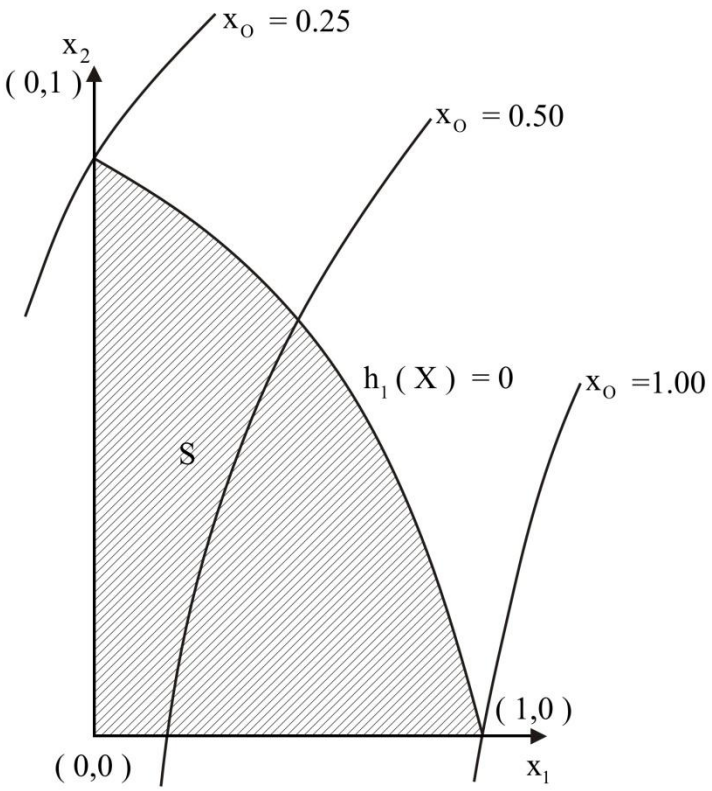

Fig. 28. Contornos da função objetivo e a região viável de um problema de otimização [89].

Quando uma solução X*, pertencente à região viável *S*, satisfaz a equação (5), é chamada de solução ótima, e, neste caso do exemplo proposto, é a solução máxima. Se

o símbolo na equação (5) fosse ” ≤ “, X* seria chamado de solução mínima. Da mesma forma, *f(X*)* é chamado de ótimo e é escrito como x_o*.

Observando-se a Fig. 28, pode-se ver que outros valores maiores para *f(X)* poderiam ser obtidos pela escolha de x_1, x_2, fora da região viável *S*. Qualquer par ordenado de números reais é denominado de solução do problema e o valor correspondente de *f(X)* é denominado de valor da solução. Mas uma solução *X*, de forma que pertença à região viável, que é a solução que interessa de fato, é denominada de solução viável. Na Fig. 28, o conjunto de pontos que satisfazem ao conjunto de restrições está marcado pela área, *S*, com hachuras. Pode-se definir:

$$S = \{(x_1, x_2): h(x_1, x_2) \leq 0, x_1 \geq 0, x_2 \geq 0\} \quad (6)$$

2.4.1. Tipos de otimização

Na otimização com restrição, o problema que está sendo resolvido é:

Min S(x) ou *Max S(x)*

sujeito a restrições de igualdade e/ou desigualdade, que definem a região viável, sendo que qualquer ponto nesta região é uma solução viável. *S(x)* é a função objetivo. Dependendo do tipo de função objetivo e de suas restrições, os problemas de otimização com restrição são comumente chamados de programação linear, programação quadrática, programação não-linear, programação inteira e programação mista.

Programação linear: A função objetivo e as restrições são lineares

$$Min\ S(x) = c^T x$$

Sujeito a: $Ax \leq b$

$$x \geq 0$$

onde A é uma matriz m x n, isto é, m restrições e n variáveis.

Programação Quadrática: A função objetivo é quadrática e as restrições são lineares

$$Min\ S(x) = c^T x + 1/2\ x^T Q x$$

Sujeito a: $Ax \leq b$

$$x \geq 0$$

Programação não-linear: A função objetivo e/ou restrições são não-lineares

$$Min\ S(x)$$

Sujeito a: $h_j(x) = 0, j = 1, 2,..., m$

$$g_j(x) \leq 0, j = 1, 2,..., p$$

onde $h_j(x)$ são m restrições de igualdade e $g_j(x)$ são p restrições de desigualdade.

Programação Inteira: As variáveis de decisão pertencem ao campo dos números inteiros.

Programação Mista: É uma combinação da programação inteira com as demais. Por exemplo, num problema de projeto de trocadores de calor, as variáveis de decisão podem ser as temperaturas das correntes (campo real) e os tipos de trocadores existentes (campo inteiro).

Cálculos de equilíbrio termodinâmico consistem na minimização da energia de Gibbs total do sistema (função objetivo). Como a função objetivo é não-linear, são aplicadas

as técnicas referentes à programação não-linear, ou, como alguns autores costumam chamar, otimização não-linear. As restrições que correspondem ao balanço de massa são lineares, mas, devido à troca de variáveis que será feita para que se possa efetuar as simulações, utilizando-se a ferramenta proposta neste trabalho (*Solver*, do Excel), ter-se-á um problema de otimização não-linear, em que tanto a função objetivo quanto as restrições são não-lineares.

2.4.2. Condições para a otimalidade

2.4.3. Otimização sem restrição

No caso da otimização sem restrições, em que se deseja encontrar os pontos extremos da função objetivo, tem-se as seguintes condições de otimalidade:

- Condição necessária de primeira ordem:

Para que $x*$ seja um mínimo ou máximo local da função *S(x)*, diferenciável em $x*$, é necessário que:

$$\nabla S(x*) = \left(\frac{\partial S(x)}{\partial x_1}, \ldots, \frac{\partial S(x)}{\partial x_n}\right)^T = 0 \qquad (7)$$

- Condição necessária de segunda ordem:

Para que $x*$ seja um mínimo local da função *S(x)*, duas vezes diferenciável em $x*$, é necessário que:

$$\nabla S(x*) = 0 \qquad \text{e}$$

$$H(x^*) \equiv \nabla^2 S(x^*) \text{ seja } \textbf{positiva semidefinida}$$

Onde *H(x*)* é chamada de *matriz Hessiana*. A matriz Hessiana de uma função *S(x)* qualquer é a matriz *n* x *n* [91]:

$$\begin{pmatrix} \frac{\partial^2 S(x)}{\partial x_1^2} & \frac{\partial^2 S(x)}{\partial x_1 \partial x_2} & \cdots \frac{\partial^2 S(x)}{\partial x_1 \partial x_n} \\ \vdots & \vdots & \vdots \\ \frac{\partial^2 S(x)}{\partial x_n \partial x_1} & \frac{\partial^2 S(x)}{\partial x_n \partial x_2} & \cdots \quad \frac{\partial^2 S(x)}{\partial x_n^2} \end{pmatrix} \tag{8}$$

Estas condições (de primeira e segunda ordem) são apenas necessárias. A condição suficiente, para que se tenha um mínimo local, pode ser assim definida:

Para *S(x)* duas vezes diferenciável em x^*, tem-se que:

$$\nabla S(x*) = 0 \text{ e}$$

H(x)* é **positiva definida**

Através da expansão da série de Taylor, ao redor do ótimo x^*, é possível visualizar a condição suficiente acima enunciada:

$$S(x) = S(x*) + \nabla^T S(x*)\Delta x + \frac{1}{2}(\Delta x^T) H(x*)\Delta x + \cdots \tag{9}$$

Onde

$$\Delta x = x - x* \tag{10}$$

é a perturbação ao redor de x^*. Assume-se que todos os termos na Eq. (9) existam e sejam contínuos, mas os termos a partir da terceira ordem são ignorados.

Assumindo-se que $x*$ seja um mínimo local, de modo que nenhum outro ponto na vizinhança de $x*$ resulte em um valor de $S(x)$ menor do que $S(x*)$,tem-se que:

$$S(x) - S(x*) \geq 0 \tag{11}$$

Da condição de primeira ordem, tem-se que

$$\nabla^T S(x*)\Delta x = 0, \tag{12}$$

pois o gradiente de $S(x)$ é igual a zero (ver Eq. (7)). Como o segundo termo da Eq.(9) é igual a zero, é necessário examinar o terceiro termo. Este termo estabelece o caráter do ponto estacionário (mínimo, máximo ou ponto de sela).

Para garantir, então, que $x*$ seja um mínimo local, é preciso que seja satisfeita a Eq. (13):

$$\frac{1}{2}(\Delta x^T)H(x*)\Delta x > 0 \tag{13}$$

Uma vez que Δx é positivo, resulta que a matriz Hessiana avaliada em $x*$, ($H(x*)$), deve ser positiva definida.

A positividade de $H(x*)$ pode ser avaliada pela análise dos autovalores de $H(x*)$. Dessa forma, a Hessiana em $x*$ será positiva definida se, e somente se, todos os autovalores de $H(x*)$ forem não-negativos [89]. A demonstração da relação existente entre autovalores e positividade de uma matriz *n x n* pode ser vista em [89] ou em livros de álgebra linear.

2.4.4. Otimização com restrição

A idéia chave para desenvolver as condições necessárias e suficientes para um problema de otimização com restrições é transformá-lo em um problema de otimização sem restrições e aplicar as condições para este caso. Uma forma de fazer esta transformação é através da introdução de uma função auxiliar, chamada de *função de Lagrange*, $\mathcal{L}(x,\lambda,\mu)$, definida como:

$$\mathcal{L}(x,\lambda,\mu) = S(x) + \lambda^T h(x) + \mu^T g(x), \qquad \mu \geq 0 \tag{14}$$

Onde λ e μ são os multiplicadores de Lagrange associados às restrições de igualdade e desigualdade, respectivamente (μ também é conhecido como multiplicador de *Kuhn-Tucker*). Aqui, *h(x)* e *g(x)* representam as restrições de igualdade e desigualdade, respectivamente. No ponto ótimo, tem-se:

$$\mathcal{L}(x*,\lambda*,\mu*) = S(x*) \tag{15}$$

Cada multiplicador de Lagrange indica o quão sensível é a função objetivo em relação à restrição associada [90].

Para entender a origem da função de Lagrange, o ótimo do exemplo acima deve satisfazer as seguintes condições:

$$dS = \frac{\partial S}{\partial x_1}\delta x_1 + \frac{\partial S}{\partial x_2}\delta x_2 = 0 \tag{16}$$

e

$$dh = \frac{\partial h}{\partial x_1}\delta x_1 + \frac{\partial h}{\partial x_2}\delta x_2 \tag{17}$$

Se *S(x)* fosse uma função sem restrição, então as suas derivadas parciais seriam nulas no ponto ótimo e *dS(x*)* seria nulo para quaisquer valores das variações δx_1 e δx_2. Entretanto, como as variáveis x_1 e x_2 estão restritas (δx_1 e δx_2 não são independentes), as suas derivadas parciais de *S(x)* não podem ser arbitrariamente igualadas a zero. Contudo, *S(x)* deve ser um extremo no ponto ótimo e, portanto, $dS(x^*) = 0$. A segunda condição, $dh(x^*) = 0$, existe porque $h(x) = 0$. Para se obter uma solução (δx_1 e δx_2) não trivial do sistema de equações dado pelas Eq.(16) e (17), a matriz dos coeficientes do sistema:

$$\begin{bmatrix} \frac{\partial S}{\partial x_1} & \frac{\partial S}{\partial x_2} \\ \frac{\partial h}{\partial x_1} & \frac{\partial h}{\partial x_2} \end{bmatrix} \tag{18}$$

Deve ter determinante nulo, ou seja, as linhas da matriz são linearmente dependentes:

$$\frac{\partial S}{\partial x_1} + \lambda \frac{\partial h}{\partial x_1} = 0 \tag{19}$$

$$\frac{\partial S}{\partial x_2} + \lambda \frac{\partial h}{\partial x_2} = 0 \tag{20}$$

Então, pode-se definir uma função auxiliar (função de Lagrange) como:

$$\mathcal{L}(x, \lambda) = S(x) + \lambda^T h(x) \tag{21}$$

As Eq.(19) e (20) são satisfeitas se:

$$\nabla_x L(x, \lambda) = 0 \tag{22}$$

Para que a restrição de igualdade, $h(x) = 0$, seja também satisfeita, é necessário que

$$\nabla_\lambda L(x, \lambda) = 0 \tag{23}$$

Portanto, no ponto ótimo é necessário que

$$\nabla L(x*, \lambda*) = 0 \tag{24}$$

A existência dos multiplicadores de Lagrange depende da forma das restrições e estará garantida se, e somente se, os gradientes das restrições de desigualdades ativas e das restrições de igualdade no ponto ótimo $x*$ forem linearmente independentes. Por exemplo, no caso de um problema somente com restrições de igualdade, a condição necessária de primeira ordem para $\mathcal{L}(x,\lambda)$ fica:

$$\nabla_x S(x) + [\nabla_x h(x)]^T \lambda = 0 \tag{25}$$

Cuja solução para λ existirá somente se $\nabla_x h(x)$ possuir posto completo, *m*, isto é, estar composta por *m* vetores linearmente independentes.

- Condição necessária de primeira ordem de Karush-Kuhn-Tucker (KKT):

Para que $x*$ seja um ótimo local do problema com restrições, com *S(x)*, *g(x)* e *h(x)* diferenciáveis em $x*$, é necessário que os gradientes das restrições de desigualdade ativas e das restrições de igualdade sejam linearmente independentes e que as seguintes condições sejam satisfeitas:

$$\nabla_x L(x*, \lambda*, \mu*) = \nabla S(x*) + (\lambda*)^T \nabla h(x*) + (\mu*)^T \nabla g(x*) = 0 \tag{26}$$

$$h(x*) = 0 \tag{27}$$

$$g(x*) \leq 0 \tag{28}$$

$$\mu_j^* g_j(x*) = 0, j = 1,2, \dots p \tag{29}$$

$$\mu^* \geq 0 \tag{30}$$

- Condição necessária de segunda ordem de *Karush-Kuhn-Tucker* (*KKT*):

Para que $x*$ seja um mínimo local do problema com restrições, com *S(x)*, *g(x)* e *h(x)* duas vezes diferenciáveis em $x*$, é necessário que a condição de primeira ordem de *KKT* seja satisfeita e, que a matriz Hessiana da função de Lagrange, $\nabla_x^2 \mathcal{L}(x*, \lambda*, \mu*)$, seja positiva semidefinida para todo vetor não nulo *d* tal que:

$$d^T \nabla h_i(x*) = 0, i = 1,2, \dots, m \tag{31}$$

E, para as restrições de desigualdade ativas, ou seja, em que $g_j(x*) = 0$, tem-se:

$$d^T \nabla \mathrm{g}_j(x*) = 0 \tag{32}$$

Isto é,

$$d^T \nabla_x^2 \mathcal{L}(x*, \lambda*, \mu*) d \geq 0 \tag{33}$$

- Condição suficiente de *Karush-Kuhn-Tucker* (*KKT*):

Para que $x*$ seja um mínimo local do problema com restrições, com *S(x)*, *g(x)* e *h(x)* duas vezes diferenciáveis em $x*$, é suficiente que a condição de primeira ordem seja satisfeita e, que a matriz Hessiana da função de Lagrange, $\nabla_x^2 \mathcal{L}(x*, \lambda*, \mu*)$, seja positiva definida para todo vetor não nulo *d* tal que as Eq. (2.199) e (2.200) sejam satisfeitas. Pode-se, então, escrever:

$$d^T \nabla_x^2 \mathcal{L}(x*, \lambda*, \mu*) d > 0 \tag{34}$$

A positividade da matriz Hessiana com restrição é garantida se todas as raízes do polinômio característico

$$p(\lambda) = \begin{vmatrix} \lambda I - \nabla_x^2 L & M \\ M^T & 0 \end{vmatrix} = 0 \tag{35}$$

forem positivas, onde *M* é a matriz formada pelos gradientes de *h(x*)* e *g(x*)* ativas, isto é, $d^T M = 0$, com $m+p^a < n$ e com posto completo (p^a é o número de restrições g ativas).

O mesmo critério se aplica para semipositividade, negatividade e seminegatividade, com os respectivos sinais das raízes.

2.4.5. Relaxação Lagrangeana

O método da relaxação Lagrangeana consiste em utilizar os multiplicadores de Lagrange para a solução de problemas com restrições. Assim, o método transforma o problema:

$$Min\ S(x)$$

$$\text{Sujeito a: } h_j(x) = 0, j = 1,2, \dots, m$$

$$g_j(x) \leq 0, j = 1,2, \dots, p$$

Onde $S(x)$, $h_j(x)$ e $g_j(x)$ são funções convexas e K é um convexo, no problema:

$$Max \quad (\lambda, \mu)$$

$$\text{Sujeito a: } \mu \geq 0$$

Onde

$$(\lambda, \mu) = min\{S(x) + \lambda^T h(x) + \mu^T f(x)\}$$

$$f_j(x) = g_j(x) + (v_j)^2$$

v_j são as variáveis de folga.

Desta forma, a relaxação Lagrangeana transforma um problema com restrições em um problema sem restrições. Observa-se também que este método minimiza a função em

relação a *x*, mas maximiza em relação aos multiplicadores, por isso este tipo de problema é também conhecido como problema *minimax* [90].

A solução do método da relaxação Lagrangeana (Método de Lagrange) consiste em aplicar as condições de otimalidade sobre $\mathcal{L}(x,\lambda,\mu)$, como apresentado nas Eq.(22) e (23). Para melhor compreensão do método, considera-se o seguinte exemplo apresentado em Himmelblau [92]:

$$Min\ S(x) = x_1 x_2$$

$$\text{Sujeito a: } g_1(x) = x_1^2 + x_2^2 - 25 \leq 0$$

A função auxiliar de Lagrange pode ser, portanto, representada por:

$$\mathcal{L}(x,\mu) = x_1 x_2 + \mu_1 (x_1^2 + x_2^2 - 25 + (v_j)^2)$$

Aplicando-se as condições de otimalidade, o seguinte sistema de equações não-linear é construído:

$$\frac{\partial \mathcal{L}}{\partial x_1} = x_2 + 2\mu_1 x_1 = 0$$

$$\frac{\partial \mathcal{L}}{\partial x_2} = x_1 + 2\mu_1 x_2 = 0$$

$$\frac{\partial \mathcal{L}}{\partial \mu_1} = x_1^2 + x_2^2 - 25 + (v_j)^2 = 0$$

$$\frac{\partial \mathcal{L}}{\partial v_1} = 2\mu_1 v_1 = 0$$

A solução do sistema de equações acima pode ser vista na Tabela I:

Tabela I. Solução do exemplo apresentado em Himmelblau [92], usando-se o método de Lagrange.

μ_1	x_1	x_2	v_1	$S(x)$	ponto
0	0	0	5	0	Sela
0,5	**3,54**	**-3,54**	**0**	**-12,5**	**Mínimo**
0,5	**-3,54**	**3,54**	**0**	**-12,5**	**Mínimo**
-0,5	3,54	3,54	0	12,5	Máximo
-0,5	-3,54	-3,54	0	12,5	Máximo

A Fig. 29 ilustra as funções do exemplo acima. Os contornos dos diferentes valores assumidos pela função objetivo são hipérboles, representadas por linhas tracejadas, e a região viável é delimitada pela área hachurada correspondente ao círculo $g(x) = 0$. Os pontos B e C correspondem aos dois mínimos, D e E correspondem aos dois máximos, e A é o ponto de sela.

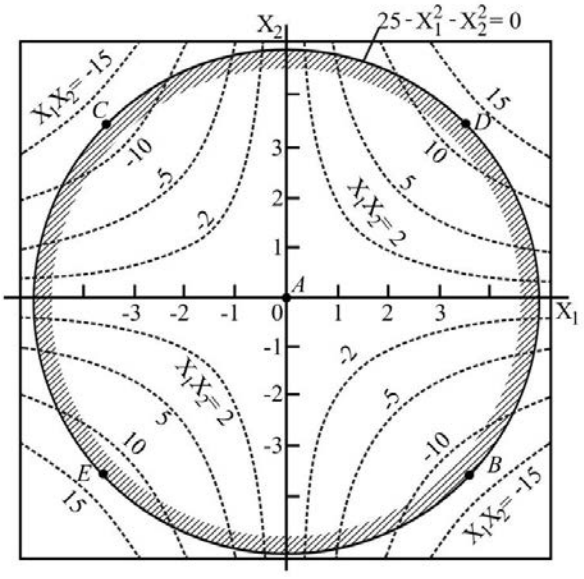

Fig. 29. Ilustração da solução do problema apresentado em Himmelblau [92].

Como o conjunto resultante de equações forma, geralmente, um sistema não linear de equações algébricas, então o método de Lagrange não é muito atrativo, pois a solução deste sistema não linear pode ser mais complexa que a solução direta do problema de otimização por outros métodos. Apesar da dificuldade da aplicação do método de Lagrange para a solução de problemas não lineares, ele é muito útil para a analisar a sensibilidade da função objetivo em relação às restrições [92].

Desse modo, para a solução de problemas de otimização não linear, métodos diretos são preferidos, como o método dos Gradientes Reduzidos Generalizados (GRG). O algoritmo GRG garante que o ótimo local seja encontrado, mas não assegura o ótimo global. Ou seja, o valor do ótimo encontrado depende da estimativa inicial. Para que o ótimo local seja também o ótimo global, o modelo necessita ser convexo [93].

2.4.6. Problemas convexos na termodinâmica

Alguns problemas da minimização da energia de Gibbs são convexos, como a mistura gasosa ideal, fases líquidas e sólidas descritas como solução ideal, bem como um sistema constituído por sólidos imiscíveis. Para cálculos de equilíbrio envolvendo modelos convexos, podem-se aplicar algoritmos que determinem o mínimo local, já que este valor corresponderá ao mínimo global. Assim, não há problemas referentes às estimativas iniciais.

Rossi e colaboradores [93] demonstram, em um trabalho recentemente publicado, que uma função dada por

$$f(\mathbf{z}) = \sum_{i=1}^{N} z_i \cdot \left[\ln z_i - \ln \sum_{j=1}^{N} a_{ij} \cdot z_j \right] \tag{36}$$

é convexa para $a_{ii} = 1$ e $a_{ij} > 0$. O problema de minimização da energia de um sistema composto por uma fase gasosa e por sólidos imiscíveis tem como função objetivo:

$$G = \sum_{i=1}^{NC} n_i^g \left[G_i^{0,g} + RT \ln n_i^g - RT \ln \left(\sum_{j=1}^{NC} n_j^g \right) \right] + \sum_{i=1}^{NC} n_i^s G_i^{0,s} \tag{37}$$

Os termos lineares da Eq.(37) são convexos, e seus termos não lineares, que são da forma da função indicada na Eq. (36), devem ter sua convexidade analisada. No caso da mistura gasosa ideal, na Eq. (36), $a_{ii} = 1$.

Um problema de minimização formulado como

$$\min f(\mathbf{z}) \tag{38}$$

Sujeito a

$$h_j(\mathbf{z}) = 0 \qquad j = 1, \ldots, m \tag{39}$$

é convexo se $f(\mathbf{z})$ é convexo, $h_j(\mathbf{z})$ são convexos, em que $\mathbf{z}$ é um vetor de variáveis.

No problema da minimização da energia de Gibbs, $h_j(\mathbf{z})$ é o conjunto de restrições do balanço de massa (Eq.(40)), que por ser linear é convexo.

$$\sum_{i=1}^{NC} n_i \alpha_{ik} = b_k \tag{40}$$

Há vários modos de avaliar a convexidade de uma função $f(\mathbf{z})$, em que $\mathbf{z}^T = (z_1, \ldots, z_N)$. $\mathbf{z}$ é o número de mols, n_i. Um modo de análise é através da matriz Hessiana e de seus autovalores [94]. Outra forma de análise da convexidade de $f(\mathbf{z})$ é por meio da verificação da desigualdade:

$$f(\beta \cdot \mathbf{z}_A + (1-\beta) \cdot \mathbf{z}_B) \leq \beta \cdot f(\mathbf{z}_A) + (1-\beta) \cdot f(\mathbf{z}_B) \tag{41}$$

Para qualquer $\mathbf{z}_A$ e $\mathbf{z}_B$ no conjunto viável e qualquer valor real β no intervalo $0 \leq \beta \leq 1$.

Assim, no trabalho de Rossi e colaboradores [93], a convexidade foi analisada dos dois modos:

(a) Análise dos autovalores da matriz Hessiana. A partir da Eq. (36), considere uma função $f_1(\mathbf{z})$ dada por:

$$f_1(\mathbf{z}) = z_1 \cdot \ln \frac{z_1}{z_1 + z_2} \tag{42}$$

$$\mathbf{z}^T = \begin{bmatrix} z_1 & z_2 \end{bmatrix} > 0 \tag{43}$$

A matriz Hessiana para $f_1(\mathbf{z})$ é dada por:

$$\mathbf{H}_{f_1} = \begin{bmatrix} \dfrac{z_2^2}{z_1 \cdot (z_1 + z_2)^2} & -\dfrac{z_2}{(z_1 + z_2)^2} \\ -\dfrac{z_2}{(z_1 + z_2)^2} & \dfrac{z_1}{(z_1 + z_2)^2} \end{bmatrix} \tag{44}$$

A matriz dada pela Eq. (44) tem como autovalores:

$$\lambda_1 = 0 \tag{45}$$

$$\lambda_2 = \frac{\left(z_1^2 + z_2^2\right)}{z_1 \cdot (z_1 + z_2)^2} > 0 \tag{46}$$

Portanto, $\mathbf{H}_{f_1}$ é convexa, já que seus autovalores são não-negativos, de modo que é uma matriz positiva definida [94].

(b) Verificação da desigualdade: Considere a função $f_i(\mathbf{z})$ dada por:

$$f_i(\mathbf{z}) = z_i \cdot \left[\ln z_i - \ln \sum_{j=1}^{N} a_{ij} \cdot z_j \right] \tag{47}$$

$$\mathbf{z}^T = \begin{bmatrix} z_1 & \cdots & z_2 & \cdots & z_N \end{bmatrix} > 0 \tag{48}$$

Em que $a_{ii} = 1$ (gas ideal). Para mostrar que $f_i(\mathbf{z})$ é convexo, define-se:

$$y_1 = z_i > 0 \tag{49}$$

$$y_2 = \sum_{j \neq i}^{N} a_{ij} \cdot z_j > 0 \tag{50}$$

Substituindo-se na expressão de $f_i(\mathbf{z})$:

$$f_i(\mathbf{z}) = y_1 \cdot \left[\ln y_1 - \ln(y_1 + y_2) \right] = y_1 \cdot \ln \frac{y_1}{y_1 + y_2} = f_1(\mathbf{y}) \tag{51}$$

Como $f_1(\mathbf{y})$ é convexo, tem-se:

$$\begin{aligned} &\left(\beta \cdot y_1^A + (1-\beta) \cdot y_1^B\right) \cdot \ln \left[\frac{\beta \cdot y_1^A + (1-\beta) \cdot y_1^B}{\beta \cdot y_1^A + \beta \cdot y_2^A + (1-\beta) \cdot y_1^B + (1-\beta) \cdot y_2^B} \right] \\ &\leq \beta \cdot y_1^A \cdot \ln \frac{y_1^A}{y_1^A + y_2^A} + (1-\beta) \cdot y_1^B \cdot \ln \frac{y_1^B}{y_1^B + y_2^B} \end{aligned} \tag{52}$$

Em que $y_1^A > 0$, $y_1^B > 0$, $y_2^A > 0$, $y_2^B > 0$, e $0 \leq \beta \leq 1$.

Usando as Eqs. (49) e (50), os termos em relação a Eq. (52) podem ser rearranjados:

$$\left(\beta \cdot z_i^A + (1-\beta)\cdot z_i^B\right)\cdot\left[\ln\left(\beta \cdot z_i^A + (1-\beta)\cdot z_i^B\right) - \ln\left(\beta \cdot \sum_{j=1}^{N} a_{ij}\cdot z_j^A + (1-\beta)\cdot \sum_{j=1}^{N} a_{ij}\cdot z_j^B\right)\right] \quad (53)$$
$$\leq \beta \cdot z_i^A \cdot \left[\ln z_i^A - \ln\left(\sum_{j=1}^{N} a_{ij}\cdot z_j^A\right)\right] + (1-\beta)\cdot z_i^B \cdot \left[\ln z_i^B - \ln\left(\sum_{j=1}^{N} a_{ij}\cdot z_j^B\right)\right]$$

Esta relação é equivalente a:

$$f_i(\lambda \cdot \mathbf{z}_A + (1-\lambda)\cdot \mathbf{z}_B) \leq \lambda \cdot f_i(\mathbf{z}_A) + (1-\lambda)\cdot f_i(\mathbf{z}_B) \quad (54)$$

Portanto, $f_i(\mathbf{z})$ é convexa.

A função dada pela Eq.(36) é dada por

$$f(\mathbf{z}) = \sum_{i=1}^{N} f_i(\mathbf{z}) \quad (55)$$

Como $f_i(\mathbf{z})$ é convexa, a soma de funções convexas também é convexa.

Assim, é demonstrado que o problema de minimização da energia de Gibbs para um sistema composto por uma fase gasosa ideal e sólidos imiscíveis é convexo, o que garante que o mínimo local seja também o mínimo global; dessa forma, não há problemas referentes à estimativa inicial. O mínimo é único.

Embora possa parecer que os problemas convexos representem um número muito limitado de aplicações da termodinâmica, tal não é verdade, visto que diversos problemas têm sido resolvidos com esta classe de modelo. Na literatura, condições otimizadas da produção de H_2, através de diferentes rotas termoquímicas, têm sido determinadas com boa concordância com dados experimentais [95-97]. Equilíbrios envolvendo diversos sólidos imiscíveis, expostos a diferentes tipos de atmosferas, têm sido calculados com modelos convexos e, novamente, a comparação com valores experimentais é satisfatória [98].

CAPÍTULO 3: METODOLOGIA

A metodologia empregada nas simulações está descrita nos artigos. No presente capítulo, são fornecidas algumas informações complementares.

3.1. *Modelo Termodinâmico*

Em um sistema em que há a fase gasosa, além de fases condensadas, representadas por soluções sólidas e líquidas, a energia total é dada por:

$$\frac{G}{RT} = \frac{1}{RT}\sum n_i^g G_i^{0g} + \sum n_i^g ln y_i^g + \frac{1}{RT}\sum n_i^l G_i^{ol} + \sum n_i^l ln a_i^l$$

$$+\frac{1}{RT}\sum n_i^s G_i^{0s} \quad + \sum n_i^s ln a_i^s + \sum n_i^g lnP \tag{56}$$

Os sobrescritos *s*, *l* e *g* denotam as fases sólida, líquida e gasosa, respectivamente. n_i, y_i representam o número de mols e a fração molar da espécie *i*, respectivamente. A fase gasosa no presente estudo é modelada idealmente como pode ser visto na Eq. (56). De fato, em baixas pressões e altas temperaturas, a fase gás pode ser considerada ideal [99]. Como os sistemas analisados na presente Tese envolvem altas temperaturas (400<T<1400K) e pressões baixas (1-5 atm), a descrição ideal para o gás pode ser aplicada. Ao variar-se a pressão *P* total do sistema, o termo da Eq. (56) $\sum n_i^g lnP$ ganha importância.

Observa-se também que as fases condensadas na Eq. (56) estão representadas por soluções sólidas e líquidas. Se ao invés de soluções fossem substâncias puras, os termos da Eq. (56) referentes à atividade (a_i^l e a_i^s) seriam iguais à unidade. Então, para um

sistema constituído por uma fase gasosa ideal e por fases condensadas estequiométricas (puras), pode-se reescrever a Eq. (56) como:

$$\frac{G}{RT} = \left(\sum_{i=1}^{N} n_i \left[\frac{G_i^0}{RT} + \ln(y_i P) \right] \right)_{gas} + \frac{1}{RT} \left(\sum_{i=1}^{N} n_i G_i^0 \right)_{condensada} \qquad (57)$$

As *N* espécies que compõem o sistema são constituídas por *M* componentes (elementos, no caso deste trabalho). Como cada espécie atômica é conservada, haverá *m* restrições de balanço de massa elementar, que podem ser representados em forma de uma matriz:

$$\begin{bmatrix} a_{11} & \cdots & a_{N1} \\ \vdots & \ddots & \vdots \\ a_{1M} & \cdots & a_{NM} \end{bmatrix} \begin{bmatrix} n_1 \\ . \\ . \\ n_N \end{bmatrix} = \begin{bmatrix} b_1 \\ . \\ . \\ b_M \end{bmatrix} \qquad (58)$$

Aqui, b_k é o número de mols do componente *k*, dado pela composição inicial do sistema e α_{ik} é o número de mols do componente *k* em um mol da espécie *i*. Outra forma equivalente de representar o balanço de massa elementar é através da seguinte notação:

$$\sum_{i=1}^{N} n_i \alpha_{ik} = b_k, \qquad k = 1 \ldots M \qquad (59)$$

3.2. *Dados Termodinâmicos*

A dependência da energia de Gibbs com a temperatura pode ser descrita através de *Cp*, o qual é frequentemente representado por uma fórmula empírica, como sugerido por Kelley [100]:

$$C_P = a + b.10^{-3}T + \frac{c.10^6}{T^2} + d.10^{-6}T^2 \quad (60)$$

A entalpia *H* e a entropia *S* podem ser calculadas a partir de *Cp*, pelas seguintes relações:

$$C_P = \frac{\partial H}{\partial T} \quad (61)$$

$$\frac{C_P}{T} = \frac{\partial S}{\partial T} \quad (62)$$

Sendo a Eq. (60) a descrição de *Cp*, e integrando-se a Eq. (61) da temperatura de referência (298K) até a temperatura *T*, obtém-se a seguinte equação para a entalpia:

$$H = aT + b.10^{-3}\frac{T^2}{2} - \frac{c.10^6}{T} + d.10^{-6}.\frac{T^3}{3} + a_0 \quad (63)$$

Da mesma forma, integrando-se a Eq. (62), nos limites da temperatura de referência (298K) até a temperatura *T*, obtém-se a seguinte equação para a entropia:

$$S = alnT + b.10^{-3}T - \frac{c.10^6}{2T^2} + \frac{d.10^{-6}}{2}T^2 + a_1 \quad (64)$$

A descrição da energia de Gibbs, à temperatura e pressão normal, é calculada a partir da relação de Gibbs-Helmholtz:

$$G = H - TS \quad (65)$$

Considerando as equações (63) até (65), obtém-se a energia de Gibbs de cada espécie:

$$G = a_0 - a_1T + aT(1 - lnT) - b.10^{-3}.\frac{T^2}{2} - \frac{c.10^6}{2T} - d.10^{-6}.\frac{T^3}{6} \quad (66)$$

Onde *a*, *b*, *c*, *d* são as mesmas constantes da equação (60) e a_0 e a_1 correspondem aos valores numéricos decorrentes do processo de integração das Eqs. (61) e (62),

respectivamente. A Tabela II mostra a compilação de dados termodinâmicos, obtidos no trabalho de Knacke e colaboradores [101], que foram usados diretamente na Eq. (66) para calcular a energia de Gibbs das diversas espécies consideradas no presente trabalho, no estado padrão substância pura. Entalpia e energia de Gibbs são dadas em J mol^{-1}, e entropia e calor específico são dados em J K^{-1} mol^{-1}.

O valor absoluto da entalpia de uma substância pura não é possível de ser conhecido. Desta forma, por convenção, é estabelecido que, para elementos, *H(298)* = 0. A temperatura do estado de referência para todos os dados termodinâmicos usados neste trabalho é 298 K.

Tabela II. Dados termodinâmicos [101].

Espécies	*a*	*b*	*c*	*d*	a_0	a_1
H_2	26.882	3.586	0.105	-	-7823	-22.966
H_2O (vapor)	34.376	7.841	-0.423	-	-253871	-11.750
H_2O (líquido)	20.355	109.198	2.033	-	-289932	-67.147
CH_4(g)	11.933	77.647	0.142	-18.414	-81242	96.731
CO (g)	30.962	2.439	-0.280	-	-120809	18.937
CO_2 (g)	51.128	4.368	-1.469	-	-413886	-87.078
O_2(g)	29.154	6.477	-0.184	-1.017	-9589	36.116
CaO (s)	50.417	4.184	-0.849	-	-653156	-255.069
$Ca(OH)_2$ (s)	101.788	17.987	-1.736	-	-1023061	-511.691
$CaCO_3$ (calcita,s)	104.516	21.924	-2.594	-	-1249193	-523.567
Ni (s)	20.589	10.159	1.615	-	-2242	-84.744
NiO (s)	39.915	12.368	2.188	-	-245712	-184.046
C(grafite)	24.435	0.435	-3.163	-	-16019	-146.304

Outras referências [102,103] também foram empregadas na compilação de dados termodinâmicos. Neste caso, a fórmula empírica para *Cp* é um pouco diferente daquela apresentada na Eq. (60).

$$C_P = a + bT + cT^2 + dT^3 \tag{67}$$

Deste modo, a descrição da entalpia, entropia e energia de Gibbs será da seguinte forma:

$$H = aT + \frac{b}{2}T^2 + \frac{c}{3}T^3 + \frac{d}{4}T^4 + a_0 \quad (68)$$

$$S = alnT + bT + \frac{c}{2}T^2 + \frac{d}{3}T^3 + a_1 \quad (69)$$

$$G = a_0 - a_1T + aT(1 - lnT) - \frac{b}{2}T^2 - \frac{1}{6}cT^3 - \frac{1}{12}dT^4 \quad (70)$$

A Tabela III mostra os dados termodinâmicos obtidos de Sandler e Prausnitz [102,103].

Tabela III. Dados termodinâmicos [102,103].

Espécies	*a*	*b*	*c*	*d*	$\Delta_f H_{298}$	$\Delta_f G_{298}$
Etileno	3.806E+0	1.566E-1	-8.348E-5	1.755E-8	5.234E+4	6.816E+4
Etano	5.409E+0	1.781E-1	-6.938E-5	8.713E-9	-8.474E+4	-3.295E+4
Propileno	3.710E+0	2.345E-1	-1.160E-4	2.205E-8	2.043E+4	6.276E+4
Propano	-4.224E+0	3.063E-1	-1.586E-4	3.215E-8	-1.039E+5	-2.349E+4
n-butano	9.487E+0	3.313E-1	-1.108E-4	-2.822E-9	-1.262E+5	-1.610E+4
Isobutano	-1.390E+0	3.847E-1	-1.846E-4	2.895E-8	-1.346E+5	-2.090E+4
1-buteno	-2.994E+0	3.532E-1	-1.990E-4	4.463E-8	-1.260E+2	7.134E+4
2-cis-buteno	4.396E-1	2.953E-1	-1.018E-4	-0.616E-9	-6.990E+3	6.590E+4
2-trans-buteno	1.832E+1	2.564E-1	-7.013E-5	-8.989E-9	-1.118E+4	6.301E+4
Isobutileno	1.605E+1	2.804E-1	-1.091E-4	9.098E-9	-1.691E+4	5.811E+4
Metanol	2.115E+1	7.092E-2	2.587E-5	-2.852E-8	-2.013E+5	-1.626E+5
Formaldeído	2.348E+1	3.157E-2	2.985E-5	-2.300E-8	-1.160E+5	-1.100E+5
Etanol	9.014E+0	2.141E-1	-8.390E-5	1.373E-9	-2.350E+5	-1.684E+5
acetaldeído	7.716E+0	1.823E-1	-1.007E-4	2.380E-8	-1.644E+5	-1.334E+5
Ácido acético	4.840E+0	2.549E-1	-1.753E-4	4.949E-8	-4.351E+5	-3.769E+5
Acetona	6.301E+0	2.606E-1	-1.253E-4	2.038E-8	-2.177E+5	-1.532E+5
Glicerol	8.424E+0	4.442E-1	-3.159E-4	9.378E-8	-5.853E+5	-3.928 E+5
Acroleína	1.197E+1	2.106E-1	-1.071E-4	1.906E-8	-7.092E+4	-6.519E+4
Álcool alílico	-1.105E+0	3.146E-1	-2.032E-4	5.321E-8	-1.321E+5	-7.130E+4
Propionaldeído	1.172E+1	2.614E-1	-1.300E-4	2.126E-8	-1.922E+5	-1.305E+5
Álcool isopropílico	3.243E+1	1.885E-1	6.406E-5	-9.261E-8	-2.726E+5	-1.735E+5
n-butanol	3.266E+0	4.180E-1	-2.242E-4	4.685E-8	-2.749E+5	-1.509E+5
Metil etil cetona	1.094E+1	3.559E-1	-1.900E-4	3.920E-8	-2.385E+5	-1.462E+5
Aldeído butírico	1.408E+1	3.457E-1	-1.723E-4	2.887E-8	-2.052E+5	-1.148E+5

$\Delta_f H_{298}$= entalpia padrão de formação a 298 K.

$\Delta_f G_{298}$= energia de Gibbs padrão de formação a 298 K.

3.3. *Minimização da energia de Gibbs e a ferramenta Solver do MS Excel*

A ferramenta Solver do Microsoft Excel utiliza o algoritmo GRG para a resolução de problemas de otimização não linear com restrições. O algoritmo foi implementado a partir de uma versão melhorada (GRG2) desenvolvida por Leon Lasdon, da

Universidade do Texas e por Allan Warren, da Universidade de Cleveland. O código GRG2 tem se demonstrado pelo seu uso, por muitos anos, como um dos métodos mais confiáveis e robustos para resolver problemas de otimização não linear. A função Solver tem um limite de 200 variáveis de decisão e 100 restrições [104].

O método da minimização da energia de Gibbs do sistema consiste em minimizar a função objetivo, dada pela Eq. (57), sujeita às restrições do balanço de massa elementar, designadas pelas Eq. (58) ou (59), que são equivalentes. Desse modo, percebe-se que se trata de um problema de otimização não linear. Na resolução deste tipo de problema, poderiam ser empregados diferentes métodos. Neste trabalho, o método dos gradientes reduzidos generalizados (GRG) implementado na ferramenta *Solver* do Excel é empregado. Esta ferramenta foi escolhida devido à sua facilidade de uso e sua robustez, como pôde ser verificado durante a realização das simulações. De fato, a ferramenta Solver demonstra um excelente desempenho na resolução de problemas convexos de otimização.

Apesar das facilidades referentes ao uso da ferramenta *Solver*, há uma deficiência do *Solver* em aplicar o algoritmo GRG quando há o envolvimento das variáveis com funções logarítmicas (veja Eq. (57)). De acordo com Lwin [99], o algoritmo GRG implementado na ferramenta *Solver* viola as restrições de não-negatividade das variáveis. De acordo com Himmelblau [92], o algoritmo GRG pode apresentar soluções não viáveis, ao tentar atingir a solução ótima. Assim sendo, no presente trabalho, é proposta uma troca de variáveis para evitar o problema com o envolvimento de funções logarítmicas. A dedução da mudança de variáveis segue abaixo. Considera-se, com o objetivo de simplificação, a função objetivo representando a descrição de um sistema constituído unicamente pela fase gasosa, em que P=1 atm.

$$\frac{G}{RT} = \frac{1}{RT}\sum_{i=1}^{N} n_i\, G_i^0 + \sum_{i=1}^{N} n_i ln \frac{n_i}{\sum n_i} \tag{71}$$

Fazendo-se:

$$n_i = e^{n\prime_i} \tag{72}$$

Pode-se escrever:

$$\frac{G}{RT} = \frac{1}{RT}\sum e^{n\prime_i} G_i^0 + \sum e^{n\prime_i} ln \frac{e^{n\prime_i}}{\sum e^{n\prime_i}} \tag{73}$$

Aplicando-se propriedades dos logaritmos:

$$\frac{G}{RT} = \frac{1}{RT}\sum e^{n\prime_i} G_i^0 + \sum e^{n'_i}(ln\, e^{n\prime_i} - ln \sum e^{n\prime_i}) \tag{74}$$

Sabendo-se que:

$$n'_i = ln e^{n\prime_i} \tag{75}$$

Pode-se escrever:

$$\frac{G}{RT} = \frac{1}{RT}\sum e^{n\prime_i} G_i^0 + \sum e^{n\prime_i}.n'_i - \sum e^{n\prime_i} ln \sum e^{n\prime_i} \tag{76}$$

Colocando-se em evidência o termo $\sum e^{n\prime_i}$, tem-se:

$$\frac{G}{RT} = \sum_{i=1}^{N} e^{n\prime_i}\left[\frac{G_i^0}{RT} + n'_i - ln\left(\sum_{i=1}^{N} e^{n\prime_i}\right)\right] \tag{77}$$

Visto que $e^{n'i}$ não pode assumir valores negativos, a deficiência da ferramenta *Solver* é superada, podendo-se realizar os cálculos de equilíbrio sem mensagens de erro.

Devido à mudança de variáveis na função objetivo, a equação referente às restrições do balanço de massa elementar passa a ser escrita da seguinte forma:

$$\sum_{i=1}^{N} e^{n'_i}\alpha_{ik} = b_k, \qquad k = 1 \dots M \qquad (78)$$

Observa-se que tanto a função objetivo, Eq. (77), quanto as restrições do balanço de massa elementar, Eq. (78), são não lineares. Assim, tem-se um problema de otimização em que a função objetivo e as restrições são não lineares nas variáveis de decisão. Note que como a função exponencial é convexa, a troca de variável não afeta a convexidade do problema. Portanto, tem-se a função objetiva convexa (vide dedução do capítulo 2, com **z**= exp(n'_i)) e restrições convexas.

Apesar das vantagens mencionadas referentes ao uso da ferramenta *Solver*, é preciso enfatizar que nem sempre a obtenção de dados termodinâmicos para a construção da função objetivo é uma tarefa simples. Depende-se de fontes bibliográficas confiáveis, e, além disso, muitos dados não estão disponíveis gratuitamente. Além disso, a ferramenta aplica-se a uma classe de problemas – problemas convexos. Pacotes comerciais, como por exemplo, o *FactSage*, têm uma ampla biblioteca de dados termodinâmicos incluídos, além da capacidade de resolver problemas não convexos, envolvendo fases com alta não idealidade.

3.4. *A atividade termodinâmica como função dos multiplicadores de Lagrange*

No capítulo 2, os multiplicadores de Lagrange foram abordados de um ponto de vista da otimização, mostrando a sua importância na transformação de um problema com restrições em um novo problema irrestrito, através da construção da função de Lagrange.

Nesta Tese, mostra-se a relação que existe entre os multiplicadores de Lagrange e a atividade termodinâmica. A dedução completa desta relação está descrita na metodologia do artigo da seção 4.1.1 (*Thermodynamic analysis of ethanol steam reforming using Gibbs energy minimization method: A detailed study of the conditions of carbon deposition*). A relação é:

$$\ln a_i = \left(-G_i^0 \Big/ RT \right) + \sum_k \left(\lambda_k \Big/ RT \right) \alpha_{ik} \qquad (79)$$

Portanto a atividade da espécie química *i* (a_i) pode ser escrita em função do multiplicador de Lagrange (λ_K). Para determinar a atividade do carbono em relação à fase grafite numa atmosfera gasosa, a Eq. (79) pode ser reescrita como segue:

$$\ln a_C = \left(-G_C^0 \Big/ RT \right) + \frac{\lambda_C}{RT} \qquad (80)$$

Rearranjando-se a Eq.(80), percebe-se facilmente que o multiplicador de Lagrange do componente carbono equivale ao potencial químico do carbono ($\lambda_C = G_C^0 + RT \ln a_C$). Neste trabalho, a atividade do carbono, a_C, na atmosfera do reformador ou do ânodo da SOFC é calculada pela Eq. (80). Após o processo de otimização, os multiplicadores de Lagrange são fornecidos através de relatórios de sensibilidade. Se a atividade do carbono (com referência à fase grafite) for maior do que a unidade, a fase gasosa está em um equilíbrio metaestável, e é provável que ocorra a deposição de carbono. Por outro lado, se $a_C < 1$, o sistema está em equilíbrio estável e a formação de carbono é termodinamicamente impossível. Quando $a_C = 1$, a fase grafite coexiste com a fase gás, e o sistema bifásico está em equilíbrio estável. A principal vantagem referente ao uso da Eq. (80) é com respeito à facilidade de determinar a atividade do carbono em diferentes

sistemas sem o conhecimento prévio das reações químicas que levariam à deposição de carbono.

A tendência para deposição de carbono também pode ser avaliada através da força motriz. Em uma dada temperatura, a força motriz para deposição de carbono com referência à fase grafite, D_{gra}, é definida como segue:

$$D_{gra} = \mu_C^{gas} - \mu_C^0 \qquad (81)$$

Onde μ_C^{gas} corresponde ao potencial químico de carbono na fase gás em uma dada temperatura, e μ_C^0 é o potencial químico de carbono no estado padrão, isto é, $\mu_C^0 = G_C^0$. D_{gra} é facilmente calculado por:

$$D_{gra} = RT \ln a_C \qquad (82)$$

Valores de atividade do carbono maiores do que a unidade podem ser computados se a fase grafite for excluída tanto da energia de Gibbs total do sistema e da restrição do balanço de massa elementar do carbono. Portanto a força motriz para a nucleação da fase grafite pode ser determinada.

3.5. *Modelo termodinâmico para a operação da SOFC*

A modelagem da célula SOFC é feita com base na termodinâmica. Portanto, considera-se que a célula opere sob condições reversíveis. É verificado o efeito que a operação da célula tem em seu potencial reversível e na tendência à deposição de carbono no ânodo. Ao conhecer a distribuição dos valores de potencial ao longo do canal, pode-se estimar a máxima eficiência da célula. Assim, em uma célula SOFC com eletrólito condutor de íons O^{2-}, avalia-se como o potencial reversível é afetado à medida

que íons oxigênio chegam ao compartimento do ânodo; do mesmo modo, para células SOFC com eletrólito condutor de íons H^+, avalia-se como o potencial reversível varia conforme íons hidrogênio deixam o compartimento do ânodo. O perfil de deposição de carbono ao longo do canal da célula é também avaliado como função de íons O^{2-} que chegam ao ânodo, ou do íons H^+ que deixam o ânodo. Em outras palavras, avalia-se como a corrente afeta a deposição de carbono e o potencial reversível da célula. Desse modo, para a realização das simulações, deve-se, fundamentalmente, adaptar as restrições do balanço de massa elementar do oxigênio (para a SOFC-O^{2-}) e do hidrogênio (para a SOFC-H^+). Nesta Tese, avaliou-se, termodinamicamente, o desempenho de células SOFC operando com glicerol. Todas as equações estão descritas nas metodologias dos dois artigos referentes a este tema (seção 4.1.3 e 4.1.4).

3.6. *Modelo para a curva de polarização da PEMFC*

Enquanto as células do tipo SOFC foram avaliadas de um ponto de vista unicamente termodinâmico, ou seja, monitorando-se como a corrente de operação afeta o potencial reversível da célula, a célula PEMFC foi modelada considerando-se todas as irreversibilidades; dessa forma, pode-se falar em um modelo para a curva de polarização. O modelo da curva de polarização para o *stack* comercial – BCS 500W – foi obtido da literatura e implementado no Excel, acoplando-o a diferentes plantas de produção de hidrogênio, as quais foram modeladas de acordo com modelos desenvolvidos na presente Tese, incluindo o balanço térmico.

O modelo para a curva de polarização da célula PEMFC foi obtido a partir do trabalho de Amphlett e colaboradores [105,106] e Mann e colaboradores [107]. Trata-se de um modelo bastante conhecido da literatura, denominado 'modelo eletroquímico generalizado estacionário' (*generalized steady-state electrochemical model*, GSSEM).

É um modelo semi-empírico, isotérmico e estático. O modelo apresenta uma parte mecanística e outra empírica, que depende de ajuste de parâmetros de acordo com o tipo de célula PEMFC empregada. No desenvolvimento do modelo mecanístico, é considerado o transporte de massa que ocorre nos canais, a difusão nos eletrodos (modelada basicamente pela equação de Stefan-Maxwell) e a difusão que ocorre através do filme de água (o transporte dos gases dissolvidos através do filme de água que recobre os sítios catalíticos no ânodo e no cátodo tem de ser considerado, e a concentração do gás dissolvido é estimada pela Lei de Henry). A parte eletroquímica do modelo é baseada fundamentalmente em parâmetros que podem ser determinados experimentalmente para cada tipo de célula. Todas as equações necessárias para a simulação da curva de polarização estão apresentadas no artigo da seção 4.1.6.

CAPÍTULO 4: RESULTADOS E DISCUSSÃO

4.1. *Artigos publicados em periódicos*

Nesta seção, estão incluídos os artigos publicados durante a realização desta Tese. Assim, a metodologia detalhada que foi utilizada em cada um dos estudos pode ser apreciada diretamente nos artigos. O mesmo vale para os resultados e a discussão.

Na seção 4.2, é feita uma discussão mais geral, integrando os diferentes artigos, ou seja, mostrando a relação que existe entre estes estudos publicados, e como os resultados se complementam.

4.1.1. Thermodynamic analysis of ethanol steam reforming using Gibbs energy minimization method: A detailed study of the conditions of carbon deposition

(Análise termodinâmica da reforma a vapor do etanol usando o método da minimização da energia de Gibbs: um estudo detalhado das condições de deposição do carbono)

Principais Resultados:

- Demonstração da relação matemática entre multiplicadores de Lagrange e a atividade termodinâmica;
- Demonstração da viabilidade de utilização de uma ferramenta fácil de ser usada – Solver, do Excel – em simulações termodinâmicas. Apresentação de estratégia (mudança de variável) para viabilizar o uso desta ferramenta;
- Apresentação de condições ótimas para aumento da produção de H_2 a partir da reforma a vapor do etanol;
- Verificação da tendência à formação de carbono (grafite) em diferentes sistemas termodinâmicos (estável e metaestável); Constatação do fato que, em sistemas metaestáveis, compostos por acetaldeído e etileno, parâmetros como temperatura e quantidade de vapor de água na mistura não afetam a atividade do carbono, já que esta é sempre muito maior do que a unidade, indicando alta tendência a depositar carbono, o que é verificado experimentalmente;
- Determinação da atividade do carbono por meio da relação deduzida, visando reproduzir condições experimentais da literatura. Com isso, é possível explicar aparentes desvios entre a termodinâmica e resultados experimentais.

INTERNATIONAL JOURNAL OF HYDROGEN ENERGY 34 (2009) 4321–4330

Available at www.sciencedirect.com

ScienceDirect

journal homepage: www.elsevier.com/locate/he

Thermodynamic analysis of ethanol steam reforming using Gibbs energy minimization method: A detailed study of the conditions of carbon deposition

Aline Lima da Silva, Célia de Fraga Malfatti, Iduvirges Lourdes Müller*

Program of Postgraduate Studies in Mining, Metals and Materials Engineering (PPGEM), Universidade Federal do Rio Grande do Sul, UFRGS, Campus do Vale, Setor 4, Prédio 75, Sala 226, Av. Bento Gonçalves 9500, CEP 91501-970, Porto Alegre, RS, Brazil

ARTICLE INFO

Article history:
Received 26 January 2009
Received in revised form
13 March 2009
Accepted 16 March 2009
Available online 10 April 2009

Keywords:
Ethanol steam reforming
Carbon deposition
Chemical equilibrium
Gibbs energy minimization method
Thermodynamic analysis

ABSTRACT

In this paper, a thermodynamic analysis of ethanol/water system, using the Gibbs energy minimization method, has been carried out. A mathematical relationship between Lagrange's multipliers and carbon activity in the gas phase was deduced. From this, it was possible to calculate carbon activities in both stable and metastable systems. For the system that corresponds to ethanol steam reforming at very low contact times, composed mainly of ethylene and acetaldehyde, carbon activities were always much greater than unity over the whole temperature range, changing from 1.2×10^7 at 400 K to 1.1×10^4 at 1200 K. Furthermore, there was practically no effect of the inlet steam/ethanol ratio on carbon activity values. These results indicate that such a system is highly favorable to carbon formation. On the other hand, by considering a more stable system, in order to represent high contact times, it was observed that carbon activities are much lower and depend greatly on the inlet steam/ethanol ratio employed. Besides, the complete conversion of ethylene and acetaldehyde into other species, such as CO, CO_2, CH_4 and H_2, lowers the total Gibbs energy of the system. By computing carbon activities in experimental systems, it was also possible to explain deviations between thermodynamic analysis and experimental results regarding carbon deposition.

© 2009 International Association for Hydrogen Energy. Published by Elsevier Ltd. All rights reserved.

1. Introduction

The use of fuel cells is a promising technology in the conversion of chemical to electrical energy. The fuel, hydrogen gas, can be produced by several routes; a promising one is the steam reforming of ethanol. This route may become an important industrial process, especially for sugarcane producing countries. Ethanol is a renewable source for hydrogen production and presents several advantages over other sources related to natural availability, storage and handling safety.

During ethanol steam reforming, carbon deposition over catalysts is the main cause for deactivation [1,2]. The direct deactivation occurs predominantly by covering active phases, due to encapsulating carbon [3]. For this reason, thermodynamic analysis has been used in many studies to predict conditions under which carbon formation is inhibited during ethanol steam reforming [4–6].

* *Corresponding author*. Tel.: +55 51 3308 9404.
E-mail address: adasilva26@gmail.com (A. Lima da Silva).
0360-3199/$ – see front matter © 2009 International Association for Hydrogen Energy. Published by Elsevier Ltd. All rights reserved.
doi:10.1016/j.ijhydene.2009.03.029

Nomenclature

G	total Gibbs energy
G_i^0	Gibbs energy of species i at its standard state
n_i	number of moles of species i
n_i^0	initial number of moles of species i
n_i'	decision variable during the optimization process, after the change of variables
$e^{n_i'}$	number of moles of species i, after the change of variables
y_i	mole fraction of species i
R	gas constant
T	temperature of the system
P	total pressure of the system
α_{ik}	number of atoms of kth element present in each molecule of species i
b_k	total number of atomic masses of kth element in the system
a_i	activity of species i
M, N	total number of elements and species, respectively
p_i	partial pressure of species i
X_{EtOH} (%)	ethanol conversion
μ_i	chemical potential of species i
λ_k	Lagrange's multipliers

Although the understanding of ethanol steam reforming has increased significantly in the last few years, many questions concerning the conditions of carbon formation inside the reactor remain still not answered. Deviations between thermodynamic predictions and experimental observations have been reported extensively in literature [3,7–9]. In a recent work, Alberton et al. [3] investigated the deactivation of Ni/Al_2O_3 catalysts during ethanol steam reforming. They employed an inlet steam/ethanol (H_2O/EtOH) ratio of 3:1, at 873 K, and observed carbon formation in significant amounts during their experimental analysis. However, the results of these authors are in disagreement with thermodynamic predictions presented in literature [4–6]. Under such conditions, theoretical analyses show that carbon deposition is thermodynamically unfavorable. According to Ginsburg et al. [10], the composition along the reformer is far from stable equilibrium. So, thermodynamic analysis, considering only the stable equilibrium, could not predict the formation of carbon.

In order to contribute to the comprehension of the conditions of carbon formation during ethanol steam reforming, the present study provides a thermodynamic analysis of the ethanol/water system using the Gibbs energy minimization method. In this work, the theoretical study is performed considering two different cases: ethanol conversion at very low and at high contact times. Previous experimental papers [2,11–13] show that the main species during ethanol steam reforming are not the same for different residence times. Thus, it is obvious that the thermodynamic system to be considered for representing very low contact times (initial stages of ethanol reforming process) must be completely different from that assumed for high contact times. The thermodynamic conditions for carbon formation, in both cases, are examined through the analysis of carbon activity in the reformer gas. In this work, a mathematical relationship between Lagrange's multipliers and the carbon activity, with reference to the graphite phase, is deduced, enabling to calculate the carbon activity in the reformer gas. From this, it is possible to predict if carbon will precipitate inside the reformer.

In order to explain deviations between thermodynamic analysis and experimental results from the literature, such as those reported by Alberton et al. [3], carbon activities are also determined in systems obtained experimentally during ethanol steam reforming, by using our procedure developed to compute metastable equilibria.

2. Methodology

2.1. *Theoretical background*

In the present study, the equilibrium compositions were calculated through the Gibbs energy minimization method. The total free energy of the system, regarded as an ideal gas phase, may be expressed as:

$$G = \sum n_i G_i^0 + \sum n_i RT \ln y_i + \sum n_i RT \ln P \quad (1)$$

Since in all calculations the value of the pressure is 1 atm, the last term of Eq. (1) vanishes. The problem is to find the different values of n_i which minimize the objective function given by Eq. (1), subject to the constraints of elemental mass balance

$$\sum_{i=1}^{N} n_i \alpha_{ik} = b_k \quad k = 1, \ldots, M \quad (2)$$

The nonlinear programming model, comprising the objective function to be minimized and the constraints, Eq. (2), is solved by using the Solver function contained in the Microsoft Excel spreadsheet package. The Solver function applies the Generalized Reduced Gradient (GRG) method to solve nonlinear programming problems. A detailed description of the use of the Microsoft Excel Solver can be found elsewhere [14]. The use of the Solver function in computing the chemical equilibrium of known substances in multicomponent systems, by the method of direct Gibbs energy minimization, is not usual in literature. Lwin [15] described, for educational purposes, how the optimization feature of the spreadsheet Solver can be used to perform equilibrium calculations for known substances in either an ideal or non-ideal gas phase by the direct Gibbs energy minimization method. According to Nguyen and Tran [16], the ability to carry out these calculations within a spreadsheet environment has a number of advantages. First, spreadsheet is a well-known and commonly employed environment for chemical engineering calculations on personal computers. Besides, it is not necessary to develop a computer program which requires considerable testing and

debugging before results can be obtained [15]. In this way, our results can be easily reproduced by other researchers.

In the present work, calculations were made considering the initial number of moles of ethanol, $n^0_{C_2H_5OH}$, equal to unity. The inlet steam/ethanol ratio (H_2O/EtOH) was varied in the range 0–10. Theoretically, a greater number of moles for steam could be used. For instance, Vasudeva et al. [5] presented their thermodynamic analysis assuming a wide range of inlet H_2O/EtOH ratios (0–80). However, this ratio must be as small as possible in order to close the energetic balance of the entire device including the fuel cell [6]. The exothermic heat produced by the Solid Oxide Fuel Cell (SOFC) electrochemical section may not satisfy the endothermic heat of the steam reforming reaction and the enthalpy requirement for water evaporation [17]. The reforming temperature analyzed was 400–1200 K.

2.2. *Mathematical relationship between Lagrange's multipliers and carbon activity*

It is possible to rewrite Eq. (2) as follows:

$$b_k - \sum_{i=1}^{N} n_i \alpha_{ik} = 0 \quad k = 1, \ldots M \tag{3}$$

There is a Lagrange's multiplier for each restriction given by Eq. (2). In the ethanol/water system, $M = 3$ (C, H, O) and, thus, there are three restrictions. Introducing the Lagrange's multipliers, one for each component, and multiplying each equation of elemental mass balance for the respective Lagrange's multiplier, we can write

$$\lambda_k \left(b_k - \sum_{i=1}^{N} n_i \alpha_{ik} \right) = 0 \tag{4}$$

The sum of these equations over k gives

$$\sum_k \lambda_k \left(b_k - \sum_{i=1}^{N} n_i \alpha_{ik} \right) = 0 \tag{5}$$

The Lagrange function, L, is composed of the objective function plus the restrictions. Thus, we can write

$$L = G + \sum_k \lambda_k \left(b_k - \sum_{i=1}^{N} n_i \alpha_{ik} \right) \tag{6}$$

The first-order condition, for L to be a minimum, is that the partial derivatives of L with respect to n_i must be equal to zero. Thus

$$\frac{\partial L}{\partial n_i} = \left(\frac{\partial G}{\partial n_i} \right)_{T,P,n_j} - \sum_k \lambda_k \alpha_{ik} = 0 \tag{7}$$

Remembering that

$$\left(\frac{\partial G}{\partial n_i} \right)_{T,P,n_j} = \mu_i \tag{8}$$

Eq. (7) can be rewritten as:

$$\mu_i - \sum_k \lambda_k \alpha_{ik} = 0 \tag{9}$$

The chemical potential is given by:

$$\mu_i = G_i^0 + RT \ln a_i \tag{10}$$

Substitution of Eq. (10) into Eq. (9) yields

$$\ln a_i = \left(\frac{-G_i^0}{RT} \right) + \sum_k \left(\frac{\lambda_k}{RT} \right) \alpha_{ik} \tag{11}$$

Eq. (11) is the mathematical relationship between Lagrange's multipliers and the activity of species i. For determining carbon activity, Eq. (11) can be rewritten as follows:

$$\ln a_C = \left(\frac{-G_C^0}{RT} \right) + \frac{\lambda_C}{RT} \tag{12}$$

In this work, the carbon activity in the reformer gas, a_C, is calculated by using Eq. (12). After the completion of optimization process, the Lagrange's multipliers are returned by the Solver function through sensitivity reports. For carbon activity (with reference to the graphite phase) greater than unity, gas phase is not in equilibrium, and carbon deposition may occur. On the other hand, if carbon activity is less than unity, carbon formation is not thermodynamically feasible.

2.3. *Thermodynamic data*

Based on previous experimental works from literature [1–3,11–13,18–20], the species considered in calculations throughout this study are: H_2, H_2O, CO, CO_2, CH_4, C_2H_4, C_2H_4O and C_2H_5OH. The Gibbs energy for the species is calculated from the Gibbs–Helmholtz relation:

$$G = H - TS \tag{13}$$

where

$$H = H^{298} + \int_{T_{298}}^{T} C_P dT \tag{14}$$

and

$$S = S^{298} + \int_{T298}^{T} \frac{C_P}{T} dT \tag{15}$$

The standard conditions are $T = 298$ K and $P = 1$ atm. The enthalpy at 298 K, H^{298}, of the state of the elements which is stable under these conditions is set to zero by convention. The entropy, S^{298}, is given by its absolute value, and the heat capacity at constant pressure, C_P, is described by a polynomial [21].

The thermodynamic data necessary for describing the Gibbs energy of the species were obtained from Knacke et al. [22] and Sandler [23].

2.4. *Non-negativity constraints and change of variables*

Besides the constraints of elemental mass balance, it is necessary to take into account the non-negativity constraints of the number of moles of species. However, as reported by Lwin [15], one drawback of the current GRG spreadsheet solver, especially in solving this type of model, is that it seems to violate the non-negativity constraints. This is due to the fact that GRG algorithm can reach at nonfeasible points in trying to get to the optimal solution [24,25], combined with the involvement of logarithmic functions of variables. So, in the

present work, a change of variables was made, and there was no need to add the non-negativity constraints. By doing

$$n_i = e^{n'_i} \tag{16}$$

it is possible to rewrite the objective function and the constraints of elemental mass balance, respectively, as follows:

$$\frac{G}{RT} = \sum_{i=1}^{N} e^{n'_i}\left[\frac{G_i^0}{RT} + n'_i - \ln\left(\sum_{i=1}^{N} e^{n'_i}\right)\right] \tag{17}$$

$$\sum_{i=1}^{N} e^{n'_i}\alpha_{ik} = b_k \tag{18}$$

Since $e^{n'_i}$ cannot assume negative values, there is no difficulty with the involvement of logarithmic functions, as can be seen in Eq. (17). As a result, it is possible to run GRG Solver continuously without error messages.

Although the problem is nonlinear, the present methodology ensures the global minimum for a given system, independently of initial estimates, since the problem is convex [26–28]. In the present study, the value of 1×10^{-10} was chosen as criterion of precision and convergence in the Solver Options dialog box during the optimization process. However, when carbon activities are computed in experimental systems, this value selected for precision and convergence will be changed, as will be better explained in Section 3.3.

3. Results and discussion

3.1. Ethanol conversion considering very low contact times

Comas and collaborators [11] studied experimentally the influence of residence time on product distribution during ethanol steam reforming over Ni/Al_2O_3 catalyst. They proposed that, at the initial stages of the process, ethylene and acetaldehyde are produced from ethanol dehydration and dehydrogenation reactions, respectively

$$C_2H_5OH = C_2H_4 + H_2O \tag{19}$$

$$C_2H_5OH = C_2H_4O + H_2 \tag{20}$$

The initial stages of ethanol steam reforming, in which it is assumed that acetaldehyde and ethylene are the main species, correspond to very low contact times. Based on the reaction scheme proposed by Comas et al. [11], we consider a homogeneous system composed only of five species ($N = 5$): C_2H_5OH, C_2H_4O, C_2H_4, H_2, and H_2O.

In order to evaluate the performance of the ethanol reforming system at very low contact times, the equilibrium conversion of ethanol is defined by the relationship:

$$X_{EtOH}(\%) = \frac{\left(n^0_{C_2H_5OH} - n_{C_2H_5OH}\right)}{n^0_{C_2H_5OH}} \times 100 \tag{21}$$

In Fig. 1, it is observed the conversion of ethanol (X_{EtOH}) as a function of inlet H_2O/EtOH ratio and temperature. It can be seen that at $T > 500$ K ethanol conversion is higher than 99% at all values of H_2O/EtOH analyzed. However, at lower temperatures, such as 400 K, the conversion values diminish and are dependent on the inlet H_2O/EtOH ratio employed. Fig. 2(a) shows the number of moles of acetaldehyde and hydrogen as function of temperature and inlet H_2O/EtOH ratios. During the calculations, it was observed that $n_{C_2H_4O} = n_{H_2}$. As can be seen, the number of moles of acetaldehyde and hydrogen increases with temperature in the whole temperature range. On the other hand, as shown in Fig. 2(b), the number of moles of ethylene reaches a maximum value at around 500 K and a further increase of temperature leads to a decrease of ethylene in the gas phase. Fatsikostas and Verykios [18], studying ethanol steam reforming over $Ni/\gamma\text{-}Al_2O_3$ catalysts, observed a similar behavior during their experiments, with ethylene peaking at around 523 K. By comparing Fig. 2(a) and (b), it can be seen that ethanol is converted preferentially into ethylene. In fact, even at short contact times, that is an experimental condition in which conversion of ethylene into other species occurs to some extent, it has been reported that ethylene is detected in the gas phase in appreciable amounts when Ni/Al_2O_3 catalysts are used [2,11].

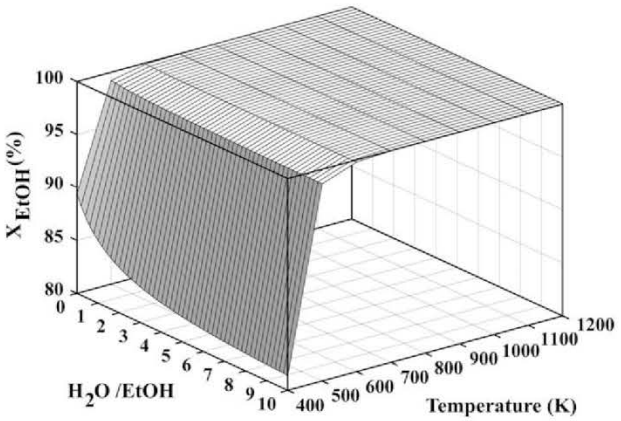

Fig. 1 – Ethanol conversion (X_{EtOH}) as a function of the inlet H_2O/EtOH ratio and temperature.

It is known from literature [2,3,18,19] that a possible route for carbon deposition is through ethylene polymerization. Since ethylene formation is thermodynamically favored, as verified in this work, a great effort to the development of catalysts that can inhibit or minimize ethylene production is necessary. Acidic supports, such as Al_2O_3, favor dehydration reactions that produce ethylene [29]. So, as some experimental papers have already suggested, ethylene formation could be avoided either by the use of catalysts that do not possess acidic sites, such as Ni/La_2O_3 [2], or by addition of alkali elements (K, Mg, Ca) to neutralize acidic sites [19,30,31].

The results obtained with our proposed methodology, as shown through Figs. 1 and 2(a) and (b), are similar to those reported by Mas et al. [6]. Small discrepancies may be due to the fact that thermodynamic data come from different sources. In a recent work, Rossi et al. [28] stated that the quality of the thermodynamic data from specialized bibliographical sources has a great impact in obtaining reliable results.

It is worth to point out that the paper published by Mas et al. [6] is the only one found in literature that shows

a thermodynamic analysis considering ethanol steam reforming at very low contact times. Those authors carried out their analysis using the stoichiometric method, that is, they accomplished their calculations by solving a system of nonlinear equations relating the moles of each species to the equilibrium constants of Eqs. (19) and (20). It should be noted, then, that the results obtained in the present work, by Gibbs energy minimization (non-stoichiometric formulation), are in agreement with those calculated with the stoichiometric method. Concerning this fact, in a previous work, Smith and Missen [32] demonstrated that stoichiometric formulation is equivalent to the non-stoichiometric one, provided that all independent reactions are considered.

However, the thermodynamic conditions of carbon deposition, when very low contact times are assumed, were not examined by Mas et al. [6]. So, the main advantage of our proposed methodology is regarding the facility in determining carbon activities in different systems by using simply the mathematical relationship deduced in this work, Eq. (12), without the necessity of knowing previously the chemical reactions that would lead to carbon deposition. Besides, it is worth to stress that the values of the Lagrange's multipliers related to the component carbon (λ_C) are very readily obtained from sensitivity reports supplied by the Solver function after each equilibrium determination. In Fig. 3(a), the values of λ_C (divided by RT) are plotted against the temperature, for two inlet H_2O/EtOH ratios of 1:1 and 10:1. The values of λ_C/RT presented in Fig. 3(a) were then substituted into Eq. (12) for determining carbon activities, with reference to the graphite phase. In Fig 3(b), it is possible to see that carbon activity values decrease with increasing temperature. However, carbon activities are much greater than unity in the whole temperature range, changing from 1.2×10^7 at 400 K to 1.1×10^4 at 1200 K. Besides, it must be noted that the inlet H_2O/EtOH ratio has practically no effect on the values of carbon activity.

Thus, from a thermodynamic point of view, the system constituted mainly by ethylene and acetaldehyde, which corresponds to the initial stages of ethanol steam reforming, is highly favorable to carbon deposition, whatever temperature and inlet H_2O/EtOH ratio used. Indeed, it is well known from literature that acetaldehyde and ethylene promote carbon deposition [33]. In this way, since increasing temperature and the inlet H_2O/EtOH ratio, so as to prevent carbon deposition at the initial stages, is useless, it is strongly recommended the development of catalysts that can inhibit ethylene and acetaldehyde production, especially ethylene formation, which is thermodynamically favored at very low contact times.

3.2. *Ethanol conversion considering high contact times*

In some experimental works [2,11], it has been reported that, during ethanol steam reforming at moderate and high contact times, acetaldehyde and ethylene are completely converted into other species, such as CO, CO_2 and CH_4. Therefore, in order to present a thermodynamic analysis assuming high contact times, the selected species to take part in equilibrium calculations are: C_2H_5OH, C_2H_4O, C_2H_4, H_2, H_2O, CO, CO_2, and CH_4. As can be seen, this system is greater than that described in Section 3.1 ($N = 8$).

In Table 1, it is possible to observe the number of moles of species and the values of Gibbs free energy, calculated for an inlet H_2O/EtOH ratio of 2:1, at 850 K, considering two different systems: (i) ethanol conversion at very low contact times and (ii) ethanol conversion at high contact times. It should be noted that the values of 2:1 and 850 K, for the inlet H_2O/EtOH ratio and temperature, respectively, were considered just for sake of illustration, that is, any other value could be considered. From Table 1, it is seen that the complete transformation of ethylene and acetaldehyde into other species, such as CO, CO_2, CH_4 and H_2, lowers the total Gibbs energy of the system. Thus, it can be stated that the system in which ethylene and acetaldehyde are the main species exists in metastable equilibrium. Besides, it is possible to affirm that acetaldehyde and ethylene behave as intermediate species in this system. Comas et al. [11] and Fatsikostas et al. [2] confirmed experimentally such behavior of these species. Mas et al. [6], taking into account the equilibrium constant values of formation and transformation reactions of ethylene and acetaldehyde (stoichiometric method), demonstrated that both species are intermediate compounds in ethanol steam reforming.

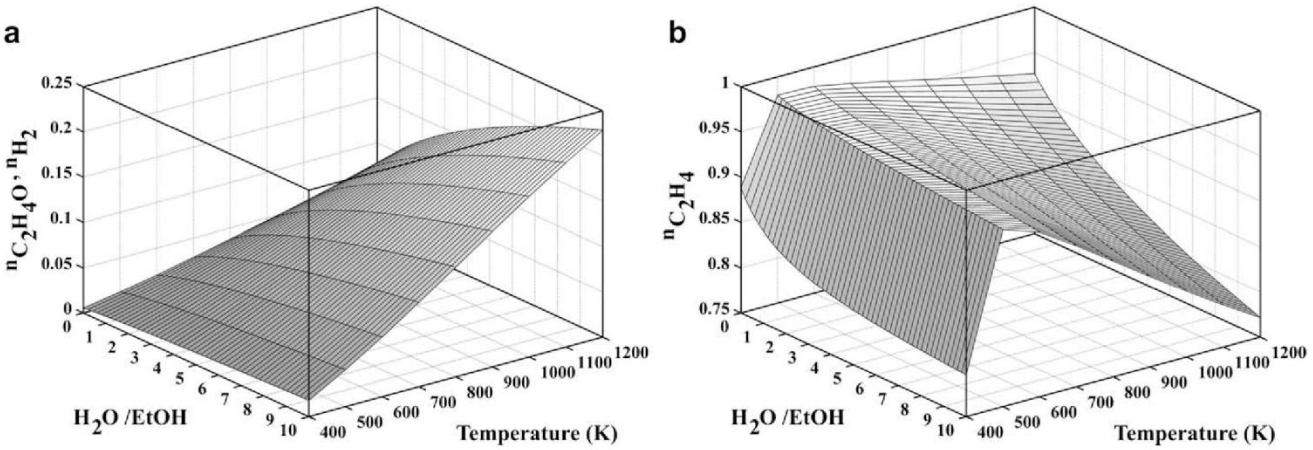

Fig. 2 – (a) Number of moles of C_2H_4O and H_2 as function of the inlet H_2O/EtOH ratio and temperature. (b) Number of moles of C_2H_4 as function of the inlet H_2O/EtOH ratio and temperature.

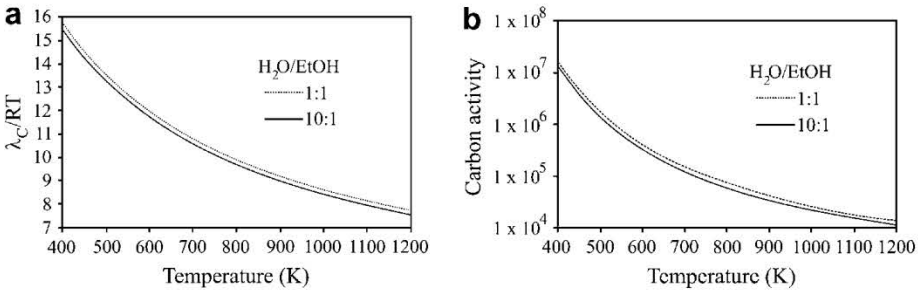

Fig. 3 – (a) Lagrange's multipliers divided by *RT* as function of temperature, for two inlet H_2O/EtOH ratios. (b) Carbon activities as function of temperature, for two inlet H_2O/EtOH ratios.

Table 2 shows the molar fractions of species C_2H_4O, C_2H_4 and C_2H_5OH, calculated for different temperatures and inlet H_2O/EtOH ratios. It can be observed that such species are not practically present in equilibrium mixture. This fact is in perfect agreement with results reported both in theoretical studies [4–6] and in experimental papers [2,11].

Fig. 4(a)–(c) shows the number of moles of H_2, CO and CH_4, at equilibrium, respectively, as function of inlet H_2O/EtOH ratio and temperature. As can be seen, high temperatures and H_2O/EtOH ratios favor hydrogen production. On the other hand, methane presents a behavior exactly the opposite of that of hydrogen. Regarding CO formation, it is possible to see that at low temperatures CO is not present in equilibrium mixture. However, at higher temperatures, high inlet H_2O/EtOH ratios are necessary in order to minimize CO production. The results that are shown in Fig. 4(a)–(c) are in excellent agreement with those reported previously by other authors [6].

In Fig. 5(a), the values of λ_C/RT that are obtained after each equilibrium determination are shown. By substituting these values into Eq. (12), carbon activities are then calculated for this more stable system that represents ethanol reforming at high contact times. Carbon activity values for this system can be seen in Fig. 5(b), for inlet H_2O/EtOH ratios varying in the range 1–5. By comparing Figs. 3(b) and 5(b), it should be noted that the values of carbon activity in systems resulting from ethanol steam reforming at high contact times are much lower than those calculated for systems obtained at very low contact times. Furthermore, as can be seen in Fig. 5(b), carbon activities are dependent on inlet H_2O/EtOH ratios. According to Fig. 5(b), working at high contact times, for an inlet H_2O/EtOH ratio of 1:1, carbon deposition is thermodynamically possible over the whole temperature range, since carbon activity is greater than unity. At $T > 550$ K, an inlet H_2O/EtOH ratio of 3:1 is suitable to avoid carbon deposition. For an inlet H_2O/EtOH ratio of 5:1, carbon deposition is not predicted for all temperatures analyzed. The range of conditions for carbon deposition, observed in Fig. 5(b) through the values of carbon activity, is in agreement with that presented by other authors [6,28,34].

It is worth to point out that, for the system that represents ethanol steam reforming at high contact times, the values of carbon activity calculated by Eq. (12) can also be obtained by considering the Boudouard reaction:

$$2CO = CO_2 + C \tag{22}$$

So, carbon activity, a_C, can be expressed by the following equation:

$$a_C = \frac{K_{22} p_{CO}^2}{p_{CO_2}} \tag{23}$$

where K_{22} represents equilibrium constant of reaction (22). For instance, at 1200 K, for an inlet H_2O/EtOH ratio of 5:1, the value of carbon activity calculated by Eq. (12) is equal to 4.54×10^{-3}. If Boudouard reaction is considered, the value of carbon

Table 1 – Moles of species and Gibbs energy of the system, at 850 K and inlet H_2O/EtOH ratio of 2:1, considering ethanol conversion (i) at very low contact times; and (ii) at high contact times.

Species	(i)	(ii)
C_2H_5OH	1.24×10^{-4}	5.1×10^{-11}
C_2H_4O	**0.073**	**5.5×10^{-10}**
C_2H_4	**0.93**	**2.8×10^{-7}**
CO	[a]	0.47
CO_2	[a]	0.72
H_2	0.073	2.28
H_2O	2.92	1.10
CH_4	[a]	0.81
G (J)	**-1.41×10^6**	**-1.55×10^6**

a Species not considered in that system.

Table 2 – Molar fractions of acetaldehyde, ethylene and ethanol, for different temperatures and inlet H_2O/EtOH ratios.

Temperature (K)		500	800	1200
H_2O/EtOH (0:1)	C_2H_4O	3.5×10^{-15}	3.1×10^{-11}	3.0×10^{-11}
	C_2H_4	7.3×10^{-13}	3.5×10^{-8}	7.6×10^{-7}
	C_2H_5OH	1.6×10^{-43}	8.4×10^{-28}	1.1×10^{-13}
H_2O/EtOH (5:1)	C_2H_4O	1.8×10^{-15}	1.0×10^{-11}	3.0×10^{-14}
	C_2H_4	1.9×10^{-13}	5.4×10^{-9}	6.8×10^{-12}
	C_2H_5OH	6.3×10^{-43}	3.7×10^{-27}	7.2×10^{-17}
H_2O/EtOH (10:1)	C_2H_4O	5.6×10^{-16}	1.6×10^{-12}	1.6×10^{-15}
	C_2H_4	5.5×10^{-14}	5.9×10^{-10}	1.6×10^{-13}
	C_2H_5OH	7.5×10^{-43}	8.0×10^{-27}	2.7×10^{-18}

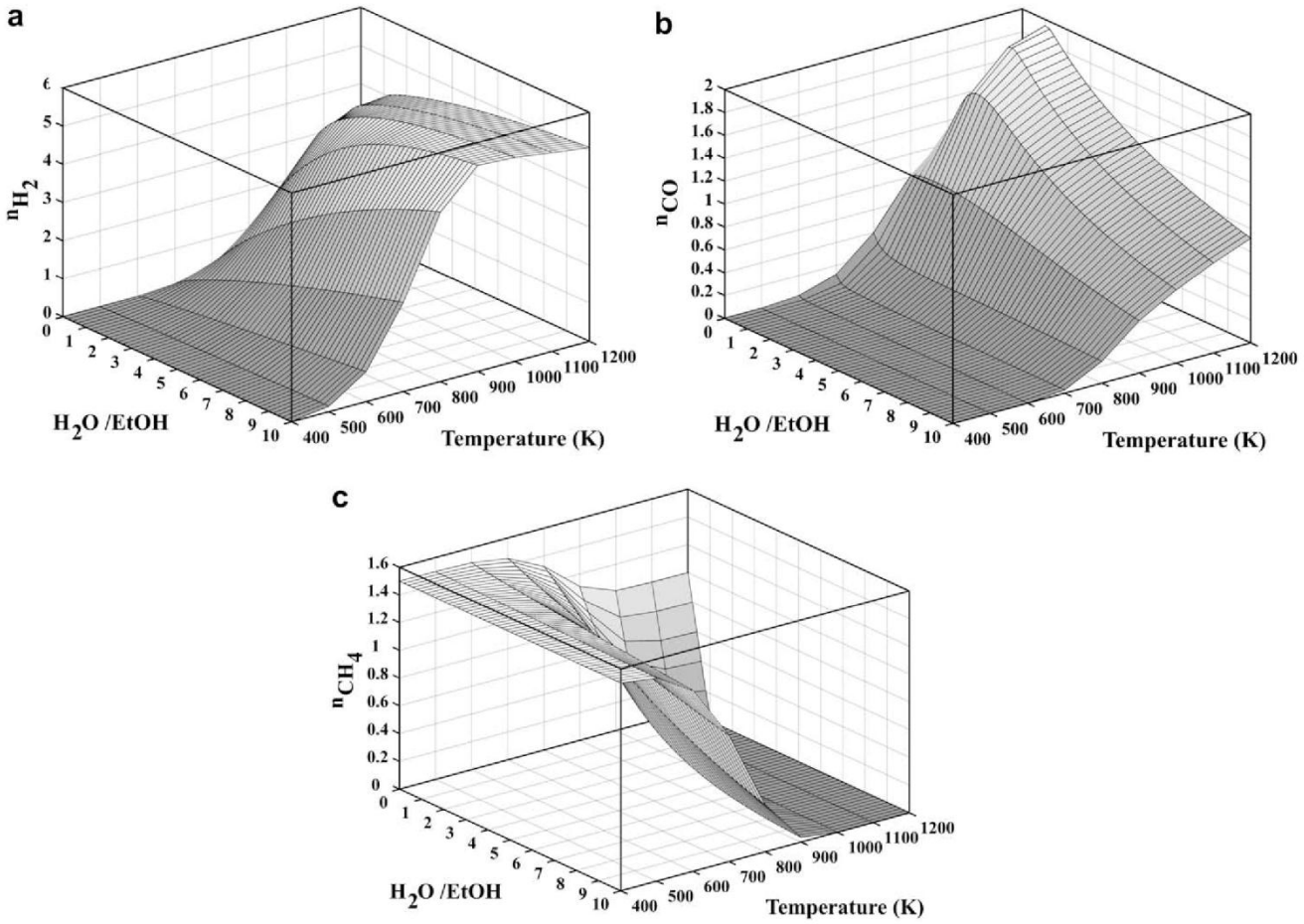

Fig. 4 – (a) Number of moles of H_2 as function of the inlet H_2O/EtOH ratio and temperature. (b) Number of moles of CO as function of the inlet H_2O/EtOH ratio and temperature. (c) Number of moles of CH_4 as function of the inlet H_2O/EtOH ratio and temperature.

activity computed by Eq. (23) is equal to 4.74×10^{-3}. In this way, it is possible to see that the values of carbon activity are essentially the same.

3.3. *Determination of carbon activities in systems obtained experimentally*

When a thermodynamic analysis is performed, it is commonly presented a study based on the stable equilibrium, *i.e.*, on the state of the system in which the value of G is the lowest. However, this stable condition may not be reached in practice, due to kinetic impediments. As a result, an analysis based on the metastable equilibrium can be helpful in order to understand experimental results. In the present section, it is described how metastable equilibria can be calculated by using our methodology. Furthermore, it is discussed under which conditions the system can be regarded to be in stable equilibrium.

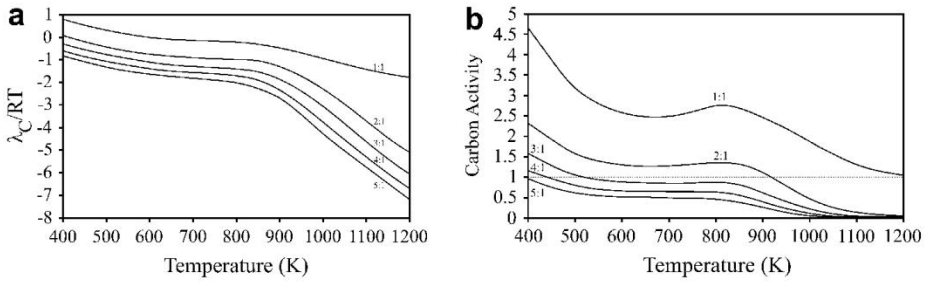

Fig. 5 – (a) Lagrange's multipliers divided by RT as function of temperature, for five different inlet H_2O/EtOH ratios. (b) Carbon activities as function of temperature, for five inlet H_2O/EtOH ratios.

The simplest way to compute metastable equilibria is by suppressing species in the system taken into account. For instance, at very low contact times, the species CO, CO_2 and CH_4 were suppressed from the system. However, when these species were considered, in order to perform calculations considering high contact times, it was observed that acetaldehyde and ethylene were completely converted into CO, CO_2 and CH_4. As a consequence, the system lowered its total Gibbs free energy, assuming, then, a more stable configuration. It is worth to emphasize that both at very low and at high contact times, graphite phase was suppressed from the system. Although this phase has not been considered in the objective function and in the restrictions of elemental mass balance, Eqs. (17) and (18), respectively, it is pointed out that carbon activity can be computed directly, after the equilibrium is calculated in the gas phase, by simply substituting the Lagrange's multiplier associated to carbon mass balance restriction, λ_C, into the relationship deduced in this work, Eq. (12). Even at high contact times, conditions may be found in which the values of carbon activity are greater than unity. In such cases, these systems are still in metastable equilibrium. So, in order to become stable, these systems should split into two phases: gas and graphite. In this way, a_C would become equal to unity. Since in this work only the gas phase is considered, a given system is regarded to be in stable equilibrium when $a_C < 1$.

Until now, all the equilibrium compositions were computed with no need to provide accurate initial estimates to the algorithm, since the global minimum, as stated before, is assured, independently of the system considered (very low or high contact times). Moreover, a rigorous value was selected, 1×10^{-10}, as criterion of precision and convergence in the Solver Options dialog box, so as to be close enough to the global minimum. Then, for a same T and inlet H_2O/EtOH ratio, the global minimum of G computed considering very low contact times is less negative than that calculated by assuming high contact times. In this way, it is stated that a system constituted mainly by acetaldehyde and ethylene exists in metastable equilibrium. On the other hand, a system is in stable equilibrium when the global minimum is determined taking into account high contact times (as done in Section 3.2) and it is verified that $a_C < 1$ in such system. In fact, achieving this condition would be desirable during the experiments, because carbon deposition is unfeasible and, consequently, the deactivation of the catalyst would be prevented. However, due to kinetic inhibitions, this stable configuration may not be reached.

Another way to calculate metastable equilibria is by increasing the values chosen as criterion of precision and convergence in the Solver Options dialog box (the greater the values of precision and convergence are, the farther the computed systems to the global minimum are) and by supplying suitable initial guesses to the algorithm. Such criteria are not examined in previous theoretical works found in literature [4,5,28]. In this way, metastable equilibria can be determined in order to reproduce experimental systems reported in literature that are far from stable equilibrium. By calculating carbon activities in such systems, apparent deviations between thermodynamic analysis and experimental observations can be explained.

As mentioned previously, Alberton et al. [3] reported that their experimental observations were in complete disagreement with thermodynamic predictions presented in literature. At 873 K, for an inlet H_2O/EtOH ratio of 3:1, most of the theoretical studies found in literature [4–6,28,34] show that carbon deposition is thermodynamically unfavorable. This discrepancy can be attributed to the fact that those analyses are based only on stable equilibrium, considering that, at high contact times, all kinetic restrictions could be overcome. By observing the value of carbon activity in Fig 5(b), in Section 3.2, where we present an analysis similar to those found in literature, it is possible to conclude that carbon deposition should not occur, because $a_C < 1$. However, during their experiments, Alberton et al. [3] observed carbon formation in significant amounts over Ni/Al_2O_3 catalysts. According to Assabumrungrat et al. [34], factors such as mass transfer or rate of reactions may affect the predictions of the carbon formation boundary. So, local compositions which would allow carbon formation may exist, although carbon formation is not favored according to the calculation based on stable equilibrium compositions.

In this way, two different systems reported by Alberton et al. [3], denoted here by 'A' and 'C', were reproduced by computing metastable equilibria. The system 'A' was obtained experimentally for 8% of Ni supported by α-Al_2O_3 while the system 'C' was obtained for 8% of Ni supported by γ-Al_2O_3. It is important to emphasize that the composition of these systems corresponds to the initial situation (homogeneous system), where deactivation of the catalyst due to carbon deposition had not been observed by the authors. So, the experimental molar fractions of species were taken from graphs presented by Alberton et al. [3], for time (h) = 0. In order to reproduce the experimental values of the systems 'A' and 'C', the following procedure was adopted. First, suitable initial estimates for the number of moles of each species were selected. For system 'A', the initial estimates were: $n'_{C_2H_5OH} = 6$; $n'_{C_2H_4O} = -2.8$; $n'_{CH_4} = -4.6$; $n'_{CO} = -2.8$; $n'_{CO_2} = -4.6$; $n'_{H_2} = -3$; $n'_{H_2O} = 0.5$; $n'_{C_2H_4} = -3.9$. For system 'C', the initial estimates were: $n'_{C_2H_5OH} = -1$; $n'_{C_2H_4O} = -10$; $n'_{CH_4} = -3.2$; $n'_{CO} = -2$; $n'_{CO_2} = -2$; $n'_{H_2} = 5$; $n'_{H_2O} = 2$; $n'_{C_2H_4} = -2.2$ (the values of n'_i are indicated, due to the change of variables shown in Eq. (16)). It should be noted that we are considering the same species that we took into account in Section 3.2 (high contact times). Second, the values of precision and convergence were increased. For the precision and convergence, the values of 1×10^{-8} and 1×10^{-4} were chosen, respectively. It is pointed out here that, if equilibrium compositions were computed by supplying to the algorithm the initial estimates as indicated above for systems 'A' and 'C', assuming, however, the value of 1×10^{-10} as criterion of precision and convergence, the global minimum would be reached. Third, the Lagrange's multipliers computed by the algorithm, after the process of optimization, were substituted into Eq. (12), so that carbon activity in the experimental systems could be calculated.

Table 3 shows the composition of these systems obtained experimentally and also calculated by the procedure described above, 'A' and 'C', along with the stable equilibrium composition 'B' (global minimum of the Gibbs energy function, assuming high contact times, for precision and convergence = 1×10^{-10}). As can be seen, the values of carbon

Table 3 – Molar fractions of species, except H_2O, and carbon activities, for the atmospheres 'A' and 'C', both experimental and calculated, and for case 'B', stable equilibrium (calculated by global minimum of G, precision and convergence = 1×10^{-10}); T = 873 K, H_2O/EtOH = 3:1.

Species	A calculated	A experimental [3]	C calculated	C experimental [3]	B stable equilibrium
C_2H_5OH	0.7	0.7	6.7×10^{-4}	–	9.0×10^{-12}
C_2H_4O	0.05	0.07	8.2×10^{-6}	–	1.0×10^{-10}
C_2H_4	0.02	0.02	0.04	0.05	6.0×10^{-8}
CO	0.04	0.06	0.11	0.1	0.12
CO_2	0.009	0.01	0.15	0.15	0.16
H_2	0.14	0.14	0.68	0.7	0.62
CH_4	0.01	0.01	0.009	0.01	0.10
λ_C/RT	13.10	–	8.11	–	-1.65
Carbon activity	**1.88×10^6**	–	**1.28×10^4**	–	**0.74**

activity in the experimental systems are very high, indicating that carbon deposition should occur, which is in perfect agreement with the experimental observations of Alberton et al. [3]. On the other hand, the value of carbon activity calculated for stable equilibrium is much lower than the one determined for experimental systems. So, it is possible to understand that there is no disagreement between thermodynamic analysis and experimental observations, if carbon activities are computed in metastable equilibria. Besides, it is clearly seen that the criteria of precision and convergence have a great impact on the values of carbon activity calculated. Fig. 6 shows the values of the Gibbs energy computed for the experimental systems 'A' and 'C', along with the stable equilibrium 'B'. Assuming that all kinetic restrictions could be excluded, the metastable states 'A' and 'C' would be able to change their compositions until the stable configuration 'B' is reached.

4. Conclusions

Thermodynamic analysis for ethanol steam reforming via Gibbs energy minimization method, using the Solver function contained in the Microsoft Excel spreadsheet package, to present a detailed study of the conditions of carbon deposition, has been carried out. The implementation of our methodology using the Solver function was shown to be robust and easy to understand and apply. The mathematical relationship between Lagrange's multipliers and carbon activity in the gas phase, deduced in the present work, enabled to calculate carbon activities, with reference to graphite phase, in both stable and metastable systems.

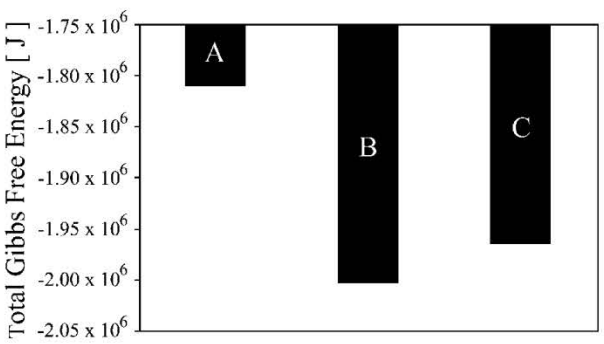

Fig. 6 – Total Gibbs free energy for the configurations 'A' and 'C' (metastable) and 'B' (stable equilibrium).

For ethanol conversion at very low contact times, it was verified that ethanol should be converted preferentially into ethylene. Besides, it was demonstrated that such a system, which corresponds to initial stages of ethanol reforming process, is highly prone to carbon deposition, which is in agreement with the well-known fact in literature that acetaldehyde and ethylene act as carbon precursors. Carbon activities were always much greater than unity over the whole temperature range, changing from 1.2×10^7 at 400 K to 1.1×10^4 at 1200 K. Furthermore, there was practically no effect of the inlet steam/ethanol ratio on carbon activity values. On the other hand, by considering a more stable system, in order to represent high contact times, it was observed that carbon activities, in this case, are much lower and depend greatly on the inlet steam/ethanol ratio employed. Besides, the complete conversion of ethylene and acetaldehyde into other species, such as CO, CO_2, CH_4 and H_2, lowers the total Gibbs energy of the system.

It is shown that the criteria of precision and convergence have a great impact on the values of carbon activity calculated. Carbon activities could be computed in systems obtained experimentally through our procedure developed to determine metastable equilibria. In this way, it was possible to demonstrate that there is no discrepancy between thermodynamic analysis and experimental observations, regarding carbon deposition.

In order to avoid deactivation due to carbon deposition during ethanol steam reforming, it is firstly recommended the development of catalysts that inhibit acetaldehyde and ethylene production, since it was shown that such species are related to extremely high values of carbon activity at the initial stages of ethanol reforming process. Especially ethylene formation should be suppressed, because this species is thermodynamically favored at very low contact times. Assuming that all kinetic restrictions could be overcome, our results indicate that, at high contact times, for $T > 550$ K an inlet steam/ethanol ratio of 3:1 would be suitable to perform steam reforming of ethanol without carbon deposition. At lower temperatures, such as 400 K, an inlet steam/ethanol ratio of 5:1 would prevent carbon formation. Despite the fact that high values of the inlet steam/ethanol ratio are appropriate for preventing carbon deposition, as indicated by the analysis at high contact times, the energetic balance including

the fuel cell should be taken into account before increasing inlet H_2O/EtOH ratios.

Acknowledgements

Authors would like to acknowledge the CNPq and CAPES for financial support.

REFERENCES

[1] Freni S, Cavallaro S, Mondello N, Spadaro L, Frusteri F. Production of hydrogen for MC fuel cell by steam reforming of ethanol over MgO supported Ni and Co catalysts. Catal Commun 2003;4:259–68.
[2] Fatsikostas AN, Kondarides DI, Verykios XE. Production of hydrogen for fuel cells by reformation of biomass-derived ethanol. Catal Today 2002;75:145–55.
[3] Alberton AL, Souza MMVM, Schmal M. Carbon formation and its influence on ethanol steam reforming over Ni/Al2O3 catalysts. Catal Today 2007;123:257–64.
[4] Garcia EY, Laborde MA. Hydrogen production by the steam reforming of ethanol: thermodynamic analysis. Int J Hydrogen Energy 1991;16:307–12.
[5] Vasudeva K, Mitra N, Umasankar P, Dhingra SC. Steam reforming of ethanol for hydrogen production: thermodynamic analysis. Int J Hydrogen Energy 1996;21: 13–8.
[6] Mas V, Kipreos R, Amadeo N, Laborde M. Thermodynamic analysis of ethanol/water system with the stoichiometric method. Int J Hydrogen Energy 2006;31:21–8.
[7] Rostrup-Nielsen JR. Equilibria of decomposition reactions of carbon monoxide and methane over nickel catalysts. J Catal 1972;27:343–56.
[8] Manning MP, Garmirian JE, Reid RC. Carbon deposition studies using nickel and cobalt catalysts. Ind Eng Chem Proc Des Dev 1982;21:404–9.
[9] Bokx PK, Kock AJHM, Boellaard E, Klop W, Geus JW. The formation of filamentous carbon on iron and nickel catalysts: thermodynamics. J Catal 1985;96:454–67.
[10] Ginsburg JM, Piña J, Solh TE, Lasa HI. Coke formation over a nickel catalyst under methane dry reforming conditions: thermodynamics and kinetics models. Ind Eng Chem Res 2005;44:4846–54.
[11] Comas J, Mariño F, Laborde M, Amadeo N. Bio-ethanol steam reforming on Ni/Al_2O_3 catalyst. Chem Eng J 2004;98:61–8.
[12] Mariño F, Boveri M, Baronetti G, Laborde M. Hydrogen production via catalytic gasification of ethanol. A mechanism proposal over copper-nickel catalysts. Int J Hydrogen Energy 2004;29:67–71.
[13] Benito M, Sanz JL, Isabel R, Padilla R, Arjona R, Daza L. Bio-ethanol steam reforming: insights on the mechanism for hydrogen production. J Power Sources 2005;151:11–7.
[14] Fylstra D, Lasdon L, Watson J, Waren A. Design and use of the Microsoft Excel Solver. Interfaces 1998;28:29–55.
[15] Lwin Y. Chemical equilibrium by Gibbs energy minimization on spreadsheets. Int J Eng 2000;16:335–9.
[16] Nguyen AV, Tran T. A simple method for predicting equilibrium composition on leaching systems. Miner Eng 2001;14:359–64.
[17] Ioannides T. Thermodynamic analysis of ethanol processors for fuel cell applications. J Power Sources 2001;92:17–25.
[18] Fatsikostas AN, Verykios X. Reaction network of steam reforming of ethanol over Ni-based catalysts. J Catal 2004; 225:439–52.
[19] Vizcaíno AJ, Arena P, Baronetti G, Carrero A, Calles JA, Laborde M, et al. Ethanol steam reforming on Ni/Al_2O_3 catalysts: effect of Mg addition. Int J Hydrogen Energy 2008; 33:3489–92.
[20] Frusteri F, Freni S, Chiodo V, Donato S, Bonura G, Cavallaro S. Steam and auto-thermal reforming of bio-ethanol over MgO and CeO_2 Ni supported catalysts. Int J Hydrogen Energy 2006; 31:2193–9.
[21] Kubaschewski O, Alcock CB, Spencer PJ. Materials thermochemistry. Oxford: Pergamon Press; 1993.
[22] Knacke O, Kubaschewski O, Hesselmann K. Thermochemical properties of inorganic substances. Berlin: Springer-Verlag; 1991.
[23] Sandler SI. Chemical and engineering thermodynamics. New York: Wiley; 1999.
[24] Edgar TF, Himmelblau DM. Optimization of chemical processes. Boston: Mcgraw-Hill; 1988.
[25] Reklaitis GV, Ravindran A, Ragsdell KM. Engineering optimization, methods and applications. New York: Wiley; 1983.
[26] White WB, Johnson SM, Danzig GB. Chemical equilibrium in complex mixtures. J Chem Phys 1958;28:751–5.
[27] McDonald CM, Floudas CA. Global optimization and analysis for Gibbs energy function using the UNIFAC, Wilson e ASOG equations. Ind Eng Chem Res 1995;34:1674–87.
[28] Rossi CCRS, Alonso CG, Antunes OAC, Guirardello R, Cardozo-Filho L. Thermodynamic analysis of steam reforming of ethanol and glycerine for hydrogen production. Int J Hydrogen Energy 2009;34:323–32.
[29] Vizcaíno AJ, Carrero A, Calles JA. Hydrogen production by ethanol steam reforming over Cu–Ni supported catalysts. Int J Hydrogen Energy 2007;32:1450–61.
[30] Frusteri F, Freni S, Chiodo V, Spadaro L, Di Blasi O, Bonura G, Cavallaro S. Steam reforming of bio-ethanol on alkali-doped Ni/MgO catalysts: hydrogen production for MC fuel cell. Appl Catal A Gen 2004;270:1–7.
[31] Lisboa JS, Santos DCRM, Passos FB, Noronha FB. Influence of the addition of promoters to steam reforming catalysts. Catal Today 2005;101:15–21.
[32] Smith WR, Missen RW. Chemical reaction equilibrium analysis: theory and algorithms. New York: Wiley; 1982.
[33] Rostrup-Nielsen JR, Hojlund N. In: Oudar J, Wise H, editors. Deactivation and poisoning of catalyst. New York: Marcel Dekker; 1985. p. 57.
[34] Assabumrungrat S, Pavarajarn V, Charojrochkul S, Laosiripojana N. Thermodynamic analysis for a solid oxide fuel cell with direct internal reforming fueled ethanol. Chem Eng Sci 2004;59:6015–20.

4.1.2. Hydrogen production by sorption enhanced steam reforming of oxygenated hydrocarbons (ethanol, glycerol, n-butanol and methanol): Thermodynamic modeling

(Produção de hidrogênio pela reforma a vapor com captura in situ de CO_2 utilizando-se diferentes hidrocarbonetos oxigenados (etanol, glicerol, n-butanol e metanol): Modelagem termodinâmica

Principais Resultados:

- A adição de CaO no reformador juntamente com o catalisador permite que hidrogênio de alta pureza (>97 mol%) possa ser obtido, mantendo-se, simultaneamente, a concentração de CO em torno de 10ppm. Portanto, um processo *single-step*, sem a necessidade de etapas adicionais envolvendo reatores do tipo WGS e COPROX, é possível. As simulações termodinâmicas são validadas com resultados experimentais da literatura para o metanol e etanol;
- Mediante a adição de CaO no reformador, a deposição de carbono pode ser evitada em baixas temperaturas e com quantidade mínima de água na mistura.
- A adição de CaO no reformador resulta em um processo com alta eficiência térmica.

INTERNATIONAL JOURNAL OF HYDROGEN ENERGY 36 (2011) 2057–2075

Available at www.sciencedirect.com

ScienceDirect

journal homepage: www.elsevier.com/locate/he

Hydrogen production by sorption enhanced steam reforming of oxygenated hydrocarbons (ethanol, glycerol, *n*-butanol and methanol): Thermodynamic modelling

*Aline Lima da Silva**, *Iduvirges Lourdes Müller*

Program of Postgraduate Studies in Mining, Metals and Materials Engineering (PPGEM), Federal University of Rio Grande do Sul – UFRGS, Campus do Vale, Setor 4, Prédio 75, Sala 226, Av. Bento Gonçalves 9500, CEP 91501-970, Porto Alegre, RS, Brazil

ARTICLE INFO

Article history:
Received 13 September 2010
Received in revised form
9 November 2010
Accepted 11 November 2010
Available online 16 December 2010

Keywords:
Biofuels
Steam reforming
Sorption enhanced
Hydrogen production
Gibbs energy minimization method
Fuel Cells

ABSTRACT

Thermodynamic analysis of steam reforming of different oxygenated hydrocarbons (ethanol, glycerol, *n*-butanol and methanol) with and without CaO as CO_2 sorbent is carried out to determine favorable operating conditions to produce high-quality H_2 gas. The results indicate that the sorption enhanced steam reforming (SESR) is a fuel flexible and effective process to produce high-purity H_2 with low contents of CO, CO_2 and CH_4 in the temperature range of 723–873 K. In addition, the separation of CO_2 from the gas phase greatly inhibits carbon deposition at low and moderate temperatures. For all the oxygenated hydrocarbons investigated in this work, thermodynamic predictions indicate that high-purity hydrogen with CO content within 20 ppm required for proton exchange membrane fuel cell (PEMFC) applications can be directly produced by a single-step SESR process in the temperature range of 723–773 K at pressures of 3–5 atm. Thus, further processes involving water–gas shift (WGS) and preferential CO oxidation (COPROX) reactors are not necessary. In the case of ethanol and methanol, the theoretical findings of the present analysis are corroborated by experimental results from literature. In the other cases, the results could provide an indication of the starting point for experimental research. At $P = 5$ atm and $T = 773$ K, it is possible to obtain H_2 at concentrations over 97 mol% along with CO content around 10 ppm and a thermal efficiency greater than 76%. In order to achieve such a reformate composition, the optimized steam-to-fuel molar ratios are 6:1, 9:1, 12:1 and 4:1 for ethanol, glycerol, *n*-butanol and methanol, respectively, with CaO in the stoichiometric ratio to carbon atom.

© 2010 Professor T. Nejat Veziroglu. Published by Elsevier Ltd. All rights reserved.

1. Introduction

These days, there is a great concern regarding the depletion of fossil oil reserves and the pollution caused by the growing demand for energy generation. In this way, a large-scale substitution of petroleum-based fuels as well as improved efficiency in energy conversion is required. In this context, fuel cells for mobile and stationary applications are highly valued due to their high theoretical efficiency and only steam as by-product in the case of fuel cells operating with pure H_2 [1,2].

Nowadays, 95% of the hydrogen production comes from steam reforming of natural gas. The expected increased demand for hydrogen for fuel cell applications, however, dictates the development of new methods for hydrogen

* *Corresponding author*. Tel.: +55 51 3308 9404.
E-mail address: adasilva26@gmail.com (A. Lima da Silva).
0360-3199/$ – see front matter © 2010 Professor T. Nejat Veziroglu. Published by Elsevier Ltd. All rights reserved.
doi:10.1016/j.ijhydene.2010.11.051

Nomenclature

G	total Gibbs energy of the system
G_i^0	Gibbs energy of species i at its standard state
n_i	number of moles of species i
y_i	mole fraction of species i
R	gas constant
T	temperature of the system
P	total pressure of the system
M, N	total number of components and species, respectively
α_{ik}	number of atoms of kth component present in each molecule of species i
b_k	total number of atomic masses of kth component in the system
H_i^T	enthalpy of species i at temperature T

production, especially from biorenewable feedstocks. The use of biofuels (ethanol, glycerol, *n*-butanol and biomethanol) for hydrogen production through different processes (steam reforming (SR), partial oxidation (PO), dry reforming (DR) or autothermal reforming (ATR)) has the significant advantage of being CO_2 neutral as carbon dioxide released into atmosphere during biofuel conversion can be absorbed in the growth of biomass [3–6]. Among the liquid biofuels, ethanol and glycerol are considered as the promising candidates as hydrogen sources [7]. Ethanol can be produced renewably from several biomass sources, including energy plants, waste materials from agro industries, organic fraction of municipal solid waste, etc. In the case of glycerol, it has been produced as by-product during biodiesel production by transesterification of vegetable oils. It is worth mentioning that 100 tons of glycerol per 1000 tons of biodiesel are obtained during this process. In this way, hydrogen production appears as an alternative able to valorize high amounts of glycerol [8]. Besides ethanol and glycerol, *n*-butanol and biomethanol are also being considered as suitable biofuels for H_2 production. Recently, Nahar and Madhani [4] investigated, by means of a thermodynamic analysis, the production of hydrogen through the steam reforming of *n*-butanol. *n*-Butanol, also called biobutanol, can be produced by classical fermentation process and its feedstocks include sugar beet, sugar cane, corn, wheat and lignocellulosic biomass [9]. However, biobutanol can also be produced in a new and potentially more significant way through the manipulation of biological systems or metabolic engineering [10]. More recently, the production of *n*-butanol from macroalgae has attracted considerable attention because seaweed is a potentially sustainable and scalable new source of biomass that crucially does not require arable land or potable water [11]. Regarding the biomethanol, this term refers to renewable methanol prepared from biomass-pyrolyzed syngas and biogas ($CO_2 + CH_4$) [5]. It is worth pointing out that, among the aforementioned potential fuels, methanol has the highest value for the hydrogen/carbon (H/C) atomic ratio, which means that its conversion could, in principle, produce a hydrogen-rich stream with low propensity to carbon deposition.

In fact, ethanol, glycerol, *n*-butanol and methanol are all oxygenated hydrocarbons. As shown by Davda et al. [12], steam reforming of oxygenated hydrocarbons is thermodynamically favorable at lower temperatures than non-oxygenated hydrocarbons. In this way, steam reforming of oxygenated hydrocarbons can take place at lower temperatures because it is more exothermic [13]. In spite of the apparent simplicity of the stoichiometric reaction for maximum hydrogen production,

$$C_xH_yO_z + (2x - z)H_2O \rightarrow (2x - z + 0.5y)H_2 + xCO_2 \quad (1)$$

the steam reforming of an oxygenated hydrocarbon involves a complex reaction system, with undesired reaction paths. Therefore, the hydrogen selectivity is affected and its production is limited by the thermodynamic equilibrium. In order to obtain the maximum hydrogen production, the conventional steam reforming process has to be carried out in three steps for proton exchange membrane fuel cell (PEMFC) applications. The first step involves the conversion of the oxygenated hydrocarbon into H_2, CH_4, CO and CO_2, followed by a lower temperature step where CO is converted into CO_2 and H_2 by the water–gas shift (WGS) reaction:

$$CO + H_2O \rightarrow CO_2 + H_2 \quad \Delta H_{298}^0 = -41.2 \text{ kJ mol}^{-1} \quad (2)$$

Since the shift reaction is limited by the thermodynamic equilibrium, and PEMFC anode must be fueled by a high-purity hydrogen stream containing CO at a concentration lower than 20 ppm to avoid platinum catalyst poisoning, an additional step has to be carried out to further remove carbon monoxide by preferential CO oxidation. So, in the conventional steam reforming, besides the reformer and WGS reactor, a third reactor (COPROX), where the remaining CO is totally converted into CO_2 through the preferential CO oxidation, is also necessary. Nevertheless, widespread commercialization of fuel cell powered generators would require a compact and powerful source of hydrogen. Small-scale fuel processors must be compact and of high efficiency by eliminating unnecessary components. In this context, sorption enhanced steam reforming (SESR) provides a promising alternative for single-step production of hydrogen with a high purity [14]. The concept of SESR is based on Le Chatelier's principle in which the reaction equilibrium will be shifted to favor hydrogen production upon *in situ* CO_2 removal. So, if CO_2 generated from the steam reforming is separated from the gas phase by using a solid acceptor such as CaO, H_2 production can be enhanced towards completion. In this case, the fuel reactor contains both the catalyst needed for the reforming process and CaO for the removal of carbon dioxide. The CO_2 capture and the overall SESR reaction are illustrated in Eqs. (3) and (4), respectively:

$$CaO_{(S)} + CO_2 \rightarrow CaCO_{3(S)} \quad \Delta H_{298\ K}^0 = -179.8 \text{ kJ mol}^{-1} \quad (3)$$

$$C_xH_yO_z + (2x - z)H_2O + xCaO \rightarrow xCaCO_3 + (2x - z + 0.5y)H_2 \quad (4)$$

In the case of the reaction given by Eq. (4), the corresponding standard reaction enthalpies for ethanol (C_2H_6O), glycerol ($C_3H_8O_3$), *n*-butanol ($C_4H_{10}O$) and methanol (CH_4O) are −186, −411, −325 and −92 kJ mol^{-1}, respectively.

In the present paper, a thermodynamic analysis of steam reforming of different oxygenated hydrocarbons (ethanol, glycerol, *n*-butanol and methanol) with and without CaO as CO_2 sorbent is carried out to determine favorable operating conditions to produce fuel cell grade hydrogen. The influence of steam-to-fuel feed molar ratio and temperature on the product gas concentration is investigated for both cases. In the SESR, pressure is varied in order to identify suitable operation conditions for a single-step process, in which high-purity hydrogen with CO content within the 20 ppm needed for PEMFC applications can be directly produced, without further processes involving WGS and COPROX reactors. The results are compared with experimental and theoretical data found in existing literature. Besides, it is well-known that, during the steam reforming of oxygenated hydrocarbons, carbon deposition over catalysts is the main cause for deactivation, resulting in low operation durability and activity loss. In this way, conditions under which carbon formation is inhibited are established for the conventional steam reforming (SR) (without CaO sorbent) and for SESR. In addition, for each fuel, the thermal efficiency is evaluated in the conventional SR and SESR processes.

2. Simulation methodology

2.1. Gibbs energy minimization method

For a system in which many simultaneous reactions take place, equilibrium calculations are performed through the Gibbs energy minimization method (non-stoichiometric approach). The total free energy of the system, composed of an ideal gas phase and pure condensed phases, may be expressed as

$$\frac{G}{RT} = \left(\sum_{i=1}^{N} n_i \left[\frac{G_i^0}{RT} + \ln(y_i P) \right] \right)_{gas} + \frac{1}{RT} \left(\sum_{i=1}^{N} n_i G_i^0 \right)_{condensed} \quad (5)$$

The problem consists of finding the different values of n_i which minimize the objective function given by Eq. (5), subject to the constraints of elemental mass balance

$$\sum_{i=1}^{N} n_i \alpha_{ik} = b_k \quad k = 1, \ldots M \quad (6)$$

In the non-stoichiometric approach, the species coexisting in the system at equilibrium must first be defined. The selection of plausible products was based on previous experimental observations reported in literature. For each system, the plausible species as well as the corresponding experimental works used in this compilation are summarized as follows.

- *Ethanol/steam system*: ethanol, ethylene, ethane, acetone, acetaldehyde, acetic acid, CO, CH_4, CO_2, H_2, and H_2O [15–17].
- *Glycerol/steam system*: glycerol, acetaldehyde, ethylene, ethanol, methanol, ethane, propylene, acetone, acrolein, formaldehyde, allyl alcohol, propionaldehyde, acetic acid, CO, CH_4, CO_2, H_2, and H_2O [18,19].
- *n-butanol/steam system*: *n*-butanol, methyl ethyl ketone, isopropyl alcohol, butyric aldehyde, propylene, ethylene, ethane, *n*-butane, 1-butene, *cis*-2-butene, *trans*-2-butene, isobutylene, isobutane, propane, CO, CH_4, CO_2, H_2, and H_2O [20,21].
- *Methanol/steam system*: methanol, CO, CH_4, CO_2, H_2, and H_2O [14,22].

Besides these gaseous species, the solid phase C (graphite) was included in the compound basis set. The same operation conditions were used for the SESR process, except that three solid phases, CaO, $Ca(OH)_2$ and $CaCO_3$, were added to the previously described set of plausible species. In this case, for the initial condition of simulation, CaO was in the stoichiometric ratio to carbon atom, that is, CaO/ethanol = 2:1, CaO/glycerol = 3:1, CaO/*n*-butanol = 4:1 and CaO/methanol = 1:1 (see Eq. (4)). The thermodynamic data necessary for describing the Gibbs energy of the species were obtained from Refs. [23–26].

The non-linear programming model comprising the objective function to be minimized and the constraints is solved by the Solver function contained in the Microsoft Excel spreadsheet package. In our previous works [27–29], the Solver function was shown to be a robust tool, able to solve convex non-linear optimization problems. A detailed explanation concerning the Generalized Reduced Gradient (GRG) algorithm and the use of the Solver function in equilibrium calculations can be seen in [27,28].

In the simulations, the reaction temperature and pressure were varied in the range of 500–1450 K and 1–5 atm. The inlet steam-to-fuel molar ratio was varied in the range of 1:1–14:1, 1.5:1 –14:1, 2:1–14:1 and 0.5:1–14:1, for ethanol, glycerol, *n*-butanol and methanol, respectively. In this way, the lowest value of the inlet steam-to-carbon (S/C) ratio assumed for all the fuels is 0.5:1.

2.2. Thermal efficiency calculation

In the present study, the calculation procedure for thermal efficiency is based on the approach developed by He and collaborators [30]. For converting a fuel into hydrogen by means of the conventional SR process, the efficiency of the reaction can be calculated by the following expression:

$$\eta_{SR}(\%) = \frac{n_{H_2}^{out} LHV_{H_2}}{\left(n_{fuel}^{in} LHV_{fuel} + Q_{input,SR} + n_{steam}^{in} \Delta H_{latent} \right)} \times 100 \quad (7)$$

where $n_{H_2}^{out}$ is the number of moles of H_2 in the outlet stream computed at the equilibrium conditions, n_{fuel}^{in} and n_{steam}^{in} are the number of moles of fuel and steam, respectively, in the inlet stream. ΔH_{latent} is the latent energy of fed steam, and LHV_{H_2} and LHV_{fuel} are the lower heating value of hydrogen and fuel, respectively. The corresponding values computed for the LHV of hydrogen, ethanol, glycerol, *n*-butanol and methanol are 239.2, 1240, 1490, 2444.6 and 651.7 kJ mol^{-1}, respectively. The maximum thermal efficiency of converting a fuel with steam is found by assuming that one mol of fuel yields 6, 7, 12 or 3 moles of H_2, for ethanol, glycerol, *n*-butanol or methanol, respectively (see Eq. (1)). Nevertheless, as previously stated, steam reforming of an oxygenated hydrocarbon involves a complex reaction system, with undesired reaction paths. As a consequence, the maximum H_2 production from a given fuel

is compromised by the equilibrium boundary, which leads to lower thermal efficiency. The equilibrium composition and energy requirement depend on the reaction conditions. In this way, the energy input in the reaction system, $Q_{input,SR}$, is conveniently treated as the enthalpy change due to the conversion of the fuel:

$$Q_{input,SR} = H_{out,T} - H_{in,T} \quad (8)$$

where $H_{out,T}$ and $H_{in,T}$ are the outlet and inlet enthalpies, respectively, in the steam reforming process at a temperature T. The inlet enthalpy depends basically on the enthalpy of each species i at a certain temperature (H_i^T) and the number of moles of each species in the inlet feed (n_i^{in}). In the conventional SR, the inlet stream comprises only one mol of fuel and a given number of moles of steam (depending on the inlet steam-to-fuel molar ratio to be analyzed). After computing the equilibrium composition at a chosen set of operational conditions, the number of moles of each outlet species (n_i^{out}) is known. Thus, $H_{out,T}$ and $H_{in,T}$ can be calculated as follows:

$$H_{out,T} = \sum_i n_i^{out} H_i^T \quad i \in \{H_2O, CH_4, CO, CO_2, H_2, C_{graphite}\} \quad (9)$$

$$H_{in,T} = \sum_i n_i^{in} H_i^T \quad i \in \{H_2O, fuel(C_2H_6O, C_3H_8O_3, C_4H_{10}O \text{ or } CH_4O)\} \quad (10)$$

where

$$H_i^T = H^{298} + \int_{T_{298}}^{T} C_P dT \quad (11)$$

The enthalpy at 298 K, H^{298}, of the state of the elements which is stable under these conditions is set to zero by convention, and the heat capacity at constant pressure, C_P, is described by a polynomial [24].

In the case of the SESR, the procedure to calculate the thermal efficiency is similar to that described for the conventional SR. However, the energy input in the SESR process, $Q_{input,\ SESR}$, takes into account both the enthalpy change due to the fuel and CaO conversion $(H_{out,T} - H_{in,T})$ and the heat required for regenerating the CaO acceptor $(\Delta H_{regeneration})$. Actually, in order to obtain an economically feasible process, the CO_2 acceptor has to be recycled through carbonation/decarbonation reactions. The decarbonation of $CaCO_3$, as indicated in Eq. (12), shows that regeneration requires a certain amount of energy.

$$CaCO_{3(S)} \rightarrow CaO_{(S)} + CO_2 \quad \Delta H^0_{298K} = +179.8 \text{ kJ mol}^{-1} \quad (12)$$

In this way, the energy input in the SESR can be expressed as:

$$Q_{input,SESR} = H_{out,T} - H_{in,T} + \Delta H_{regeneration} \quad (13)$$

Due to the fact that the enthalpy change of the regeneration reaction (Eq. (12)) varies only slightly with temperature, its variation is assumed to be negligible in the thermal efficiency estimation. Thus, for all the values of T, $\Delta H_{regeneration} = n_{CaCO_3} \times (+179.8 \text{ kJ mol}^{-1})$, where n_{CaCO_3} is the number of moles of $CaCO_3$ computed at the equilibrium conditions. In Eq. (13), $H_{out,T}$ and $H_{in,T}$ are calculated as indicated in Eqs. (9) and (10), respectively. However, it should be noted that, in the case of the SESR process, the inlet feed comprises one mol of fuel, a given number of moles of steam (according to the inlet steam-to-fuel molar ratio considered in the simulation) and a certain amount of CaO (2, 3, 4 or 1 mol, for ethanol, glycerol, *n*-butanol or methanol, respectively). Thus, so as to compute the inlet enthalpy in the SESR process, it should be considered that $i \in \{H_2O, CaO, fuel (C_2H_6O, C_3H_8O_3, C_4H_{10}O \text{ or } CH_4O)\}$ in Eq. (10). After calculating the equilibrium composition at a given reaction condition, n_i^{out} is determined, and hence the outlet enthalpy in the SESR can be evaluated by Eq. (9), with $i \in \{H_2O, CH_4, CO, CO_2, H_2, C_{(graphite)}, CaO, Ca(OH)_2, CaCO_3\}$. As can be observed, the number of moles of solid phases (CaO, $Ca(OH)_2$, $CaCO_3$), computed at the equilibrium conditions, are also included in Eq. (9) to calculate the outlet enthalpy in the SESR.

In this way, the efficiency of the SESR process can be estimated as follows:

$$\eta_{SESR}(\%) = \frac{n^{out}_{H_2} LHV_{H_2}}{\left(n^{in}_{fuel} LHV_{fuel} + Q_{input,SESR} + n^{in}_{steam} \Delta H_{latent}\right)} \times 100 \quad (14)$$

As indicated by Eqs. (13) and (14), the thermal efficiency depends on the production of hydrogen and the consumption of the heat for regenerating the CO_2 acceptor. It is worth mentioning that the outlet species concentrations and the thermal efficiency are determined based only on a thermodynamic viewpoint. Mass and heat diffusion effects, which would affect the exothermic carbonation reaction (Eq. (3)), for example, are not considered in the present approach.

3. Results and discussion

3.1. *Thermodynamically feasible products*

For the steam reforming of all the fuels considered in this work, the main species present at equilibrium are H_2, CO, CO_2, CH_4, H_2O and C (graphite), over the whole range of temperature, pressure and inlet steam-to-fuel molar ratio examined in this work. Even for a temperature as low as 500 K and an inlet steam-to-carbon (S/C) ratio of 0.5:1, Table 1 shows that the fuel is completely converted, and other oxygenated species (such as acetone, acetaldehyde, formaldehyde, acrolein, isopropyl alcohol etc.) as well as C_2–C_4 non-oxygenated species (ethylene, propane, butane, etc.) exist only at trace amounts in equilibrium (much lower than 1 ppm). All these species can be considered as intermediates of the incomplete reforming reaction and are not thermodynamically stable products. Their occurrence in experimental work is due to the fact that the reforming reactions are in practice under kinetic control. However, suitable catalysts and supports, able to completely convert the fuel and avoid intermediate products (or convert these intermediate species too quickly to be detected under experimental conditions), have been successfully developed [7,8,15,17,31–33].

3.2. *Ethanol/steam system*

3.2.1. *Product distribution in the gas phase*

Fig. 1 illustrates the effects of temperature and steam-to-ethanol (H_2O/C_2H_6O) molar ratios on the dry basis concentration (mol%)

Table 1 – Product gas concentration (mol%) on a wet basis and moles of C (graphite)/mol of fed fuel, at 500 K, steam-to-carbon (S/C) ratio of 0.5:1 and $P = 1$ atm, for the steam reforming of ethanol, glycerol, *n*-butanol and methanol.

Species	Thermodynamic system			
	Ethanol/steam	Glycerol/steam	*n*-Butanol/steam	Methanol/steam
H_2	1.23	0.95	1.29	1.11
H_2O	54.38	62.85	50.28	57.95
CO	9.8×10^{-4}	1.5×10^{-3}	8.7×10^{-4}	1.2×10^{-3}
CO_2	5.94	13.36	4.67	8.32
CH_4	38.45	22.84	43.76	32.62
Ethylene (C_2H_4)	5.4×10^{-11}	3.2×10^{-11}	6.4×10^{-11}	–
Ethane (C_2H_6)	5.8×10^{-5}	2.7×10^{-5}	6.7×10^{-5}	–
Propylene (C_3H_6)	–	1.6×10^{-14}	3.2×10^{-14}	–
Propane (C_3H_8)	–	–	6.9×10^{-10}	–
n-Butane (C_4H_{10})	–	–	1.0×10^{-14}	–
Isobutane (C_4H_{10})	–	–	1.7×10^{-14}	–
1-butene (C_4H_8)	–	–	3.8×10^{-19}	–
2-*cis*-butene (C_4H_8)	–	–	1.0×10^{-18}	–
2-*trans*-butene (C_4H_8)	–	–	1.8×10^{-18}	–
Isobutylene (C_4H_8)	–	–	5.3×10^{-18}	–
Methanol (CH_4O)	–	8.4×10^{-10}	–	9.1×10^{-10}
Formaldehyde (CH_2O)	–	7.5×10^{-11}	–	–
Ethanol (C_2H_6O)	4.7×10^{-13}	3.2×10^{-13}	–	–
Acetaldehyde (C_2H_4O)	3.8×10^{-13}	3.4×10^{-13}	–	–
Acetic acid ($C_2H_4O_2$)	5.6×10^{-10}	7.5×10^{-10}	–	–
Acetone (C_3H_6O)	1.5×10^{-14}	1.0×10^{-14}	–	–
Glycerol ($C_3H_8O_3$)	–	2.8×10^{-33}	–	–
Acrolein (C_3H_4O)	–	1.3×10^{-17}	–	–
Allyl alcohol (C_3H_6O)	–	5.5×10^{-23}	–	–
Propionaldehyde (C_3H_6O)	–	7.4×10^{-17}	–	–
Isopropyl alcohol (C_3H_8O)	–	–	8.0×10^{-17}	–
n-Butanol ($C_4H_{10}O$)	–	–	6.1×10^{-23}	–
Methyl ethyl ketone (C_4H_8O)	–	–	5.5×10^{-19}	–
Butyric aldehyde (C_4H_8O)	–	–	2.5×10^{-22}	–
C (graphite)	0.66	1.18	1.56	0.18

– Species not considered in that system.

of H_2 (a, b), CO (c, d), CO_2 (e, f) and CH_4 (g, h) in the conventional SR (a, c, e and g) and SESR (b, d, f and h).

In the conventional SR process, only small contents of hydrogen (Fig. 1a) and almost no carbon monoxide (Fig. 1c) can be found at low temperatures. However, under these conditions, carbon dioxide (Fig. 1e) and methane (Fig. 1g) are the mostly occurring species. The carbon dioxide content is practically constant at ~25%, for temperatures below 700 K and steam-to-ethanol ratios above 3:1. Below this steam-to-ethanol ratio, CO_2 decreases because of the carbon formation. The methane production was highest at the lowest temperature, 500 K, due to the exothermic methanation reactions (Eqs. (15)–(18)):

$$2CO + 2H_2 \rightarrow CH_4 + CO_2 \quad \Delta H^0_{298\ K} = -247.4\ kJ\ mol^{-1} \tag{15}$$

$$CO_2 + 4H_2 \rightarrow CH_4 + 2H_2O \quad \Delta H^0_{298\ K} = -164.9\ kJ\ mol^{-1} \tag{16}$$

$$CO + 3H_2 \rightarrow CH_4 + H_2O \quad \Delta H^0_{298\ K} = -206.2\ kJ\ mol^{-1} \tag{17}$$

$$C + 2H_2 \rightarrow CH_4 \quad \Delta H^0_{298\ K} = -74.8\ kJ\ mol^{-1} \tag{18}$$

The composition of H_2 is strongly enhanced with the increase in temperature. However, no prominent change of H_2 concentration can be observed above 850 K because of the inhibition of the exothermic WGS reaction (Eq. (2)). The hydrogen content in the effluent is at high concentrations of 55–74 mol% for reforming temperatures above 850 K and increases slightly with raising the steam-to-ethanol ratio. Besides, for $T > 850$ K, the concentration of methane is greatly decreased, and CO_2 concentration decreases gradually. Meanwhile, the concentration of CO increases continuously with temperature, and it has a maximum at low steam-to-ethanol ratios and high temperatures (at $T > 1000$ K and H_2O/C_2H_6O of 1:1–1.5:1, its concentration is ~30 mol%). This behavior of CO at high temperatures and very low S/C ratios could be attributed to the reverse WGS reaction (reverse of Eq. (2)). The observed trends of the species H_2, CH_4, CO and CO_2 with the increase in temperature are in perfect agreement with the thermodynamic analysis via response reactions carried out by Fishtik et al. [34]. The authors report that the reactions of methane dry reforming (reverse of Eq. (15)) and steam reforming (reverse of Eqs. (16) and (17)) are predominant at the reaction temperatures above 800 K. Besides, experimental results corroborate these theoretical findings. Li et al. [31] recently investigated the temperature effect on the product gas composition (%) during ethanol steam reforming over NiMg6 catalyst, for H_2O/C_2H_6O molar ratio of 6:1. With increasing temperature from 723 to 973 K, those authors observed that the composition of CO_2 and CH_4 gradually

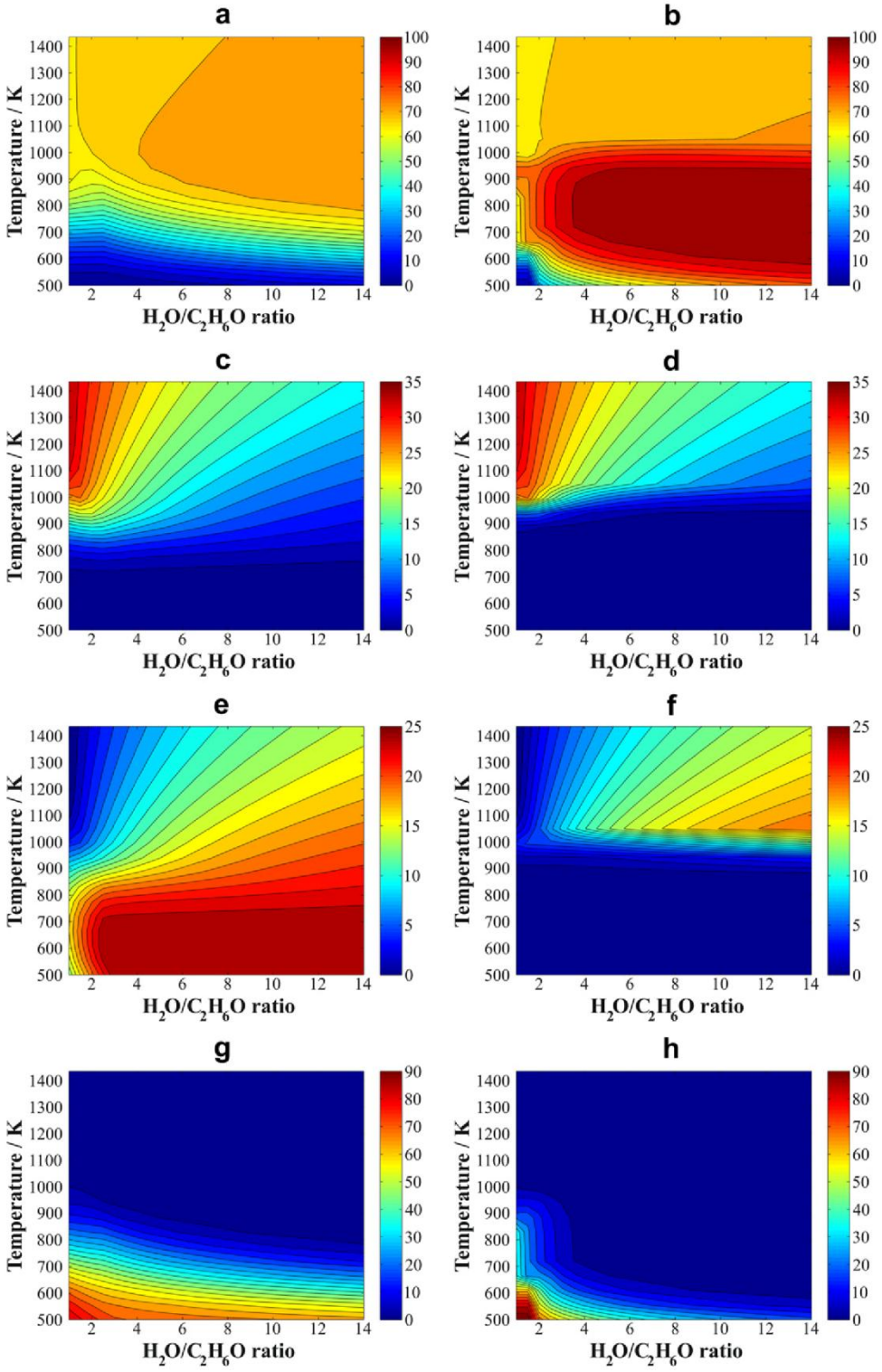

Fig. 1 – Effects of temperature and steam-to-ethanol ratio on the product gas concentration (mol%, on the dry basis). (a, b) H_2, (c, d) CO, (e, f) CO_2 and (g, h) CH_4. The plots (a, c, e, g) are for the conventional SR (without CaO) and (b, d, f, h) for the SESR process. $P = 1$ atm.

decreased, while the composition of CO and H_2 increased. Taking into account these same conditions adopted by Li et al., our theoretical results indicate that H_2 and CO concentrations increase from 49.5 to 71.6 and 1.2 to 12.3 mol%, respectively, while CO_2 and CH_4 concentrations vary from 24.1 to 15.8 and 25.0 to 0.27 mol%, respectively. These theoretical values are close to the experimental ones reported by those authors. In fact, the thermodynamic results shown in Fig. 1(a, c, e and g) for the conventional SR of ethanol can be validated with several experimental data found in literature. For instance, Profeti

et al. [7] investigated the catalytic activity of $Ni/CeO_2–Al_2O_3$ catalysts promoted with noble metals (Pt, Ir, Pd and Ru) for ethanol steam reforming at 873 K, using an inlet H_2O/C_2H_6O molar ratio of 3:1. They observed that the composition of the gaseous product remained approximately constant during the experiment at 60% H_2, 10% CO, 20% CO_2 and 10% CH_4, irrespective of the presence or nature of the noble metal. Under these conditions, the results thermodynamically predicted in the present work are 62% H_2, 11% CO, 16% CO_2 and 10% CH_4. He et al. [35] evaluated the catalytic activity and stability of a series of Co–Ni catalysts derived from hydrotalcite-like materials during ethanol steam reforming at 848 K with steam-to-ethanol molar ratio of 6:1. For the different catalysts, the gaseous product distribution was: 67–70% H_2, 14–18% CO_2, 3.4–4.5% CH_4 and 7.1–13.7% CO. This composition is fairly close to the thermodynamic equilibrium computed in the present study: 67.8% H_2, 20.1% CO_2, 5.5% CH_4 and 6.5% CO. In another work, Zhang et al. [36] verified that the Ir/CeO_2 catalyst kept rather stable for more than 300 h on stream at 923 K, for the inlet H_2O/C_2H_6O molar ratio of 3:1. The concentrations of H_2, CO_2 and CO were about 71%, 11% and 17%, respectively. Such values compare reasonably well with the equilibrium composition computed in the present work: 66.5% H_2, 12.8% CO_2, 16.2% CO. At this same temperature, but with an inlet H_2O/C_2H_6O molar ratio much higher (13:1), Deng et al. [33], using a $NiO/ZnO/ZrO_2$ catalyst, obtained a product distribution of 74.3% H_2, 19.6% CO_2, 6.1% CO and 0% CH_4, which is in agreement with our theoretical results: 73.6% H_2, 21% CO_2, 5.3% CO and 0.1% CH_4. In this way, it is clearly seen that thermodynamic analysis can be used as a benchmark to compare the experimental results. It is worth mentioning the significant effect of water on the equilibrium concentrations of the products in the conventional SR. The addition of water increases the H_2 and CO_2 production while reducing the CO and methane concentrations. Methane is reformed according to the reverse of Eqs. (16) and (17) to produce CO or CO_2 and H_2 [37], and the WGS reaction (Eq. (2)) is influenced to react towards less carbon monoxide. As can be observed, the reforming temperature has to be high enough in order to obtain a stream with high hydrogen content in the conventional steam reforming. However, it should be noted that elevated temperatures also promote the CO production, which is undesirable. Thus, the H_2O/C_2H_6O molar ratio should be increased so as to minimize the CO formation.

In the SESR process, the hydrogen concentration (Fig. 1b) is greatly enhanced, achieving a concentration as high as 99.9 mol%. In the temperature range of 723–873 K, for inlet H_2O/C_2H_6O ratios greater than 4:1, the H_2 concentration is over 97%. However, for temperatures above 950 K, the H_2 concentration decreases with the increase of temperature, which indicates that the CO_2 separation from the gas phase is no longer favored because the adsorption reaction of CO_2 (Eq. (3)) is exothermic and inhibited at high temperatures. For $T > 1000$ K, the H_2 concentration is in the range of 65–73 mol%, similar to conventional SR. It should be noted that the H_2 content also decreases for temperatures lower than 700 K, when the inlet steam-to-ethanol ratio is very low (1:1–2:1). In this case, lowering temperature increases the affinity between CaO and steam (see Eq. (19)) and less CaO is available to capture CO_2.

$$CaO + H_2O \rightarrow Ca(OH)_2 \quad \Delta H^0_{298\ K} = -109.2\ kJ\ mol^{-1} \tag{19}$$

However, even at a temperature as low as 500 K, for example, it can be seen from Fig. 1b that, as the inlet steam-to-ethanol ratio is increased, the H_2 production is significantly favored. At 500 K, its concentration increases from 4.4 to 73%, with increasing the H_2O/C_2H_6O molar ratio from 1:1 to 10:1. This trend could be explained by the fact that, in the presence of significant amount of steam, CO_2 can react with $Ca(OH)_2$, as shown in Eq. (20).

$$Ca(OH)_2 + CO_2 \rightarrow CaCO_3 + H_2O \quad \Delta H^0_{298\ K} = -70.54\ kJ\ mol^{-1} \tag{20}$$

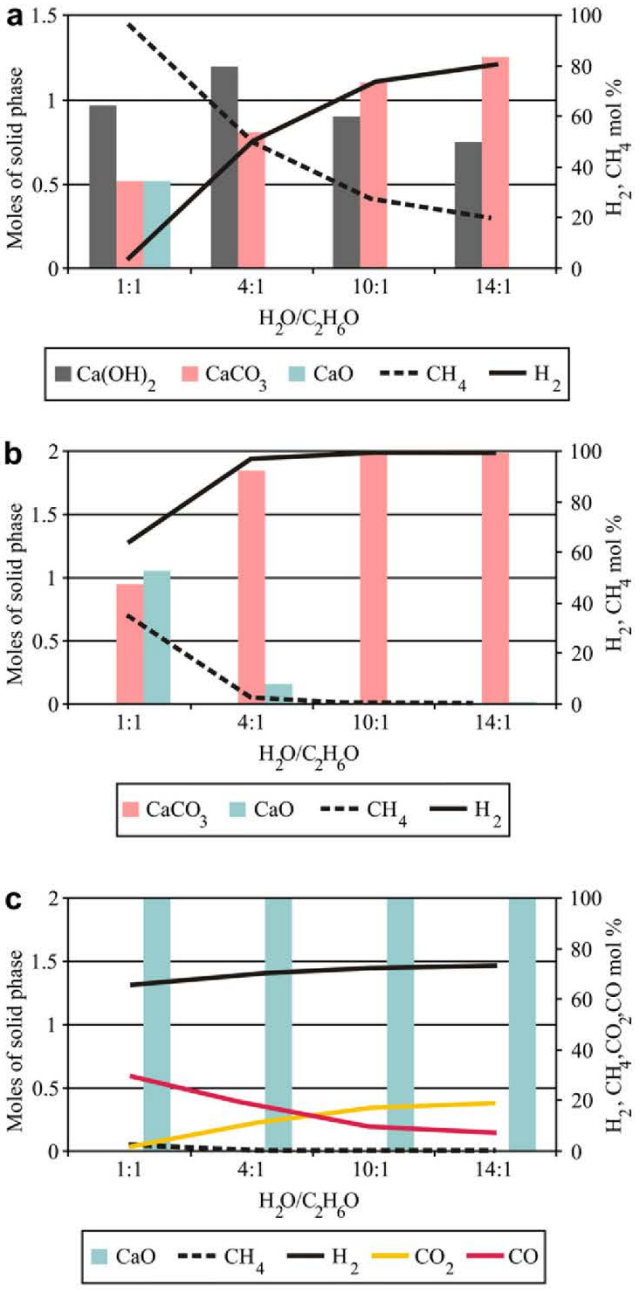

Fig. 2 – Moles of solid phases (CaO, $Ca(OH)_2$ and $CaCO_3$) formed per mol of ethanol and product gas concentration (mol%, on the dry basis) for different steam-to-ethanol molar ratios at (a) 500 K, (b) 830 K and (c) 1050 K. P = 1 atm.

Comparatively, Fig. 1a shows that, in the conventional SR, at 500 K and for the H_2O/C_2H_6O molar ratio equal to 10:1, the H_2 concentration is lower than 10%. With respect to the CO, at temperatures below 950 K, its concentration in SESR is lower than that in conventional SR (compare Fig. 1c and d). The enhanced WGS reaction (Eq. (2)) due to CO_2 adsorption results in a decrease of the CO production, accompanied by an increase in H_2 concentration. At higher temperatures, however, the CO concentrations in SR and SESR have a similar tendency. The effect of CO_2 adsorption on the reduction of carbon dioxide concentration in the gas phase at temperatures below 1000 K is noteworthy (compare Fig. 1e and f). Nonetheless, there are similar CO_2 concentrations in both SR and SESR at higher temperatures. It should be noted that the reduction in CO_2 and CO in SESR favors the methane steam reforming reactions (reverse of Eqs. (16) and (17)). This is the reason why the CH_4 concentration is greatly reduced at temperatures below 873 K, for inlet H_2O/C_2H_6O ratios greater than 4:1 (compare Fig. 1g and h). Nevertheless, at low temperatures (close to 500 K) and for very low inlet steam-to-ethanol ratios (1:1–2:1), the CH_4 concentration from SESR is greater than that from SR. Under these conditions, as previously discussed, H_2O more easily reacts with CaO to form $Ca(OH)_2$ (see Eq. (19)). As a consequence, the inhibition of methane steam reforming leads to higher CH_4 concentrations. However, for inlet H_2O/C_2H_6O ratios greater than 4:1, even at 500 K, the methane content obtained from the SESR process is significantly lower than that from the conventional SR, because, in the presence of steam, CO_2 can be captured by the $Ca(OH)_2$, according to Eq. (20).

Fig. 2 depicts the gas phase composition along with the number of moles of solid phases (CaO, $CaCO_3$ and $Ca(OH)_2$) formed per mol of ethanol, at 500, 830 and 1050 K, for different inlet steam-to-ethanol ratios. Fig. 2a shows that, at 500 K, CaO is converted into $Ca(OH)_2$ and $CaCO_3$. For relatively low values of the inlet H_2O/C_2H_6O molar ratio (1:1 and 4:1), $Ca(OH)_2$ is the predominant solid phase. However, with increasing the inlet steam-to-ethanol molar ratio, the amount of $Ca(OH)_2$ diminishes, while the number of moles of $CaCO_3$ increases, which could correspond to the CO_2 capture by the $Ca(OH)_2$, as indicated by Eq. (20). Under these conditions, the H_2 concentration increases significantly, accompanied by a great decrease in the CH_4 content. From Fig. 2b and c, it can be seen that, as the temperature is increased, the $Ca(OH)_2$ phase disappears, which is in agreement with the exothermic character of the reaction given by Eq. (19). As shown in Fig. 2b, at 830 K (which is within the temperature range of 723–873 K, suitable for the SESR, as previously discussed), for H_2O/C_2H_6O ratios > 4:1, CaO is completely converted into $CaCO_3$, according to Eq. (3), and high-purity H_2 (>97%) can be obtained. At higher temperatures, as illustrated in Fig. 2c for $T = 1050$ K, CaO remains unconverted, and the equilibrium gas phase obtained from the SESR is identical to that from the conventional SR process, since CO_2 is not captured by the CaO. In this way, Fig. 2 illustrates how the increase in the H_2 concentration is correlated to the formation of the solid phase $CaCO_3$.

From these results, it can be seen that the SESR process benefits the production of H_2-rich gas with less CO, CO_2 and methane, in the temperature range of 723–873 K, for inlet H_2O/C_2H_6O molar ratios greater than 4:1. Obviously, in practical operation, the catalyst is required to have high activity at the low temperatures where CO_2 adsorption is favored. Recently, He et al. [38] carried out SESR of ethanol over a mixture of hydrotalcite-like material derived Co–Ni catalysts and calcined dolomite (mainly CaO) with steam-to-ethanol ratio of 6:1 at 823 K. The authors reported that the best result was obtained over 40Ni and 20Co–20Ni/HTLs catalysts, where the gaseous product had composition of more than 99% H_2, 0.4% CH_4, 0.1% CO, and 0.2% CO_2. This experimental result is close to the theoretical prediction of the present work: 99.40% H_2, 0.46% CH_4, 0.05% CO, and 0.09% CO_2.

3.2.2. *Carbon formation*

Fig. 3 shows the effect of steam-to-ethanol molar ratios and temperature on the number of moles of carbon (graphite) in the conventional SR (a) and SESR (b). In fact, Fig. 3 can also be understood as the boundary of carbon formation [28], which is defined as the minimum inlet steam-to-ethanol ratio, calculated at a given temperature, necessary to inhibit carbon deposition. For inlet steam-to-ethanol ratios greater than those indicated at the boundary of carbon formation, graphite phase is thermodynamically unpredicted. In the conventional SR, the limit of the boundary of carbon formation corresponds to a steam-to-ethanol ratio of ~3:1 (500 K). In the case of the SESR process, this limit for carbon free operation is decreased

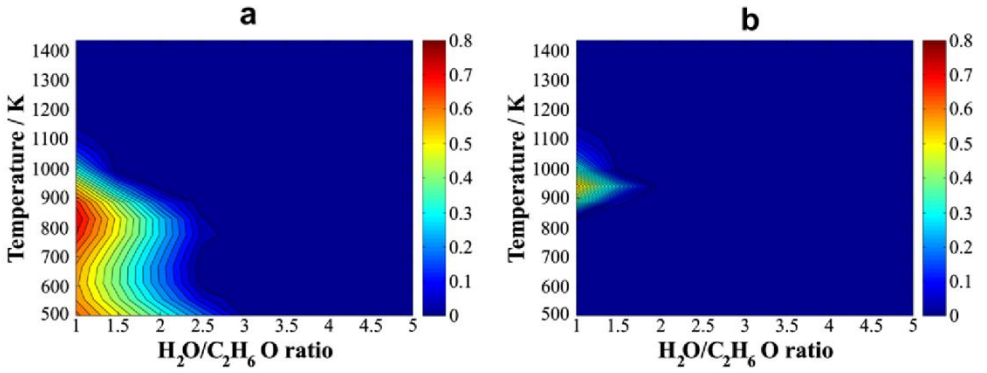

Fig. 3 – Effect of temperature and steam-to-ethanol ratio on moles of carbon formed per mol of ethanol in (a) SR and (b) SESR. P = 1 atm.

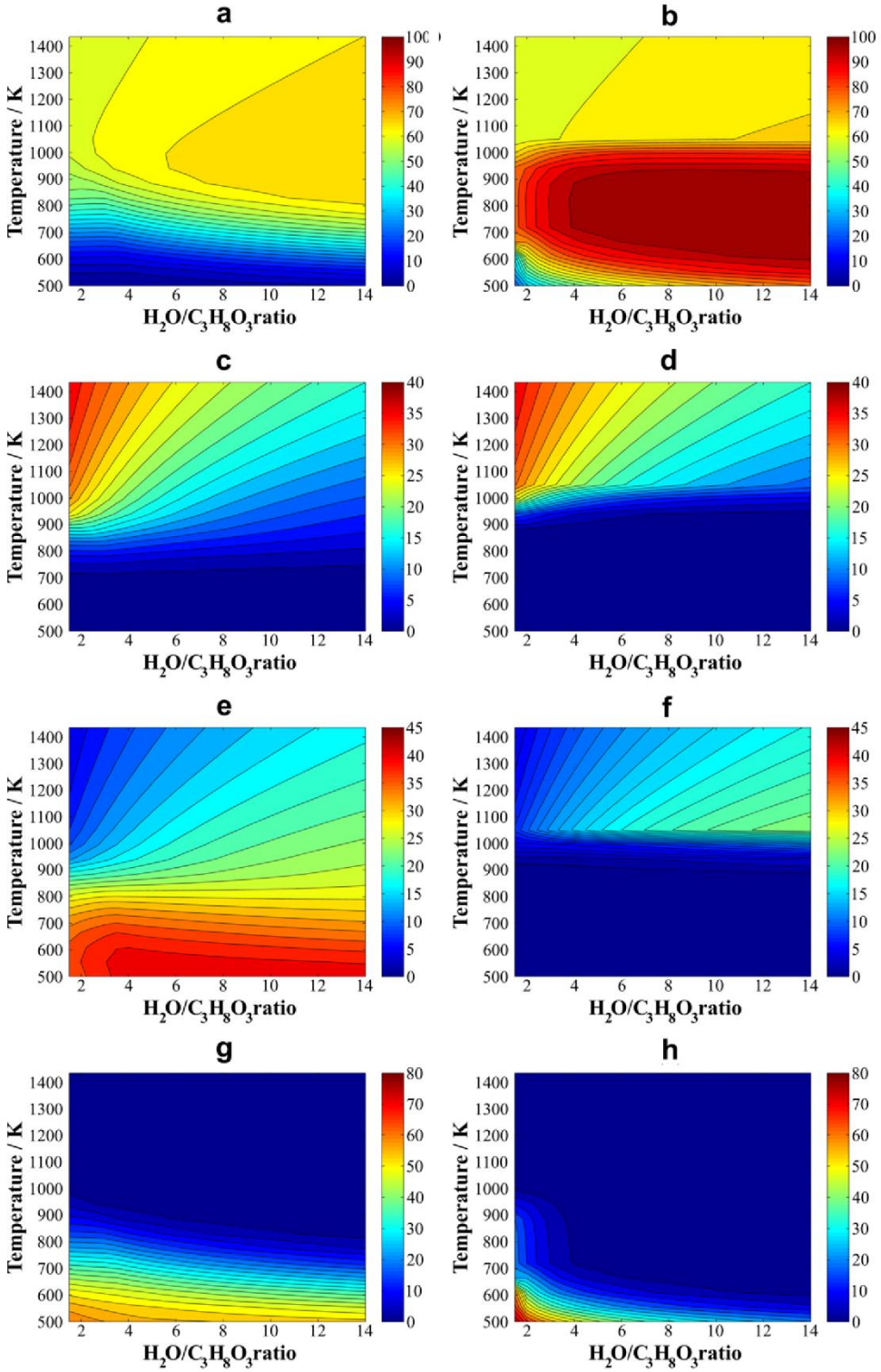

Fig. 4 – Effects of temperature and steam-to-glycerol ratio on the product gas concentration (mol%, on the dry basis). (a, b) H_2, (c, d) CO, (e, f) CO_2 and (g, h) CH_4. The plots (a, c, e, g) are for the conventional SR (without CaO) and (b, d, f, h) for the SESR process. $P = 1$ atm.

to ~2:1 (900 K). Besides, as can be seen in Fig. 3b, carbon formation is suppressed at temperatures below ~800 K even at a steam-to-ethanol ratio as low as 1:1. Thus, the SESR process has very low risk of solid carbon formation. This fact is directly related to the reduction in CO content. Li [39] also verified, in his thermodynamic study, that graphite formation is suppressed with CO_2 adsorption. According to this author, the Boudouard reaction

$$2CO \rightarrow CO_2 + C \quad \Delta H^0_{298\,K} = -172.5\ \text{kJ mol}^{-1} \tag{21}$$

is shifted backwards because its equilibrium constant is related to the square of CO concentration.

3.3. Glycerol/steam system

3.3.1. Product distribution in the gas phase

Fig. 4 depicts the effects of temperature and steam-to-glycerol ($H_2O/C_3H_8O_3$) molar ratios on the dry basis concentration (mol %) of H_2 (a, b), CO (c, d), CO_2 (e, f) and CH_4 (g, h) in the conventional SR (a, c, e and g) and SESR (b, d, f and h). The trends exhibited by the species in Fig. 4 are very similar to those seen in the case of ethanol in Fig. 1. In fact, it is worth pointing out here that all the oxygenated hydrocarbons analyzed in this work behave similarly during the reforming process. This fact was expected, since in all the cases the main species present at equilibrium are H_2, CO, CO_2, CH_4, H_2O and C (graphite), over the whole range of conditions examined in this study. Thus, the explanation of the gas composition change as operating conditions (T and inlet steam-to-fuel ratio) vary, based on chemical reactions, as can seen in Section 3.2 for the ethanol/steam system, is also valid for the systems involving glycerol, *n*-butanol and methanol throughout the Sections 3.3, 3.4 and 3.5, respectively.

As can be observed in Fig. 4a, high temperature and high inlet steam-to-glycerol ratio favor the H_2 production in the conventional SR process. For inlet $H_2O/C_3H_8O_3$ ratios greater than 7:1, the H_2 concentration is of 64–68% in the temperature range of 885–1215 K. The maximum number of moles of H_2 produced per mol of glycerol is 6.3 (concentration of 68%) in the temperature range of 885–940 K with a $H_2O/C_3H_8O_3$ ratio of 14 (note that from Eq. (1) the stoichiometric value is 7 for glycerol steam reforming). Interestingly, with a $H_2O/C_3H_8O_3$ ratio of 12 at 925 K, the maximum H_2 production is 6.2 (67.5%), which is identical to the value reported by Wang et al. [40]. However, in the SESR process, high-purity H_2 (>96%) (Fig. 4b) can be obtained in the temperature range of 723–873 K for $H_2O/C_3H_8O_3$ ratios greater than 4:1. Under these conditions, as a result of the shifted equilibrium in the process with *in situ* CO_2 removal, much lower contents of CO (compare Fig. 4c and d), CO_2 (compare Fig. 4e and f) and methane (compare Fig. 4g and h) can be seen in the product gas. For steam-to-glycerol ratios greater than 6:1, the number of moles of H_2 produced per mol of glycerol is greater than 6.8 in the temperature range of 723–873 K, which corresponds to a H_2 concentration of ~99% in a dry basis. He et al. [30] experimentally obtained hydrogen with purity at ~99% by the SESR process of glycerol with a $H_2O/C_3H_8O_3$ ratio of 9:1 at 848 K, which is in agreement with our theoretical results. In a recent thermodynamic analysis, Li et al. [41] reported that under the optimal conditions (900 K, steam-to-glycerol ratio = 4:1) H_2 at a concentration of 96 mol% could be achieved. Despite of this fact, it was reported that H_2 at a concentration of 99% can be attained in practice. In this way, the optimal conditions are shifted towards higher inlet steam-to-glycerol ratios (6:1–9:1) and lower temperatures (723–873 K). In Section 3.8, the optimal operating conditions (production of high-purity H_2 with CO content within the 20 ppm required for PEMFC applications) will be shown.

3.3.2. Carbon formation

Fig. 5 shows the effect of steam-to-glycerol molar ratios and temperature on the number of moles of carbon (graphite) in the conventional SR (a) and SESR (b). In the SR process, the number of moles of carbon computed as a function of steam-to-glycerol ratio and temperature is in agreement with the values presented by Wang et al. [40]. At a moderate temperature of 800 K, for example, an inlet $H_2O/C_3H_8O_3$ ratio of 3:1 is necessary to prevent carbon formation. In the SESR process, however, the formation of carbon is dramatically decreased. In fact, with a steam-to-glycerol ratio as low as 1.5:1, it would be possible to operate at temperatures lower than 885 K without any risk of carbon deposition. For $H_2O/C_3H_8O_3$ molar ratios greater than 2:1, carbon deposition is completely inhibited over the whole temperature range.

3.4. n-Butanol/steam system

3.4.1. Product distribution in the gas phase

Fig. 6 illustrates the effects of temperature and steam-to-*n*-butanol ($H_2O/C_4H_{10}O$) molar ratios on the dry basis concentration (mol%) of H_2 (a, b), CO (c, d), CO_2 (e, f) and CH_4 (g, h) in the conventional SR (a, c, e and g) and SESR (b, d, f and h). In the SR process, in order to optimize the H_2 production, the temperature and inlet steam-to-*n*-butanol ratios must be high. In this case, between 950 and 1173 K, for steam-to-*n*-butanol ratios of 9:1–14:1, a H_2 concentration between 69 and 72% is obtained, with CO at concentrations of 11–20%. It is clearly seen that, in the SESR process, the optimal conditions for H_2 production are shifted towards lower temperatures, 723–873 K. In this temperature range, the CO and CO_2 contents are enormously decreased. Besides, for inlet $H_2O/C_4H_{10}O$ molar ratios >8:1, the

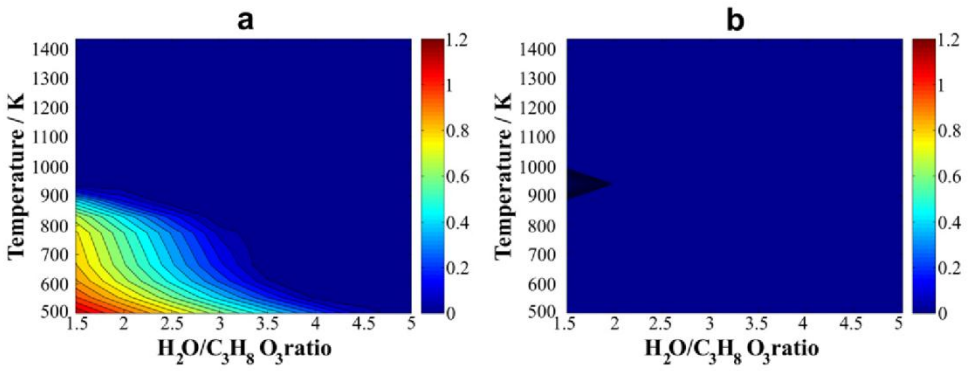

Fig. 5 – Effect of temperature and steam-to-glycerol ratio on moles of carbon formed per mol of glycerol in (a) SR and (b) SESR. P = 1 atm.

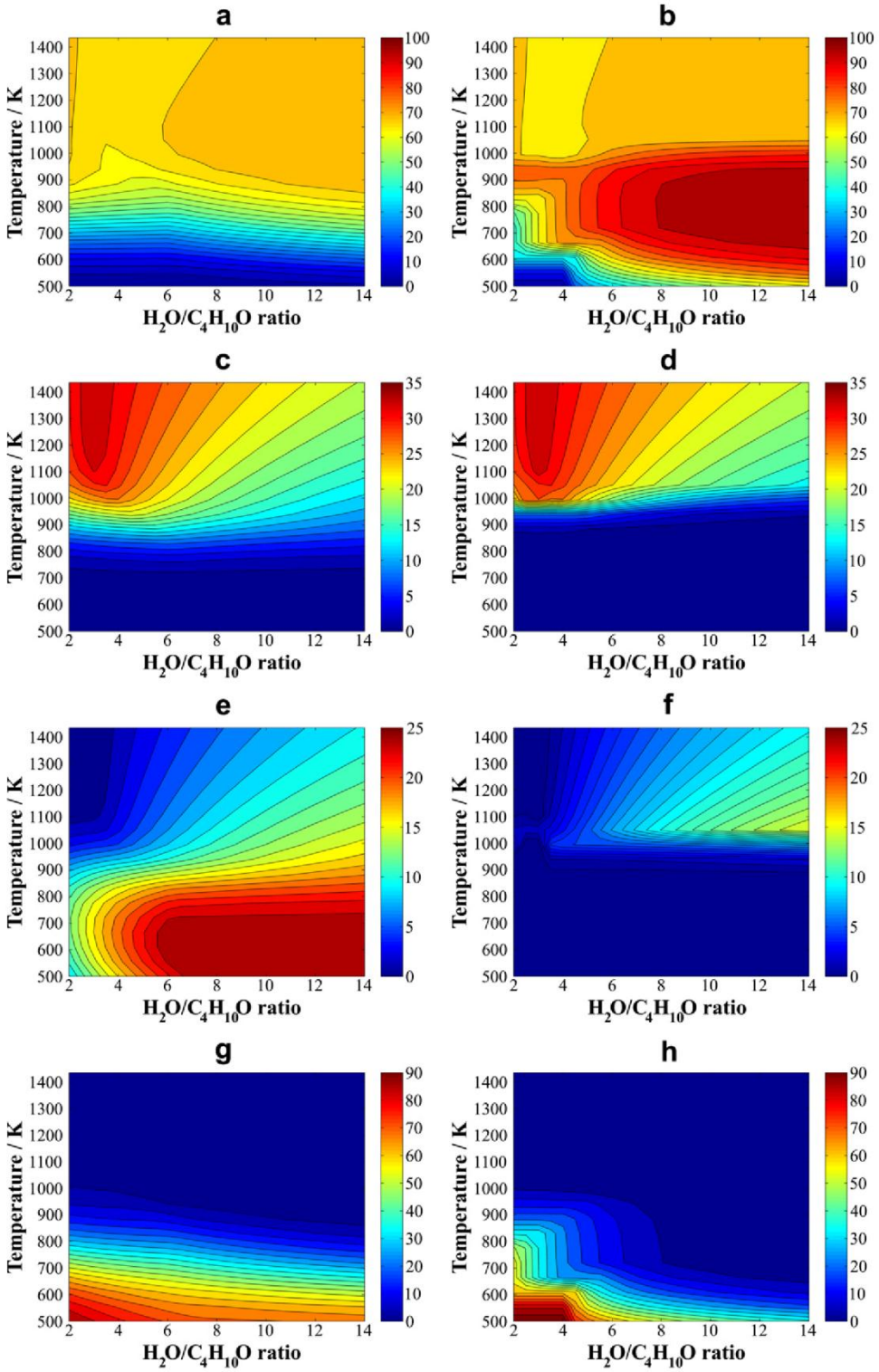

Fig. 6 – Effects of temperature and steam-to-*n*-butanol ratio on the product gas concentration (mol%, on the dry basis). (a, b) H_2, (c, d) CO, (e, f) CO_2 and (g, h) CH_4. The plots (a, c, e, g) are for the conventional SR (without CaO) and (b, d, f, h) for the SESR process. $P = 1$ atm.

H_2 concentration is greater than 95%, and the CH_4 content is lower than 5% (in the SR, under these conditions, CH_4 concentration is of 7.0–35%). Again, it is noteworthy that the separation of CO_2 from the gas phase by CaO sorbents promotes H_2 and decreases CH_4 and CO contents.

Unfortunately, there is a lack of experimental research dealing with hydrogen production by SR and SESR of *n*-butanol. In this way, it is expected that the theoretical results from the present work can be used as a guide in further experimental investigation.

3.4.2. *Carbon formation*

Fig. 7 shows the effect of steam-to-*n*-butanol molar ratios and temperature on the number of moles of carbon (graphite) in the conventional SR (a) and SESR (b). During SR of *n*-butanol, large amounts of carbon are produced. In fact, among all the oxygenated hydrocarbons considered in this wok, the SR of *n*-butanol produces the greatest amounts of graphite. For instance, at 600 K, an inlet $H_2O/C_4H_{10}O$ molar ratio close to 7:1 should be used to avoid carbon deposition over the catalyst. This result is in agreement with the findings of Nahar and Madhani [4]. Besides, in the temperature range of 800–950 K, for steam-to-*n*-butanol ratios between 2:1 and 3:1, the graphite formation is increased (1.7–1.9 moles per mol of *n*-butanol), which can be attributed to an increase in thermal decomposition of *n*-butanol [4]:

$$C_4H_{10}O \rightarrow CO + 2CH_4 + H_2 + C \quad (22)$$

In the SESR process, carbon formation is greatly inhibited at low and moderate temperatures. Thus, lower inlet $H_2O/C_4H_{10}O$ molar ratios can be used. For example, with a steam-to-*n*-butanol ratio of 3:1, carbon deposition is prevented at temperatures below 800 K. Under these conditions, in the SR process, the moles of carbon would be between 1.3 and 1.5.

3.5. *Methanol/steam system*

3.5.1. *Product distribution in the gas phase*

Fig. 8 illustrates the effects of temperature and steam-to-methanol (H_2O/CH_4O) molar ratios on the dry basis concentration (mol%) of H_2 (a, b), CO (c, d), CO_2 (e, f) and CH_4 (g, h) in the SR (a, c, e and g) and SESR (b, d, f and h). In the SR process, the highest concentrations of H_2, 71–74%, are found for inlet H_2O/CH_4O molar ratios greater than 2:1 at high temperatures (950–1100 K). In this temperature range, at moderate inlet steam-to-methanol ratios of 2:1–4:1, the CO content is between 8 and 18%, the CO_2 concentration is of 12–19%, while CH_4 concentration is lower than 1%. On the other hand, in the SESR process, for inlet H_2O/CH_4O molar ratios of 2:1–4:1, it is possible to produce H_2 at concentrations of 98–99% in the temperature range of 723–873 K. Under these conditions, the CH_4 concentration is greatly reduced due to CO_2 capture (compare Fig. 8g and h), and the CO and CO_2 contents are lower than 1.0%.

It is worth mentioning that many experimental works dealing with conventional methanol steam reforming are conducted over Cu-based catalyst [42,43], which means that CH_4 can be suppressed. However, the Cu-based catalysts deactivate rapidly because of the sintering of the active Cu at the operating temperature (723–873 K) of the SESR process. For this reason, other catalysts such as Ni should be used in the SESR of methanol, as in the Ref. [14]. In this way, CH_4 was considered in the compound basis set in the present study.

3.5.2. *Carbon formation*

Fig. 9 shows the effect of steam-to-methanol molar ratios and temperature on the number of moles of carbon (graphite) in SR (a) and SESR (b). Even in the conventional SR of methanol, it is possible to see that this system exhibits low tendency to deposit carbon. The maximum production of carbon occurs at 500 K, for the inlet H_2O/CH_4O ratio of 0.5:1 (0.18 mol of carbon/mol of methanol). The region of carbon formation is confined to the H_2O/CH_4O molar ratios lower than 1:1 in the temperature range of 500–1000 K, which is in agreement with the findings reported by Faungnawakij et al. [44] for a compound basis set including graphite and methane. In the SESR of methanol, carbon deposition is completely inhibited for all the inlet steam-to-methanol ratios over the whole temperature range.

3.6. *Thermal efficiency analysis*

Fig. 10 shows the influence of temperature and steam-to-fuel molar ratio on the thermal efficiency of ethanol (a, b), glycerol (c, d), *n*-butanol (e, f) and methanol (g, h) in SR (a, c, e and g) and SESR (b, d, f and h). In the SR process, it can be seen that at a certain temperature, the thermal efficiency of the process increases with the increase of the inlet steam-to-fuel molar ratio. In this case, as suggested by He et al. [30], the cost of the energy for generating extra steam can be compensated by promoting hydrogen production in the reforming process. At temperatures lower than 1000 K, the effect of steam on the thermal efficiency is noteworthy. At 873 K, the thermal efficiency increases from 52 to 68%, 52 to 67%, and 38 to 57%, as steam-to-fuel ratio increases from 3:1 to 9:1, for ethanol, glycerol and *n*-butanol, respectively. For methanol, the efficiency increases from 47 to 70%, as steam-to-methanol ratio is

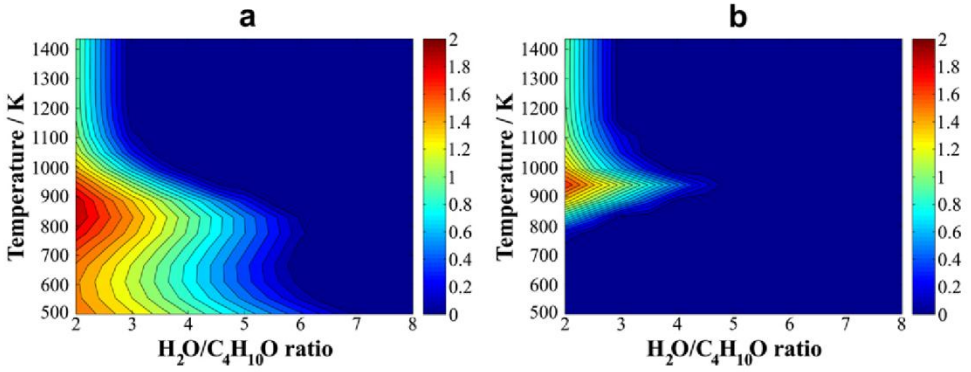

Fig. 7 – Effect of temperature and steam-to-*n*-butanol ratio on moles of carbon formed per mol of *n*-butanol in (a) SR and (b) SESR. $P = 1$ atm.

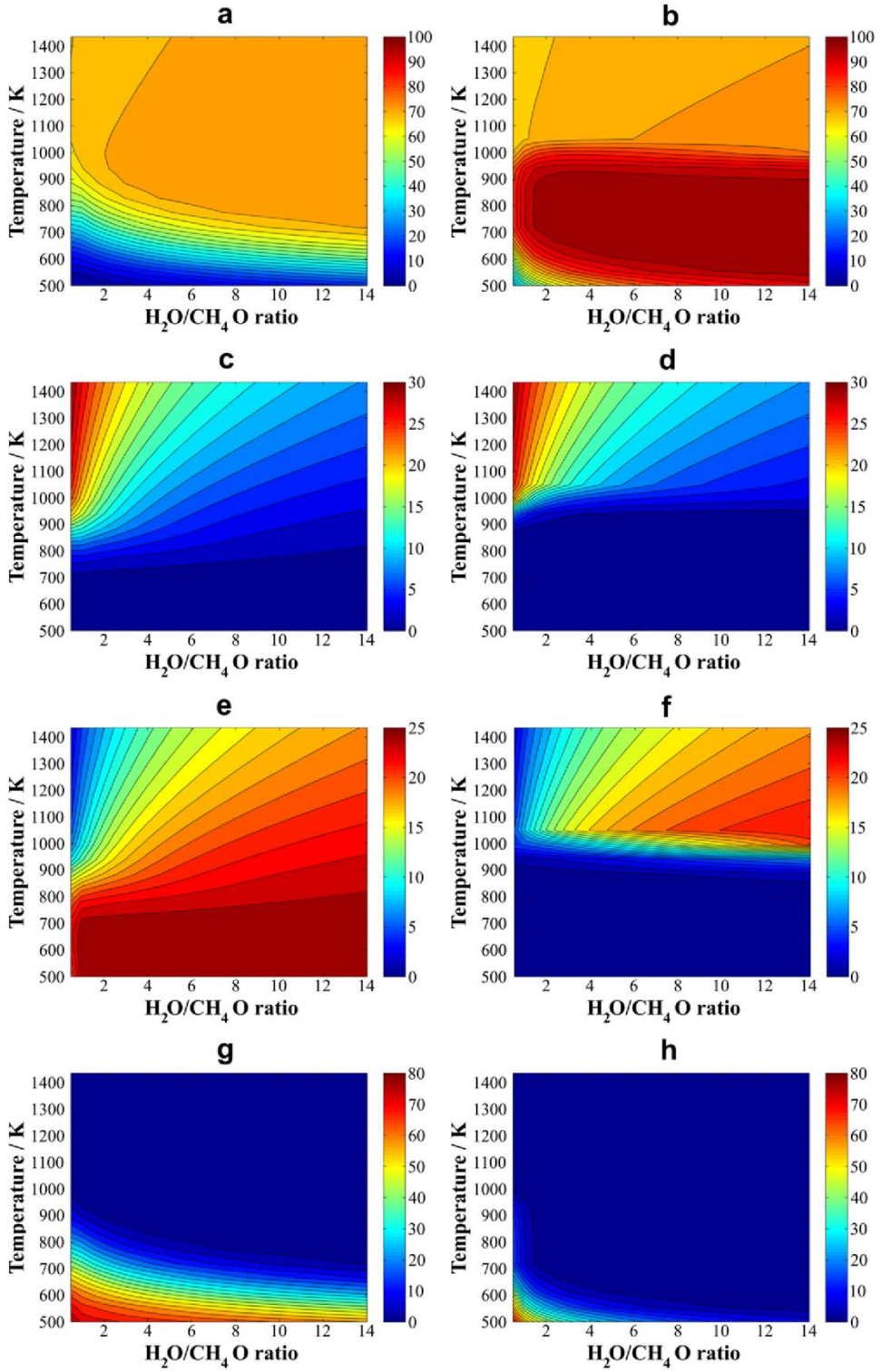

Fig. 8 – Effects of temperature and steam-to-methanol ratio on the product gas concentration (mol%, on the dry basis). (a, b) H_2, (c, d) CO, (e, f) CO_2 and (g, h) CH_4. The plots (a, c, e, g) are for the conventional SR (without CaO) and (b, d, f, h) for the SESR process. $P = 1$ atm.

increased from 0.5:1 to 4:1. In the case of glycerol, the thermal efficiency values are in agreement with those reported by He et al. [30] (53 and 69%, for steam-to-glycerol ratio = 3:1 and 9:1, respectively). While in the SR process the highest values of efficiency (67–70%) are concentrated in the temperature range of 900–1000 K, in the SESR process the optimal efficiencies (80–87% in the case of methanol, and 79–83% in the other cases) are shifted towards lower temperatures, in the range of 723–873 K. Thus, it can be seen that the thermal efficiency of the process is closely correlated to the hydrogen production. It

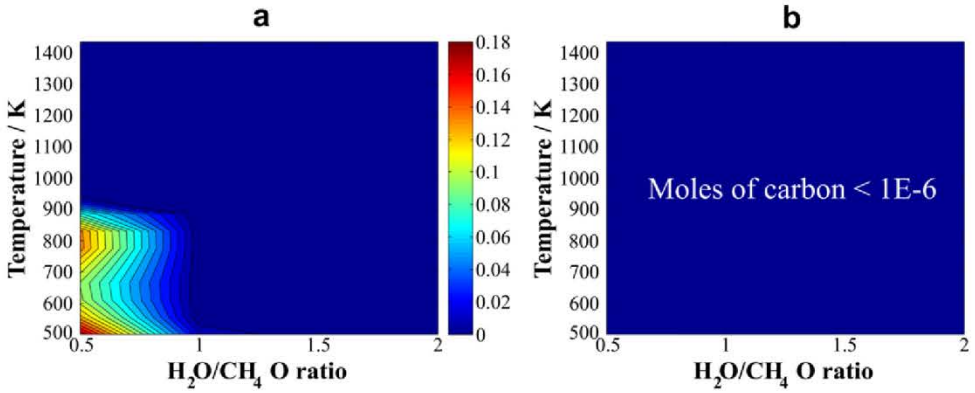

Fig. 9 – Effect of temperature and steam-to-methanol ratio on moles of carbon formed per mol of methanol in (a) SR and (b) SESR. $P = 1$ atm.

is worth pointing out that the use of lower temperatures could bring beneficial effects on the life of the catalysts and the construction materials of the reformers [45]. In addition to this, for all the fuels analyzed, it should be observed that in the SESR process the highest efficiencies occur in a limited range of steam-to-fuel ratio. In the case of methanol (Fig. 10h), this behavior is remarkable. For this fuel, at 775 K, the thermal efficiency of the process increases from 60 to 86% as steam-to-methanol increases from 0.5:1 to 2.5:1. At this same temperature, however, with a greater amount of steam in the inlet mixture, for example, a steam-to methanol ratio equal to 9:1, the thermal efficiency is decreased to 65%. As can be observed in Fig. 8b, the hydrogen concentration is nearly constant, increasing only slightly (97.5–99.9%), in the steam-to-methanol range of 2:1–14:1, when the temperature is between 723 and 873 K. Thus, it is clearly seen that the small benefit brought by the enhancement in the H_2 concentration is mitigated by the energy cost of steam generation, which is in agreement with theoretical results reported for glycerol [30]. For *n*-butanol, this behavior is also observed. Since such a fuel requires high amounts of steam, the optimal efficiencies occur for a steam-to-*n*-butanol ratio in the range of 8.5:1–14:1. For higher amounts of steam, the thermal efficiency starts to decrease.

3.7. *Pressure effect on the SESR process*

Fig. 11 illustrates the pressure effect on the dry basis concentration of H_2 (mol%) and CO, CO_2 (ppm) in the SESR of ethanol (a–c), glycerol (d–f), *n*-butanol (g–i) and methanol (j–l). In all the cases, the H_2 concentration slightly decreases as the pressure is increased. In fact, at higher pressures, Eq. (19) is shifted towards the products, favoring CaO hydration. Thus, H_2O more easily reacts with CaO to form $Ca(OH)_2$. In this way, the inhibition of methane steam reforming leads to higher CH_4 concentrations, decreasing the H_2 concentration. Besides, increasing operating pressure reduces CO and CO_2 contents, which can be attributed to the enhancement of CO_2 capture (Eq. (3)). In the temperature range of 723–898 K, the H_2 concentration is nearly constant. However, the CO and CO_2 contents increase greatly over the same temperature range. In this way, for single-step operation, in which high-purity H_2 is required, with CO concentration within the 20 ppm needed for PEMFC applications, the operation temperature should be in the range of 723–773 K, at $P = 3$–5 atm. Besides, a suitable inlet steam-to-fuel molar ratio should be selected in order to obtain H_2 >97% with extremely low CO content. In fact, the greater the inlet steam-to-fuel molar ratio, the lower the effect of pressure on the H_2 concentration. In the case of ethanol and methanol, the theoretical results of the present work are corroborated by the experimental results reported by Lysikov et al. [14]. Those authors verified that both lower outlet reactor temperature and higher reforming pressure were responsible for very low residual levels of CO and CO_2. For ethanol and methanol, the experimental conditions used in that study were: $P = 3$ atm, steam-to-ethanol ratio = 5:1 and steam-to-methanol ratio = 4:1. In the SESR process, they used an admixture of CaO sorbent with Ni reforming catalyst for both hydrocarbons. As can be seen in Fig. 11b, in the case of ethanol SESR at $P = 3$ atm, the theoretically predicted H_2 purity is 97.5%, while the CO and CO_2 contents are of 23 and 51 ppm, respectively, at 773 K. In Ref. [14], it is observed that, during the time range of 600–1200 s of ethanol reforming, the outlet reactor temperature is ~773 K. Under these conditions, Lysikov et al. report a hydrogen purity of 98–99% with both CO and CO_2 impurities of about 10–20 ppm. In this way, it is clearly seen that experimental results and thermodynamic predictions are in reasonable agreement. It should be pointed out that Lysikov et al. successfully fed a PEMFC stack with the H_2 produced by the single-step ethanol SESR without any loss of efficiency. In the case of methanol SESR, those authors report the same reformate composition as that of ethanol. At ~600 s of methanol SESR, the outlet reactor temperature was ~723 K. As can be seen in Fig. 11l, at this same temperature (723 K), at $P = 3$ atm, the H_2 purity is 99.6% with CO and CO_2 contents of 1.4 and 11 ppm, respectively. It is worth mentioning that in all the cases shown in Fig. 11 carbon deposition is thermodynamically unfeasible.

3.8. *Summary of the optimal operating conditions for the SESR process*

Table 2 shows the optimal conditions for the SESR of ethanol, glycerol, *n*-butanol and methanol. For all the hydrocarbons, it can be seen that it is possible to obtain a H_2 purity of ~99% at

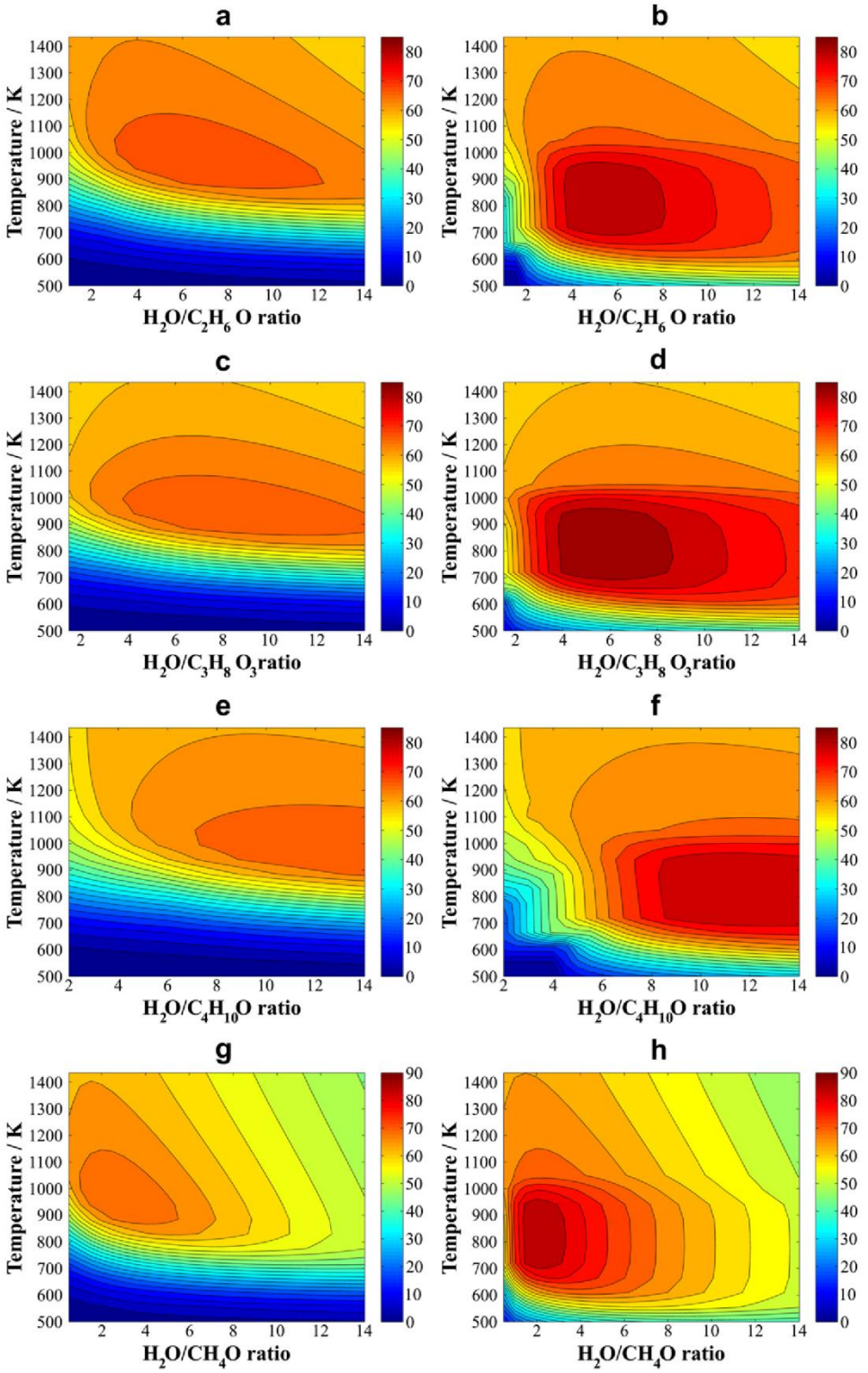

Fig. 10 – Effect of temperature and steam-to-fuel molar ratio on the thermal efficiency (%) of ethanol (a, b), glycerol (c, d), *n*-butanol (e, f) and methanol (g, h) in SR (a, c, e and g) and SESR (b, d, f and h) processes. $P = 1$ atm.

$P = 1$ atm and $T = 848$ K. However, at atmospheric pressure, the condition required from CO concentration <20 ppm for the PEMFC application is not possible to be achieved. In this way, a further process (the preferential CO oxidation performed in a COPROX reactor) is necessary. For comparison purposes, the product gas concentration obtained in the conventional SR process is also shown. As can be seen, the H_2 content is greatly reduced (64–71%), in comparison with the

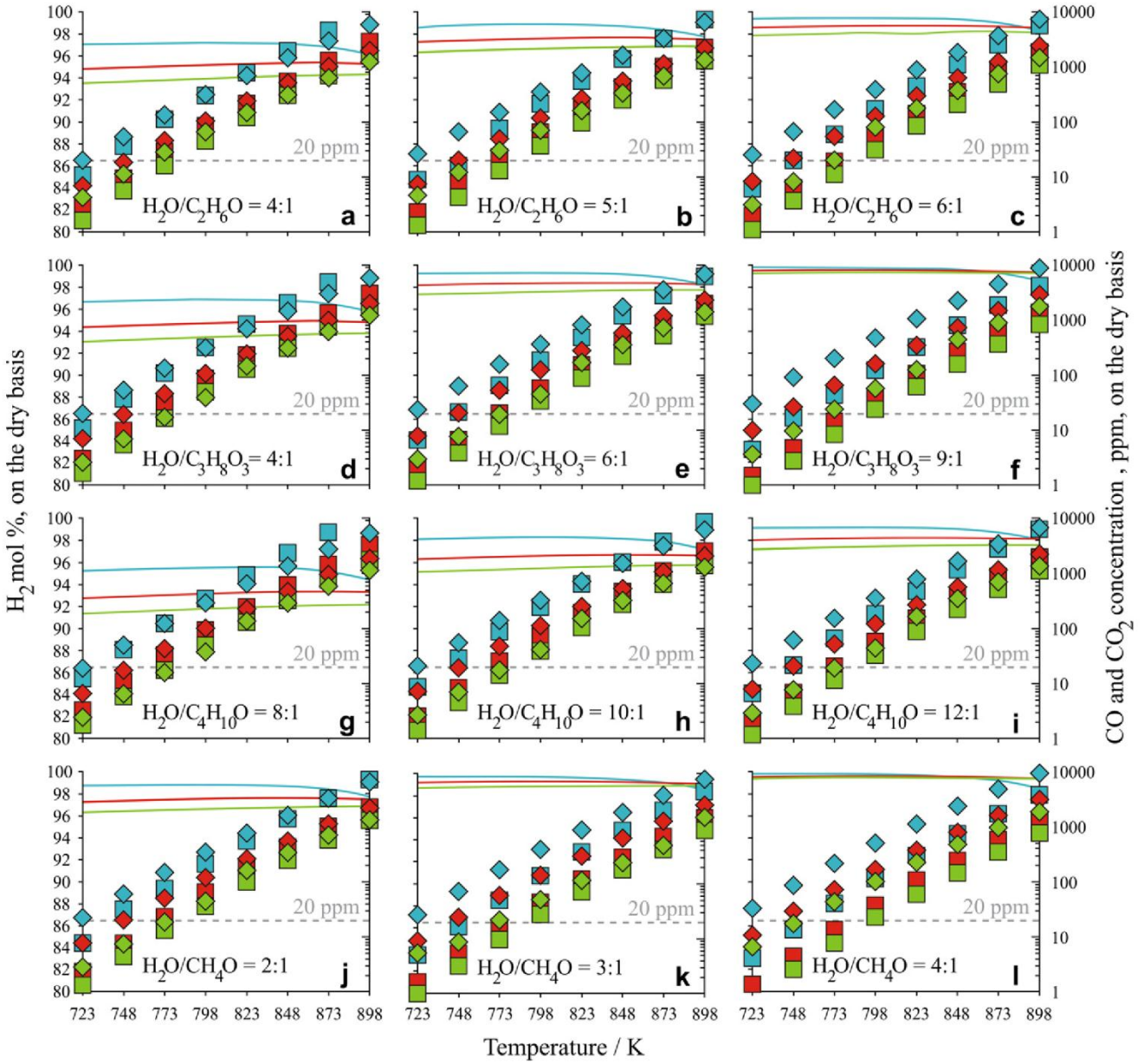

Fig. 11 – Pressure effect on the SESR process of ethanol (a–c), glycerol (d–f), *n*-butanol (g–i) and methanol (j–l). The solid lines refer to H_2, and the markers refer to (□) CO and (◆) CO_2. P = 1 (blue), 3 (red) and 5 atm (green). (For interpretation of the references to colour in this figure legend, the reader is referred to the web version of this article).

SESR process at the same T and P, and the CO content is too high for PEMFC applications. Thus, in the conventional SR, both the WGS and COPROX reactors are necessary afterward. Interestingly, as can also be observed in Table 2, at 773 K and P = 5 atm, it is possible to obtain, via the SESR process, high H_2 concentrations (over 97 mol%) along with CO contents around 10 ppm and a thermal efficiency greater than 76%. In this way, it is clearly seen that, by increasing the pressure from 1 to 5 atm and simultaneously decreasing the temperature from 848 to 773 K, high-purity H_2 for PEMFC anode can be produced in a single-step SESR process. Thus, further purification involving WGS and COPROX reactors would be unnecessary. In order to achieve such a reformate composition and high thermal efficiencies, the optimized steam-to-fuel molar ratios indicated in Table 2 are 6:1, 9:1, 12:1 and 4:1 for ethanol, glycerol, *n*-butanol and methanol, respectively, with CaO in the stoichiometric ratio to carbon atom.

It is worth pointing out that the values presented in this study for the SESR process, with respect to the reformate composition and thermal efficiency, were estimated based only on a thermodynamic analysis. As shown in a recent experimental study [46], due to the distributed nature of a real SESR reactor, part of the hydrogen inevitably goes to the regeneration exhaust instead of the product gas. Obviously, such an undesirable effect would affect the efficiency of the SESR process, because, as shown in Section 3.6, the thermal efficiency is closely correlated to the hydrogen concentration in the product gas.

Table 2 – Product gas concentration (mol%, on the dry basis) and thermal efficiency for conventional and sorption enhanced steam reforming process of ethanol, glycerol, *n*-butanol and methanol.

Steam-to-fuel ratio	Ethanol			Glycerol			*n*-Butanol			Methanol		
	6:1			9:1			12:1			4:1		
	SESR ($P = 1$ atm)[a]	SESR ($P = 5$ atm)[b]	SR ($P = 1$ atm)[a]	SESR ($P = 1$ atm)[a]	SESR ($P = 5$ atm)[b]	SR ($P = 1$ atm)[a]	SESR ($P = 1$ atm)[a]	SESR ($P = 5$ atm)[b]	SR ($P = 1$ atm)[a]	SESR ($P = 1$ atm)[a]	SESR ($P = 5$ atm)[b]	SR ($P = 1$ atm)[a]
H_2	99.26	98.00	67.85	99.57	99.30	64.50	99.06	97.40	66.91	99.60	99.50	71.34
CO	0.11	11×10^{-4}	6.52	0.08	9×10^{-4}	6.36	0.12	12×10^{-4}	6.86	0.07	8×10^{-4}	4.98
CO_2	0.18	34×10^{-4}	20.11	0.22	24×10^{-4}	26.14	0.17	33×10^{-4}	19.86	0.24	44×10^{-4}	21.26
CH_4	0.45	2.00	5.52	0.13	0.70	3.00	0.65	2.60	6.37	0.09	0.50	2.42
Efficiency (%)	82.2	78.5	60.9	80.6	79.37	64.5	81.3	76.6	58.4	79.3	78.5	67.1
Further process	COPROX	Not necessary	WGS reactor COPROX	COPROX	Not necessary	WGS reactor COPROX	COPROX	Not necessary	WGS reactor COPROX	COPROX	Not necessary	WGS reactor COPROX

a Temperature: 848 K.
b Temperature: 773 K.

4. Conclusions

Thermodynamic analysis of steam reforming of different oxygenated hydrocarbons (ethanol, glycerol, *n*-butanol and methanol) with and without CaO as CO_2 sorbent is carried out to determine favorable operating conditions to produce high-quality H_2 gas. The influence of steam-to-fuel feed molar ratio and temperature on the product gas concentration is investigated for both cases. For the steam reforming of all the fuels considered in this work, the main species present at equilibrium are H_2, CO, CO_2, CH_4, H_2O and C (graphite), over the whole range of conditions examined. Besides, the oxygenated hydrocarbons analyzed in this study behave similarly during the reforming process. Indeed, both conventional SR and SESR are fuel flexible processes. In the conventional SR, for inlet steam-to-carbon ratios of 2:1–4:1 in the case of methanol and 2:1–3:1 in the other cases, the highest concentrations of H_2 (70–72, 65–66, 68–71 and 70–73 mol%, for ethanol, glycerol, *n*-butanol and methanol, respectively) can be obtained at elevated temperatures (~973 K) together with high amounts of CO (>5%). In the SESR, however, high-purity H_2 (>97%) can be obtained with low contents of CO, CO_2 and CH_4 in the temperature range of 723–873 K. In addition, the separation of CO_2 from the gas phase greatly inhibits carbon deposition at low and moderate temperatures. In the case of methanol, the use of CaO sorbent prevents the carbon formation over the whole range of operational conditions investigated.

Under atmospheric conditions, in the conventional SR process, the highest values of efficiency (67–70%) are concentrated in the temperature range of 900–1000 K, whereas in the SESR process the optimal efficiencies (80–87% in the case of methanol, and 79–83% in the other cases) are shifted towards lower temperatures, in the range of 723–873 K.

For all the oxygenated hydrocarbons, thermodynamic predictions indicate that high-purity hydrogen with CO content within 20 ppm, required for PEMFC applications, can be directly produced by a single-step SESR process in the temperature range of 723–773 K at pressures of 3–5 atm. Thus, further processes involving water–gas shift (WGS) and preferential CO oxidation (COPROX) reactors are not necessary. In the case of ethanol and methanol, the theoretical findings of the present analysis are corroborated by experimental results from literature. In the other cases, the results could provide an indication of the starting point for experimental research. At $P = 5$ atm and $T = 773$ K, it is possible to obtain H_2 at concentrations over 97 mol % with CO content around 10 ppm and a thermal efficiency greater than 76%. In order to achieve such a reformate composition, the optimized steam-to-fuel molar ratios are 6:1, 9:1, 12:1 and 4:1 for ethanol, glycerol, *n*-butanol and methanol, respectively, with CaO in the stoichiometric ratio to carbon atom.

In this way, the SESR technology represents a potential low-temperature method for high-quality H_2 production with low tendency to deposit carbon. Moreover, the use of lower temperatures could bring beneficial effects on the life of the catalysts and the construction materials of the reformers. Besides these technological aspects, other advantages of the SESR are expected, such as easy CO_2 sequestration. In this case, the use of biofuels in conjunction with SESR could be a potentially viable carbon-negative process [47].

It is worth pointing out that, in this work, a mixture of water and pure fuel was assumed throughout the simulations. However, a crude biofuel contains impurities, such as esters, amine, formates, and sulfates. Further theoretical/experimental investigations should be carried out taking into account the effect of these impurities in the production of high-quality H_2 stream with low contents of CO and CO_2.

Acknowledgments

The authors would like to acknowledge the CNPq, Brazil for financial support. Special thanks to Mr. José Walter Farfan Valverde for his contribution in this work.

REFERENCES

[1] Larminie J, Dicks A. Fuel cell systems explained. New York: Wiley; 2000.
[2] Dunn S. Hydrogen futures: toward a sustainable energy system. Int J Hydrogen Energy 2002;27:235–64.
[3] Fatsikostas AN, Kondarides DI, Verykios XE. Production of hydrogen for fuel cells by reformation of biomass-derived ethanol. Catal Today 2002;75:145–55.
[4] Nahar GA, Madhani SS. Thermodynamics of hydrogen production by the steam reforming of butanol: analysis of inorganic gases and light hydrocarbons. Int J Hydrogen Energy 2010;35:98–109.
[5] Hohn KL, Lin YC. Catalytic partial oxidation of methanol and ethanol for hydrogen generation. ChemSusChem 2009;2:927–40.
[6] Cortright RD, Davda RR, Dumesic JA. Hydrogen from catalytic reforming of biomass-derived hydrocarbons in liquid water. Nature 2002;418:964–7.
[7] Profeti LPR, Ticianelli EA, Assaf EM. Production of hydrogen via steam reforming of biofuels on $Ni/CeO_2–Al_2O_3$ catalysts promoted by noble metals. Int J Hydrogen Energy 2009;34:5049–60.
[8] Iriondo A, Barrio VL, Cambra JF, Arias PL, Guemez MB, Sanchez-Sanchez MC, et al. Glycerol steam reforming over Ni catalysts supported on ceria and ceria-promoted alumina. Int J Hydrogen Energy 2010;35:11622–33.
[9] Hipolito CN, Crabbe E, Badillo CM, Zarrabal OC, Morales Mora MA, Flores GP, et al. Bioconversion of industrial wastewater from palm oil processing to butanol by *Clostridium saccharoperbutylacetonicum* N1-4 (ATCC 13564). J Cleaner Prod 2008;16:632–8.
[10] Atsumi S, Hanai T, Liao JC. Non-fermentative pathways for synthesis of branched-chain higher alcohols as biofuels. Nature 2008;451:86–9.
[11] Advanced Research Projects Agency, US Department of Energy. See: http://www.energy.gov/news/8207.htm; Oct 26, 2009.
[12] Davda R, Shabaker J, Huber G, Cortright R, Dumesic J. A review of catalytic issues and process conditions for renewable H_2 and alkanes by aqueous-phase reforming of oxygenated hydrocarbons over supported metal catalysts. Appl Catal B: Environ 2005;56:171–86.
[13] Sutton D, Kelleher B, Ross J. Review of literature on catalysts for biomass gasification. Fuel Process Technol 2001;73:155–73.
[14] Lysikov AI, Trukhan SN, Okunev AG. Sorption enhanced hydrocarbons reforming for fuel cell powered generators. Int J Hydrogen Energy 2008;33:3061–6.
[15] Benito M, Sanz JL, Isabel R, Padilla R, Arjona R, Daza L. Bio-ethanol steam reforming: insights on the mechanism for hydrogen production. J Power Sources 2005;151:11–7.
[16] Fatsikostas AN, Verykios XE. Reaction network of steam reforming of ethanol over Ni-based catalysts. J Catal 2004;225:439–52.
[17] Biswas P, Kunzru D. Steam reforming of ethanol for production of hydrogen over $Ni/CeO_2–ZrO_2$ catalyst: effect of support and metal loading. Int J Hydrogen Energy 2007;32:969–80.
[18] Valliyappan T, Ferdous D, Bakhshi NN, Dalai AK. Production of hydrogen and syngas via steam gasification of glycerol in a fixed-bed reactor. Top Catal 2008;49:59–67.
[19] Stein YS, Antal MJ, Jones M. A study of the gas-phase pyrolysis of glycerol. J Anal Appl Pyrolysis 1983;4:283–96.
[20] Lazier WA, Adkins H. Dehydrogenation and dehydration of alcohols over a zinc oxide catalyst. J Am Chem Soc 2002;47:1719–22.
[21] Gayubo AG, Aguayo AT, Atutxa A, Aguado R, Olazar M, Bilbao J. Transformation of oxygenate components of biomass pyrolysis oil on a HZSM-5 zeolite. II. Aldehydes, ketones, and acids. Ind Eng Chem Res 2004;43:2619–26.
[22] Caixia Qi, Amphlett JC, Peppley BA. Product composition as a function of temperature over NiAl-layered double hydroxide derived catalysts in steam reforming of methanol. Appl Catal A: General 2006;302:237–43.
[23] Yaws CL. Chemical properties handbook. New York: McGraw-Hill; 1999.
[24] Knacke O, Kubaschewski O, Hesselmann K. Thermochemical properties of inorganic substances. 2nd ed. Berlin: Springer-Verlag; 1991.
[25] Sandler SI. Chemical and engineering thermodynamics. 3rd ed. New York: Wiley; 1999.
[26] Reid RC, Prausnitz JM, Poling BE. The properties of gases and liquids. 4th ed. New York: McGraw-Hill; 1987.
[27] Lima da Silva A, Malfatti CF, Müller IL. Thermodynamic analysis of ethanol steam reforming using Gibbs energy minimization method: a detailed study of the conditions of carbon deposition. Int J Hydrogen Energy 2009;34:4321–30.
[28] Lima da Silva A, Müller IL. Thermodynamic study on glycerol-fuelled intermediate-temperature solid oxide fuel cells (IT-SOFCs) with different electrolytes. Int J Hydrogen Energy 2010;35:5580–93.
[29] Lima da Silva A, Müller IL. Operation of solid oxide fuel cells on glycerol fuel: a thermodynamic analysis using the Gibbs free energy minimization approach. J Power Sources 2010;195:5637–44.
[30] He L, Parra JMS, Blekkan EA, Chen D. Towards efficient hydrogen production from glycerol by sorption enhanced steam reforming. Energy Environ Sci 2010;3:1046–56.
[31] Ma Li, Wang X, Li S, Wang S, Ma X. Hydrogen production from ethanol steam reforming over nickel based catalyst derived from Ni/Mg/Al hydrotalcite-like compounds. Int J Hydrogen Energy 2010;35:6699–708.
[32] Liu JY, Lee CC, Wang CH, Yeh CT, Wang CB. Application of nickel–lanthanum composite oxide on the steam reforming of ethanol to produce hydrogen. Int J Hydrogen Energy 2010;35:4069–75.
[33] Deng X, Sun J, Yu S, Xi J, Zhu W, Qiu X. Steam reforming of ethanol for hydrogen production over $NiO/ZnO/ZrO_2$ catalysts. Int J Hydrogen Energy 2008;33:1008–13.
[34] Fishtik I, Alexander A, Datta R. A thermodynamic analysis of hydrogen production by steam reforming of ethanol via response reactions. Int J Hydrogen Energy 2000;25:31–45.
[35] He L, Berntsen H, Ochoa-Fernandez E, Walmsley JC, Blekkan EA, Chen D. Co–Ni catalysts derived from hydrotalcite-like materials for hydrogen production by ethanol steam reforming. Top Catal 2009;52:206–17.

[36] Zhang B, Tang X, Li Y, Cai W, Xu Y, Shen W. Steam reforming of bio-ethanol for the production of hydrogen over ceria-supported Co, Ir and Ni catalysts. Catal Commun 2006;7:367–72.
[37] Amphlett JC, Evans MJ, Jones RA, Mann RF, Weir RD. Hydrogen production by the catalytic steam reforming of methanol part 1: the thermodynamics. Can J Chem Eng 1981;59:720–7.
[38] He L, Berntsen H, Chen D. Approaching sustainable H_2 production: sorption enhanced steam reforming of ethanol. J Phys Chem A 2010;114:3834–44.
[39] Li M. Thermodynamic analysis of adsorption enhanced reforming of ethanol. Int J Hydrogen Energy 2009;34:9362–72.
[40] Wang X, Li S, Wang H, Liu B, Ma X. Thermodynamic analysis of glycerin steam reforming. Energy Fuels 2008;22:4285–91.
[41] Li Y, Wang W, Chen B, Cao Y. Thermodynamic analysis of hydrogen production via glycerol steam reforming with CO_2 adsorption. Int J Hydrogen Energy 2010;35:7768–77.
[42] Papavasiliou J, Avgouropoulos G, Ioannides T. Steam reforming of methanol over copper-manganese spinel oxide catalysts. Catal Commun 2005;6:497–501.
[43] Peppley BA, Amphlett JC, Kearns LM, Mann RF. Methanol-steam reforming on $Cu/ZnO/Al_2O_3$. Part 1: the reaction network. Appl Catal A: Gen 1999;179:21–9.
[44] Faungnawakij K, Kikuchi R, Eguchi K. Thermodynamic evaluation of methanol steam reforming for hydrogen production. J Power Sources 2006;161:87–94.
[45] Rostrup-Nielsen JR, Sehested J, Nørskov JK. Hydrogen and synthesis gas by steam- and CO_2 reforming. In: Advances in catalysis. Academic Press; 2002. p. 65–139.
[46] Duraiswamy K, Chellappa A, Smith G, Liu Y, Li M. Development of a high-efficiency hydrogen generator for fuel cells for a distributed power generation. Int J Hydrogen Energy 2010;35:8962–9.
[47] Florin NH, Harris AT. Enhanced hydrogen production from biomass with in situ carbon dioxide capture using calcium oxide sorbents. Chem Eng Sci 2008;63:287–316.

4.1.3. Operation of solid oxide fuel cells on glycerol fuel: a thermodynamic analysis using the Gibbs free energy minimization approach

(Operação de células a combustível do tipo óxido sólido com glicerol: uma análise termodinâmica usando a abordagem da minimização da energia livre de Gibbs)

Principais Resultados:

- Desenvolvimento de metodologia para computar a composição da atmosfera do ânodo em função da densidade de corrente de operação; consequentemente, a metodologia permite avaliar a quantidade de carbono depositada e o potencial reversível da célula em função da densidade de corrente de operação;
- Elaboração de diagramas da composição da atmosfera do ânodo e do potencial reversível em função da densidade de corrente; estes diagramas permitem que pesquisadores que estejam realizando investigação experimental da célula SOFC operando com glicerol possam calcular a eficiência de suas células, mediante o quociente entre o potencial medido e o potencial reversível calculado em uma determinada densidade de corrente; Estes diagramas também mostram qual deve ser o valor mínimo para a densidade de corrente a fim de evitar a deposição de carbono no ânodo;
- Simulação com respeito à deposição de carbono é consistente com trabalho experimental da literatura;

Journal of Power Sources 195 (2010) 5637–5644

Contents lists available at ScienceDirect

Journal of Power Sources

journal homepage: www.elsevier.com/locate/jpowsour

Operation of solid oxide fuel cells on glycerol fuel: A thermodynamic analysis using the Gibbs free energy minimization approach

Aline Lima da Silva*, Iduvirges Lourdes Müller

Program of Postgraduate Studies in Mining, Metals and Materials Engineering (PPGEM), Federal University of Rio Grande do Sul, UFRGS, Campus do Vale, Setor 4, Prédio 75, Sala 226, Av. Bento Gonçalves 9500, CEP 91501-970, Porto Alegre, RS, Brazil

ARTICLE INFO

Article history:
Received 3 March 2010
Received in revised form 23 March 2010
Accepted 23 March 2010
Available online 30 March 2010

Keywords:
Solid oxide fuel cells
Direct utilization
Glycerol
Electrochemical thermodynamics
Carbon deposition
Gibbs energy minimization method

ABSTRACT

Solid oxide fuel cells (SOFCs) are very flexible, unlike other fuel cells. In principle, SOFCs can operate on almost any fuel. Currently much effort is invested in the development of SOFCs for portable applications operating directly on liquid fuels such as methanol and ethanol rather than hydrogen. However, there are very few publications dealing with the direct use of glycerol in SOFCs for portable systems. A recently published study shows that the performance achieved for an SOFC fueled by pure glycerol is quite interesting even when there is a thick electrolyte membrane, indicating that glycerol is a promising fuel for portable applications. For this reason a thermodynamic analysis for SOFCs operating directly on glycerol fuel is performed in the present study. The Gibbs energy minimization method computes the equilibrium compositions of the anode gas mixture, carbon deposition boundaries and electromotive forces (EMFs) as a function of fuel utilization and temperature. Moreover, the minimum amounts of H_2O, CO_2 (direct internal reforming case) and air (partial oxidation case) to be added to glycerol in the feedstock to avoid carbon deposition at the open circuit voltage (OCV) are calculated. Finally, a thermodynamic analysis is performed, taking into account the experimental conditions employed in a previous study. Experimental observations concerning carbon deposition in an SOFC operating on glycerol can be explained by the theoretical analysis developed in the present study. Additionally, the effect of mixed electronic–ionic conduction of the electrolyte on carbon deposition at the anode is discussed based on the thermodynamic analysis of the C–O system.

© 2010 Elsevier B.V. All rights reserved.

1. Introduction

Solid oxide fuel cells (SOFCs) are regarded as a promising source of clean and efficient electricity generation [1]. A major advantage of SOFCs is that they potentially have great fuel flexibility, which in principle may allow operation on any combustible fuel [2]. Moreover, SOFCs have a great potential as portable electric generators and as energy sources for transportation. The simplicity afforded by not having to reform the hydrocarbon fuels is a significant advantage of these cells [3]. In fact, the portable applications of SOFCs have been recently extended [4–7]. For these applications, selecting a proper fuel is a crucial step for its commercialization. Such a fuel should be cheap, safe and easy to store and transport [5]. In this context, methanol and ethanol have been considered promising candidate fuels for portable SOFC applications, since both have a very low impurity content and are oxygenated, which reduces the risks of poisoning and may reduce carbon deposition if used in SOFCs [6–8].

However, there are very few reports about SOFCs operating directly on glycerol. In a recent work, Lo Faro et al. [9] experimentally investigated the electrochemical oxidation of glycerol ($C_3H_8O_3$) as an alternative to hydrogen and methane at an intermediate temperature SOFC (IT-SOFC) by using a noble metal-free anode catalyst. It was found that the SOFC cell showed suitable power density especially under anhydrous conditions (327 mW cm^{-2}, at 1073 K). The performance achieved for pure glycerol was quite interesting even in the presence of a thick electrolyte membrane (250 μm). Hence, glycerol could also be a promising candidate for portable SOFC applications.

It could also be mentioned that only a small amount of glycerol from the biodiesel production is purified for use in the food, pharmaceutical, tobacco and cosmetic industries, so the majority is simply wasted. Consequently, with increased production of biodiesel, a glut of glycerol is expected on the world market [10]. Therefore it is important to find efficient and effective uses for glycerol.

Glycerol is a green chemical (non-toxic, non-volatile and non-flammable) which makes it ideal for a wide variety of power uses. It has also high energy density (6.260 kWh L^{-1} for the pure liquid) making it a very attractive fuel for energy purposes [11]. Besides,

* Corresponding author. Tel.: +55 51 3308 9404.
E-mail address: adasilva26@gmail.com (A. Lima da Silva).

0378-7753/$ – see front matter © 2010 Elsevier B.V. All rights reserved.
doi:10.1016/j.jpowsour.2010.03.066

Nomenclature

G	total Gibbs energy of the system
G_i^0	Gibbs energy of species i in its standard state
n_i	number of moles of species i
n_i^0	initial number of moles of species i
n_i'	decision variable during the optimization process, after the change of variables
$\exp(n_i')$	number of moles of species i, after the change of variables
y_i	mole fraction of species i
R	gas constant
T	temperature of the system
P	total pressure of the system
a_i	activity of species i
M, N	total number of components and species, respectively
p_i	partial pressure of species i
μ_i	chemical potential of species i
λ_C	Lagrange's multiplier related to the elemental mass balance of carbon
CDB	carbon deposition boundary
CGO	gadolinia-doped ceria electrolyte
OCV	open circuit voltage
α_{ik}	number of atoms of kth element present in each molecule of species i
b_k	total number of atomic masses of kth element in the system
b_O^{echem}	additional number of moles of oxygen (O) in the system, due to the electrochemical reaction
D_{gra}	chemical driving force for nucleation of graphite phase
U_f	operating fuel utilization (%)
F	Faraday constant (96,485.34 C mol^{-1})
E	electromotive force of cell (V) for reversible conditions
K_{H_2O}	equilibrium constant of hydrogen oxidation
j	current density
t_{ion}	transference number of oxygen ions
z	number of electrons produced per glycerol molecule

Superscripts

an.	anode
cat.	cathode

glycerol is oxygenated, like methanol and ethanol. Hence, the direct oxidation of glycerol in SOFCs to produce electricity is of interest, due to its wide availability and to its renewable character.

To the best of our knowledge, there is no thermodynamic study on the direct utilization of glycerol in SOFCs. Thus, the purpose of the study reported here is to obtain the equilibrium compositions of the anode gas mixture, carbon deposition boundaries and electromotive forces (EMFs) as a function of fuel utilization and temperature. Moreover, the minimum amounts of H_2O, CO_2 (direct internal reforming case) and air (partial oxidation case) to be added to glycerol in the feedstock to avoid carbon deposition at the open circuit voltage (OCV) are calculated. It is relevant to establish ranges of operating conditions at which carbon formation is thermodynamically unfavorable, because it is known that deposited carbon covers the active anode sites, resulting in rapid, irreversible cell deactivation [12].

There are few theoretical studies dealing with the influence of the degree of oxidation of a fuel on the equilibrium composition of the anode gas mixture. Cimenti and Hill [8] performed a thermodynamic analysis for direct utilization of alcohol fuels (methanol and ethanol) in SOFCs. Since their theoretical analysis provides a general treatment of the equilibrium for SOFCs fueled by oxygenated hydrocarbons, the work of these authors was used as a guide for the present study.

Furthermore, thermodynamic analysis is conducted taking into account the same conditions employed by Lo Faro et al. [9]. In this way, experimental observations reported by these authors, regarding carbon deposition during the operation of an SOFC on glycerol fuel, are explained by the thermodynamic approach developed in the present work.

2. Methodology

2.1. Theoretical background

For a system in which many simultaneous reactions take place, equilibrium calculations are performed through the Gibbs energy minimization method. The total free energy of the system, composed of an ideal gas phase and pure condensed phases, may be expressed as

$$\frac{G}{RT} = \left(\sum_{i=1}^{N} n_i \left[\frac{G_i^0}{RT} + \ln(y_i P) \right] \right)_{gas} + \frac{1}{RT} \left(\sum_{i=1}^{N} n_i G_i^0 \right)_{condensed} \quad (1)$$

The problem consists in finding the different values of n_i which minimize the objective function given by Eq. (1), subject to the constraints of elemental mass balance:

$$\sum_{i=1}^{N} n_i \alpha_{ik} = b_k \quad k = 1 \ldots M \quad (2)$$

Based on previous experimental work [13–15], the following species were considered in the simulations: glycerol, acetaldehyde, ethylene, ethanol, methanol, ethane, propylene, acetone, acrolein formaldehyde, allyl alcohol, propionaldehyde, acetic acid (the ideal gas phase), and C (graphite), as a pure condensed phase. Thus, $M = 3$ (C, H and O). The thermodynamic data necessary for describing the Gibbs energy of the species were obtained from Refs. [16–19]. Besides, $P = 1$ atm throughout this work.

The non-linear programming model comprising the objective function to be minimized and constraints is solved by the Solver function contained in the Microsoft Excel spreadsheet package. A thermodynamic analysis for ethanol steam reforming in a reformer using the Solver tool was done in a previous study [20], and the results obtained were satisfactory. Nevertheless, one should take into account the fact that when the Solver applies the Generalized Reduced Gradient (GRG) algorithm, it seems to violate the non-negativity constraints. In order to overcome this drawback, a change of variables was proposed ($n_i = \exp(n_i')$). Thus, no difficulty is caused by the involvement of logarithmic functions of the objective function and there is no need to add non-negativity constraints. The value of 1×10^{-10} was chosen as a criterion of precision and convergence in the Solver Options dialog box during the optimization process.

When an SOFC is producing a current, there is a net input of oxygen ions (O^{2-}) to the anodic compartment that changes the equilibrium conditions of the system. Thus, moles of oxygen must be added to the elemental mass balance of oxygen (O), as shown in Eq. (3). While b_O corresponds to the moles of oxygen in the system, obtained from the inlet feed mixture at the anode, b_O^{echem} is the extra number of moles of oxygen due to the electrochemical reaction:

$$\sum_{i=1}^{N} n_i \alpha_{iO} = b_O + b_O^{echem} \quad (3)$$

Fuel utilization (U_f) is related to b_O^{echem} as follows:

$$b_O^{echem} = 0.5 z U_f n_{glycerol}^0 \quad (4)$$

where z is the number of electrons produced by the oxidation of 1 glycerol molecule (14 electrons).

The number of moles of oxygen available at the anode, for complete diffusion of the oxygen ions from the cathode to the anode, through the dense electrolyte, can be calculated using Faraday's Law:

$$b_O^{echem}\ (\text{mol cm}^{-2}\,\text{s}^{-1}) = \frac{j}{2F} \quad (5)$$

where j is the current density in A cm^{-2} and F is Faraday's constant. Combining Eqs. (4) and (5), current density can be related to fuel utilization:

$$j = zFU_f n_{glycerol}^0 \quad (6)$$

The reversible electrical potential difference across the electrolyte of an SOFC can be calculated as follows [21]:

$$E = \frac{RT}{2F} \ln \frac{p_{H_2}^{an.} \cdot K_{H_2O} \cdot (p_{O_2}^{cat.})^{0.5}}{p_{H_2O}^{an.}} \quad (7)$$

The value of $p_{O_2}^{cat.}$ is 0.206 atm. K_{H_2O} is the equilibrium constant of the reaction of hydrogen oxidation. It is necessary to stress that Eq. (7) is true in the ideal case of a pure ionic electrolyte, where $t_{ion} = 1$. t_{ion} is the transference number of oxygen ions which is defined as the ratio of ionic conductivity to total conductivity. If the electrolyte shows non-negligible electronic conduction, it is preferable to use the Wagner Equation [22]:

$$E = \frac{RT}{4F} \int_{p_{O_2}^{cat.}}^{p_{O_2}^{an.}} t_{ion} d\ \ln p_{O_2} \quad (8)$$

2.2. Carbon deposition conditions

Carbon activity in the equilibrium system (a_C) can be readily computed, with no need to consider any chemical reaction regarding carbon formation, simply by using the following mathematical relationship [20]:

$$\ln a_C = \left(\frac{-G_C^0}{RT}\right) + \frac{\lambda_C}{RT} \quad (9)$$

After the optimization process is completed, the Lagrange's multiplier related to the elemental mass balance of the element C (λ_C) can be obtained from the sensitivity reports created by the Solver tool. If carbon activity (with reference to the graphite phase) is smaller than unity, carbon formation is thermodynamically impossible. On the other hand, if $a_C = 1$, the system is in a state of equilibrium, and carbon is present along with the gas phase. Finally, when $a_C > 1$, the system is a metastable gas phase and carbon deposition should occur.

As carbon deposition is undesirable, conditions under which carbon starts to disappear are established. At fixed temperature, a given parameter (e.g. fuel utilization, amount of H_2O, CO_2 or air) is varied, and the carbon activity is monitored. The carbon deposition boundary (CDB) is defined as the value of the parameter whose corresponding a_C is approaching the unity. If the value of the operational parameter is greater than that indicated at the CDB, carbon formation in the equilibrium mixture is thermodynamically impossible, because, under these conditions, $a_C < 1$.

The tendency for carbon deposition can also be evaluated through the chemical driving force. At a given temperature, the driving force for carbon deposition with reference to the graphite phase, D_{gra}, can be calculated as follows:

$$D_{gra} = RT \ln a_C \quad (10)$$

Carbon activity values greater than unity can be computed if the graphite phase is excluded both from the total Gibbs free energy of the system and from the constraints of the elemental mass balance of carbon. Therefore, the positive driving force for the nucleation of the graphite phase may be determined.

3. Results and discussion

3.1. Glycerol pyrolysis

Fig. 1(a) and (b) shows the equilibrium composition as a function of temperature for glycerol pyrolysis. As can be seen, the main species present at equilibrium are H_2, CO, CO_2, CH_4, H_2O and C (graphite). Glycerol is completely decomposed over the whole temperature range. Table 1 shows that other species do not exist in the equilibrium mixture from a practical viewpoint. As shown in Fig. 1(a), carbon deposition is predicted over the entire temperature range. Under the operational conditions of IT-SOFCs, i.e. 773–1073 K, the concentration of carbon decreases from 26.3 to 3.34 mol%. Fig. 1(b) shows that the production of H_2 and CO is favored by a temperature increase whereas the concentration of CH_4 and H_2O decreases as temperature increases. This behavior may be attributed to the endothermic steam reforming of methane ($CH_4 + H_2O = CO + 3H_2$). At 1073 K, the anode gas phase is composed of ~55 vol.% of H_2 and ~39 vol.% of CO. Besides, the concentration of CO_2 in the anode gas phase decreases as temperature increases. Such a trend may be explained by the endothermic dry reforming of CH_4 ($CH_4 + CO_2 = 2CO + 2H_2$) [23]. With increase in temperature, the H_2 to CO (H_2/CO) ratio approaches 1.3 (1.333 ...). At 1223 K, the H_2/CO ratio is ~1.332, $n_{CO} = 2.932$ and $n_{H_2} = 3.907$. This indicates that the direct decomposition of glycerol to H_2 and CO ($C_3H_8O_3 = 3CO + 4H_2$) is the predominant reaction at high temperatures. At elevated temperatures, methanol was also found to decompose mainly into H_2 and CO ($CH_3OH = CO + 2H_2$) [8]. Such a similarity may be ascribed to the fact that both fuels are oxygenated hydrocarbons having a C:O ratio equal to 1:1 [24].

As seen in Fig. 1(a), the amount of carbon decreases as temperature increases. This is in accordance with the temperature dependence of the driving force for the nucleation of graphite (Fig. 2). $D_{gra} > 0$ and $a_C > 1$ over the entire temperature range, indicating the thermodynamic feasibility of carbon formation.

Table 1
Gas-phase concentrations (vol.%) at 773, 923 and 1073 K, computed for glycerol pyrolysis.

	Temperature (K)		
	773	923	1073
Glycerol	1.5×10^{-27}	5.5×10^{-27}	5.2×10^{-28}
Acetaldehyde	2.1×10^{-9}	8.2×10^{-9}	5.9×10^{-9}
Ethylene	1.2×10^{-6}	1.1×10^{-5}	2.7×10^{-5}
Ethanol	1.4×10^{-10}	1.7×10^{-10}	3.8×10^{-11}
Methanol	2.4×10^{-7}	3.9×10^{-7}	1.5×10^{-7}
Ethane	1.7×10^{-4}	6.9×10^{-5}	1.4×10^{-5}
Propylene	8.6×10^{-10}	5.3×10^{-9}	7.8×10^{-9}
Acetone	1.6×10^{-11}	2.6×10^{-11}	7.4×10^{-12}
Acrolein	2.7×10^{-10}	1.2×10^{-8}	5.1×10^{-8}
Formaldehyde	1.6×10^{-6}	1.4×10^{-5}	2.5×10^{-5}
Allyl alcohol	1.4×10^{-16}	2.1×10^{-15}	2.8×10^{-15}
Propionaldehyde	1.2×10^{-12}	3.8×10^{-12}	1.8×10^{-12}
Acetic acid	1.2×10^{-8}	6.3×10^{-9}	5.5×10^{-10}

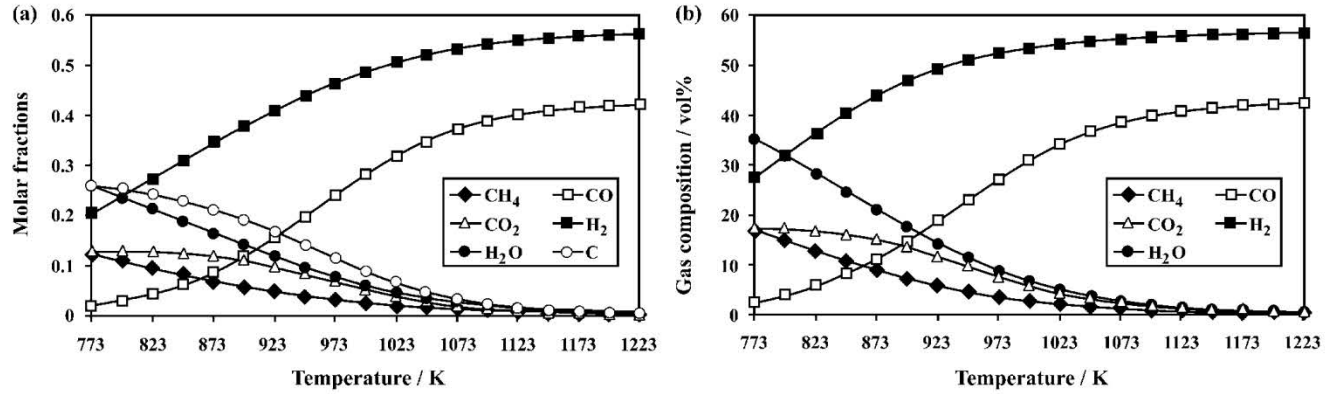

Fig. 1. (a) Molar fractions of the species at the anode as a function of temperature and (b) gas-phase concentrations as a function of temperature.

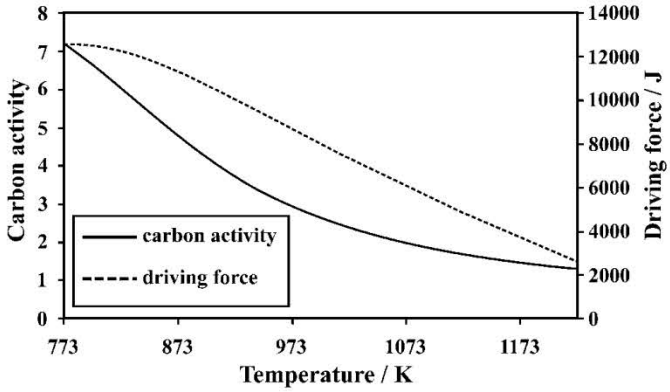

Fig. 2. Carbon activity and driving force for the nucleation of the graphite phase as a function of temperature.

3.2. Effect of fuel utilization and current density on carbon deposition

Fig. 3(a)–(d) shows the equilibrium composition of the main species (H_2, CO, CO_2, H_2O, CH_4 and C (graphite)) and EMFs as a function of fuel utilization, at 773, 873, 973 and 1073 K, respectively, for an SOFC operating on pure glycerol. For instance, the equilibrium compositions and EMFs are also shown as a function of current density, assuming that the anode is fueled with a practical flow rate corresponding to the fuel stoichiometry required by the Faradaic process when the SOFC operates at 1 A cm^{-2} (thus, 7.4×10^{-7} mol s^{-1} of pure glycerol). The amount of carbon is maximal at the OCV. Carbon concentration decreases with increased load up to a fuel utilization beyond which carbon deposition is no longer thermodynamically favored (CDB). Up to the CDB, carbon activity is equal to unity. After the CDB, the driving force for carbon deposition becomes increasingly negative. It may be observed that the minimum fuel utilization in an SOFC fed on pure glycerol to operate in the carbon free region decreases as temperature increases. At high temperatures, the values computed for fuel utilization at the CDB are close to those reported for SOFCs operating on pure methanol [8]. For instance, at 1073 K, the U_f values at the CDB are 3.6 and 2.1% for glycerol and methanol, respectively. The current density at which carbon is reduced to zero (CDB) is known as threshold current density [25,26]. For the conditions examined here, the threshold current densities are 564, 392, 159 and 36 mA cm^{-2}, at 773, 873, 973 and 1073 K, respectively. The molar fraction of CO increases within the carbon deposition region, while it decreases after the threshold current density. Up to the CDB, H_2 exists at a constant concentration and there is little increase in H_2O. After the CDB, H_2 decreases, and the concentration of H_2O increases significantly. Carbon dioxide concentration increases with fuel utilization. At higher temperatures, however, its production increases abruptly after the threshold current density (Fig. 3(c)–(d)). The amount of methane is almost zero for the entire fuel utilization range at 1073 K. At lower temperatures, methane concentration is constant up to the CDB. After the CDB, its concentration decreases rapidly as U_f increases. The OCVs are 1.029, 1.032, 1.048 and 1.080 V at 773, 873, 973 and 1073 K, respectively. Besides, EMFs decrease with fuel utilization. Fuel components might be, in principle, fully utilized in an SOFC. However, the maximum value of U_f examined here is 80% to obtain a reasonable value of EMF, e.g., 0.88 V at 1073 K. Besides, in practice, the acceptable level of partial pressure of residual hydrogen is around 0.1 atm (~80%U_f) [27]. Lower values may result in high concentration overpotentials. The trends seen in Fig. 3(a)–(d), for the species and EMFs, are very similar to those observed in previous work [8,25,26].

It is worthwhile pointing out that all these predictions depend on favorable kinetics, since carbon is not easily removed once formed [28]. Moreover, the carbon deposition boundary is determined assuming that the stable configuration of the system may be reached, with no kinetic impediments. Nevertheless, the equilibrium situation may not always occur. One deviation from equilibrium, for instance, concerns the incomplete conversion of glycerol and the formation of intermediate species. Therefore, there may be more carbon than predicted.

3.3. Direct internal reforming and partial oxidation of glycerol

As shown in Fig. 1(a), at the OCV (U_f = 0%), carbon deposition is predicted over the entire temperature range. Steam, CO_2 or air can be added to glycerol in the feedstock to avoid carbon deposition at the OCV. Fig. 4(a)–(c) shows the minimum amounts of H_2O, CO_2 (direct internal reforming case) and air (partial oxidation case), respectively, needed to prevent carbon deposition as a function of temperature.

The CDB shifts towards lower H_2O/glycerol ratio as temperature increases, in accordance with the results previously shown for glycerol pyrolysis (Fig. 1(a) and 2). Wang et al. [29] computed the CDB for glycerol steam reforming, in the temperature range 550–1000 K. The CDB in Fig. 4(a) shows a satisfactory agreement with the results reported by these authors.

As shown in Fig. 4(b), for temperatures lower than 973 K, high inlet CO_2/glycerol ratios are required to suppress carbon formation. Accordingly, Cimenti and Hill [8] found that large amounts of CO_2 should be added to ethanol or methanol to prevent carbon deposition at lower temperatures. Besides, as in the case of methanol, the CO_2/glycerol ratio approaches zero as temperature increases. By comparing Fig. 4(a) and (b), one can verify that steam is a more effective choice than CO_2 in preventing carbon deposition at low

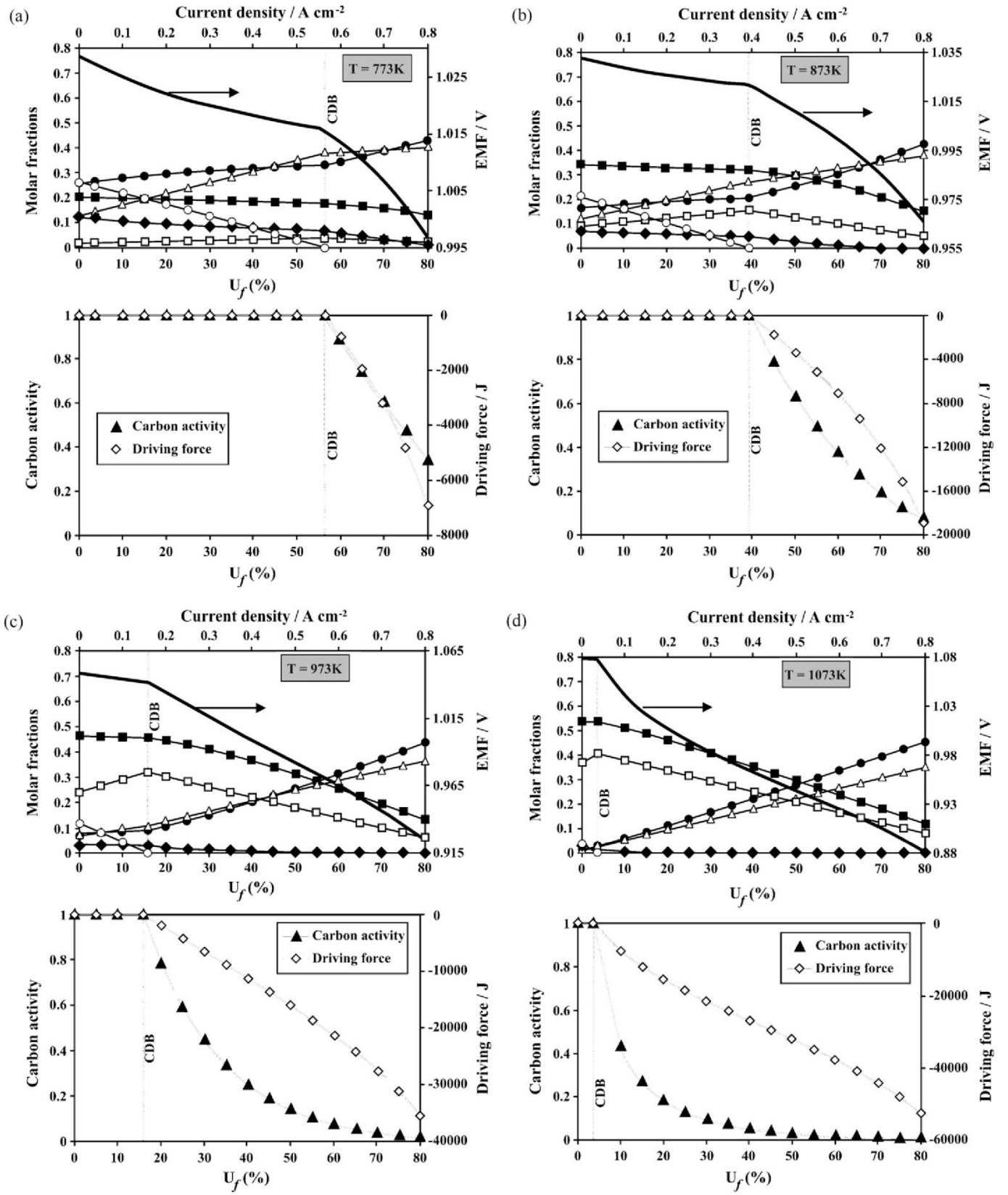

Fig. 3. Calculated equilibrium diagram of carbon (graphite) and the main species in the gas phase and electromotive force as a function of fuel utilization and current density for SOFC anode operating on pure glycerol at 7.4×10^{-7} mol s^{-1}. Carbon activity and driving force as a function of fuel utilization: (a) 773 K, (b) 873 K, (c) 973 K, and (d) 1073 K. The species at equilibrium are: (♦) CH_4, (△) CO_2, (□) CO, (●) H_2O, (○) C (graphite), and (■) H_2.

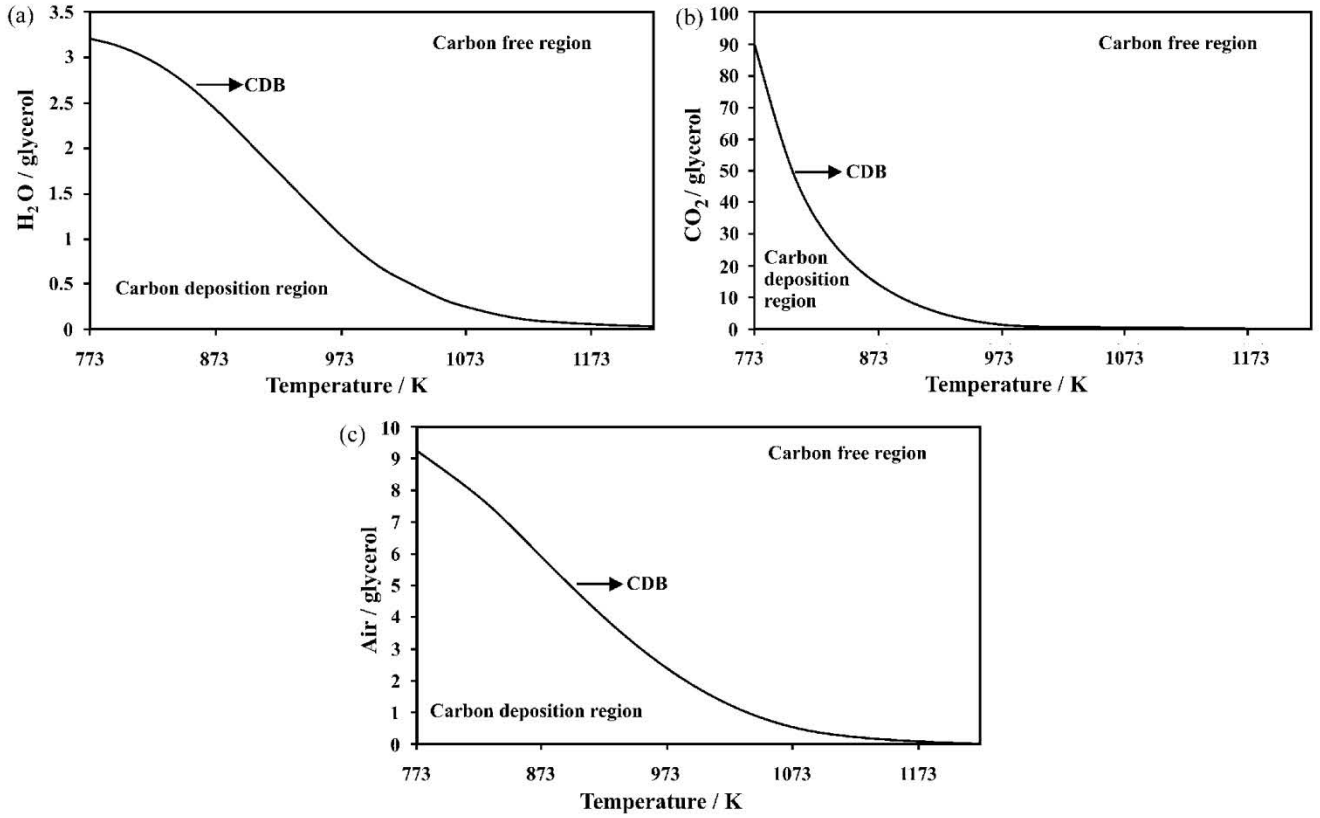

Fig. 4. Carbon deposition boundary (CDB) as a function of temperature for glycerol (a) steam reforming, (b) dry reforming and (c) partial oxidation with air.

temperatures. At higher temperatures, however, CO_2 and steam have a comparable effect.

When air is added (Fig. 4(c)), a similar trend is seen to that of the addition of steam. Steam is a more effective choice, particularly at lower temperatures, due to the higher air/glycerol ratio required compared with the H_2O/glycerol ratio. This is in perfect agreement with the findings of Assabumrungrat et al. [30].

By analyzing the equilibrium compositions calculated at the CDB for direct internal reforming (steam and dry reforming) and partial oxidation with air, it is seen that, in all cases, the H_2/CO ratio approaches 1.3 as temperature increases, indicating that glycerol forms almost exclusively H_2 and CO. Consistently, the number of moles of H_2 approaches 4 and the moles of methane tend to zero.

In practical operation, CO_2 is unlikely to be added to the system for suppressing carbon deposition. Steam and air are more practical additive choices. In principle, the integration of the exothermic heat from partial oxidation with air and the endothermic reforming reactions might make the use of air attractive [30]. Nevertheless, an operating SOFC is strongly exothermic, and the heat released in a fuel cell can provide the heat for internal steam reforming which, under typical operational conditions, is about half the total heat produced [31]. Partial oxidation with air to prevent carbon deposition represents a waste of fuel and an overall inefficient process, because part of the fuel energy is lost due to the exothermic character of this reaction, which lowers the efficiency of the system. However, partial oxidation might be suitable for small-scale portable applications where system simplicity and rapid start-up rather than system efficiency are crucial factors [7]. Although the direct internal reforming approach is an efficient process, simplifying the overall system design, one should take into account the fact that the endothermic reforming reaction on the Ni cermet anode catalyst is so rapid that it causes a strong cooling effect at the fuel entry, leading to inefficient electrochemical kinetics. In this way, partial external steam reforming is the preferred mode of operation, in which waste heat obtained by combusting the anode exit stream in an SOFC operating at ~80% fuel utilization is used.

3.3.1. *Effect of steam content*

Fig. 5 shows the equilibrium diagram with the main species, at 973 K, for the molar flow rate of pure glycerol equal to 7.4×10^{-7} mol s^{-1} and the inlet H_2O/glycerol ratio equal to 2. There is no carbon deposition. This was expected, because this ratio is higher than that indicated at the CDB in Fig. 4(a). The molar fractions of H_2 and CO decrease throughout the range of fuel utilization (or current density) due to possible oxidation to water and carbon dioxide, respectively, which increase continuously as fuel utiliza-

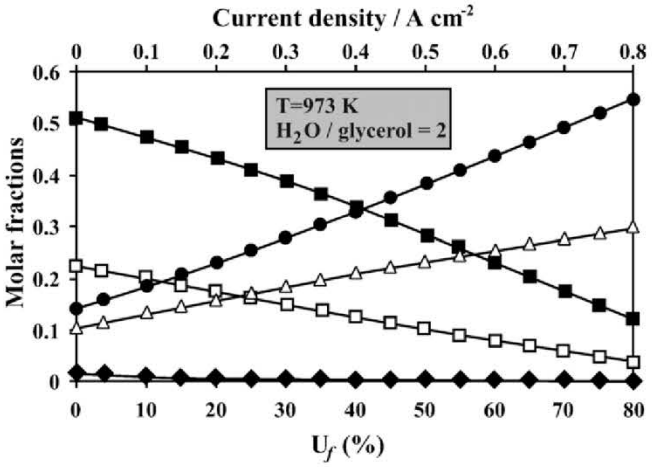

Fig. 5. Equilibrium diagram of the main species as a function of fuel utilization and current density for H_2O/glycerol = 2, at T = 973 K. The species at equilibrium are: (♦) CH_4, (△) CO_2, (□) CO, (●) H_2O and (■) H_2.

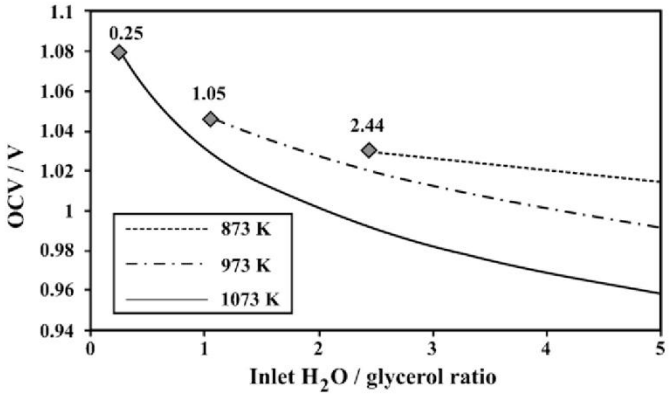

Fig. 6. Open circuit voltage (OCV) as a function of the inlet H_2O/glycerol ratio, at T = 873, 973 and 1073 K. The markers indicate the inlet H_2O/glycerol ratio at the CDB computed for glycerol steam reforming.

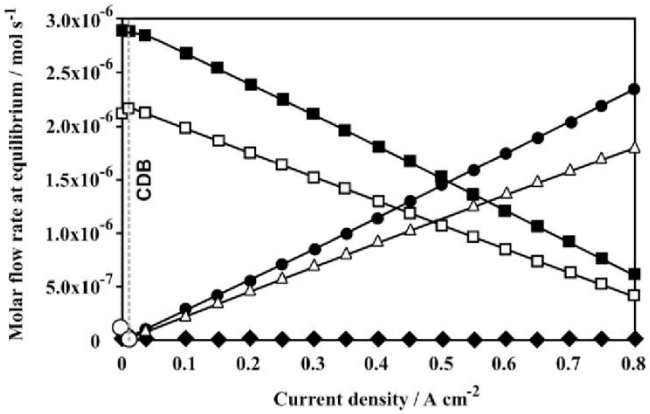

Fig. 7. Equilibrium diagram of carbon (graphite) and the main species in the gas phase as a function of current density for SOFC anode operating on an inlet stream of 7.4×10^{-7} mol s^{-1} of pure glycerol in 20 cm^3 min^{-1} N_2 (carrier gas), at 800 °C. The species at equilibrium are: (♦) CH_4, (△) CO_2, (□) CO, (●) H_2O, (■) H_2 and (○) C (graphite).

tion increases. At 973 K, the molar fraction of methane is almost zero. Note that the trends are similar to those seen in Fig. 3(c) after the threshold current density.

The effect of steam content on the OCV is shown in Fig. 6. The OCV decreases with the inlet H_2O/glycerol ratio. Therefore, if steam is added to the feed stream, the maximum OCV is reached at the carbon deposition boundary.

3.4. Theoretical determination of carbon deposition conditions and comparison with experimental reports

Lo Faro et al. [9] experimentally investigated the electrochemical oxidation of glycerol at 800 °C. The anode was fed on glycerol with a flow rate as close as possible to the fuel stoichiometry required by the Faradaic process when the SOFC operates at 1 A cm^{-2} (7.4×10^{-7} mol s^{-1} of pure glycerol). N_2 carrier gas (20 cm^3 min^{-1}) was used in the glycerol fuel stream. The anode electrocatalyst was based on a Ni-modified $La_{0.6}Sr_{0.4}Fe_{0.8}Co_{0.2}O_3$ (LSFCO) perovskite and gadolinia-doped ceria electrolyte (CGO). The maximum current density is ~0.8 A cm^{-2} based on their polarization curves. These authors stated that no carbon deposits were observed for anodes which had operated in both direct oxidation and internal reforming modes. However, deposited carbon was observed in the alumina tube at the inlet of the stream. Their experimental observations regarding carbon deposition may be explained by thermodynamic analysis. For this purpose, calculations were conducted reflecting the experimental operating conditions adopted by these authors. In this way, two different approaches are considered.

3.4.1. Equilibrium diagram of main species as a function of current density

The molar flow rate of species as a function of current density is shown in Fig. 7. At the OCV (j = 0 A cm^{-2}), carbon deposition is thermodynamically predicted, which is consistent with the observation of the deposited carbon in the alumina tube at the inlet of the stream. As can be seen from this diagram, a very low threshold current density (10.5 mA cm^{-2}) is required to suppress carbon formation under dry conditions, at 800 °C. It may be assumed that the carbon initially formed at the OCV was easily removed, since the threshold current density is much lower than the maximum current density. Thus, even when no steam is added to the feed stream, carbon formation is not possible from a thermodynamic viewpoint under the conditions examined. Indeed, very low values of threshold current density are computed for glycerol, especially at high temperatures. This may be ascribed to its oxygenated character. It is worthwhile pointing out that if methane, for example, were employed under the same conditions, the threshold current density would be much greater (253 mA cm^{-2}). Besides, the addition of the inert gas shifted the threshold current density from 36 to 10.5 mA cm^{-2}. The effect of an inert carrier gas is similar to that obtained with a decrease in total pressure of the system [32]. Thus, if carbon deposition occurs by means of the Boudouard reaction ($C + CO_2 = 2CO$), it is expected that N_2 carrier gas shifts this reaction towards CO, preventing carbon formation, which results in a lower threshold current density.

Lo Faro et al. [9] did not characterize their electrochemical system by impedance spectroscopy technique. Our validation is based on their polarization curve and reports from optical microscopy and CHNS-O analyses. Further experimental work would be very helpful to understand the electrochemical reactions involved in the glycerol oxidation in SOFCs as well as the conditions of carbon deposition.

3.4.2. The effect of mixed electronic–ionic conduction of the electrolyte

The OCV calculated using Eq. (7), considering the equilibrium composition shown in the diagram of Fig. 7 for j = 0 A cm^{-2}, is 1.14 V. Nevertheless, under dry conditions, the experimental value of the OCV is ~0.78 V. This low value can be ascribed to mixed electronic–ionic conduction of the CGO electrolyte, which does not allow the cell to reach high OCVs associated with a very low oxygen partial pressure at the anode [33]. Some mixed conducted electrolytes such as doped CeO_2 are less stable under reduced anodic atmosphere [22]. In fact, the partial pressure of oxygen computed at the OCV was 7.81×10^{-23} atm, corresponding to a strongly reducing atmosphere. Therefore, electronic conduction is expected to appear due to electrons generated by the reduction reactions ($O_O^x = (1/2)O_2 + V_O^{\bullet\bullet} + 2e'$). The electronic defect (e') is due to the Ce reduction ($Ce^{4+} \rightarrow Ce^{3+}$) [33]. For mixed conducted electrolytes, Zha et al. [22] show that the EMF (E) can be calculated as follows:

$$E = \frac{RT}{F} \ln \frac{\left(p^*_{O_2}\right)^{1/4} + \left(p^{cat.}_{O_2}\right)^{1/4}}{\left(p^*_{O_2}\right)^{1/4} + \left(p^{an.}_{O_2}\right)^{1/4}} \quad (11)$$

$p^*_{O_2}$ is an intrinsic property of the electrolyte. The temperature dependence of $p^*_{O_2}$ for the CGO electrolyte was obtained from Kudo and Obayashi [34]. At 1073 K, $p^*_{O_2} = 9.08 \times 10^{-17}$ atm. Thus, the OCV computed by Eq. (11) is 0.81 V, which is close to the experimental value. As a consequence, the thermodynamic possibility of carbon deposition in an atmosphere in which $p_{O_2} = p^*_{O_2}$ should

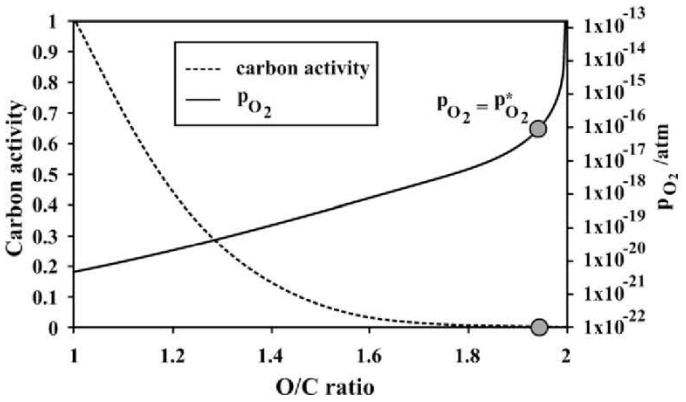

Fig. 8. Carbon activity and partial pressure of O_2 as a function of the O/C ratio, computed for the C–O system at 1073 K.

be analyzed. In this way, the C–O system was studied, and the following species were considered in the Gibbs energy minimization procedure: CO, CO_2, O_2 and C (graphite). Fig. 8 shows that carbon activity decreases as p_{O_2} increases. When p_{O_2} is increased towards $p^*_{O_2}$, carbon activity is only 5×10^{-4}, meaning that carbon deposition is greatly inhibited from a thermodynamic viewpoint. At $p^*_{O_2}$ graphite is oxidized mainly to CO_2. In this way, it can be seen that, at high temperatures, the large availability of oxygen at the anode/electrolyte interface, due to mixed electronic–ionic conduction of the CGO electrolyte, is able to completely oxidize the deposited carbon even at the OCV from a thermodynamic viewpoint.

4. Conclusions

A thermodynamic analysis was performed for the direct utilization of glycerol in SOFCs. The following conclusions can be drawn from the results of the present study:

- H_2 and CO are the main products of glycerol pyrolysis. At high temperatures, the reaction $C_3H_8O_3 = 3CO + 4H_2$ dominates the decomposition equilibrium. Carbon deposition is predicted in the temperature range 773–1223 K. Under the operational conditions of IT-SOFCs (773–1073 K), the concentration of carbon decreases from 26.3 to 3.34 mol%.
- When an SOFC is producing current, carbon deposition becomes thermodynamically less favorable. If the SOFC operates on pure glycerol, at a practical flow rate corresponding to the fuel stoichiometry required by the Faradaic process when the SOFC operates at 1 A cm^{-2}, the threshold current densities are 564, 392, 159 and 36 mA cm^{-2}, at 773, 873, 973 and 1073 K, respectively. At 1073 K, the addition of inert carrier gas to the anode feed stream shifts the threshold current density towards a lower value, preventing carbon formation.
- The minimum amounts of steam, CO_2 and air to be added to glycerol in the feedstock to avoid carbon at the OCV were determined. Steam is a more effective choice than CO_2 mainly at lower temperatures, since very high inlet CO_2/glycerol ratios are required at $T < 973$ K. Air was also found to be less attractive than steam, due to the higher air/glycerol ratio required compared with the H_2O/glycerol ratio. The effect of steam, CO_2 and air on carbon suppression was comparable at high temperatures.
- With respect to the pyrolysis and the direct utilization in SOFCs, glycerol behaves similarly to methanol at high temperatures, which can be ascribed to the fact that both fuels have a C:O ratio equal to 1:1.
- Regarding carbon deposition in an SOFC operating on glycerol, experimental observations may be explained by the theoretical analysis developed in this paper. The combined effect of the oxygenated character of glycerol, which results in very low values of threshold current density at higher temperatures, and the large availability of oxygen at the anode/electrolyte interface, promoted both by the electrochemical reaction during the operation of the SOFC and mixed electronic–ionic conduction of the CGO electrolyte, would seem to prevent irreversible carbon deposition at the anode.
- Although SOFC may not operate at equilibrium, thermodynamic analysis of the decomposition gas compositions and carbon deposition provides a useful guideline for further experimental research. Nevertheless, electrochemical models that consider all overpotentials involved in SOFC operation must be developed. Besides, energy analyses must be performed in order to quantify the optimal operating parameters.

Acknowledgments

The authors thank CNPq and CAPES for financial support.

References

[1] Z. Shao, S.M. Haile, J. Ahn, P.D. Ronney, Z. Zhan, S.A. Barnett, Nature 435 (2005) 795–798.
[2] S. McIntosh, R.J. Gorte, Chem. Rev. 104 (2004) 4845–4866.
[3] S. Park, J.M. Vohs, R.J. Gorte, Nature 404 (2000) 265–267.
[4] P.K. Cheekatamarla, C.M. Finnerty, C.R. Robinson, S.M. Andrews, J.A. Brodie, Y. Lu, P.G. DeWald, J. Power Sources 193 (2009) 797–803.
[5] S. Farhad, F. Hamdullahpur, J. Power Sources 195 (2010) 3084–3090.
[6] M. Cimenti, J.M. Hill, J. Power Sources 195 (2010) 54–61.
[7] M. Cimenti, J.M. Hill, Energies 2 (2009) 377–410.
[8] M. Cimenti, J.M. Hill, J. Power Sources 186 (2009) 377–384.
[9] M. Lo Faro, D. La Rosa, M. Minutoli, G. Monforte, V. Antonucci, A.S. Aricò, ECS Trans. 25 (2) (2009) 2241–2248.
[10] S. Adhikari, S. Fernando, S.R. Gwaltney, S.D. Filip To, R. Mark Bricka, P.H. Steele, A. Haryanto, Int. J. Hydrogen Energy 32 (2007) 2875–2880.
[11] R.L. Arechederra, B.L. Treu, S.D. Minteer, J. Power Sources 173 (2007) 156–161.
[12] B. Huang, X.F. Ye, S.R. Wang, H.W. Nie, J. Shi, Q. Hu, J.Q. Qian, X.F. Sun, T.L. Wen, J. Power Sources 162 (2006) 1172–1181.
[13] T. Valliyappan, N.N. Bakhshi, A.K. Dalai, Bioresour. Technol. 99 (2008) 4476–4483.
[14] W. Buhler, E. Dinjus, H.J. Ederer, A. Kruse, C. Mas, J. Supercrit. Fluids 22 (2002) 37–53.
[15] X. Xu, Y. Matsumura, J. Stenberg, M.J. Antal Jr., Ind. Eng. Chem. Res. 35 (1996) 2522–2530.
[16] C.L. Yaws, Chemical Properties Handbook, McGraw-Hill, New York, 1999.
[17] O. Knacke, O. Kubaschewski, K. Hesselmann, Thermochemical Properties of Inorganic Substances, second ed., Springer-Verlag, Berlin, 1991.
[18] S.I. Sandler, Chemical and Engineering Thermodynamics, third ed., Wiley, New York, 1999.
[19] R.C. Reid, J.M. Prausnitz, B.E. Poling, The Properties of Gases and Liquids, fourth ed., MCGraw-Hill, New York, 1987.
[20] A. Lima da Silva, C.F. Malfatti, I.L. Müller, Int. J. Hydrogen Energy 34 (2009) 4321–4330.
[21] A. Demin, P. Tsiakaras, Int. J. Hydrogen Energy 26 (2001) 1103–1108.
[22] S.W. Zha, C.R. Xia, G.Y. Meng, J. Appl. Electrochem. 31 (2001) 93–98.
[23] A.N. Fatsikostas, D.I. Kondarides, X.E. Verykios, Catal. Today 75 (2002) 145–155.
[24] R.R. Davda, J.W. Shabaker, G.W. Huber, R.D. Cortright, J.A. Dumesic, Appl. Catal. B 56 (2005) 171–186.
[25] J. Mermelstein, M. Millan, N. Brandon, J. Power Sources 195 (2010) 1657–1666.
[26] D. Singh, E. Hernández-Pacheco, P.N. Hutton, N. Patel, M.D. Mann, J. Power Sources 142 (2005) 194–199.
[27] A.K. Demin, P.E. Tsiakaras, V.A. Sobyanin, S.Y. Hramova, Solid State Ionics 152–153 (2002) 555–560.
[28] J.-H. Koh, Y.-S. Yoo, J.-W. Park, H.C. Lim, Solid State Ionics 149 (2002) 157–166.
[29] X. Wang, S. Li, H. Wang, B. Liu, X. Ma, Energy Fuels 22 (2008) 4285–4291.
[30] S. Assabumrungrat, N. Laosiripojana, P. Piroonlerkgul, J. Power Sources 159 (2006) 1274–1282.
[31] P. Aguiar, D. Chadwick, L. Kershenbaum, Chem. Eng. Sci. 57 (2002) 1665–1677.
[32] L. Hernández, V. Kafarov, J. Power Sources 192 (2009) 195–199.
[33] J.H. Joo, G.M. Choi, Solid State Ionics 178 (2007) 1602–1607.
[34] T. Kudo, H. Obayashi, J. Electrochem. Soc. 123 (1976) 415–419.

4.1.4. Thermodynamic study on glycerol-fuelled intermediate-temperature solid oxide fuel cells (IT-SOFCs) with different electrolytes

(Estudo termodinâmico aplicado a células a combustível de temperatura intermediária do tipo óxido sólido, com diferentes eletrólitos, abastecidas com glicerol)

Principais Resultados:

- Avaliação do efeito do tipo de eletrólito na eficiência e na tendência à deposição de carbono no ânodo;
- Em comparação com as células SOFC condutoras de íons O^{2-}, as células SOFC com eletrólito condutor de íons H^{+} exibem maior eficiência e maior tendência à deposição de carbono no ânodo;
- A diminuição da temperatura de operação aumenta a eficiência, mas aumenta também a tendência à deposição de carbono;
- A eficiência de uma SOFC operando com glicerol é similar a de uma SOFC operando com etanol;

INTERNATIONAL JOURNAL OF HYDROGEN ENERGY 35 (2010) 5580–5593

Available at www.sciencedirect.com

ScienceDirect

journal homepage: www.elsevier.com/locate/he

Thermodynamic study on glycerol-fuelled intermediate-temperature solid oxide fuel cells (IT-SOFCs) with different electrolytes

Aline Lima da Silva, Iduvirges Lourdes Müller*

Program of Postgraduate Studies in Mining, Metals and Materials Engineering (PPGEM), Universidade Federal do Rio Grande do Sul – UFRGS, Campus do Vale, Setor 4, Prédio 75, Sala 226, Av. Bento Gonçalves 9500, CEP 91501-970 Porto Alegre, RS, Brazil

ARTICLE INFO

Article history:
Received 19 October 2009
Received in revised form
3 February 2010
Accepted 1 March 2010
Available online 26 March 2010

Keywords:
Solid oxide fuel cells
Direct internal reforming
Glycerol
Electrochemical thermodynamics
Carbon deposition
Gibbs energy minimization method

ABSTRACT

In this paper, a thermodynamic analysis was carried out to provide useful information about the operation of intermediate-temperature Solid Oxide Fuel Cells (IT-SOFCs) with direct internal reforming (DIR) fuelled by glycerol. A methodology, based on the principle of minimizing the Gibbs energy of a given system, using spreadsheets and the Microsoft Excel's Solver function, was described for DIR operation of the SOFC with oxygen ion conducting electrolyte (SOFC-O^{2-}) and proton conducting electrolyte (SOFC-H^{+}). The effect of temperature, fuel utilization and type of electrolyte on the equilibrium composition of the anode gas mixture as well as on the boundary of carbon formation has been investigated in the temperature range of 773–1073 K. Based on the results of this thermodynamic study, glycerol can be considered an alternative fuel with suitable characteristics for electricity generation in IT-SOFCs. Operating at carbon-free conditions, between 773 and 1073 K, with a fuel utilization of 99.99% in the anode channel outlet, glycerol-fuelled IT-SOFCs systems attain high theoretical efficiencies in the range of 80.7–89.9% (SOFC-O^{2-} case) and 90.3–96.7% (SOFC-H^{+} case). Regarding the maximum values of the average electromotive force (EMF) and efficiency, it was verified that glycerol exhibits very similar potential for power generation with ethanol. Although glycerol fed SOFC-H^{+} is superior to SOFC-O^{2-} in terms of maximum theoretical efficiency, it should be taken into account that the SOFC-H^{+} shows a greater tendency for carbon deposition than does the SOFC-O^{2-} during the operation. Besides, it was found that decreasing temperature increases the efficiency but also favors carbon formation, for both SOFC-O^{2-} and SOFC-H^{+}. When the system runs at 70% of its maximum power and the partial pressure of residual hydrogen in the anode outlet is kept equal to 0.1 atm, the highest efficiency (67%) is achieved by operating an SOFC-H^{+} at 823 K.

© 2010 Professor T. Nejat Veziroglu. Published by Elsevier Ltd. All rights reserved.

1. Introduction

Solid oxide fuel cells (SOFCs) are regarded as a promising source for clean and efficient electricity generation [1]. Two types of solid electrolytes can be employed in SOFC operation: namely, oxygen ion and proton conducting electrolytes. Conventionally, an SOFC employs oxygen ion conducting ceramics as its electrolyte (SOFC-O^{2-}). In order to achieve good ionic conductivity, high operating temperature (e.g., 1273 K) is required for conventional SOFCs-O^{2-} based on

* *Corresponding author*. Tel.: +55 51 3308 9404.
E-mail address: adasilva26@gmail.com (A. Lima da Silva).
0360-3199/$ – see front matter © 2010 Professor T. Nejat Veziroglu. Published by Elsevier Ltd. All rights reserved.
doi:10.1016/j.ijhydene.2010.03.003

Nomenclature

G	total Gibbs energy of the system
G_i^0	Gibbs energy of species i at its standard state
n_i	number of moles of species i
n_i^0	initial number of moles of species i
n_i'	decision variable during the optimization process, after the change of variables
n_T	total number of moles at anode side
$e^{n_i'}$	number of moles of species i, after the change of variables
y_i	mole fraction of species i
R	gas constant
T	temperature of the system
P	total pressure of the system
a_i	activity of species i
M, N	total number of components and species, respectively
p_i	partial pressure of species i
λ_C	Lagrange's multiplier related to the elemental mass balance of carbon
WGR	inlet water to glycerol ratio
α_{ik}	number of atoms of kth element present in each molecule of species i
b_k	total number of atomic masses of kth element in the system
b_O^{echem}	additional moles of oxygen (O) in the system, due to the electrochemical reaction
b_H^{echem}	moles of hydrogen (H) consumed by the electrochemical reaction
x	relative channel length
U_f	operating fuel utilization, %
U_f^L	fuel utilization at the anode channel outlet, %
$p_{H_2}^L$	partial pressure of H_2 at the anode channel outlet
U_O	oxygen utilization
F	Faraday constant, 96,485.34 C mol^{-1}
W	electrical work
q	electrical charge
E	electromotive force of the cell (V) for reversible conditions
$\overline{E}U_f^L$	average electromotive force at a given value of fuel utilization at the anode channel outlet, for reversible conditions
η_{max}	maximum theoretical efficiency of the SOFC system
$-\Delta H^0$	lower heating value (LHV) of glycerol
K_{H_2O}	equilibrium constant of hydrogen oxidation
ρ_r	relative power

Superscripts

an	anode
cat	cathode

yttria stabilized zirconia (YSZ). However, at present, a lot of research efforts have been made to operate SOFCs at intermediate temperatures (773–1073 K) [2,3]. In fact, reduction of operation temperature is very important in SOFC commercialization in the aspect of cost reduction and long-term durability [4]. For this reason, alternative electrolytes for SOFCs-O^{2-} with higher oxygen ion conductivity are being investigated [5]. Among them, scandia stabilized zirconia (ScSZ) [4,6] and dysprosia stabilized zirconia (DySZ) [7] are considered promising candidates for use in intermediate-temperature SOFCs (IT-SOFCs). Besides, electrode-supported SOFCs have been developed in an attempt to minimize ohmic losses under lower temperature operation. In these cells, one of the two electrodes is the thickest component and supports mechanically the structure, while the electrolyte is required to have high ionic conductivity and/or small thickness [8]. Additionally, it has been reported that some proton conducting ceramics show good ionic conductivity at intermediate temperatures and are, thus, suitable candidates for use in IT-SOFCs as well [9]. Hence, there is an increasing interest in SOFCs employing proton conducting electrolytes (SOFC-H^+). Nevertheless, developing new proton conducting materials with high protonic conductivity as well as chemical stability under CO_2 and H_2O atmospheres over the range of IT-SOFCs operating conditions is a practical challenge. Recently, it has been shown that $BaZr_{0.4}Ce_{0.4}Y_{0.2}O_{3-\delta}$ is a potential electrolyte material for SOFC-H^+ due to the favorable chemical stability against CO_2 and relative high power density attained by employing this electrolyte in a fuel cell [10].

The fuel, hydrogen gas, can be produced by several different routes; a promising one being the steam reforming of H_2-containing fuels. The steam reforming reactions can be performed either in an external reformer or directly on the anode of an SOFC. The latter mode of operation is known as direct internal reforming (DIR). According to DIR operation, a hydrogen-containing fuel is reformed in the anode compartment of a fuel cell and part of hydrogen produced from the steam reforming process is electrochemically used to produce H_2O, electricity and heat. With an SOFC-O^{2-}, steam (due to electrochemical reaction) is produced at the anode side, whereas it is formed at the cathode side in the case of an SOFC-H^+. Assabumrungrat et al. [11] stated that the great benefit of DIR operation is the coupling of the endothermic reforming reaction and the exothermic electrochemical reaction in a single unit. So, DIR operation is expected to improve the system performance and reduce its size.

Among the various types of H_2-containing fuel, glycerol ($C_3H_8O_3$), which is byproduct of biodiesel production, has been considered an excellent candidate for hydrogen production [12]. With increased production of biodiesel, a glut of glycerol is expected in the world market. Therefore, finding alternative uses for glycerol is important [13]. According to Haas et al. [14], the utilization of glycerol to produce hydrogen gas could potentially reduce the production costs of biodiesel. In addition, glycerol is a green chemical (non-toxic, non-volatile and non-flammable) which makes it ideal for a wide variety of power use [15]. It has been shown, in experimental works [16–21], that glycerol can be efficiently converted into hydrogen by means of its catalytic reaction with steam. Despite

the fact that steam reforming of glycerol may become an important industrial process for hydrogen production, there are few studies published up to now dealing with thermodynamic analysis of glycerol steam reforming in a reformer [12,13,22,23]. Furthermore, to the best of our knowledge, there is no thermodynamic study on SOFCs operating with direct internal reforming (DIR) fuelled by glycerol.

In the present paper, a detailed thermodynamic analysis is carried out, in the temperature range of 773–1073 K, to provide useful information for the operation of IT-SOFCs with direct internal reforming fuelled by glycerol. The effect of temperature and hydrogen consumption by the electrochemical reaction on the equilibrium composition of the anode gas mixture as well as on the carbon activity values in the anode gas phase, for both SOFC-O^{2-} and SOFC-H^{+}, is analyzed. Besides, ranges of operating conditions, in which carbon formation is not thermodynamically feasible, are established. This is important because a problem related to DIR operation is the carbon deposition over the anode and subsequent electrocatalyst deactivation, leading to loss of cell performance and poor durability [24]. According to Clarke et al. [25], carbon filaments that are attached to anode crystallites generate massive forces within the electrode structure leading to its rapid breakdown. Then, in this paper, theoretical efficiencies are determined for both SOFC-O^{2-} and SOFC-H^{+} fuelled by glycerol under conditions in which carbon formation is thermodynamically inhibited.

Although the calculation seems to be more complicated than that for conventional reformers, since part of hydrogen produced from the glycerol steam reforming at the anode side is used in the electrochemical reaction to produce H_2O, electricity and heat, in this paper, a robust and easy to apply methodology is proposed, in which chemical equilibrium is computed by Gibbs energy minimization method on spreadsheets.

2. Steam/glycerol system

Chen et al. [23] have shown that only six species (H_2, CO, CO_2, CH_4, H_2O and glycerol) are enough to perform a thermodynamic analysis of the steam/glycerol system. They found that the concentrations of other species, such as methanal, methanol, ethylene, ethane, ethanal, ethanol, propane, propene, propanal and propanone, are all negligible with mole fractions below 1×10^{-6}, under a typical set of operating conditions.

Based on the main species reported by Chen et al. [23] and the chemical reactions indicated in previous works [13,16,21,26], the possible reactions involved in the glycerol steam reforming can be summarized as depicted in Table 1.

3. Methodology

3.1. *Theoretical background*

For a system with a lot of simultaneous chemical reactions taking place, the equilibrium composition is directly obtained from minimization of the total Gibbs free energy of the system (non-stoichiometric approach) [27]:

$$\frac{G}{RT} = \frac{1}{RT}\sum_{i=1}^{N} n_i G_i^0 + \sum_{i=1}^{N} n_i \ln y_i + \sum_{i=1}^{N} n_i \ln P \quad (1)$$

According to Eq. (1), the system is regarded as an ideal gas phase. Indeed, at low pressure and high temperatures, the system can be considered as ideal [28,29]. In all calculations performed in this work, it is assumed $P = 1$ atm.

The problem consists in finding the different values of n_i which minimize the objective function given by Eq. (1), subject to the constraints of elemental mass balance

$$\sum_{i=1}^{N} n_i \alpha_{ik} = b_k, \quad k = 1 \ldots M \quad (2)$$

Based on the findings of Chen et al. [23], the following species were considered in our simulations: H_2, CH_4, CO, CO_2, H_2O and $C_3H_8O_3$ ($N = 6$). Thus, only C, H, and O are used for elemental mass balance ($M = 3$). The thermodynamic data necessary for describing the Gibbs energy of the species were obtained from Refs. [30–32].

In this work, it is assumed that the steam reforming of glycerol occurs directly on the anode of the SOFC. As a consequence, when an SOFC-O^{2-} is producing a current, there is a net input of oxygen ions (O^{2-}) to the anodic compartment that changes the equilibrium conditions of the system. On the other hand, when an SOFC-H^{+} is producing current, part of the H_2 produced from the glycerol steam reforming reactions leaves the anode gas phase, undergoing the electrochemical reaction at the triple-phase boundary ($H_2 \rightarrow 2H^{+} + 2e^{-}$).

Thus, for an SOFC-O^{2-}, moles of oxygen must be added in the elemental mass balance of oxygen (O), as shown in Eq. (3).

Table 1 – Possible reactions involved in the glycerol steam reforming.

Reaction n°	Reaction	Reaction type
1	$C_3H_8O_3 \rightarrow 3CO + 4H_2$	Glycerol decomposition
2	$CO + H_2O \rightarrow CO_2 + H_2$	Water–gas shift reaction
3	$CO + 3H_2 \rightarrow CH_4 + H_2O$	Methanation reactions
4	$CO_2 + 4H_2 \rightarrow CH_4 + 2H_2O$	
5	$2CO + 2H_2 \rightarrow CH_4 + CO_2$	
6	$C + 2H_2 \rightarrow CH_4$	
7	$CH_4 + H_2O \rightarrow CO + 3H_2$	Methane steam reforming
8	$CH_4 + 2H_2O \rightarrow CO_2 + 4H_2$	
9	$CH_4 + CO_2 \rightarrow 2CO + 2H_2$	Methane dry reforming
10	$CO_2 + H_2 \rightarrow CO + H_2O$	Reverse water–gas shift reaction
11	$CH_4 \rightarrow C + 2H_2$	Carbon formation by CH_4 decomposition
12	$2CO \rightarrow CO_2 + C$	Carbon formation by Boudouard reaction
13	$H_2 + CO \rightarrow C + H_2O$	Carbon monoxide reduction reaction
14	$2H_2 + CO_2 \rightarrow C + 2H_2O$	Carbon dioxide reduction reaction
15	$C + H_2O \rightarrow H_2 + CO$	Carbon gasification
16	$C + 2H_2O \rightarrow 2H_2 + CO_2$	
17	$C_3H_8O_3 + 3H_2O \rightarrow 7H_2 + 3CO_2$	Overall reaction of glycerol steam reforming

While b_O is the number of moles of oxygen (O) in the system, obtained from the inlet water to glycerol ratio (WGR), b_O^{echem} is the extra number of moles of oxygen (O) due to the electrochemical reaction. In the case of an SOFC-H^+, moles of hydrogen must be removed from the elemental mass balance of hydrogen (H), as shown in Eq. (4). While b_H is the number of moles of hydrogen (H) in the system, obtained from the inlet WGR, b_H^{echem} is the number of moles of hydrogen (H) consumed by the electrochemical reaction.

$$\sum_{i=1}^{N} n_i \alpha_{iO} = b_O + b_O^{echem} \tag{3}$$

$$\sum_{i=1}^{N} n_i \alpha_{iH} = b_H - b_H^{echem} \tag{4}$$

In a previous study [33], we performed a thermodynamic analysis for ethanol steam reforming in a reformer by the Gibbs energy minimization method. The Solver function contained in the Microsoft Excel spreadsheet package was used to solve the nonlinear programming model, and the results obtained were satisfactory. Therefore, it is interesting to apply the Solver function to the thermodynamic studies on DIR operation of SOFCs as well. However, when the Solver applies the Generalized Reduced Gradient (GRG) algorithm, it seems to violate the non-negativity constraints. This is due to the fact that GRG algorithm can reach nonfeasible points in trying to get to the optimal solution [34,35], combined with the involvement of logarithmic functions of variables. In order to overcome this drawback, a change of variables was proposed ($n_i = e^{n_i'}$) [33]. In this way, since $e^{n_i'}$ cannot assume negative values, there is no difficulty with the involvement of logarithmic functions of the objective function. Moreover, there is no need to add non-negativity constraints. It should be stressed that, although the problem is nonlinear, the present methodology ensures the global minimum for a given system, independently of initial estimates, since the problem is convex [12,36,37]. The value of 1×10^{-10} was chosen as criterion of precision and convergence in the Solver Options dialog box during the optimization process.

It should be stressed that the procedure described above could be indifferently applied to other fuels (e.g., methanol, ethanol, etc…) and oxidants (CO_2, O_2) or even for direct utilization of these fuels in SOFCs.

In the calculations performed throughout this work, it is considered $n^0_{C_3H_8O_3} = 1$.

During the operation of an SOFC-O^{2-}, the additional number of moles of oxygen, b_O^{echem}, could be, in principle, used to electrochemically oxidize any species of the anode gas mixture (H_2, CO, CH_4). However, it has been reported that CO mostly participates in the water–gas shift reaction (R-2) rather than in electrochemical processes [38]. The electrochemical oxidation of methane is only possible in case of absence (or near absence) of steam at feed. In the presence of steam, the fast reforming reaction (R-7) will dominate over any electrochemical oxidation of methane [39]. In this way, for both SOFC-O^{2-} and SOFC-H^+, it is assumed that solely H_2 is able to undergo electrochemical reaction. So, the fuel utilization (U_f) can be defined as the moles of H_2 consumed by the electrochemical reaction divided by the maximum number of moles of hydrogen produced from glycerol (7 moles hydrogen/mol glycerol, see reaction (R-17)).

In this study, L is the length of the SOFC channel, whereas l is the distance from the channel inlet. Thus, so as to compute the equilibrium composition of the anode gas mixture at a distance l, the following relationships can be used for the SOFC-O^{2-} and SOFC-H^+, respectively:

$$b_O^{echem} = 7U_f^L x \tag{5}$$

$$b_H^{echem} = 14U_f^L x \tag{6}$$

where $x = l/L$ is the relative channel length and U_f^L is the fuel utilization at the anode channel outlet ($x = 1$). By using Eqs. (5) and (6), it is considered that U_f increases gradual and uniformly along the anode channel until reaching the value of U_f^L. This assumption, used to simulate the mode of operation known as plug flow, has been used in other works [40–43].

While the anode is continuously supplied with a steam/glycerol mixture, the cathode compartment of the SOFC is exposed to atmospheric air, which contains some amount of humidity. In the SOFC-H^+, protons (H^+) are transported through the electrolyte to the cathode chamber and undergo electrochemical reactions with oxygen molecules to form H_2O at the cathode. For plug flow operation mode of an SOFC-H^+, in which air and fuel flow are co-current, output cathode gas is air with low partial pressure of O_2 and elevated partial pressure of steam. In this case, the partial pressures of O_2 and H_2O at any x position in the cathode channel, $p^x_{O_2}$ and $p^x_{H_2O}$, respectively, can be calculated according to the following equations:

$$\text{SOFC-H}^+\text{:}\quad p^x_{O_2} = \frac{p^{x=0}_{O_2}(1 - xU_O)}{1 + xU_O p^{x=0}_{O_2}} \tag{7}$$

$$\text{SOFC-H}^+\text{:}\quad p^x_{H_2O} = \frac{p^{x=0}_{H_2O} + 2p^{x=0}_{O_2} xU_O}{1 + xU_O p^{x=0}_{O_2}} \tag{8}$$

For the SOFC-O^{2-}, $p^x_{O_2}$ is given by the relationship:

$$\text{SOFC-O}^{2-}\text{:}\quad p^x_{O_2} = \frac{p^{x=0}_{O_2}(1 - xU_O)}{1 - xU_O p^{x=0}_{O_2}} \tag{9}$$

In Eqs. (7)–(9), U_O is the oxygen utilization. U_O is defined as the ratio of consumed oxygen by the electrochemical reaction to the input oxygen in air. The superscript '$x = 0$' refers to the value of partial pressure at the channel inlet. In this work, $U_O = 0.2$ (400% excess air). It is worth to point out that 300–600% excess air is commonly used in SOFC operations for good heat management in SOFC cell stacks [40]. It was assumed that input air humidity, $p^{x=0}_{H_2O}$, is 0.02 atm, and $p^{x=0}_{O_2} = 0.2058$ atm. The deduction of Eqs. (7)–(9) is too straightforward to be shown here. In fact, similar formulas to Eqs. (7) and (8) were previously used in other works [42,43].

3.2. Electromotive force (EMF) calculation

The reversible EMF (E) is calculated as follows [43]:

$$E = \frac{RT}{2F} \ln \frac{p^{an.}_{H_2} \cdot K_{H_2O} \cdot \left(p^{cat.}_{O_2}\right)^{0.5}}{p_{H_2O}} \tag{10}$$

The above equation is applicable to both SOFC-O^{2-} and SOFC-H^+. However, p_{H_2O} refers to partial pressure of H_2O at

anode of the SOFC-O^{2-}, while it refers to partial pressure of H_2O at the cathode of the SOFC-H^+. In the latter case, p_{H_2O} is calculated by Eq. (8). $p_{O_2}^{cat.}$ is computed by Eqs. (7) and (9), for the SOFC-H^+ and SOFC-O^{2-}, respectively. K_{H_2O} is the equilibrium constant of the reaction of hydrogen oxidation.

3.3. Theoretical SOFC efficiency

For the operation of SOFC under reversible conditions, the electrical work produced can be calculated by using the equation:

$$W = q\overline{E} \tag{11}$$

where q ($=14FU_f^L$) represents the electrical charge transferred through the electrolyte. The average EMF ($\overline{E}$) values were computed by means of numerical integration of EMF along the stack:

$$\overline{E} = \int_0^1 E\,dx \tag{12}$$

The SOFC system efficiency is defined as the ratio of electrical work produced by the SOFC to the chemical energy of fuel spent in the SOFC system [41]. Therefore, the maximum SOFC efficiency, η_{max}, at a given U_f^L, can be obtained as follows:

$$\eta_{max} = U_f^L \frac{14F\overline{E}U_f^L}{-\Delta H^0} \tag{13}$$

where $-\Delta H^0 = 1490$ kJ/mol ($\sim$16.2 MJ/kg) and represents the lower heating value (LHV) of glycerol at standard conditions. Such value was estimated by using the definition of LHV [44] and the thermodynamic data adopted in the present study. Other works report similar values for the LHV of glycerol: 16 MJ/kg [45] and 16.3 MJ/kg [46]. $\overline{E}U_f^L$ is cell's average EMF at a given U_f^L and temperature.

3.4. Carbon formation

Carbon activity in the equilibrium system (a_C) can be readily computed, with no need of considering any chemical reaction regarding carbon formation, simply by using the following mathematical relationship [33]:

$$\ln a_C = \left(-G_C^0/RT\right) + \frac{\lambda_C}{RT} \tag{14}$$

After the completion of optimization process, the Lagrange's multiplier related to the elemental mass balance of the element C (λ_C) is returned by the Solver function through sensitivity reports. For carbon activity (with reference to the graphite phase) greater than unity, gas phase is not in equilibrium, and carbon deposition may occur. On the other hand, if carbon activity is less than unity, carbon formation is not thermodynamically feasible.

In order to establish the range of SOFC operation, in which the formation of carbon is unfavorable, the operating temperature and fuel utilization are specified. Then, the inlet WGR is varied and the corresponding values of a_C are calculated. The boundary of carbon formation is defined as the WGR that has a value of a_C approaching unity. This value corresponds to the minimum WGR at which carbon formation in the equilibrium mixture is thermodynamically unfeasible.

4. Results and discussion

4.1. Effect of temperature on the anode species

The influence of temperature on the composition of the anode gas phase, for WGR = 4, is analyzed. In the present section, solely the effect of temperature is evaluated, so, $U_f = 0\%$. Over the whole temperature range, it was found that the number of moles of glycerol is close to zero, which is in agreement with previous studies [12,13,22]. Furthermore, it is worth to mention that equilibrium constants of reaction (R-1) are great enough for complete decomposition of glycerol, changing from 7.5×10^{21}, at 773 K, to 1×10^{27}, at 1073 K, which is consistent with our calculations (100% conversion of glycerol, at all the temperatures considered).

Fig. 1 shows the number of moles of species as function of temperature. As can be seen, the number of moles of hydrogen increases with increasing temperature, goes through its maximum value at around 998 K (5.22 moles), and slightly decreases thereafter. Additionally, it can be observed that moles of hydrogen decrease together with CO_2, at $T > 998$ K, and, simultaneously, moles of CO and steam increase. Similar behavior was reported in a previous work, which was attributed to the reverse water–gas shift reaction (R-10) [13]. Besides, Adhikari et al. [13] verified that the maximum hydrogen production, for WGR equal to 6:1 and 9:1, occurs at 960 K. It is also seen from Fig. 1 that CH_4 production decreases when the temperature increases. At $T > 973$ K, there are only trace amounts of methane in the equilibrium gas mixture. On the other hand, the number of moles of CO increases with the increase in temperature. It should be noted that moles of steam decrease with increasing temperature, go through a minimum at 948 K, and then increase slightly at higher temperatures. There is a temperature range at which moles of CH_4 and steam decrease, and at the same time, moles

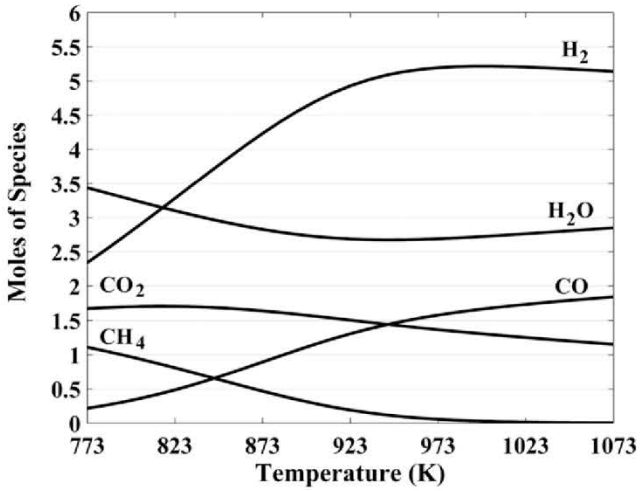

Fig. 1 – Number of moles of species as function of temperature for $U_f = 0\%$ and WGR = 4.

of CO, CO_2 and H_2 increase. This is likely due to the reforming of CH_4 with steam, according to the endothermic reactions (R-7 and R-8) [47]. It can also be observed that the number of moles of CO_2 slightly increases with temperature, from 1.67, at 773 K, to the maximum value at 823 K, 1.71, and then decreases at higher temperatures. This could be ascribed to the endothermic dry reforming of CH_4 (R-9) [48].

4.2. *Effect of temperature and fuel utilization on the anode species*

Fig. 2(a)–(e) shows the partial pressure profiles of H_2, CO, CO_2, CH_4 and H_2O, respectively, for the SOFC-O^{2-}, from $U_f = 0\%$ (anode channel inlet) to $U_f^L = 99.99\%$ (anode channel outlet), at different temperatures, for WGR = 4. As hydrogen is consumed by the electrochemical reaction, steam partial pressure increases along the anode channel. Besides, with the increase in the fuel utilization, carbon monoxide partial pressure decreases, whereas the partial pressure of carbon dioxide increases. This can be attributed to the enhanced water–gas shift reaction (R-2), due to both H_2 consumption by the electrochemical reaction and the steam production along the anode channel. With increasing fuel utilization, it is observed that methane partial pressure decreases. This may be ascribed to the reforming of CH_4 by arising oxidants (H_2O, CO_2), according to reactions (R-7 to R-9). Therefore, output anode gas of the SOFC-O^{2-} is composed mainly of steam and some amount of CO_2.

Fig. 3(a)–(e) shows the partial pressure profiles of H_2, CO, CO_2, CH_4 and H_2O, respectively, for the SOFC-H^+, from $U_f = 0\%$ to $U_f^L = 99.99\%$, at different temperatures, for WGR = 4. By comparing Figs. 2 and 3, it is seen that the type of electrolyte has a significant effect on the partial pressure profiles of the species along the anode. Especially in the case of CO (compare

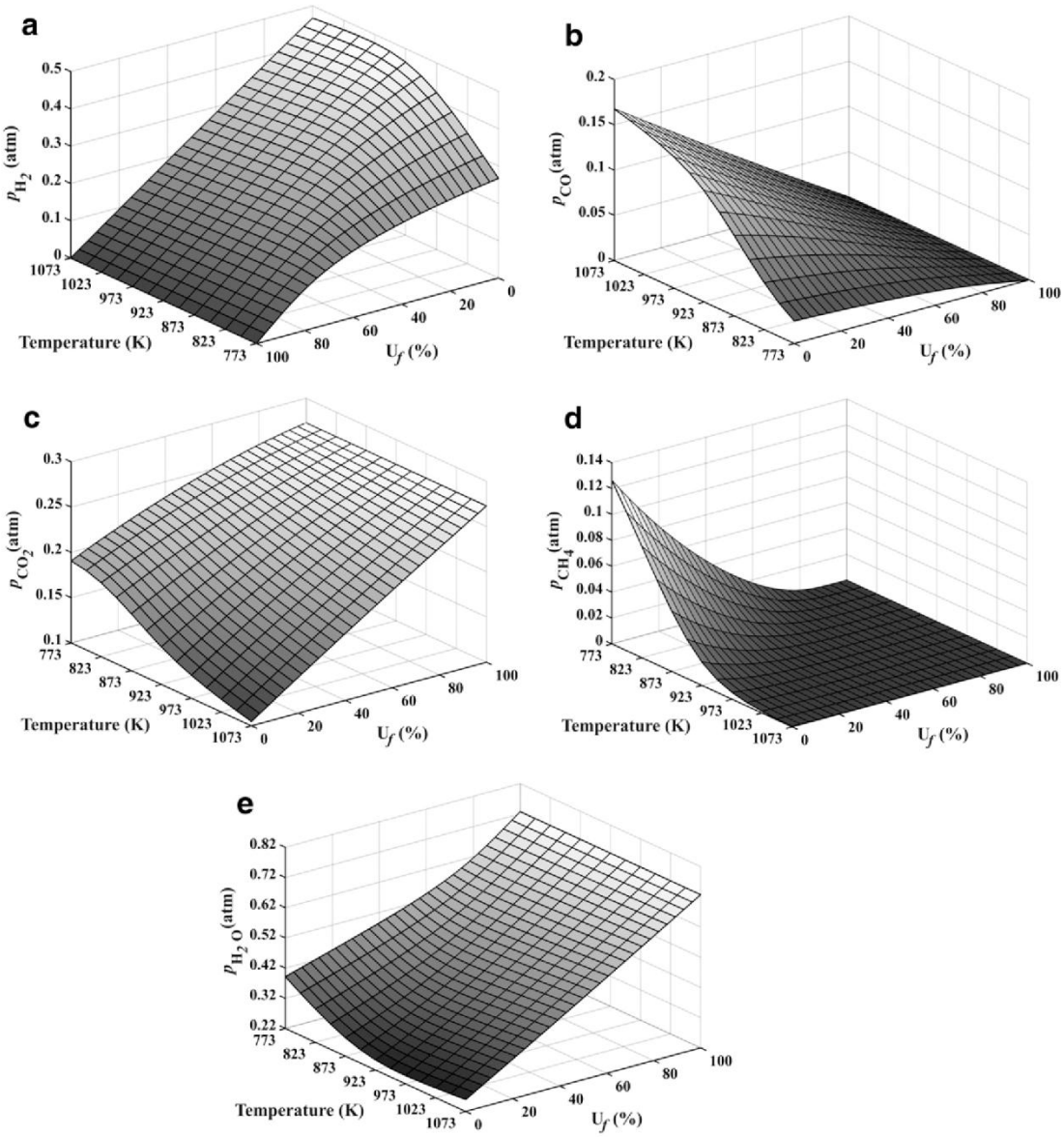

Fig. 2 – Partial pressure of the species along the anode channel at different fuel utilizations and temperatures, in the case of the SOFC-O^{2-}, for WGR = 4: (a) H_2; (b) CO; (c) CO_2; (d) CH_4; (e) H_2O.

Figs. 2(b) and 3(b)) and steam (compare Figs. 2(e) and 3(e)) this effect is remarkable. As a consequence, the tendency for carbon formation in an SOFC-O^{2-} is not the same as that in an SOFC-H^{+}. This will be better explained later in this work. The partial pressures of steam for the SOFC-O^{2-} and SOFC-H^{+} are considerably different due to the different location of steam generation by the electrochemical reaction. Moreover, in the case of an SOFC-H^{+}, the trend exhibited by the partial pressure profile of steam along the anode channel is influenced by temperature. While at lower temperatures, such as 773 K, the partial pressure of steam decreases continuously with increasing U_f, at higher temperatures, e.g., 1073 K, its partial pressure increases slightly, up to ~80% of U_f, and decreases significantly thereafter (Fig. 3(e)). In all other cases, the partial pressure profile of a given species follows a same trend (upward (e.g. CO_2), downward (e.g. CH_4) or both upward and downward (e.g. CO in an SOFC-H^{+})) along the anode channel, whatever the temperature considered. Another interesting feature verified in the case of the SOFC-H^{+} is that, at very high fuel utilizations, both the partial pressure of CO (Fig. 3(b)) and steam (Fig. 3(e)) decrease with a high slope, whereas the partial pressure of CO_2 (Fig. 3(c)) rises in an exponential way. Increase in the H_2 consumption by the electrochemical reaction likely shifted the equilibrium towards the water–gas shift reaction (R-2) and hence higher CO_2 production was observed.

Jamsak et al. [40] calculated equilibrium compositions, for both SOFC-O^{2-} and SOFC-H^{+}, at 1200 K, assuming the inlet water/ethanol ratio equal to 3:1. The partial pressure profiles of the species, observed in Figs. 2 and 3 of the present work, at 1073 K, are similar to those seen in the work of Jamsak et al. [40].

The values of partial pressure, shown in Figs. 2 and 3, were used in Eq. (10) to compute the values of EMF along the SOFC channel, when it is considered $U_f^{\circ} = 99.99\%$.

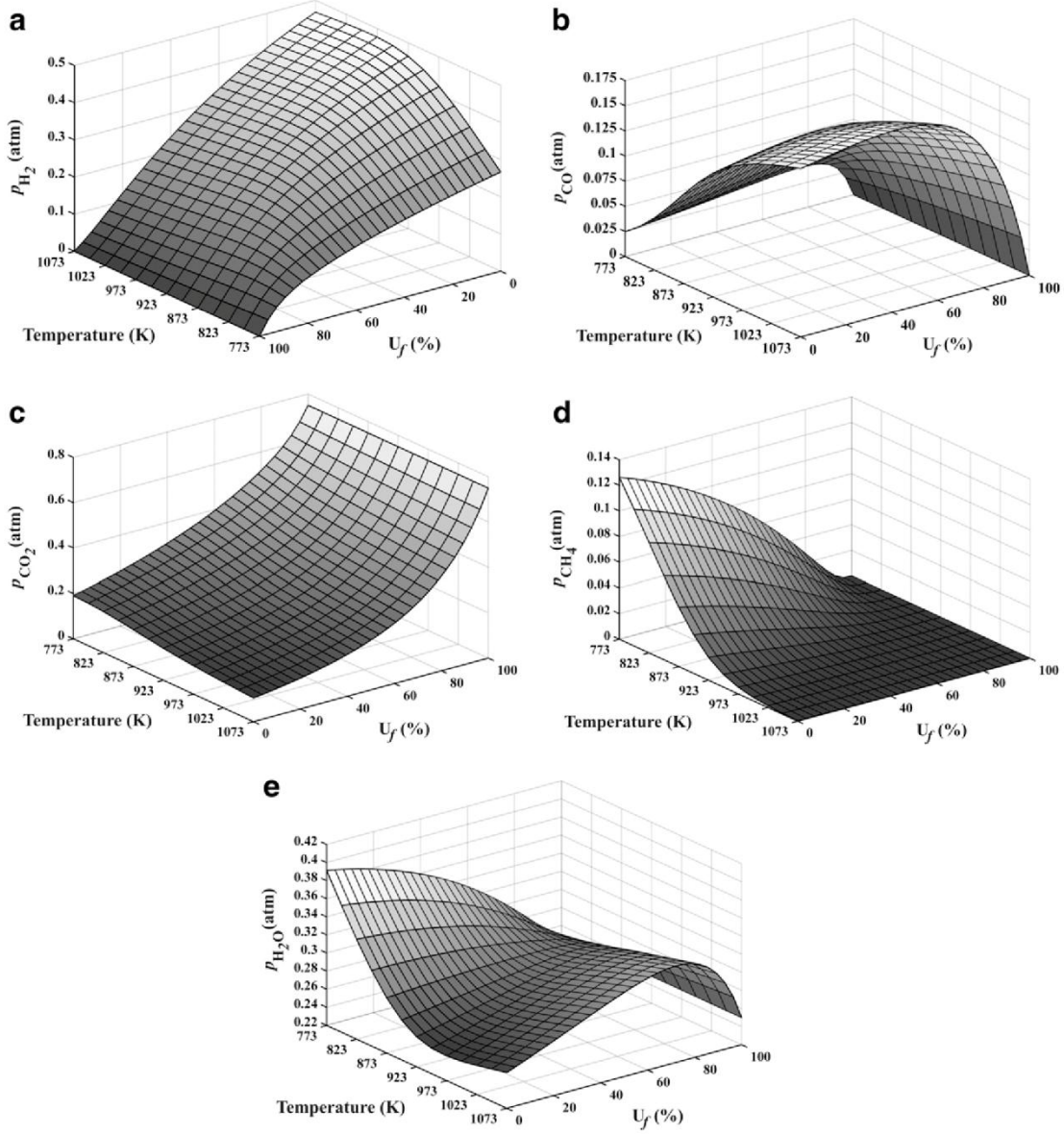

Fig. 3 – Partial pressure of the species along the anode channel at different fuel utilizations and temperatures, in the case of the SOFC-H^{+}, for WGR = 4: (a) H_2; (b) CO; (c) CO_2; (d) CH_4; (e) H_2O.

4.3. *Effect of temperature and fuel utilization on carbon formation*

Fig. 4(a) and (b) shows the boundary of carbon formation, i.e., the minimum inlet WGR at which carbon formation is thermodynamically unfeasible, for SOFC-O^{2-} and SOFC-H^{+}, respectively. The surfaces in the 3-D plots refer to the system in which carbon (graphite phase) is in equilibrium with the gas phase. In the region above the equilibrium surface, carbon deposition is impossible to occur from a thermodynamic point of view. The required inlet WGR needed to prevent carbon formation decreases with temperature. Our results shown in Fig. 4, for the particular case when $U_f = 0\%$, were compared with those reported by Wang et al. [22] and found to be in perfect agreement.

As observed in Fig. 4(a), for an SOFC-O^{2-}, higher fuel utilization results in a decrease of the boundary of carbon formation, over the whole temperature range. The boundary of carbon formation decreases so dramatically with increasing U_f that there is an entire region of the plot in which carbon deposition is thermodynamically inhibited for the inlet WGR equal to zero. Even at 773 K, which is the lowest temperature analyzed, from a value of U_f near 55%, carbon formation is suppressed for WGR equal to zero. For comparison, at 1073 K, from $U_f \sim 7\%$, carbon deposition is avoided for WGR = 0.

On the other hand, when an SOFC-H^{+} is employed, the behavior of the boundary of carbon formation, with respect to fuel utilization, is completely different from that of SOFC-O^{2-}. As can be seen in Fig. 4(b), at lower temperatures, such as 773 and 823 K, the required inlet WGR for avoiding carbon deposition increases with increasing U_f, reaches a maximum value at ~57% of fuel utilization, and decreases thereafter. However, as temperature increases, the effect of U_f on the boundary of carbon formation becomes less evident. When the operating temperature is higher than 973 K, the required inlet WGR for inhibiting carbon formation varies only slightly with increasing U_f. In Fig. 4(b), there is a region where the lines of the mesh are red. In this particular region, for each temperature, from a high value of U_f, the boundary of carbon formation begins to increase with increasing U_f. This is due to the fact that, in the case of an SOFC-H^{+}, moles of hydrogen are removed from the respective elemental mass balance. Thus, under this region, there is no convergence during the optimization process, since the elemental mass balance of hydrogen cannot be satisfied. It must be noted, in Fig. 4(b) that, for $U_f \sim 100\%$, the required inlet WGR, so that the algorithm can converge, is 3, regardless of the operating temperature. This fact is expected based on reaction (R-17).

By comparing the results in Fig. 4(a) and (b), it is observed that SOFC-H^{+} exhibits a greater tendency for carbon deposition than does the SOFC-O^{2-}, which is in agreement with previous reports [11,49]. For example, at 773 K, the inlet value of WGR equal to 3.25 would be enough to prevent carbon deposition during the operation of an SOFC-O^{2-}. At this same temperature, considering, however, an SOFC-H^{+}, the inlet value of WGR should be at least equal to 4, so as to avoid carbon formation at the anode. For unification, WGR = 4 is used in all calculations performed throughout this work, for both SOFC-O^{2-} and SOFC-H^{+}. In this way, it is guaranteed that the SOFC operation is in the region free of carbon deposition, for all values of fuel utilization over the whole temperature range.

The behavior observed in Fig. 4(a) and (b) can be explained based on the carbon activity. Fig. 5(a) shows the effect of temperature and U_f on the carbon activity in the anode gas mixture of SOFC-O^{2-} and SOFC-H^{+}, for WGR = 4. For both types of electrolyte, carbon activity decreases with increasing temperature. At a same temperature, the values of a_C calculated for the SOFC-H^{+} are always greater than those for the SOFC-O^{2-}. Such difference, however, tends to become smaller as temperature increases. For an SOFC-O^{2-}, a_C decreases continuously with increasing U_f, at all the temperatures. On the other hand, in the case of an SOFC-H^{+}, the U_f dependence of the carbon activity is greatly influenced by the temperature. At lower temperatures (773–823 K), a_C increases with U_f, goes through a maximum value, and then decreases at higher U_f values. At more elevated temperatures, a_C varies only slightly with U_f (up to $U_f \sim 60\%$), and decreases significantly thereafter. The values of λ_C/RT presented in Fig. 5(b), obtained from the sensitivity reports, were substituted into Eq. (14) for determining the carbon activities shown in Fig. 5(a). The term λ_C/RT becomes more negative with the increase in the operating temperature. In the case of the SOFC-O^{2-}, λ_C/RT decreases with increasing U_f, over the whole temperature range. For the SOFC-H^{+}, at lower temperatures, λ_C/RT shows an increasing trend with U_f until reaching a maximum value, whereas, at higher temperatures, this term decreases continuously with U_f. At very high fuel utilizations, λ_C/RT

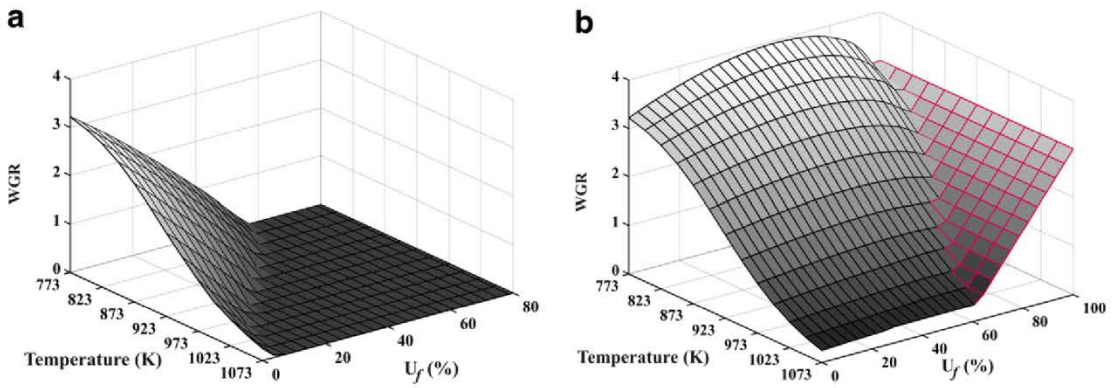

Fig. 4 – Boundary of carbon formation as function of temperature and fuel utilization for (a) SOFC-O^{2-} and (b) SOFC-H^{+}.

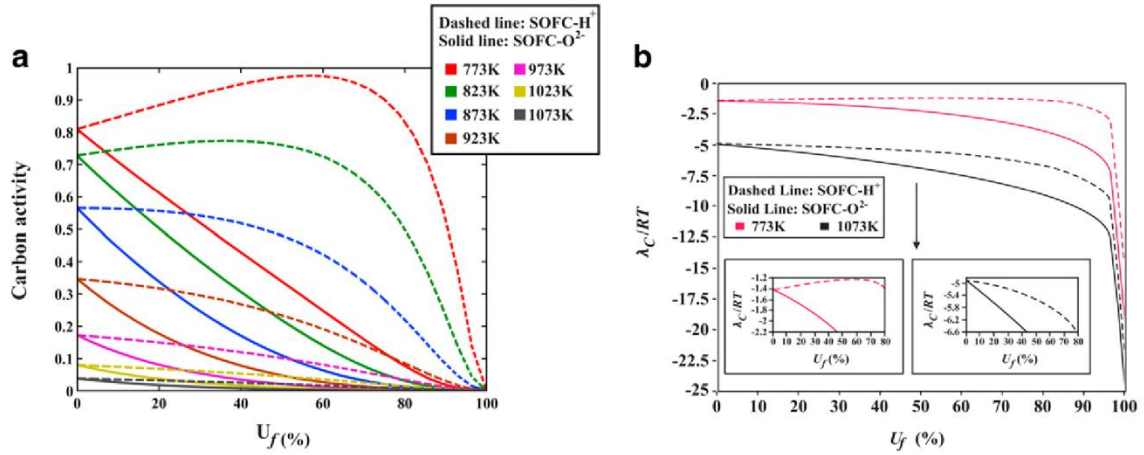

Fig. 5 – (a) Carbon activity as function of fuel utilization for different values of temperature. (b) Lagrange's multipliers related to the elemental mass balance of carbon (divided by *RT*) as function of fuel utilization, for *T* = 773 and 1073 K. WGR = 4.

decreases considerably, regardless of the type of electrolyte considered.

The carbon activity behavior, illustrated in Fig. 5(a), could also be understood based on the Boudouard reaction (R-12). Due to the exothermicity of this reaction, it is expected that carbon deposition becomes unfavorable with increasing temperature. In an SOFC-O^{2-}, it was seen that CO partial pressure decreases (Fig. 2(b)), whereas the partial pressure of CO_2 increases (Fig. 2(c)) with U_f, at all the temperatures. Since CO is the source for carbon formation according to the Boudouard reaction, the increase in CO_2 concentration prevents the carbon deposition by this reaction. For an SOFC-H^+, from a high value of U_f, a_C begins to decrease considerably, whatever the temperature employed. This is attributed to the fact that, at high fuel utilizations, the anode gas mixture of an SOFC-H^+ is composed mainly of CO_2 (see Fig. 3(a)–(e)).

The boundary of carbon formation presented in this work is determined by assuming that there are no kinetic restrictions, and the stable configuration of the system, in which H_2, H_2O, CO, CO_2 and CH_4 are the dominant products, may be reached. Nevertheless, the equilibrium situation might not always be the case. Therefore, there may be more carbon than predicted. Experimental studies, including kinetics, would be greatly helpful in determining the most suitable inlet WGR ratios. Furthermore, works related to the development of anode materials should be performed. It is well known that the optimization of anode microstructure plays an important role in reducing carbon formation [50].

4.4. *Theoretical efficiency analysis*

Fig. 6(a) and (b) depicts the EMF distribution along the SOFC-O^{2-} and SOFC-H^+ channel dimensionless length, respectively. It can be seen that only at the channel outlet EMF varies strongly. Indeed, this is expected, since it was considered $U_f^L = 99.99\%$. Thus, the values of the partial pressure of H_2 at the anode channel outlet, $p_{H_2}^L$, are very low, changing from 5.9×10^{-5} to 4.7×10^{-5} atm (SOFC-O^{2-} case), and from 1.1×10^{-4} to 4.8×10^{-5} atm (SOFC-H^+ case), in the temperature range of 773–1073 K. The average EMF for SOFC-H^+ is higher than the average EMF for SOFC-O^{2-}, under these conditions, by 76–105 mV.

Fig. 7 illustrates the temperature dependence of the maximum thermodynamic efficiency, η_{max}, of the glycerol-fuelled SOFC-O^{2-} and SOFC-H^+. It can be observed that the maximum theoretical efficiency of the SOFC-H^+ is superior to

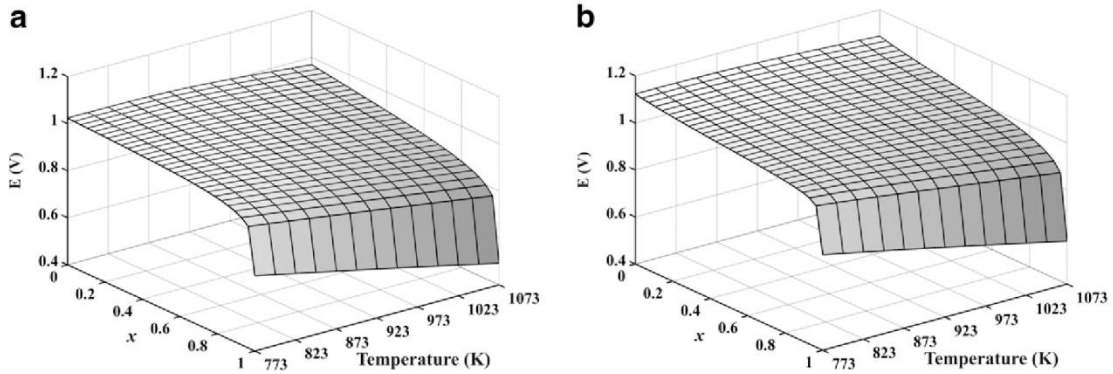

Fig. 6 – Influence of temperature on electromotive force along SOFC length for: (a) SOFC-O^{2-}; (b) SOFC-H^+. WGR = 4; U_f^L = 99.99%; U_O = 0.2; humidity = 0.02 atm.

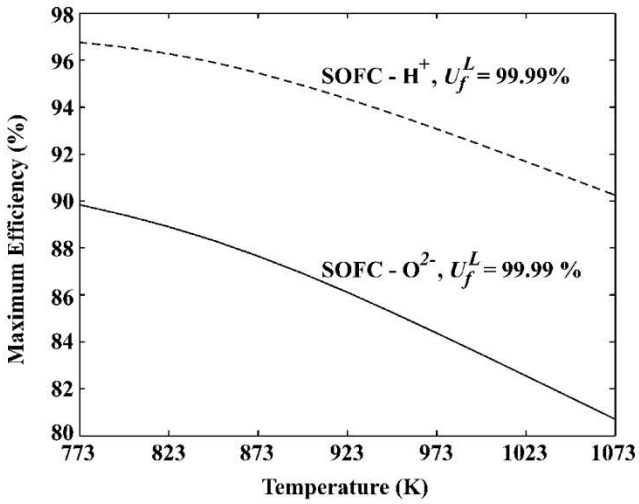

Fig. 7 – Maximum theoretical efficiency as function of temperature, for SOFC-O^{2-} and SOFC-H^+. WGR = 4; U_f^L = 99.99%; U_O = 0.2; humidity = 0.02 atm.

that of the SOFC-O^{2-} over the whole range of temperature. This is in good agreement with previous theoretical studies reporting that the SOFC-H^+ provides a maximum efficiency higher than the SOFC-O^{2-}, considering SOFCs fuelled by ethanol [40], methane [42], hydrogen [43] and ammonia [51]. As can be seen, glycerol utilization in IT-SOFCs allows the system to attain high theoretical efficiencies, which indicates that glycerol can be considered an alternative fuel with suitable characteristics for electricity generation in IT-SOFCs. In this way, operating at an intermediate temperature, such as 773 K, seems to be very attractive from the point of view of the maximum theoretical efficiency, especially in the case of the SOFC-H^+. On the other hand, it should be taken into account that lowering temperature increases the tendency for carbon deposition and, as a consequence, higher values of WGR must be employed. It is also known, however, that excessive water in the mixture is not favored, because the exothermic heat produced by the SOFC electrochemical section may not satisfy the endothermic heat of the steam reforming reaction and the enthalpy requirement for water evaporation [52]. Thus, it is necessary to consider the energetic balance as well.

It is worth to point out that the average EMF values computed for glycerol fed SOFCs are very similar to those calculated for SOFCs fuelled by ethanol. In the present study, the average EMFs were also computed for ethanol fed SOFCs, exactly under the same conditions that were assumed for glycerol, for comparison purposes only. Ethanol is a biofuel which has been considered very attractive for electricity generation in SOFCs [40,41,53]. In Table 2, the values of $\overline{E}$ and η_{max}, calculated for both SOFC-O^{2-} and SOFC-H^+ fuelled by ethanol or glycerol, at 773 K and 1073 K, are shown. Although ethanol and glycerol provide practically the same value for the average EMF, ethanol gives values of η_{max} about 3–4% higher than those calculated for glycerol. This can be attributed to the fact that the LHV of ethanol (1235 kJ/mol [41]) is lower than the LHV of glycerol (1490 kJ/mol). In the case of ethanol, our calculations were compared with the results of Jamsak et al.

Table 2 – Average EMF and maximum theoretical efficiency computed for SOFCs fuelled by ethanol or glycerol, for U^L = 99.99% and inlet water to glycerol (or ethanol) ratio equal to 4:1, at different temperatures.

Fuel	Ethanol		Glycerol	
Temperature (K)	773	1073	773	1073
SOFC-O^{2-} $\overline{E}$ (V)	0.992	0.893	0.991	0.890
η_{max} (%)	92.9	83.7	89.9	80.7
SOFC-H^+ $\overline{E}$ (V)	1.072	1.004	1.067	0.996
η_{max} (%)	100.0	94.1	96.7	90.3

[40] and found to be in good agreement. Using the same operating conditions U_f^L = 80%, T = 1200 K, water/ethanol ratio = 3:1, absence of humidity, 400% excess air, $p_{O_2}^{x=0}$ = 0.21 atm, our calculations gave the average EMFs equal to 0.883 V and 1.027 V, whereas those authors obtained 0.89 V and 1.03 V, for SOFC-O^{2-} and SOFC-H^+, respectively.

The values computed for η_{max}, as shown in Fig. 7, are very high because it was considered U_f^L = 99.99%, which means that $p_{H_2}^L$ is extremely low. Nevertheless, it is known that electrochemical kinetics is influenced by the partial pressure of a reactant of electrochemical reaction. In the case of SOFCs, such reactant is hydrogen. Over voltage of an electrochemical reaction is diversely proportional to partial pressure of the reactant and becomes unacceptably high at low concentration of the reactant. In practice, it is assumed that acceptable level of partial pressure of residual hydrogen is around 0.1 atm [42]. Fig. 8 shows the temperature dependence of U_f^L for SOFC-O^{2-} and SOFC-H^+, considering $p_{H_2}^L$ = 0.1 atm. It is seen that SOFC-H^+ allows higher fuel utilization than does the SOFC-O^{2-}. This is mainly because of the higher hydrogen partial pressure and lower steam partial pressure in the anode compartment of an SOFC-H^+ in comparison with an SOFC-O^{2-}. More interestingly, it is verified that U_f^L goes through a maximum value at 823 K in the case of the SOFC-H^+. As temperature decreases, the

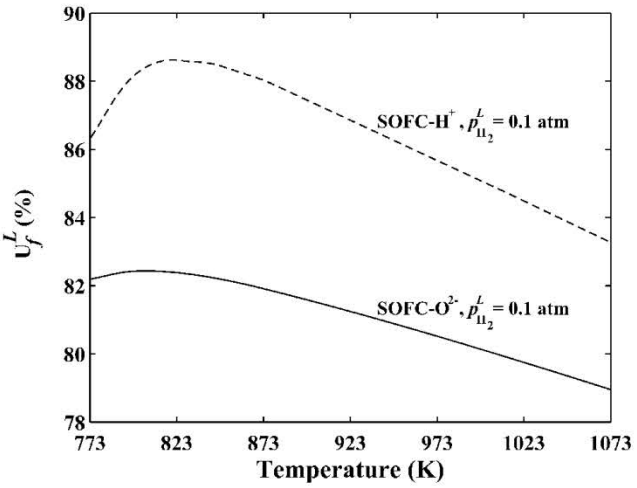

Fig. 8 – Temperature dependence of the fuel utilization at the anode channel outlet, for $p_{H_2}^L$ = 0.1 atm. WGR = 4; U_O = 0.2; humidity = 0.02 atm.

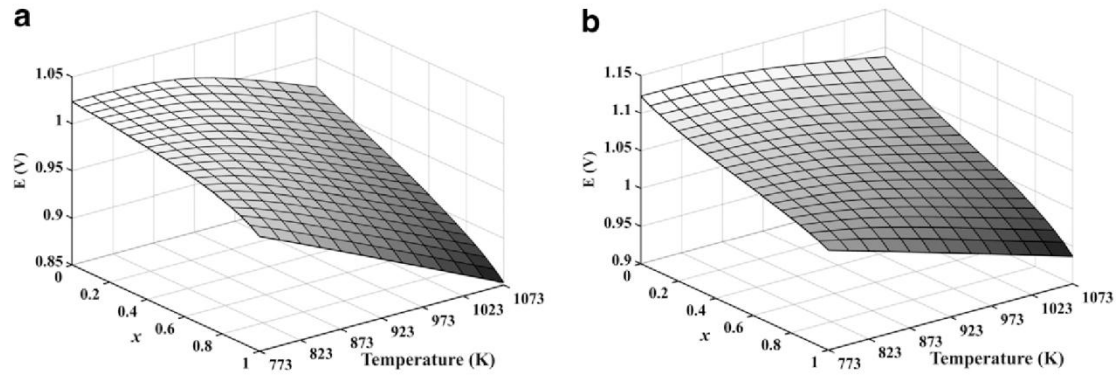

Fig. 9 – Influence of temperature on electromotive force along SOFC length for: (a) SOFC-O^{2-}; (b) SOFC-H^{+}. WGR = 4; $p^{L}_{H_2}$ = 0.1 atm; U_O = 0.2; humidity = 0.02 atm.

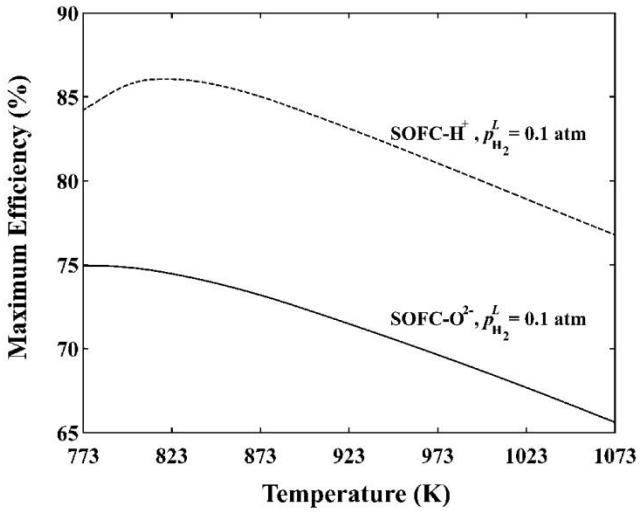

Fig. 10 – Maximum theoretical efficiency as function of temperature for SOFC-O^{2-} and SOFC-H^{+}. WGR = 4; $p^{L}_{H_2}$ = 0.1 atm; U_O = 0.2; humidity = 0.02 atm.

water–gas shift reaction (R-2), which is slightly exothermic, is favored. Thus, U^{L}_{f} increases with temperature decreasing. Further lowering of temperature leads, however, to lower values of U^{L}_{f}, possibly because of the exothermic methanation reactions (R-3-to R-6), which are enhanced under these conditions. This may be the reason why a maximum value is observed in Fig. 8. Equilibrium compositions were, then, re-calculated by using the values of U^{L}_{f} indicated in Fig. 8 and Eqs. (5) and (6). Fig. 9(a) and (b) shows EMF distribution along the SOFC-O^{2-} and SOFC-H^{+} channel dimensionless length, respectively, for $p^{L}_{H_2} = 0.1$ atm. As can be seen, at lower temperatures, EMF varies only slightly, whereas, at higher temperatures, EMF varies more significantly along the channel length. Besides, EMF decreases with increasing temperature.

Fig. 10 depicts the values of maximum theoretical efficiency for $p^{L}_{H_2} = 0.1$ atm. By comparing Figs. 7 and 10, it is seen that η_{max} decreases when U^{L}_{f} also decreases. Moreover, in Fig. 10, it is verified that the maximum efficiency occurs, for the SOFC-H^{+}, at 823 K. This is a direct consequence of the behavior of U^{L}_{f} observed in Fig. 8.

It is important to estimate the actual efficiency of an SOFC when it operates far from reversible conditions, i.e., when SOFC runs under non-equilibrium conditions in which the average cell voltage is less than $\bar{E}$. In this way, a useful characteristic of the SOFC is its relative power, ρ_r, equal to the ratio of the current power to the maximum achievable power. It is possible to show that the dependence of the actual efficiency (η) on the relative power and the maximum efficiency is given by:

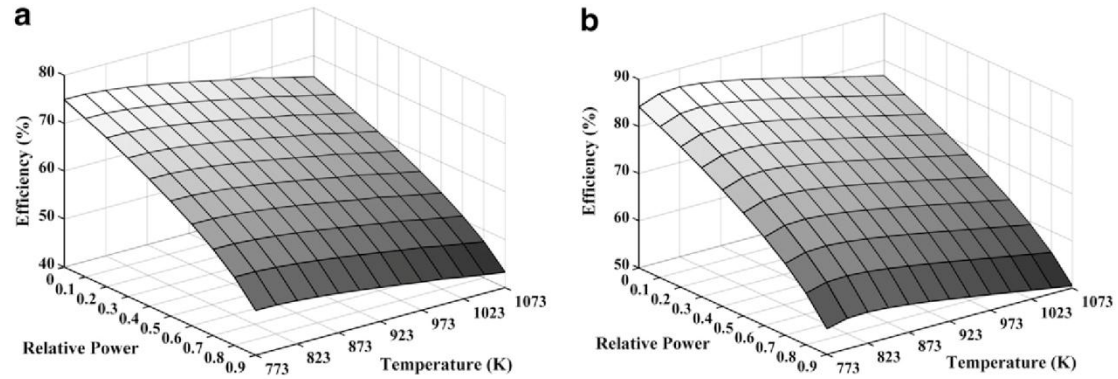

Fig. 11 – Efficiency of SOFC system as function of relative power and temperature: (a) SOFC-O^{2-} and (b) SOFC-H^{+}. WGR = 4; $p^{L}_{H_2}$ = 0.1 atm; U_O = 0.2; humidity = 0.02 atm.

$$\eta = 0.5\eta_{max}\left(1+\sqrt{1-\rho_r}\right) \quad (15)$$

A more detailed explanation regarding relative power, ρ_r, and Eq. (15) can be seen elsewhere [42,43,54].

Fig. 11(a) and (b) shows the efficiency as function of temperature and relative power, for SOFC-O^{2-} and SOFC-H^+, respectively. It is reported that one of the acceptable regimes of fuel cell operation is when the system runs at 70% of its maximum power [54]. It can be seen that, for glycerol-fuelled SOFC-O^{2-}, the system efficiency is between 58% (773 K) and 51% (1073 K), whereas, in the case of the SOFC-H^+, the system efficiency is between 67% (823 K) and 59% (1073 K), for $\rho_r = 0.7$.

5. Conclusions

A thermodynamic analysis for IT-SOFCs fuelled by glycerol with direct internal reforming was carried out. A robust and easy to apply methodology, based on the principle of minimizing the Gibbs free energy of a given system on spreadsheets, using the Microsoft Excel's Solver function, was described for operation of the SOFC-O^{2-} and SOFC-H^+. The following conclusions can be drawn from the results of the present study:

* Glycerol was found to be completely converted into a mixture of H_2, CO, CO_2, H_2O and CH_4. When solely the effect of the temperature is evaluated, it is verified that H_2 and CO production is favored at high temperatures. At $T > 973$ K, there are only trace amounts of methane in the gas mixture.
* In the case of the SOFC-O^{2-}, with increasing fuel utilization, the partial pressures of CO and CH_4 decrease, whereas the partial pressures of CO_2 and H_2O increase, over the whole temperature range. Therefore, during the operation, carbon activity becomes increasingly smaller, which results in a lesser tendency for carbon deposition.
* The partial pressure profiles of CO and H_2O along the anode channel are strongly influenced by the type of electrolyte employed. As a consequence, the tendency for carbon formation in an SOFC-O^{2-} is different from that in an SOFC-H^+. Carbon deposition is more pronounced in the SOFC-H^+ system.
* For the SOFC-H^+, at lower temperatures, such as 773 K and 823 K, the required inlet WGR for avoiding carbon deposition increases with increasing fuel utilization, goes through a maximum value at ~57% of U_f, and then decreases at higher fuel utilizations. However, at $T > 973$ K, the inlet WGR needed for preventing carbon formation varies only slightly with fuel utilization.
* Glycerol utilization in IT-SOFCs allows the system to attain high theoretical efficiencies in the range of 80.7–89.9% (SOFC-O^{2-} case) and 90.3–96.7% (SOFC-H^+ case) operating at carbon-free conditions (WGR = 4), between 773 and 1073 K, for $U_f^L = 99.99\%$. Glycerol-fuelled SOFCs exhibits very similar potential for power generation with ethanol.
* The actual efficiency was also estimated. When the system runs at 70% of its maximum power, assuming the partial pressure of residual hydrogen in the anode channel outlet equal to 0.1 atm, the highest efficiency (67%) can be reached by operating an SOFC-H^+ at 823 K.
* Although the combined effect of proton conducting electrolyte and lower temperatures provides the highest values of efficiency, it must be taken into account that, under these conditions, the tendency for carbon deposition is much greater than in the case of the SOFC-O^{2-} operated at high temperatures.
* The present thermodynamic study gives useful information for the operation of IT-SOFCs with DIR fuelled by glycerol. Nevertheless, electrochemical models that consider all overpotentials involved in SOFC operation must be developed. Besides, energy and exergy analyses must be performed in order to quantify the optimal operating parameters. Search for solid oxides with high ionic conductivity and stability in intermediate temperatures is still a very important task for developing efficient electrochemical generators.

Acknowledgments

Authors would like to acknowledge the CNPq and CAPES for financial support.

REFERENCES

[1] Shao Z, Haile SM, Ahn J, Ronney PD, Zhan Z, Barnett SA. A thermally self sustained micro solid-oxide fuel-cell stack with high power density. Nature 2005;435:795–8.
[2] Peña-Martinez J, Marrero-López D, Ruiz-Morales JC, Buergler BE, Núñez P, Gauckler LJ. Fuel cell studies of perovskite-type materials for IT-SOFC. J Power Sources 2006; 159:914–21.
[3] Horita T, Yamaji K, Yokokawa H, Toji A, Uehara T, Ogasawara K, et al. Effects of Si and Al concentrations in Fe–Cr alloy on the formation of oxide scales in H_2–H_2O. Int J Hydrogen Energy 2008;33:6308–15.
[4] Lee D, Lee I, Jeon Y, Song R. Characterization of scandia stabilized zirconia prepared by glycine nitrate process and its performance as the electrolyte for IT-SOFC. Solid State Ionics 2005;176:1021–5.
[5] Yamamoto O, Arati Y, Takeda Y, Imanishi N, Mizutani Y, Kawai M, et al. Electrical conductivity of stabilized zirconia with ytterbia and scandia. Solid State Ionics 1995;79: 137–42.
[6] Politova TI, Irvine JTS. Investigation of scandia–yttria–zirconia system as an electrolyte material for intermediate temperature fuel cells – influence of yttria content in system $(Y_2O_3)_x(Sc_2O_3)_{(11-x)}(ZrO_2)_{89}$. Solid State Ionics 2004;168:153–65.
[7] Maiti S, Pastor M, Sundaram RS, Ravichandran J, Kumar A, Biswas K, et al. Synthesis and characterization of nanocrystalline dysprosia stabilized zirconia based electrolyte for intermediate-temperature solid oxide fuel cell. J Alloys Compd 2009;475:587–91.
[8] Aguiar P, Adjiman CS, Brandon NP. Anode-supported intermediate-temperature direct internal reforming solid oxide fuel cell: II. Model-based dynamic performance and control. J Power Sources 2005;147:136–47.
[9] Ni M, Leung DYC, Leung MKH. An improved electrochemical model for the NH_3 fed proton conducting solid oxide fuel cells at intermediate temperatures. J Power Sources 2008;185: 233–40.

[10] Guo Y, Lin Y, Ran R, Shao Z. Zirconium doping effect on the performance of proton-conducting $BaZr_yCe_{0.8-y}Y_{0.2}O_{3-\delta}$ ($0 \le y \le 0.8$) for fuel cell applications. J Power Sources 2009; 193:400–7.
[11] Assabumrungrat S, Laosiripojana N, Pavarajarn V, Sangtongkitcharoen W, Tangjitmatee A, Praserthdam P. Thermodynamic analysis of carbon formation in a solid oxide fuel cell with a direct internal reformer fuelled by methanol. J Power Sources 2005;139:55–60.
[12] Rossi CCRS, Alonso CG, Antunes OAC, Guirardello R, Cardozo-Filho L. Thermodynamic analysis of steam reforming of ethanol and glycerine for hydrogen production. Int J Hydrogen Energy 2009;34:323–32.
[13] Adhikari S, Fernando S, Gwaltney SR, Filip To SD, Mark Bricka R, Steele PH, et al. A thermodynamic analysis of hydrogen production by steam reforming of glycerol. Int J Hydrogen Energy 2007;32:2875–80.
[14] Haas MJ, McAloon AJ, Yee WC, Foglia TA. A process model to estimate biodiesel production costs. Bioresour Technol 2006; 97:671–8.
[15] Arechederra RL, Treu BL, Minteer SD. Development of glycerol/O_2 biofuel cell. J Power Sources 2007;173:156–61.
[16] Buffoni IN, Pompeo F, Santori GF, Nichio NN. Nickel catalysts applied in steam reforming of glycerol for hydrogen production. Catal Commun 2009;10:1656–60.
[17] Adhikari S, Fernando SD, Haryanto A. Hydrogen production from glycerin by steam reforming over nickel catalysts. Renew Energy 2008;33:1097–100.
[18] Profeti LPR, Ticianelli EA, Assaf EM. Production of hydrogen via steam reforming of biofuels on Ni/CeO_2–Al_2O_3 catalysts promoted by noble metals. Int J Hydrogen Energy 2009;34: 5049–60.
[19] Zhang B, Tang X, Li Y, Xu Y, Shen W. Hydrogen production from steam reforming of ethanol and glycerol over ceria-supported metal catalysts. Int J Hydrogen Energy 2007;32:2367–73.
[20] Hirai T, Ikenaga N-O, Miyake T, Suzuki T. Production of hydrogen by steam reforming of glycerin on ruthenium catalyst. Energy Fuels 2005;19:1761–2.
[21] Dou B, Dupont V, Rickett G, Blakeman N, Williams PT, Chen H, et al. Hydrogen production by sorption-enhanced steam reforming of glycerol. Bioresour Technol 2009;100: 3540–7.
[22] Wang X, Li S, Wang H, Liu B, Ma X. Thermodynamic analysis of glycerin steam reforming. Energy Fuels 2008;22:4285–91.
[23] Chen H, Zhang T, Dou B, Dupont V, Williams P, Ghadiri M, et al. Thermodynamic analyses of adsorption-enhanced steam reforming of glycerol for hydrogen production. Int J Hydrogen Energy 2009;34:7208–22.
[24] Aguiar P, Adjiman CS, Brandon NP. Anode-supported intermediate temperature direct internal reforming solid oxide fuel cell. I: Model-based steady-state performance. J Power Sources 2004;138:120–36.
[25] Clarke SH, Dicks AL, Pointon K, Smith TA, Swann A. Catalytic aspects of the steam reforming of hydrocarbons in internal reforming fuel cells. Catal Today 1997;38:411–23.
[26] Davda RR, Shabaker JW, Huber GW, Cortright RD, Dumesic JA. A review of catalytic issues and process conditions for renewable hydrogen and alkanes by aqueous-phase reforming of oxygenated hydrocarbons over supported metal catalysts. Appl Catal B 2005;56:171–86.
[27] Koh JH, Kang BS, Lim HC, Yoo YS. Thermodynamic analysis of carbon deposition and electrochemical oxidation of methane for SOFC anodes. Electrochem Solid-State Lett 2001; 4:A12–5.
[28] Vasudeva K, Mitra N, Umasankar P, Dhingra SC. Steam reforming of ethanol for hydrogen production: thermodynamic analysis. Int J Hydrogen Energy 1996;21: 13–8.
[29] Lwin Y, Daud WRW, Mohamad AB, Yaakob Z. Hydrogen production from steam-methanol reforming: thermodynamic analysis. Int J Hydrogen Energy 2000;25: 47–53.
[30] Yaws CL. Chemical properties handbook. New York: McGraw-Hill; 1999.
[31] Knacke O, Kubaschewski O, Hesselmann K. Thermochemical properties of inorganic substances. Berlin: Springer-Verlag; 1991.
[32] Sandler SI. Chemical and engineering thermodynamics. New York: Wiley; 1999.
[33] Lima da Silva A, Malfatti CF, Müller IL. Thermodynamic analysis of ethanol steam reforming using Gibbs energy minimization method: a detailed study of the conditions of carbon deposition. Int J Hydrogen Energy 2009;34:4321–30.
[34] Edgar TF, Himmelblau DM. Optimization of chemical processes. Boston: Mcgraw-Hill; 1988.
[35] Reklaitis GV, Ravindran A, Ragsdell KM. Engineering optimization, methods and applications. New York: Wiley; 1983.
[36] White WB, Johnson SM, Dantzig GB. Chemical equilibrium in complex mixtures. J Chem Phys 1958;28:751–5.
[37] McDonald CM, Floudas CA. Global optimization and analysis for the Gibbs free energy function using the UNIFAC, Wilson e ASOG equations. Ind Eng Chem Res 1995;34:1674–87.
[38] Holtappels P, De Haart LGJ, Stimming U, Vinke IC, Mogensen M. Reaction of CO/CO_2 gas mixtures on Ni-YSZ cermet electrodes. J Appl Electrochem 1999;29:561–8.
[39] Ho TX, Kosinski P, Hoffmann AC, Vik A. Numerical analysis of a planar anode-supported SOFC with composite electrodes. Int J Hydrogen Energy 2009;34:3488–99.
[40] Jamsak W, Assabumrungrat S, Douglas PL, Laosiripojana N, Charojrochkul S. Theoretical performance analysis of ethanol-fuelled solid oxide fuel cells with different electrolytes. Chem Eng J 2006;119:11–8.
[41] Tsiakaras P, Demin A. Thermodynamic analysis of a solid oxide fuel cell system fuelled by ethanol. J Power Sources 2001;102:210–7.
[42] Demin AK, Tsiakaras PE, Sobyanin VA, Hramova SY. Thermodynamic analysis of a methane fed SOFC system based on a protonic conductor. Solid State Ionics 2002;152-153:555–60.
[43] Demin A, Tsiakaras P. Thermodynamic analysis of a hydrogen fed solid oxide fuel cell based on a proton conductor. Int J Hydrogen Energy 2001;26:1103–8.
[44] Lyons WC, Plisga GJ. Standard handbook of petroleum & natural gas engineering. Amsterdam, The Netherlands: Elsevier; 2005.
[45] Svoboda K, Pohorely M, Hartman M, Martinec J. Pretreatment and feeding of biomass for pressurized entrained flow gasification. Fuel Process Technol 2009;90:629–35.
[46] Centi G, van Santen RA. Catalysis for renewables. Weinheim: Wiley-VCH; 2007.
[47] Amphlett JC, Evans MJ, Jones RA, Mann RF, Weir RD. Hydrogen production by the catalytic steam reforming of methanol, part 1: the thermodynamics. Can J Chem Eng 1981; 59:720–7.
[48] Fatsikostas AN, Kondarides DI, Verykios XE. Production of hydrogen for fuel cells by reformation of biomass-derived ethanol. Catal Today 2002;75:145–55.
[49] Assabumrungrat S, Pavarajarn V, Charojrochkul S, Laosiripojana N. Thermodynamic analysis for a solid oxide fuel cell with direct internal reforming fueled by ethanol. Chem Eng Sci 2004;59:6015–20.
[50] Mermelstein J, Millan M, Brandon N. The impact of steam and current density on carbon formation from biomass gasification tar on Ni/YSZ, and Ni/CGO solid oxide fuel cell anodes. J Power Sources 2010;195:1657–66.

[51] Ni M, Leung DYC, Leung MKH. Thermodynamic analysis of ammonia fed solid oxide fuel cells: comparison between proton-conducting electrolyte and oxygen ion-conducting electrolyte. J Power Sources 2008;183:682–6.
[52] Ioannides T. Thermodynamic analysis of ethanol processors for fuel cell applications. J Power Sources 2001;92:17–25.
[53] Douvartzides SL, Coutelieris FA, Demin AK, Tsiakaras PE. Electricity from ethanol fed SOFCs: the expectations for sustainable development and technological benefits. Int J Hydrogen Energy 2004;29:375–9.
[54] Demin A, Tsiakaras P, Gorbova E, Hramova S. A SOFC based on a co-ionic electrolyte. J Power Sources 2004;131:231–6.

4.1.5. Towards H_2-rich gas production from unmixed steam reforming of methane: Thermodynamic modeling

(Rumo à produção de um gás rico em H_2 a partir da rota 'unmixed reforming', usando-se metano como combustível: Modelagem termodinâmica)

Principais Resultados:

- Modelagem termodinâmica do processo de *unmixed reforming* validada com resultados experimentais da literatura; Verificação da importância da relação NiO (reagido)/metano como parâmetro de entrada no processo de minimização da energia de Gibbs; A relação NiO (reagido)/metano é um parâmetro que afeta a composição de equilíbrio durante o sopro de combustível; este parâmetro decresce à medida que o tempo passa.
- Identificação de dois estágios durante o sopro de combustível; no início do sopro, a relação NiO (reagido)/metano assume um valor mais elevado, com as reações de redução de NiO sendo o mecanismo mais importante, e as espécies predominantes na mistura gasosa são CO_2 e H_2O; Conforme o tempo passa, e a relação NiO (reagido)/metano vai assumindo valores menores, a reforma a vapor passa a ser o mecanismo mais importante, aumentando a produção de H_2 e CO; durante o sopro de combustível, o processo vai ficando cada vez mais endotérmico, justamente pela maior importância das reações de reforma à medida que o tempo passa;
- Verificação da importância da adição de CaO no processo; a adição de CaO juntamente com NiO permite que H_2 de alta pureza possa ser obtido desde o início do sopro de combustível, quando predominam as reações de redução de NiO, até o fim do sopro, onde predomina a reforma; no início do sopro, a alta concentração de CO_2 devido à redução de NiO favorece a reação de carbonatação;
- O calor liberado pela reação de carbonatação supre a demanda energética do processo durante o sopro de combustível; o calor liberado durante a oxidação de Ni no reator de ar é usado na decomposição do $CaCO_3$, regenerando o CaO, o que proporciona um processo economicamente viável;

Journal of Power Sources 196 (2011) 8568–8582

Contents lists available at ScienceDirect

Journal of Power Sources

journal homepage: www.elsevier.com/locate/jpowsour

Towards H_2-rich gas production from unmixed steam reforming of methane: Thermodynamic modeling

Aline Lima da Silva*, Iduvirges Lourdes Müller

Program of Postgraduate Studies in Mining, Metals and Materials Engineering (PPGEM), Federal University of Rio Grande do Sul – UFRGS, Campus do Vale, Setor 4, Prédio 75, Sala 226, Av. Bento Gonçalves 9500, CEP 91501-970, Porto Alegre, RS, Brazil

ARTICLE INFO

Article history:
Received 13 April 2011
Received in revised form 7 June 2011
Accepted 7 June 2011
Available online 15 June 2011

Keywords:
Hydrogen
Chemical looping
Unmixed reforming
Fuel cells
Thermodynamic analysis
Nickel oxide

ABSTRACT

In this work, the Gibbs energy minimization method is applied to investigate the unmixed steam reforming (USR) of methane to generate hydrogen for fuel cell application. The USR process is an advanced reforming technology that relies on the use of separate air and fuel/steam feeds to create a cyclic process. Under air flow (first half of the cycle), a bed of Ni-based material is oxidized, providing the heat necessary for the steam reforming that occurs subsequently during fuel/steam feed stage (second half of the cycle). In the presence of CaO sorbent, high purity hydrogen can be produced in a single reactor. In the first part of this work, it is demonstrated that thermodynamic predictions are consistent with experimental results from USR isothermal tests under fuel/steam feed. From this, it is also verified that the reacted NiO to CH_4 ($NiO_{reacted}/CH_4$) molar ratio is a very important parameter that affects the product gas composition and decreases with time. At the end of fuel/steam flow, the reforming reaction is the most important chemical mechanism, with H_2 production reaching ~75 mol%. On the other hand, at the beginning of fuel/steam feed stage, NiO reduction reactions dominate the equilibrium system, resulting in high CO_2 selectivity, negative steam conversion and low concentrations of H_2. In the second part of this paper, the effect of $NiO_{reacted}/CH_4$ molar ratio on the product gas composition and enthalpy change during fuel flow is investigated at different temperatures for inlet H_2O/CH_4 molar ratios in the range of 1.2–4, considering the USR process operated with and without CaO sorbent. During fuel/steam feed stage, the energy demand increases as time passes, because endothermic reforming reaction becomes increasingly important as this stage nears its end. Thus, the duration of the second half of the cycle is limited by the conditions under which auto-thermal operation can be achieved. In absence of CaO, H_2 at concentrations of approximately 73 mol% can be produced under thermo-neutral conditions (H_2O/CH_4 molar ratio of 4, with $NiO_{reacted}/CH_4$ molar ratio at the end of fuel flow of ~0.8, in temperature range of 873–1073 K). In the presence of CaO sorbent, using an inlet H_2O/CH_4 molar ratio of 4 at 873 K, H_2 at concentrations over 98 mol% can be obtained all through fuel/steam feed stage. At 873 K, carbonation reaction provides all the heat necessary for H_2 production when $NiO_{reacted}/CH_4$ molar ratio reached at the end of fuel/steam feed is greater or equal to1. In this way, the heat released during air flow due to Ni oxidation can be entirely used to decompose $CaCO_3$ into CaO. In this case, a calcite-to-nickel molar ratio of 1.4 (maximum possible value) can be used during air flow. For longer durations of fuel/steam feed, corresponding to lower $NiO_{reacted}/CH_4$ molar ratios, some heat is necessary for steam reforming, and a calcite-to-nickel molar ratio of about 0.7 is more suitable. With the USR technology, CaO can be regenerated under air feeds, and an economically feasible process can be achieved.

© 2011 Elsevier B.V. All rights reserved.

1. Introduction

Hydrogen is considered to be an ideal clean energy carrier for the future because it is generally consumed as the fuel in low-temperature fuel cells, namely, proton exchange membrane fuel cells (PEMFCs). Over the years, much progress in PEMFCs has been implemented and this makes hydrogen production from the fuel processing of some feedstocks, such as fossil fuels and biomass, become increasingly important. Nowadays, 95% of the hydrogen production comes from steam reforming of natural gas, whose main component is methane. In addition to steam reforming, other thermo-chemical techniques including auto-thermal reforming (ATR) and (catalytic) partial oxidation (CPO or POX) have been regarded as efficient processes to hydrogen production [1–3]. In this context, unmixed steam reforming (USR) can be considered as an alternative process of catalytic steam reforming that relies

* Corresponding author. Tel.: +55 51 3308 9404.
E-mail address: adasilva26@gmail.com (A. Lima da Silva).

0378-7753/$ – see front matter © 2011 Elsevier B.V. All rights reserved.
doi:10.1016/j.jpowsour.2011.06.035

Nomenclature

G	total Gibbs energy of the system
G_i^0	Gibbs energy of species i at its standard state
n_i	number of moles of species i
y_i	mole fraction of species i
R	gas constant
T	temperature of the system
P	total pressure of the system
M, N	total number of components and species, respectively
α_{ik}	number of atoms of kth component present in each molecule of species i
b_k	total number of atomic masses of kth component in the system
ΔH	enthalpy change during fuel flow
in.	inlet
out.	outlet
Sel.	selectivity
Conv.	conversion
TN	thermo-neutral

on the use of separate air and fuel/steam feeds to create a cyclic process. Thus, the air and fuel/steam feeds do not mix, contrary to conventional ATR that uses pure oxygen for partial oxidation of the fuel to provide heat for the endothermic steam reforming reaction. Instead, USR makes use of an oxygen transfer material (OTM), which in its reduced form behaves as a steam reforming catalyst. In this study, Ni was chosen to be the OTM, since it is the most common catalyst for the steam reforming reactions and can be readily oxidized and reduced [4–11]. During USR, an air feed (first half of the cycle, in which Ni is converted into NiO) is followed by a fuel/steam feed (second half of the cycle, in which NiO regenerates to metallic Ni, and reforming reactions occur). Oxidation of the reduced catalyst under air flow is highly exothermic, thus generating the heat required by the endothermic steam reforming reactions that take place during the subsequent fuel/steam feed, and allowing the separation of inert N_2 from the reformate. Therefore, the USR process can run auto-thermally. Besides, the USR technology can be improved by introducing a CO_2-sorbent such as CaO into the reactor. In fact, calcite ($CaCO_3$) can be introduced along with Ni in the reactor. Under air flow, some heat released during Ni oxidation is utilized to thermally decompose calcite into CaO (calcination). In this way, the steam reforming reactions occur alongside CO_2 capture from the gas phase during the second half of the cycle. CaO reacts with CO_2 forming calcite again (carbonation). Consequently, water–gas shift (WGS) reaction is enhanced due to CO_2 adsorption, resulting in a decrease of the CO production, accompanied by an increase in H_2 concentration. The potential advantages of using CaO as a CO_2 acceptor have been previously demonstrated [12,13]. However, in order to obtain an economically feasible process, CaO has to be regenerated once it is fully converted to $CaCO_3$, and regeneration requires a certain amount of energy. Thus, the USR process offers a potential solution to this problem. While Ni oxidizes under the following air flow, some heat liberated is then utilized to decompose calcite to calcium oxide, regenerating the sorbent for the next cycle. In this way, under air flow, the reactor effluent is an oxygen-depleted and CO_2-rich air stream, whereas under fuel/steam feed, the gaseous species CO, CO_2 and H_2 evolve from the reactor. Based on the chemical reactions indicated in previous works [4,7,8], the main reactions involved in the unmixed steam reforming of methane can be summarized as depicted in Table 1. Under air feed, Ni on the catalyst support consumes oxygen via Ni oxidation to NiO generating heat (R-1) and the carbon deposits (formed in a previous fuel/steam feed) are burnt via complete (R-3) or partial oxidation (R-4). In the presence of calcite, some heat liberated in (R-1) allows the CaO sorbent to regenerate through calcination (R-2). Under fuel/steam feed, (R-6) is the global reaction that illustrates the OTM reduction with methane. While NiO is converted into Ni, significant carbon deposition may occur from fuel thermal decomposition (R-5). Once Ni is sufficiently reduced, methane steam reforming (R-9) occurs on the Ni catalyst, and water–gas shift reaction (R-10) takes place. In the presence of CaO sorbent, the reactions (R-6), (R-9) and (R-10) are followed by the carbonation reaction (R-11). Thus, the carbonation of the CaO sorbent allows not only the elimination of CO_2 from reformate, but also the shift of (R-6) and (R-10) to the right, enhancing the H_2 production. The USR process with CaO, as described in Fig. 1, was proposed in Ref. [7,14]. As can be seen, as nickel is cycled between NiO and catalytically active Ni, calcium is cycled between CaO and $CaCO_3$. The white regions are hotter from exothermic reactions (air flow) or heat storage (fuel/steam feed). USR first appeared in scientific literature through the publications of Kumar et al. [14] and Lyon and Cole [6]. More recently, Dupont et al. have experimentally investigated the production of hydrogen by USR of a variety of fuels, including methane [7,8], sunflower oil [8] and waste cooking oil [10,11]. The experimental results reported in these previous works indicate that USR is a promising fuel flexible technology able to produce fuel cell grade H_2 in a single reactor. Other advantages are claimed for the USR process, such as [6,7,14]: (i) economical at small scale, unlike the conventional process, which makes thus USR interesting for the use in distributed power generation; (ii) insensitivity to coking and sulfur (both could undergo oxidation under the air feed rather than irreversibly poisoning the reforming catalyst); (iii) potential for auto-thermal operation without the need for pure O_2 that would require a costly air separator; (iv) low cost reac-

Table 1
Summary of the main reactions of unmixed steam reforming process.

Half of the cycle	Reaction	Reaction type	$\Delta H^0_{298\,K}$ ($\times 10^5$ J mol^{-1})
First: air feed (oxidizing mode)	$Ni + 0.5O_2 + 1.881N_2 \rightarrow NiO + 1.881N_2$ (R-1)	Oxidation of OTM and separation of N_2 from air	−2.39
	$CaCO_3 \rightarrow CaO + CO_2$ (R-2)	Thermal decomposition of calcite/regeneration of CaO sorbent	+1.79
	$C + O_2 \rightarrow CO_2$ (R-3)	Carbon complete oxidation	−3.93
	$C + 0.5O_2 \rightarrow CO$ (R-4)	Carbon partial oxidation	−1.10
Second: fuel/steam feed (reducing mode)	$CH_4 \rightarrow C + 2H_2$ (R-5)	Thermal decomposition of methane	+0.75
	$CH_4 + 4NiO \rightarrow CO_2 + 2H_2O + 4Ni$ (R-6)	Unmixed combustion of methane	+1.56
	$H_2 + NiO \rightarrow Ni + H_2O$ (R-7)	OTM reduction with H_2	−0.02
	$CO + NiO \rightarrow Ni + CO_2$ (R-8)	OTM reduction with CO	−0.44
	$CH_4 + H_2O \rightarrow CO + 3H_2$ (R-9)	Methane steam reforming	+2.06
	$CO + H_2O \rightarrow CO_2 + H_2$ (R-10)	Water–gas shift	−0.41
	$CaO + CO_2 \rightarrow CaCO_3$ (R-11)	Carbonation of CO_2 sorbent	−1.79
	$CH_4 + CaO + 2H_2O \rightarrow CaCO_3 + 4H_2$ (R-12)	Sorption enhanced reforming of methane	−0.14

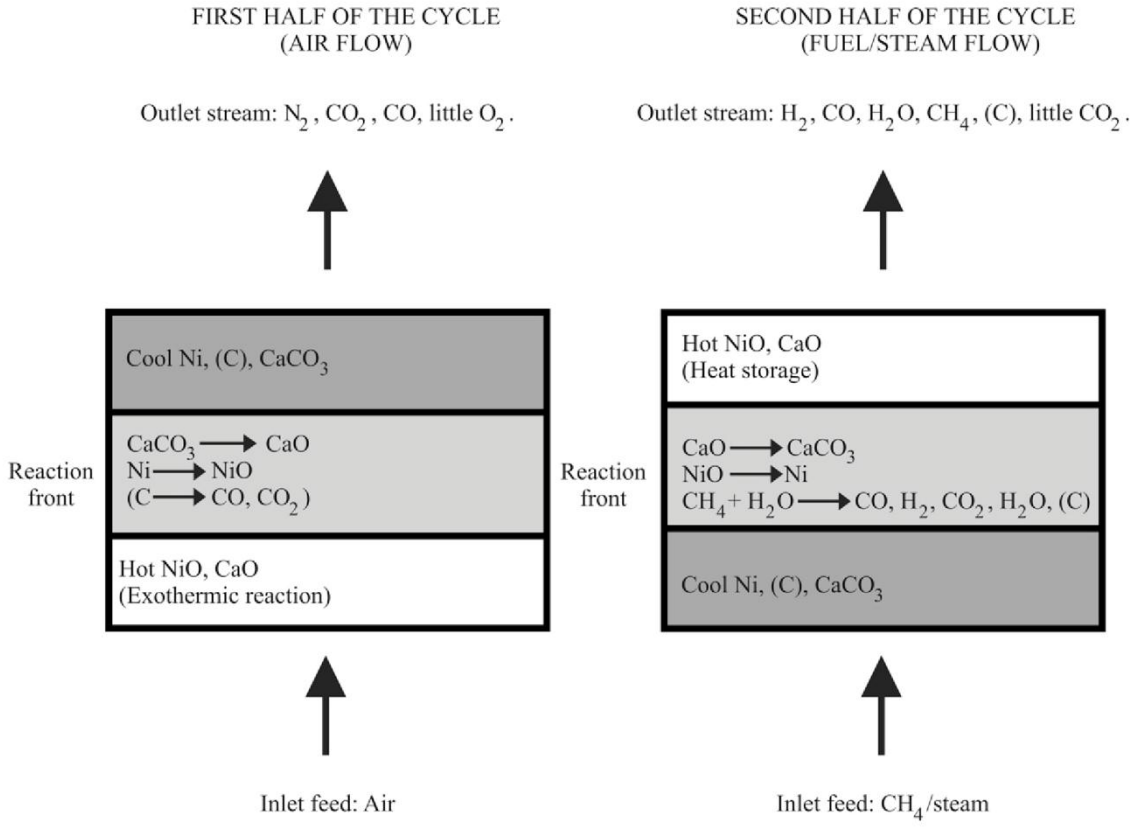

Fig. 1. Unmixed steam reforming process.

tor materials due to a hotter reactor center and colder walls, since USR allows the delivery of heat uniformly throughout a volume; (v) coupling of endothermic and exothermic reactions within a single reactor rather than relying on external heating, which ensures the compactness of the process. It is worth mentioning that the USR process offers similarities of chemical mechanism to chemical looping reforming (CLR). The term CLR, however, has been so far applied to interconnected fluidized beds through which the OTM circulates undergoing redox stages (see, for example, the references [4,5,9]). According to Dupont et al. [7], unmixed steam reforming is the term that could be used for the chemical looping reforming in a packed bed reactor.

Despite the relevance of such advanced reforming technology, there are only few papers dealing with the USR process. To the best of our knowledge, a comprehensive theoretical study dealing with the effect of the USR operating parameters on reformate composition has not yet been published. In this way, the present paper reports a detailed thermodynamic analysis of the methane unmixed steam reforming. Firstly, this work demonstrates that thermodynamic predictions are consistent with experimental results from USR isothermal tests under fuel/steam feed (CH_4/steam). The experimental data were compiled from Ref. [8]. Secondly, the effect of different parameters, like reactor temperature, inlet H_2O/CH_4, and $NiO_{reacted}/CH_4$ molar ratios, on the product gas composition and the conversions of CH_4 and H_2O is investigated for the USR process with/without calcium oxide. Additionally, an energy analysis is carried out, and the conditions for auto-thermal operation are identified. Finally, a summary of the optimized operating conditions under which H_2 production is maximized during auto-thermal USR is presented for both cases (with/without CO_2 acceptor). It is expected that the simulation results may provide an improved understanding of the chemical mechanism involved in the USR process, specially of the effect that the $NiO_{reacted}/CH_4$ molar ratio has on the reformate composition and energy demand. Moreover, the results of the present study could aid in monitoring and designing new experiments.

2. Simulation methodology

For a system in which many simultaneous reactions take place, equilibrium calculations are performed through the Gibbs energy minimization method (non-stoichiometric approach). The total free energy of the system, composed of an ideal gas phase and pure condensed phases, may be expressed as

$$\frac{G}{RT} = \left(\sum_{i=1}^{N} n_i \left[\frac{G_i^0}{RT} + \ln(y_i P) \right] \right)_{\text{gas}} + \frac{1}{RT} \left(\sum_{i=1}^{N} n_i G_i^0 \right)_{\text{condensed}} \quad (1)$$

The problem consists in finding the different values of n_i which minimize the objective function given by Eq. (1), subject to the constraints of elemental mass balance

$$\sum_{i=1}^{N} n_i \alpha_{ik} = b_k, \quad k = 1, \ldots, M \quad (2)$$

In the non-stoichiometric approach, the species coexisting in the system at equilibrium must first be defined. For the USR of methane, under fuel/steam feed, the following species were considered: H_2, H_2O, CO, CO_2, CH_4 (ideal gas phase), C (graphite), Ni, and NiO (pure solid phases). In the presence of CO_2 sorbent, the following solid phases are also included in the compound basis set: CaO, $Ca(OH)_2$ and $CaCO_3$. The thermodynamic data necessary for describing the Gibbs energy of the species were obtained from Ref. [15].

The non-linear programming model comprising the objective function to be minimized and the constraints is solved by the Solver function contained in the Microsoft Excel spreadsheet package. In our previous works [12,16,17], the Solver function was shown to be a robust tool, able to solve convex non-linear optimization problems. A detailed explanation concerning the Generalized Reduced Gradient (GRG) algorithm and the use of the Solver function in equilibrium calculations can be seen in Ref. [16].

The present analysis was carried out over the following variable ranges: temperature of 873–1073 K, inlet H_2O/CH_4 molar ratio of 1.2–4 and $NiO_{reacted}/CH_4$ molar ratio of 0.12–3.12. In the presence of CaO sorbent, the inlet CaO/CH_4 molar ratio was of 1. For inlet H_2O/CH_4 molar ratios in the range of 1.2–4, it is found that graphite formation is suppressed. Thus, the simulations are performed in the carbon-free region. Even though carbon deposited during fuel flow can be burnt in the next air flow, and, thus, catalyst poisoning can be avoided, unlike conventional catalytic steam reforming, it remains desirable to prevent carbon deposition from the viewpoint of both optimizing heat transfer and achieving a maximum H_2 yield. Without carbon deposition, the heat transfer would be expected to move deeper in the reactor bed and allow better coupling of the exothermic and endothermic reactions [11].

Basic operating parameters for the USR process are the feed flow rate and the time duration of each feed stage [6]. The approach developed in the present work demonstrates that the time parameter monitored over fuel/steam feed stage (second half of the cycle) can be correlated to the $NiO_{reacted}/CH_4$ molar ratio to be used in the thermodynamic simulation. From the experimental values of CH_4 molar flow rate and the reduction molar rate of nickel oxide, it is possible to determine the $NiO_{reacted}/CH_4$ molar ratio to be considered as input parameter in the Gibbs energy minimization method. In this way, the experimental values recorded over the fuel/steam feed stage can be compared with the equilibrium data.

The steam conversion, given by

$$H_2O\ \text{Conv.}\ (\%) = 100 \times \frac{n_{H_2O,in} - n_{H_2O,out}}{n_{H_2O,in}}, \quad (3)$$

and methane conversion efficiency, calculated by

$$CH_4\ \ \text{Conv.}\ (\%) = 100 \times \frac{n_{CH_4,in} - n_{CH_4,out}}{n_{CH_4,in}}, \quad (4)$$

are output parameters which, when maximized, could increase H_2 production, indicating a higher efficiency of the steam reforming reaction [8]. It is worth mentioning that, differently from the USR process, in the conventional steam reforming, steam conversion is not closely monitored and is rarely reported in the literature [7]. From Eq. (3), one can see that when steam conversion is negative, there is a net production of steam, when positive, there is a net consumption of steam.

Throughout this work, the selectivity of the carbon-containing products in the gas phase during fuel/steam feed stage was defined as:

$$\text{Sel.}_{CH_4\ \text{or CO or}\ CO_2}(\%) = 100 \times \frac{y_{CH_4\ \text{or CO or}\ CO_2}}{y_{CH_4} + y_{CO} + y_{CO_2}} \quad (5)$$

3. Results and discussion

3.1. Comparison with experimental values

In Fig. 2, it is possible to see the results obtained from two different experiments described in Ref. [8] along with thermodynamic equilibrium values computed in the present work. The experiments were performed at 1073 K, using an inlet H_2O/CH_4 molar ratio of 1.8 and different inlet molar flow rates of methane (1.13×10^{-4} and 3×10^{-4} mol s^{-1}). In all cases, the duration of fuel/steam feed was 600 s. Fig. 2 shows H_2 concentration (a), CO and CO_2 selectivity (b), CH_4 and H_2O conversions (c), and experimental values of NiO reduction molar rate along with inlet methane molar flow rate (d). As can be seen, there is a time value (inferior axis) corresponding to each $NiO_{reacted}/CH_4$ molar ratio (superior axis). To obtain $NiO_{reacted}/CH_4$ molar ratio as a function of time, one should divide the experimental value of NiO reduction molar rate by the constant inlet molar flow rate of methane. From Fig. 2(d), one can easily see that NiO reduction molar rate sharply decreases with time in a packed bed reactor, indicating that the reduction reactions occur mainly at the beginning of fuel/steam feed. Since the reactor is fed by a constant molar flow rate of methane, $NiO_{reacted}/CH_4$ molar ratio also decreases with time. As can be seen in Fig. 2, thermodynamic results are in agreement with the experimental ones. At the beginning of fuel/steam feed ($NiO_{reacted}/CH_4$ molar ratio of 3), the reduction reactions (R-6)–(R-8) dominate the equilibrium system, resulting in high CO_2 selectivity, negative steam conversion and low concentrations of H_2 (40–50 mol%). However, as fuel/steam feed stage nears its end ($NiO_{reacted}/CH_4$ molar ratio of ~0.25), CO selectivity, steam conversion and H_2 concentration increase, whereas CO_2 selectivity decreases. This trend suggests that the reforming reaction (R-9) becomes much more important than the reduction reactions as time passes. At the end of fuel flow, CO selectivity is ~70%, steam conversion reaches a plateau of ~50%, and H_2 concentration is ~75 mol%. This behavior also indicates that H_2 production is limited by the equilibrium of reaction (R-10). Note that time axis starts in a value different from $t = 0$ s. In fact, there is an initial period, termed by Dupont et al. [8] as 'dead-time', under which thermal decomposition of methane plays an important role in the chemical mechanism, and hardly any output gases can be measured. In this initial period, H_2 concentration is close to zero, and significant carbon deposition occurs, resulting in disagreement with thermodynamic analysis, since at an inlet H_2O/CH_4 molar ratio of 1.8 at 1073 K graphite formation is thermodynamically inhibited. By the end of 'dead-time', carbon deposition is greatly reduced, as reported in Ref. [8]. In this way, the period corresponding to 'dead-time' is not shown in Fig. 2, because thermodynamic modeling does not apply to this early stage.

It is worth pointing out that, if the $NiO_{reacted}/CH_4$ molar ratio were neglected in the simulations, and only the inlet H_2O/CH_4 molar ratio and temperature were considered as input data in the Gibbs energy minimization method, discrepancies between thermodynamic predictions and experimental results could be seen. Fig. 3 shows the experimental data along with the results of the simulations carried out with/without $NiO_{reacted}/CH_4$ molar ratio as input parameter. As can be seen, when $NiO_{reacted}/CH_4$ molar ratio is not considered, H_2 concentration, CO selectivity and steam conversion are overestimated, whereas CO_2 selectivity is underestimated, mainly at the beginning of fuel/steam feed, because the effect of the reactions (R-6)–(R-8) is not taken into account. Therefore, it is evident that the reacted NiO to CH_4 molar ratio must be carefully determined from the operating parameters, such as inlet molar flow rate of methane, and experimental outputs, like NiO reduction molar rate, so that the thermodynamic equilibrium values can be satisfactorily compared with the experimental ones all through fuel/steam feed stage. de Diego et al. [4] carried out a thermodynamic analysis for the chemical looping reforming of methane in a circulating fluidized bed reactor. Taking into account the conversions reached by two different oxygen carriers (NiO18-αAl_2O_3 and NiO21-γAl_2O_3) and solid circulation flow rate, they estimated $NiO_{reacted}/CH_4$ molar ratios for these oxygen carriers. Thermodynamic calculations were also performed including $NiO_{reacted}/CH_4$ molar ratios. Interestingly, even working with different oxygen carriers which had different conversions during CLR, very similar gas composition at the outlet of the fuel reactor was obtained when $NiO_{reacted}/CH_4$ molar ratio was the same. Besides, the product

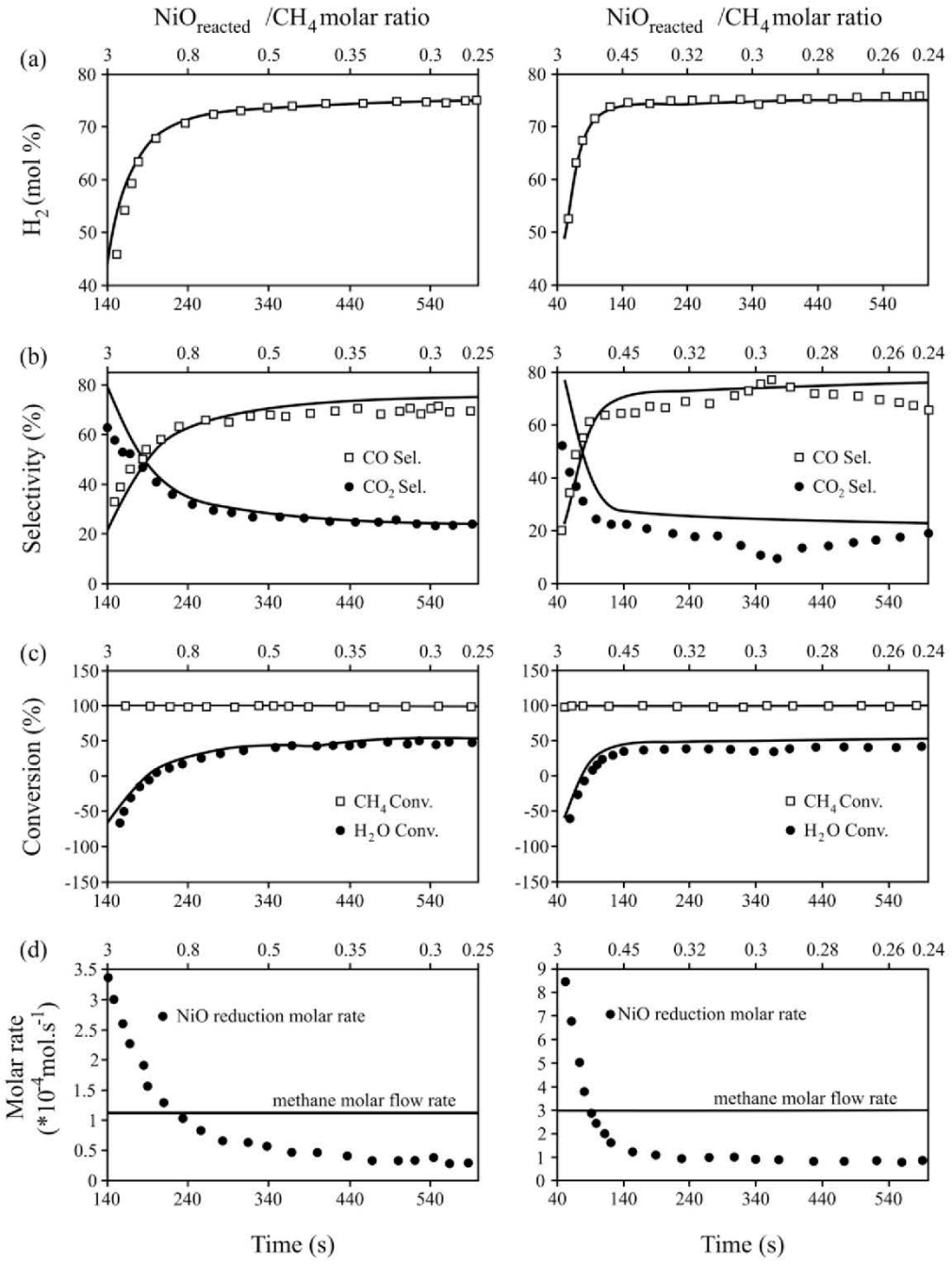

Fig. 2. (a) H_2 (mol%, dry basis), (b) CO and CO_2 selectivity, (c) CH_4 and H_2O conversion and (d) NiO reduction molar rate as a function of time. Markers: experimental data from [8]; solid lines: thermodynamic equilibrium data; methane molar flow rate used in the experiments: 1.13×10^{-4} (left plots) and 3×10^{-4} mol s^{-1} (right plots). Superior axis shows the $NiO_{reacted}/CH_4$ molar ratio corresponding to each time value.

gas compositions measured at the outlet of the fuel reactor were close to thermodynamic equilibrium. Thus, $NiO_{reacted}/CH_4$ molar ratio was found to be a suitable parameter to perform a thermodynamic analysis and compare results from different experiments with equilibrium values in a same diagram.

Obviously, for a given initial amount of NiO in a packed bed reactor and a fixed inlet flow rate of CH_4, thermodynamic analysis is not capable to predict NiO reduction molar rate as a function of time, because this depends on the kinetics of the gas-solid reaction. It is worth pointing out that, in Figs. 2 and 3, the product gas composition was presented as a function of time, because, at a given time t, NiO reduction molar rate is known from the experiments of Ref. [8]. In this way, the $NiO_{reacted}/CH_4$ molar ratio corresponding to each time value can be easily estimated, and the equilibrium composition throughout the fuel/steam feed stage can be calculated. Thermodynamic calculations, besides of being a reliable tool to verify if the experimental values are consistent and plausible, are useful to evaluate how different parameters (temperature, inlet H_2O/CH_4 and $NiO_{reacted}/CH_4$ molar ratios) affect the production of H_2 and the energy demand of the USR process with and without CaO sorbent. Thus, the viability of producing high purity H_2 under auto-thermal operation with *in situ* sorbent regeneration is investigated by means of a thermodynamic study. The next sections are focused on the effect of these parameters on the product gas

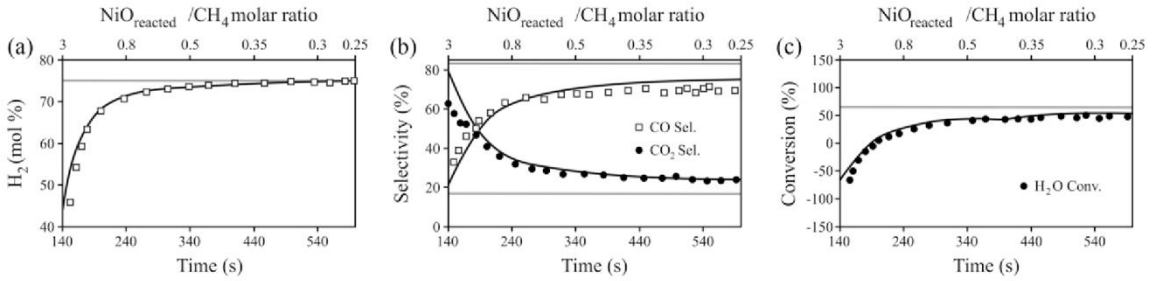

Fig. 3. (a) H_2 (mol%, dry basis), (b) CO and CO_2 selectivity, and (c) H_2O conversion as a function of time. Markers: experimental data from [8]; solid lines: results of the simulation with (black) and without (gray) $NiO_{reacted}/CH_4$ molar ratio as input parameter in the simulation. Experimental conditions from Ref. [8]: inlet $H_2O/CH_4 = 1.8$, $T = 1073$ K, methane molar flow rate (1.13×10^{-4} mol s^{-1}).

composition, CH_4 and H_2O conversions and enthalpy change during fuel/steam feed. The results are expressed in terms of a wide range of $NiO_{reacted}/CH_4$ molar ratios, because it is of interest to present generalized diagrams, which can be used as a benchmark to compare results from different experiments. Based on the results of Fig. 2, it was verified that $NiO_{reacted}/CH_4$ molar ratio decreases with time during fuel flow. In this way, the diagrams also indicate how product gas composition, H_2O and CH_4 conversions, and energy demand vary as time passes. Nevertheless, time values will depend on experimental conditions and kinetics. For example, in Fig. 2, for $NiO_{reacted}/CH_4$ molar ratio of ~3, thermodynamic and experimental results show that H_2 is obtained at a concentration of ~50 mol%. However, while this composition is reached at only 60 s in the case of the experiment performed with a methane inlet flow rate of 3×10^{-4} mol s^{-1}, for the experiment performed with a lower fuel flow rate (1.13×10^{-4} mol s^{-1}), this composition is achieved at ~160 s.

3.2. Effect of reactor temperature, inlet H_2O/CH_4 and $NiO_{reacted}/CH_4$ molar ratios in absence of CaO

Fig. 4 depicts the effect of $NiO_{reacted}/CH_4$ molar ratio on the concentrations (mol%, dry basis) of H_2 (a), CO (b), CO_2 (c) and the selectivity (%) of CO (d) and CO_2 (e), at 873, 973 and 1073 K for inlet H_2O/CH_4 molar ratios in the range of 1.2–4. At the beginning of fuel/steam feed stage ($NiO_{reacted}/CH_4$ molar ratio around 3), H_2 is found at low concentrations (35–45 mol%), with CO_2 being the major component of the gas phase (50–55 mol%), independently of inlet H_2O/CH_4 molar ratio and temperature. Note that, under these conditions, CO_2 selectivity is greater than 90% in all cases. This behavior suggests that, at the beginning of fuel flow, the OTM reduction reactions (R-6)–(R-8) are the main chemical mechanisms. However, as fuel/steam feed nears its end ($NiO_{reacted}/CH_4$ molar ratios ≤0.5), H_2 and CO concentration increase significantly. Thus, at the end of fuel flow, the endothermic reaction (R-9) is the main chemical mechanism. As can be seen, H_2 yield can be increased at the end of fuel/steam feed by using higher inlet H_2O/CH_4 molar ratios and more elevated temperatures, which is expected based on reaction (R-9). CO selectivity decreases with inlet H_2O/CH_4 molar ratio, whereas CO_2 selectivity increases, due to reaction (R-10). However, higher temperatures enhance CO production, because of the reverse water–gas shift reaction. The maximum H_2 content (~75%) is obtained at the inlet H_2O/CH_4 molar ratio equal to 4, with $NiO_{reacted}/CH_4$ molar ratio at the end of fuel/steam feed ≤0.5. Under these conditions, the main chemical mechanisms are the reactions (R-9) and (R-10), with minor effects of the reactions (R-6)–(R-8).

Fig. 5 shows the effect of $NiO_{reacted}/CH_4$ molar ratio on methane and steam conversions at 873 (a), 973(b) and 1073 K (c) for inlet H_2O/CH_4 molar ratios in the range of 1.2–4. As can be seen, at the beginning of fuel/steam feed, methane conversion is very high (>97%) and steam conversion is a negative value, independently of temperature and inlet H_2O/CH_4 molar ratio. This can be attributed to reaction (R-6), which is a very important mechanism at the beginning of fuel flow. At 1073 K, methane conversion over 98% can be obtained all through fuel/steam feed, for inlet H_2O/CH_4 molar ratios in the range of 1.2–4. In this case, the endothermic reactions (R-6) and (R-9) are enhanced due to the elevated temperature. On the other hand, at 873 K, methane conversion decreases as time passes, mainly at low inlet H_2O/CH_4 molar ratios. This is due to the fact that steam reforming is not so favored at lower temperatures. At a given inlet H_2O/CH_4 molar ratio, steam conversion increases with operation time, because steam reforming becomes increasingly important as time passes. Besides, the highest steam conversions are achieved at higher temperatures, due to the endothermicity of the reforming reaction. Experimental results corroborate these findings. Dupont et al. [7] report that, at an inlet H_2O/CH_4 molar ratio of 1.8, CH_4 and H_2O conversions of 55 and 42%, respectively, are obtained at the end of fuel/steam feed at 873 K, whereas higher conversions of methane (99%) and steam (49%) are obtained at the end of fuel flow at 1073 K. In addition, it is worth pointing out that the highest steam conversions are reached with lower inlet H_2O/CH_4 molar ratios. Abundant water in the feed stream results in a great amount of non-reacted steam in the system.

3.3. Effect of reactor temperature, inlet H_2O/CH_4 and $NiO_{reacted}/CH_4$ molar ratios in the presence of CaO

The USR is meant to operate in the presence of a CO_2 sorbent [7]. Fig. 6 depicts the effect of $NiO_{reacted}/CH_4$ molar ratio on the concentrations (mol%, dry basis) of H_2 (a), CO (b), CO_2 (c) and CaO conversion (d) at 873 and 973 K, for inlet H_2O/CH_4 molar ratios in the range of 1.2–4. In all cases, a CaO/CH_4 molar ratio of 1 was used. At 873 K, with an inlet H_2O/CH_4 molar ratio of 4, H_2 can be produced at concentrations over 98 mol% all through fuel/steam feed. Accordingly, Fig. 6 (d) indicates that under these conditions CaO conversions reach values near 100%. On the other hand, with lower inlet H_2O/CH_4 molar ratios (e.g. 1.2), high purity H_2 is obtained during the initial stage of fuel flow, corresponding to higher $NiO_{reacted}/CH_4$ molar ratios. As time passes, and $NiO_{reacted}/CH_4$ molar ratio diminishes, H_2 concentration and CaO conversion decrease. At the end of fuel/steam feed, H_2 concentration is ~82 mol%, and CaO conversion is ~55%. At the beginning of fuel flow, complete CaO conversion and high purity H_2 are obtained at 873 K, independently of inlet H_2O/CH_4 molar ratio. From Fig. 4(e) at 873 K, it is observed that CO_2 selectivity is ~100% at the beginning of the process, due to reaction (R-6). Thus, very favorable conditions for the carbonation reaction (R-11) are achieved at the beginning of fuel flow. However, as fuel/steam feed approaches its end, CO_2 selectivity decreases. At the end of fuel flow, for an inlet H_2O/CH_4 molar ratio of 1.2, CO_2 selectivity is of only 10% at 873 K (see Fig. 4e). In this way, the results indicate that higher inlet H_2O/CH_4 molar

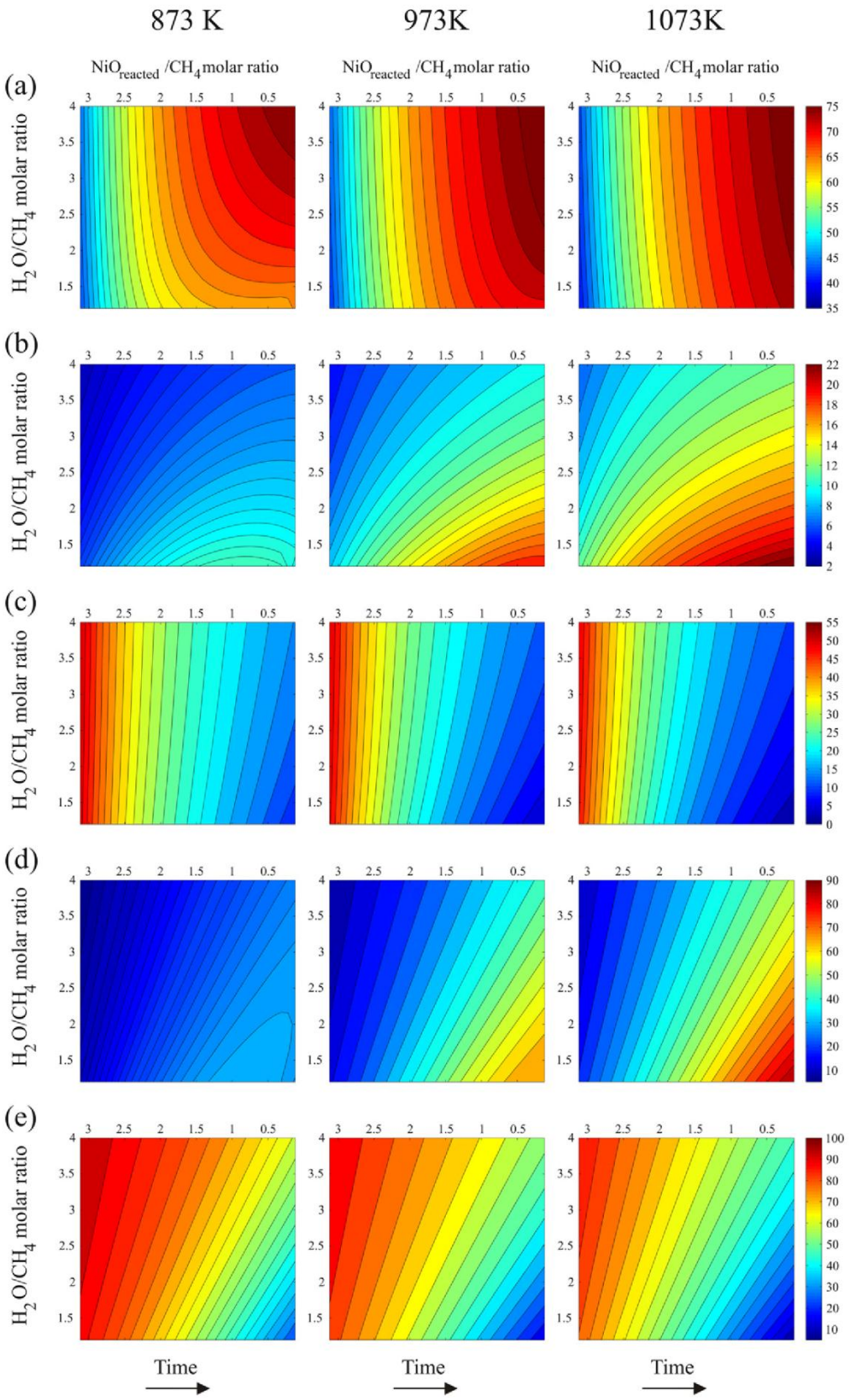

Fig. 4. H_2 (a), CO (b), CO_2 (c) concentration (mol%, dry basis) and CO (d), CO_2 (e) selectivity (%) as a function of inlet H_2O/CH_4 and $NiO_{reacted}/CH_4$ molar ratio at 873, 973 and 1073 K. Time duration of fuel/steam feed stage increases in the direction of the arrow.

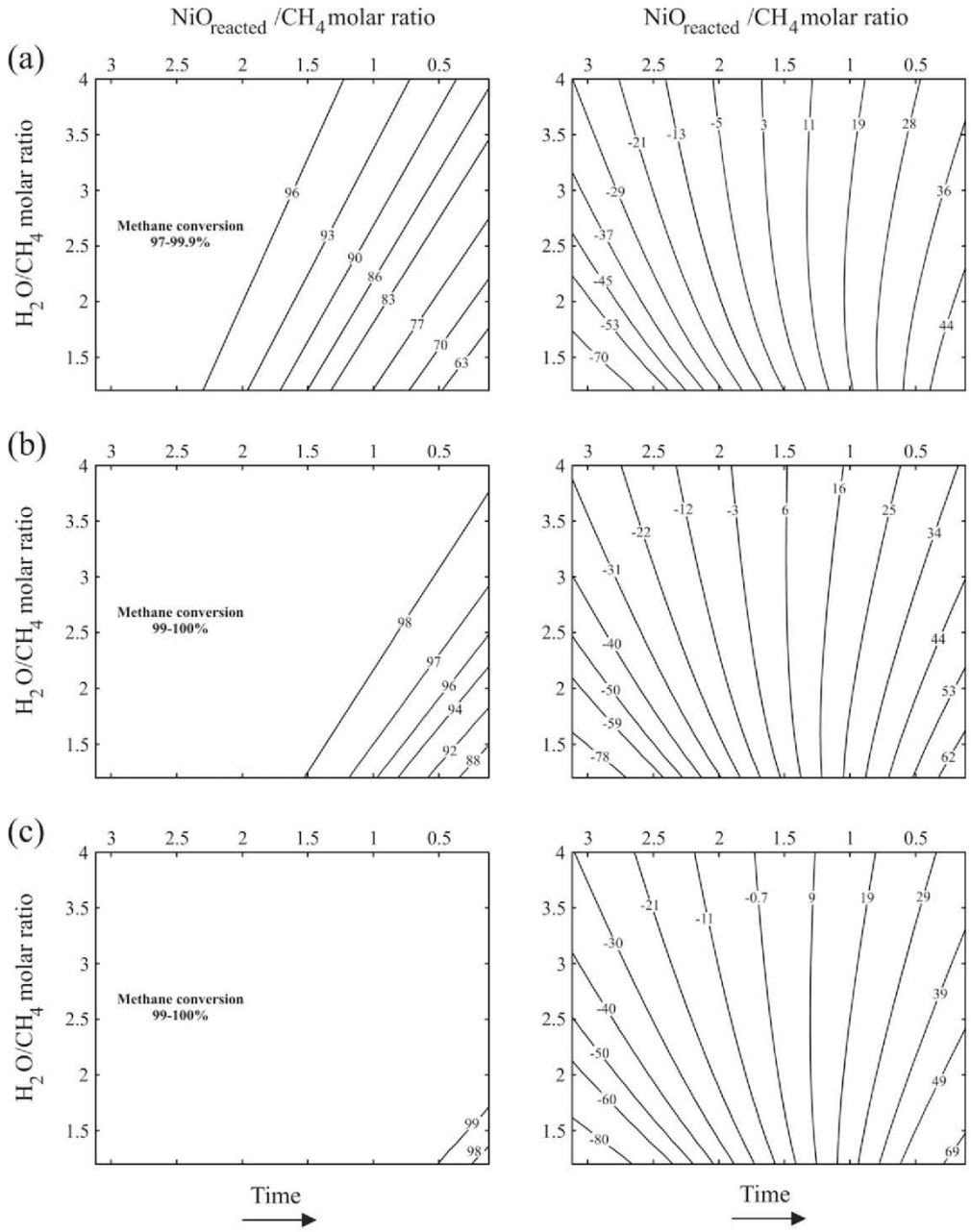

Fig. 5. Methane (left plots) and steam conversions (right plots), in %, as a function of inlet H_2O/CH_4 and $NiO_{reacted}/CH_4$ molar ratio at 873 (a), 973 (b) and 1073 K (c). Time duration of fuel/steam feed stage increases in the direction of the arrow.

ratios are suitable to produce H_2 during long periods at 873 K. In fact, reaction (R-12) shows that hydrogen production is enhanced with increasing steam in the feedstock. Nevertheless, in practice, the period of H_2-rich gas production depends on CO_2 breakthrough curve of the sorbent. Due to the fixed amount of sorbent in an experimental run, CO_2 concentration in the product gas raises rapidly once the sorbent reaches a certain capacity. This is termed CO_2 breakthrough [18]. During the pre-CO_2 breakthrough period, high purity H_2 is produced. By comparing Figs. 4(b) vs. 6(b) and Figs. 4(c) vs. 6(c), one can see that CO and CO_2 concentrations are enormously decreased in the presence of CaO sorbent. In absence of CaO, CO and CO_2 concentrations of ~12 and 55%, respectively, can be reached at 873 K, whereas in the presence of CO_2-acceptor, both CO and CO_2 concentrations are inferior to 1.6%. Unlike the process at 873 K, in which high purity H_2 is produced in a wide range of inlet H_2O/CH_4 and $NiO_{reacted}/CH_4$ molar ratios, Fig. 6(a) shows that at 973 K the region of high concentrations of H_2 is much narrower. Thus, at 973 K, H_2-rich gas is produced during shorter periods than at 873 K. Besides, the maximum H_2 concentration achieved at 973 K is ~90 mol%. Indeed, the exothermic carbonation (R-11) is not favored with temperature and, as a consequence, CaO conversion diminishes (compare Fig. 6(d) – 873 K vs. 973 K). Moreover, at 973 K, CO and CO_2 can be found at concentrations of approximately 16 mol%.

Methane and steam conversions are higher in the presence than in absence of CaO sorbent. This effect is noteworthy at 873 K. By comparing Figs. 5(a) vs. 7(a), one can see that, in the presence of CaO, using an inlet H_2O/CH_4 molar ratio greater than 3.5, the region of maximum methane conversion (>97%) can be extended until the end of fuel/steam feed (lower $NiO_{reacted}/CH_4$ molar ratios), due to

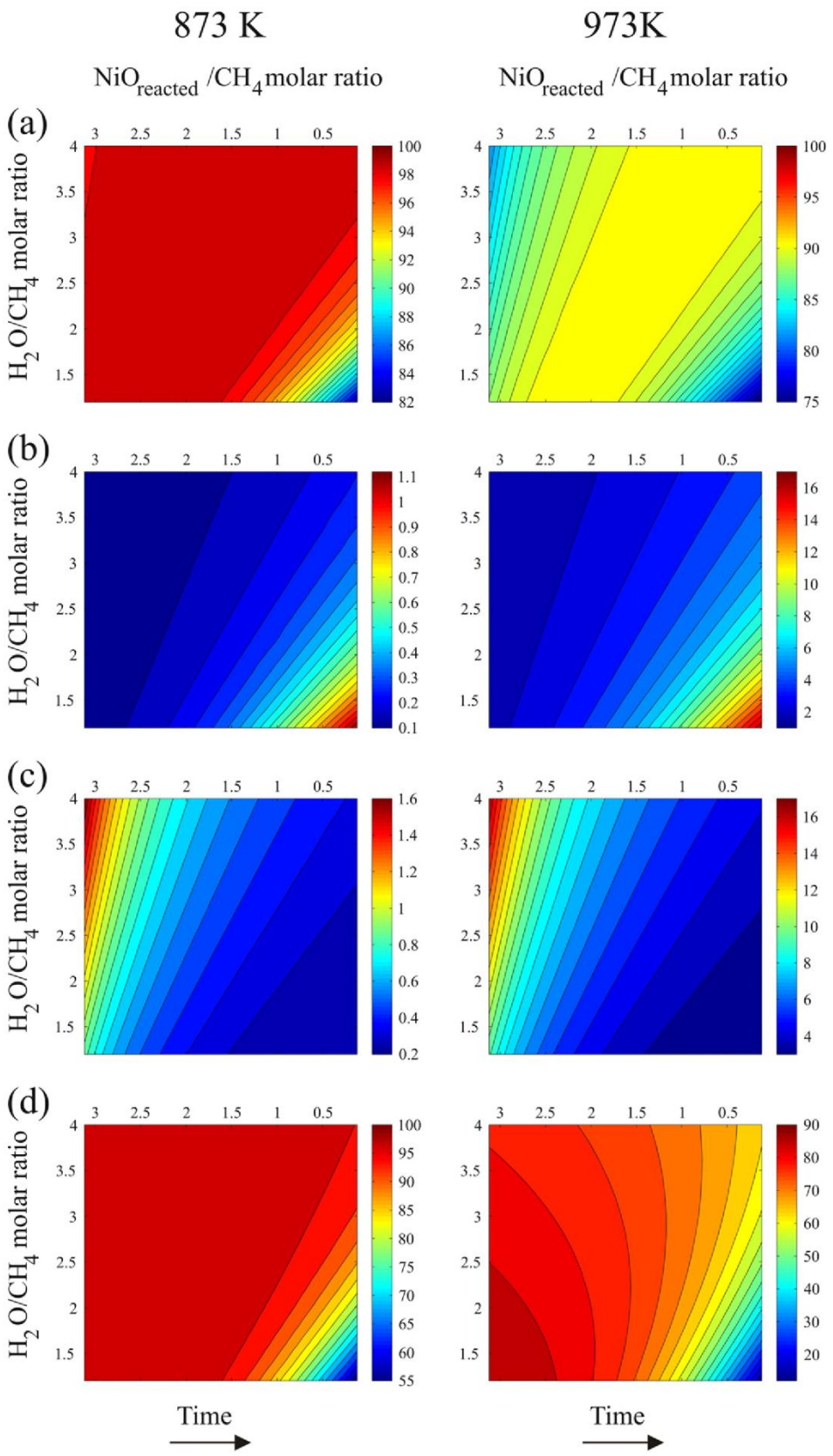

Fig. 6. H_2 (a), CO (b), CO_2 (c) concentration (mol%, dry basis) and CaO conversion (d) as a function of inlet H_2O/CH_4 and $NiO_{reacted}/CH_4$ molar ratio at 873 and 973 K. CaO/CH_4 molar ratio = 1. Time duration of fuel/steam feed stage increases in the direction of the arrow.

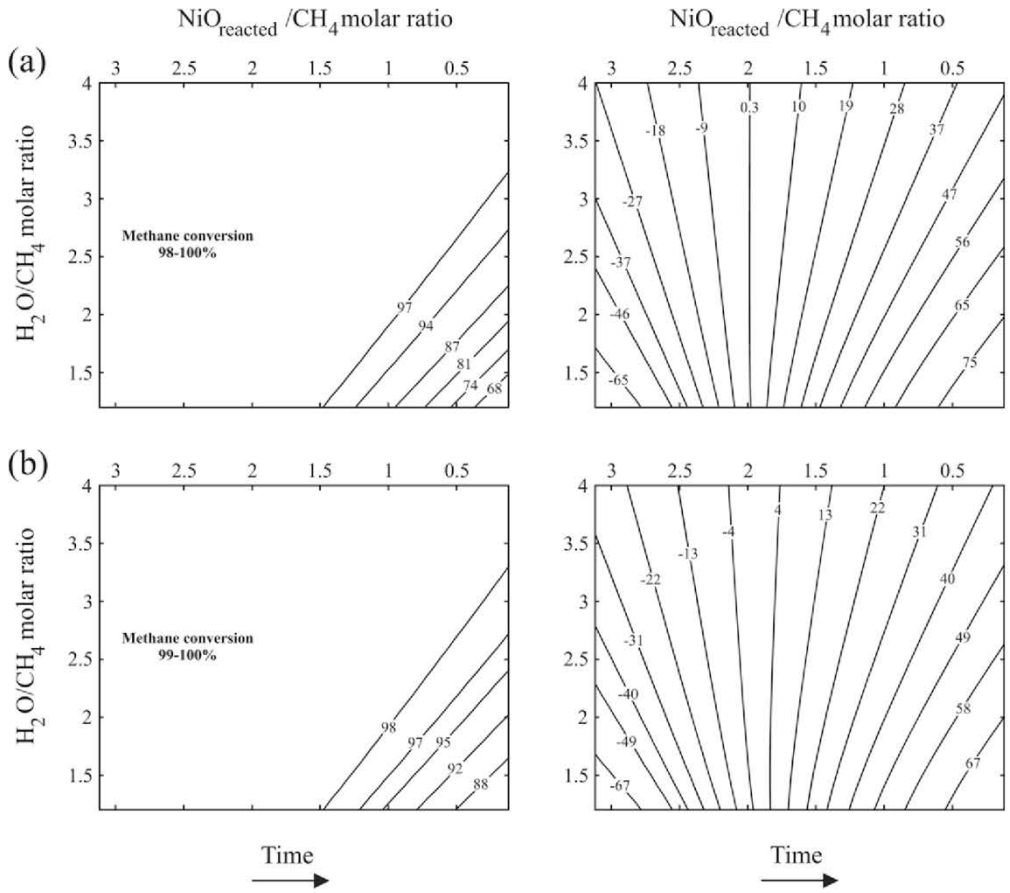

Fig. 7. Methane (left plots) and steam conversions (right plots), in %, as a function of inlet H_2O/CH_4 and $NiO_{reacted}/CH_4$ molar ratio at 873 (a) and 973 K (b). CaO/CH_4 molar ratio = 1. Time duration of fuel/steam feed stage increases in the direction of the arrow.

the enhanced reforming process. Besides, the maximum steam conversion reached in a process with CO_2-acceptor is much greater than that without CaO sorbent, *i.e.* 75% instead of 44%.

3.4. Molar composition during fuel/steam stage

Fig. 8 depicts the effect of $NiO_{reacted}/CH_4$ molar ratio on the moles of H_2 (a), CO_2 (b), CO (c) and H_2O (d) at 873 K, for inlet H_2O/CH_4 molar ratios in the range of 1.2–4, in a process without (left graphs) and with (right graphs) CaO sorbent. As can be seen, the number of moles of H_2 increases as time passes, because steam reforming becomes increasingly important with decreasing $NiO_{reacted}/CH_4$ molar ratio. In the presence of CaO sorbent, for inlet H_2O/CH_4 molar ratios >3, the number of moles of H_2 approaches 4 (3.7 mol H_2 per mol of CH_4), which is in agreement with reaction (R-12). At the beginning of fuel/steam feed stage, the inlet H_2O/CH_4 molar ratio exerts almost no influence on the number of moles of H_2. Under these conditions, the number of moles of H_2 is very low, due to reaction (R-7), which is favored at high $NiO_{reacted}/CH_4$ molar ratios. In fact, as can be seen in Fig. 8(d), there is a great steam production due to OTM reduction at the beginning of fuel flow. In absence of CaO sorbent, the number of moles of CO_2 is approximately 1 at the beginning of fuel flow, indicating that unmixed combustion of methane (reaction (R-6)) is an important chemical mechanism in the initial stages. In the presence of CaO, the number of moles of CO_2 is close to zero, independently of $NiO_{reacted}/CH_4$ molar ratio, which means that CO_2 is removed from the gas phase by the reaction (R-11) all through fuel/steam feed. The number of moles of CO increases as fuel/steam stage nears its end, because reaction (R-9) is the most important mechanism at the end of the fuel stage. Besides, CO is favored at lower inlet H_2O/CH_4 molar ratios, due to the reverse of water–gas shift reaction. The number of moles of CO in a process with CaO sorbent is much lower than that in a process without CaO, because of the enhanced water–gas shift reaction (R-10).

Fig. 9 depicts the effect of $NiO_{reacted}/CH_4$ molar ratio on the moles of H_2 (a), CO_2 (b) and CO (c) at 973 K, for inlet H_2O/CH_4 molar ratios in the range of 1.2–4, in a process without (left graphs) and with (right graphs) CaO sorbent. As can be observed, the trends of the number of moles of species with $NiO_{reacted}/CH_4$ molar ratio are the same as those shown in Fig. 8. In the presence of CaO, the number of moles of CO_2 and CO at 973 K is greater than at 873 K. This is due to the fact that the reaction (R-11) is exothermic and, thus, more favored at lower temperatures. Consequently, in a sorption enhanced reforming process, the number of moles of H_2 at 973 K is lower than at 873 K. In absence of CaO, by comparing Fig. 8 vs. Fig. 9, one can see that, at higher temperatures, the number of moles of H_2 and CO increase, due to endothermicity of reaction (R-9), whereas the number of moles of CO_2 decreases, because of the reverse of reaction (R-10).

3.5. Energy analysis

The USR process should be carried out as close to auto-thermal as possible, that is, with little or any heat being supplied to the reactor [11]. Table 2 depicts the input conditions and outputs for the auto-thermal operation of the methane USR. The amounts of reactants were calculated taking into account the thermo-neutral

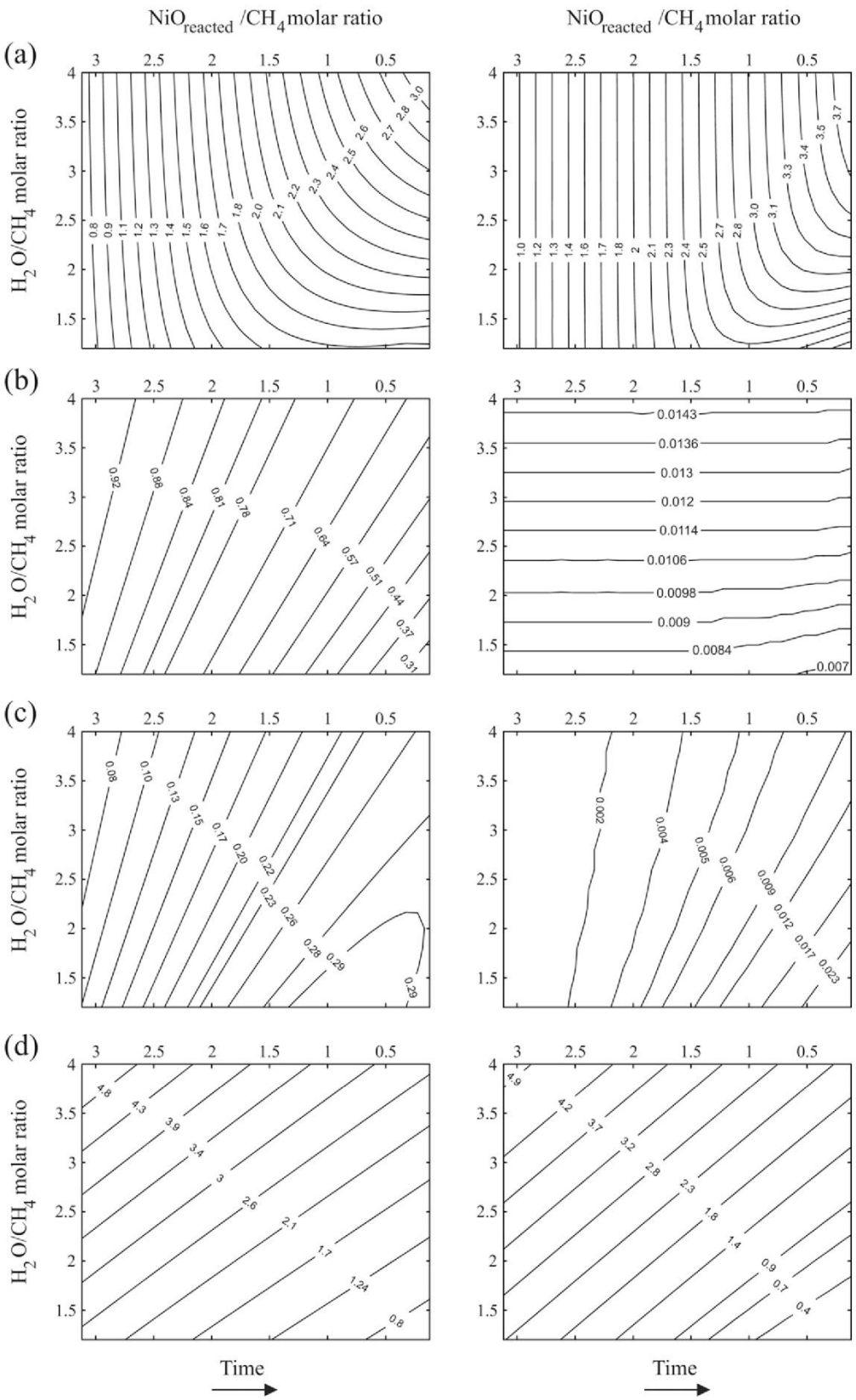

Fig. 8. Moles of species per mol of methane as a function of inlet H_2O/CH_4 and $NiO_{reacted}/CH_4$ molar ratio at 873 K. (a) H_2, (b) CO_2, (c) CO and (d) H_2O. Left contour plots: USR without CaO sorbent. Right contour plots: USR with CaO sorbent (CaO/CH_4 molar ratio = 1). Time duration of fuel/steam feed stage increases in the direction of the arrow.

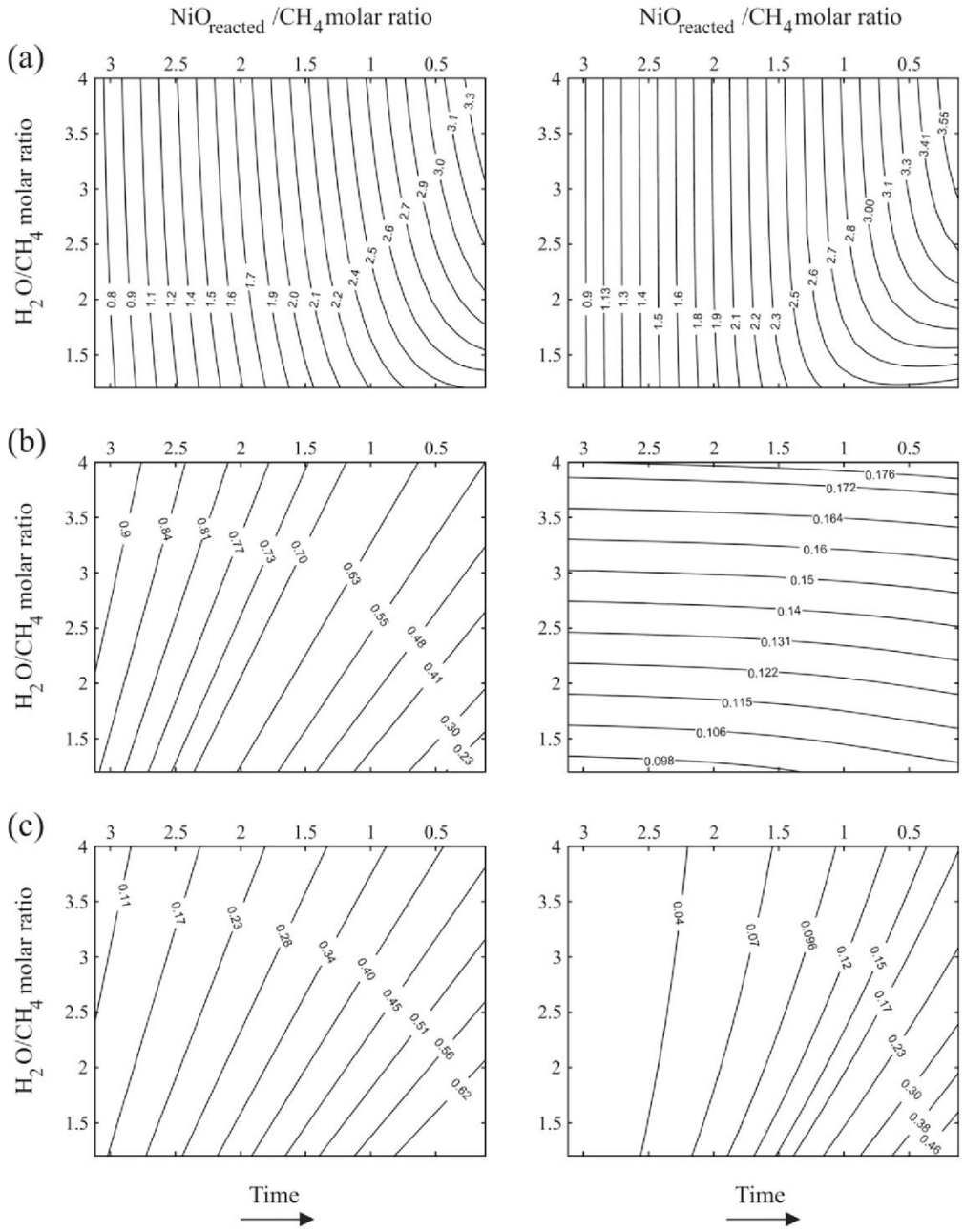

Fig. 9. Moles of species per mol of methane as a function of inlet H_2O/CH_4 and $NiO_{reacted}/CH_4$ molar ratio at 973 K. (a) H_2, (b) CO_2, and (c) CO. Left contour plots: USR without CaO sorbent. Right contour plots: USR with CaO sorbent (CaO/CH_4 molar ratio = 1). Time duration of fuel/steam feed stage increases in the direction of the arrow.

Table 2
Thermodynamic equilibrium results for USR process (with/without CaO sorbent) and comparison of USR (without sorbent) with ATR under thermo-neutral conditions.

Reforming technology	T (K)	Inlet molar ratio	Conversion (%)	H_2 (dry basis, %)	CO selectivity	CO_2 selectivity	ΔH (J mol^{-1}) (reactant)
(1) USR-fuel flow	1073	$NiO_{reacted}/CH_4 = 0.84$ $H_2O/CH_4 = 4$	H_2O: 18.33 CH_4: 99.97	73.21	42.59	57.37	2.334×10^5 (NiO)
(2) USR-air flow	1273	$O_2/Ni = 0.5$ $N_2/Ni = 1.881$	Ni: 100 O_2: 100	–	–	–	-2.336×10^5 (Ni)
(3) ATR thermo-neutral conditions	1073	$O_2/CH_4 = 0.42$ $H_2O/CH_4 = 4$	H_2O: 18.33 CH_4: 99.97	73.21	42.59	57.37	-0.01×10^5 (CH_4)
(1) USR-fuel flow with CaO sorbent	873	$NiO_{reacted}/CH_4 = 0.22$ $H_2O/CH_4 = 4$ $CaO/CH_4 = 1$	H_2O: 43.73 CH_4: 98.90 CaO: 96.54	99.08	25.54	42.38	0.737×10^5 (NiO)
(2) USR-air flow with $CaCO_3$	1273	$O_2/Ni = 0.5$ $N_2/Ni = 1.881$ $CaCO_3/Ni = 0.958$	Ni: 100 O_2: 100 $CaCO_3$: 100	–	–	–	-0.733×10^5 (Ni)

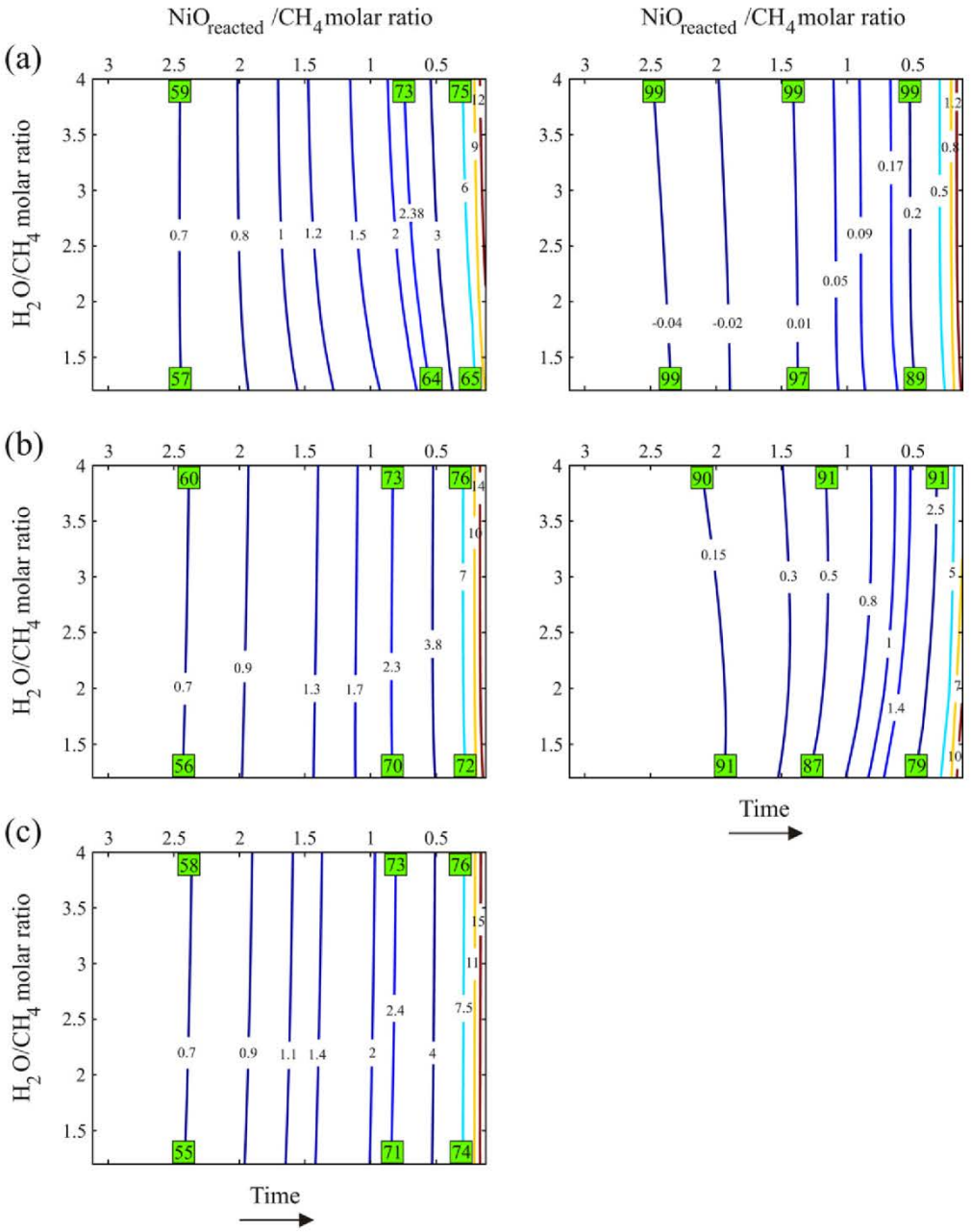

Fig. 10. Enthalpy change ($\times 10^5$ J mol^{-1} (NiO)) as a function of inlet H_2O/CH_4 and $NiO_{reacted}/CH_4$ molar ratio at 873 (a), 973 (b) and 1073 K (c). Left contour plots: USR without CaO sorbent. Right contour plots: USR with CaO sorbent (CaO/CH_4 molar ratio = 1). H_2 concentration (mol%, dry basis) is indicated at inlet H_2O/CH_4 molar ratios of 1.2 and 4. Time duration of fuel/steam feed stage increases in the direction of the arrow.

Table 3
Process outputs under optimized conditions; maximum H_2 concentration produced during auto-thermal methane USR with/without CaO.

T (K)	Without CaO			With CaO			
	873	973	1073	873		973	
Inlet H_2O/CH_4 molar ratio		4				4	
$NiO_{reacted}/CH_4$ molar ratio at the end of fuel/steam feed	0.76	0.82	0.84	1.22	0.12	1.82	1.02
H_2 (mol%, dry basis)	73.4	73.8	73.2	99	99	90	91
CO (mol%, dry basis)	6.1	9.1	11.4	0.16	0.25	2.5	3.1
CO_2 (mol%, dry basis)	18.9	17	15.4	0.5	0.4	5.6	7.5
CH_4 conversion (%)	93.6	99.6	99.9	99	99	99	99
H_2O conversion (%)	22.1	20.7	18.3	19	46	3	22
ΔH ($\times 10^5$ J mol^{-1} (NiO))	2.32	2.34	2.34	0.03	1.2	0.21	0.56
Inlet $CaCO_3$/Ni under air flow	–	–	–	1.4	0.7	1.3	1.1
Moles of graphite	–	–	–	–	–	–	–

conditions, that is, conditions under which the enthalpy change during fuel flow (ΔH), generally endothermic, is of the same magnitude of the heat released during air flow. Note that an adiabatic process is assumed. Additionally, a comparison of the USR (without sorbent) with the conventional ATR process under thermo-neutral conditions is shown. As can be seen, USR and ATR produce the same output (gas composition and conversions) on a same inlet H_2O/CH_4 molar ratio. The oxidation of the nickel catalyst is exothermic (-2.34×10^5 J mol^{-1}), and the heat necessary to decompose calcite through (R-2) is endothermic ($+1.673 \times 10^5$ J mol^{-1} at 1273 K). Therefore, for a $CaCO_3$/Ni molar ratio of 1.4, the oxidation of Ni provides the total amount of heat required to decompose $CaCO_3$ into CaO. In the specific case illustrated in Table 2 for the USR process with CaO sorbent, one can see that, during fuel flow, a heat input of $+0.737 \times 10^5$ J mol^{-1} is necessary. As some heat is needed for the reforming process, the $CaCO_3$/Ni molar ratio should be lower, *i.e.* of 0.958 instead of 1.4. It is worth mentioning that, by adding the CaO sorbent, it is possible to change the steam reforming reaction from an equilibrium that is strongly endothermic to one that is weakly exothermic [6], because of the exothermicity of carbonation reaction (R-11). When the heat for the steam reforming process is completely provided by the carbonation reaction ($\Delta H \sim 0$), the heat released during air flow can be entirely used to decompose the $CaCO_3$ into CaO. Consequently, the $CaCO_3$/Ni molar ratio of 1.4 can be used. It is worth pointing out that, when in auto-thermal operation, the reactor temperature oscillates during each cycle, with the lowest temperatures during the fuel feed and the highest at air flow [7]. In this work, the temperature at air flow is assumed to be 1273 K. Thus, the heat released during Ni oxidation is 2.34×10^5 J mol^{-1}.

Fig. 10 shows the enthalpy change during fuel flow as a function of the inlet H_2O/CH_4 and $NiO_{reacted}/CH_4$ molar ratio, without (left graphs) and with (right graphs) CaO sorbent, at 873 (a), 973(b) and 1073 K (c). At 1073 K, carbonation reaction is not favored. As a general trend, the energy demand is lower at the beginning of fuel/steam feed and increases continuously as time passes. At the beginning of fuel flow ($NiO_{reacted}/CH_4$ molar ratios >2.5), the exothermic reduction reactions (R-7) and (R-8) are favored. On the other hand, as fuel flow nears its end ($NiO_{reacted}/CH_4$ molar ratios <0.5), the endothermic steam reforming reaction (R-9) becomes the main chemical mechanism. In absence of CaO sorbent, energy demand at the end of fuel flow is high and increases with temperature due to the endothermicity of steam reforming (12, 14 and 15×10^5 J mol^{-1}, at 873, 973 and 1073 K, respectively). Note that hydrogen concentration also increases with time. However, the USR process should be carried out as close to auto-thermal as possible. In this way, the maximum concentration of H_2 is limited by thermo-neutral conditions, *i.e.*, the enthalpy change during fuel flow should be around 2.34×10^5 J mol^{-1}. As can be seen, with an inlet H_2O/CH_4 molar ratio of 4, H_2 at a concentration of 73 mol% can be obtained under these conditions. Therefore, longer operation times would result in high energy demand, with H_2 concentration being increased only slightly. In the presence of CaO sorbent, due to the exothermic carbonation reaction (R-11), the energy demand is much lower than that of the process without CaO. In fact, at 873 K, the energy demand is lower than 2.34×10^5 J mol^{-1} (NiO) all through fuel/steam feed. Thus, some heat released during air flow can be used to decompose $CaCO_3$ into CaO. If $NiO_{reacted}/CH_4$ molar ratio reached at the end of fuel/steam feed is low (e.g. 0.12), the energy demand during fuel flow is $\sim 1.2 \times 10^5$ J mol^{-1} (NiO). Thus, a $CaCO_3$/Ni molar ratio of ~0.7 can be used during air feed, in order to achieve an overall auto-thermal operation. If the duration of fuel/steam feed is not so long, and $NiO_{reacted}/CH_4$ molar ratio reached at the end of fuel flow is greater (~1.22), the enthalpy change during fuel/steam feed is near zero (0.05×10^5 J mol^{-1} (NiO)), which means that the heat required for steam reforming is completely provided by the carbonation reaction. In this way, a $CaCO_3$/Ni molar ratio of 1.4 (maximum possible value) can be used during air flow. These results indicate that high purity H_2 can be produced in an auto-thermal process, in which the sorbent is regenerated under air feeds. Interestingly, for the USR process operated with CaO sorbent at 873 K, it is found that weakly exothermic conditions are achieved at the beginning of the flow. As stated in the section 3.2, CO_2 selectivity is initially very high, due to reaction (R-6). Under these conditions, the exothermic reaction (R-11) is greatly favored, resulting in an exothermic equilibrium. At 973 K, the carbonation reaction is less favored than at 873 K. In this way, the energy demand at 973 is greater than that at 873 K.

3.6. Summary of the best operational conditions for the USR of methane

Table 3 shows the optimal conditions for the methane USR process with and without CaO sorbent. As can be seen, high H_2 concentrations can be reached under thermo-neutral conditions, with no carbon deposition during fuel flow. In absence of CaO, the reformate composition is suitable to feed the anode of solid oxide fuel cells (SOFC) or molten carbonate fuel cells (MCFC), which are more tolerant to other syngas compounds, and H_2 purity may not be so critical. For PEMFCs application, whose anode must be fueled by a high purity hydrogen stream containing CO at concentrations lower than 20 ppm to avoid platinum catalyst poisoning, the USR process should be operated with CaO in order to produce a H_2-rich gas. Besides, an additional step, including a COPROX (preferential CO oxidation) reactor, is also needed.

As can be seen in Table 3, it is possible to obtain H_2 at concentrations of about 99% at 873 K, using an inlet H_2O/CH_4 molar ratio of 4. During isothermal tests in the presence of a CO_2-sorbent, it is reported that H_2 contents above 90% can be obtained, using the same amount of water in the feed stream at 873 K [8]. Auto-thermal operation should be experimentally investigated for the methane USR process. More recently, Dupont et al. [11] reported catalyst and CO_2-sorbent regeneration, along with long periods of auto-thermal operation, for the USR process with waste cooking oil as a fuel.

4. Conclusions

The Gibbs energy minimization method is applied to investigate the unmixed steam reforming (USR) of methane to generate hydrogen for fuel cell application. The following conclusions can be drawn from the results of the present study:

- The methodology works in the region after the 'dead time'. After the initial period known as 'dead time', under which thermal decomposition of methane plays an important role in the chemical mechanism, and hardly any output gases can be measured, the experimental values of H_2 concentration, CO and CO_2 selectivities, and CH_4 and H_2O conversions approach the thermodynamic predictions. The methodology developed in the present study allows that the time parameter monitored over fuel/steam feed stage can be correlated to the $NiO_{reacted}/CH_4$ molar ratio to be used as input data in thermodynamic simulations. For a constant inlet molar flow rate of methane in a packed bed reactor, NiO reduction molar rate decreases as time passes. In this way, $NiO_{reacted}/CH_4$ molar ratio also decreases with time. Thermodynamic shows that, with decreasing $NiO_{reacted}/CH_4$ molar ratio, H_2 concentration, CO selectivity and steam conversion gradually increase, whereas CO_2 selectivity decreases. This behavior indicates that, as fuel/steam feed nears its end, the reforming reaction becomes increasingly important, with H_2 production limited by

the water–gas shift reaction. On the other hand, at the beginning of fuel/steam feed stage, the effect of the reactions involving NiO reduction is greater, resulting in low production of H_2 and high concentrations of CO_2 and H_2O.

- Thermodynamic calculations showed to be a reliable tool to verify if the experimental values are consistent and plausible. Besides, the results of the present work contribute towards a better understanding of the behavior of the product gas composition and enthalpy change during fuel/steam stage. Nevertheless, further investigations, including kinetics and reactor modeling, are encouraged to provide an accurate estimative of NiO reduction molar rate and output gas composition as a function of time.
- In absence of CaO sorbent, H_2-rich gas without carbon deposition can be obtained at inlet H_2O/CH_4 molar ratios greater than 1.2, with $NiO_{reacted}/CH_4$ molar ratios $\leq$0.5. Under these conditions, steam reforming is the main chemical mechanism, and H_2 at concentrations of 74–75 mol% can be produced. However, as time passes during fuel/steam feed stage, $NiO_{reacted}/CH_4$ molar ratio decreases, and, consequently, the overall process becomes increasingly endothermic, since the reforming reaction becomes more important than exothermic reduction reactions. In this way, the heat released during air flow may not be sufficient to supply the energy demand needed to produce H_2 at the highest concentrations. The duration of fuel/steam feed is limited by the conditions under which auto-thermal operation can be achieved. Thus, the maximum H_2 concentration that can be reached under thermo-neutral conditions (H_2O/CH_4 molar ratio of 4 and $NiO_{reacted}/CH_4$ molar ratio at the end of fuel/steam feed of ~0.8) is approximately 73 mol%.
- Unlike the USR process operated without CaO sorbent, in which H_2 concentration gradually increases with time, thermodynamic results indicate that, in the presence of CaO, using an inlet H_2O/CH_4 molar ratio of 4 at 873 K, H_2 at concentrations over 98% can be obtained all through fuel/steam feed stage. At the beginning of fuel/steam flow, $NiO_{reacted}/CH_4$ molar ratios are high (~3). Under these conditions, CO_2 concentrations would be very high in a process without CaO. However, in the presence of CaO sorbent, carbonation reaction is greatly enhanced at the beginning of fuel/steam feed, due to the great availability of CO_2, favoring the production of high purity hydrogen even at conditions under which NiO reduction reactions play an important role in the chemical mechanism. Comparatively, in absence of CaO sorbent, H_2 at concentrations of only 40 mol% are expected at the beginning of fuel flow. Thus, in the presence of a sorbent, with a suitable inlet H_2O/CH_4 molar rate, pure hydrogen can be produced continuously under fuel/steam feed at 873 K. Besides, the heat necessary for the steam reforming is provided by the carbonation reaction. In this way, the heat released during air flow can be entirely used to decompose the $CaCO_3$ into CaO. Therefore, with the USR technology, CaO can be regenerated under air flows, and an economically feasible process can be achieved. If $NiO_{reacted}/CH_4$ molar ratio reached at the end of fuel/steam stage is low (e.g. 0.12), a $CaCO_3$/Ni molar ratio of ~0.7 can be used during air feed, which results in an overall auto-thermal operation. If the duration of fuel/steam feed is not so long, and $NiO_{reacted}/CH_4$ molar ratio reached at the end of fuel/steam stage is greater (e.g. 1.22), a $CaCO_3$/Ni molar ratio of 1.4 (maximum possible value) can be used. Although theoretical results suggest that high purity H_2 can be produced during long periods of auto-thermal operation, in practice, the period of pure hydrogen production will be limited by the CO_2 breakthrough curve of the sorbent.
- In the presence of CaO, lower temperatures are preferred. By increasing 100 K, H_2 production can be greatly decreased, because the carbonation reaction is very sensitive to temperature. At 973 K, CaO conversion decreases with time even at an inlet H_2O/CH_4 molar ratio of 4. In this case, the maximum H_2 concentration is 90 mol%, obtained in a narrow range of $NiO_{reacted}/CH_4$ molar ratios. Thus, at 973 K, H_2-rich gas is produced during shorter periods than at 873 K.
- At 873 K, with CaO sorbent, it is possible to obtain 3.7 moles of H_2 per mol of CH_4, using inlet H_2O/CH_4 molar ratios greater than 3.
- The generalized diagrams of concentration, selectivity, moles and enthalpy change as a function of inlet H_2O/CH_4 and $NiO_{reacted}/CH_4$ molar ratio can aid in monitoring and designing new experiments involving the USR and chemical looping reforming technologies.
- Future work will include a detailed thermodynamic analysis of the USR process with sulfur-containing fuels.

Acknowledgments

The authors would like to acknowledge the CNPq-Brazil for financial support. Special thanks to Mr. José Walter Farfan Valverde for his contribution in this work.

References

[1] W.H. Chen, M.R. Lin, J.J. Lu, Y. Chao, T.S. Leu, Int. J. Hydrogen Energy 35 (2010) 11787–11797.
[2] Y.S. Seo, A. Shirley, S.T. Kolaczkowski, J. Power Sources 108 (2002) 213–225.
[3] Y. Li, Y. Wang, X. Zhang, Z. Mi, Int. J. Hydrogen Energy 33 (2008) 2507–2514.
[4] L.F. de Diego, M. Ortiz, F. García-Labiano, J. Adánez, A. Abad, P. Gayán, J. Power Sources 192 (2009) 27–34.
[5] T. Mattisson, M. Johansson, A. Lyngfelt, Fuel 85 (2006) 736–747.
[6] R.K. Lyon, J.A. Cole, Combust. Flame 121 (2000) 249–261.
[7] V. Dupont, A.B. Ross, E. Knight, I. Hanley, M.V. Twigg, Chem. Eng. Sci. 63 (2008) 2966–2979.
[8] V. Dupont, A.B. Ross, I. Hanley, M.V. Twigg, Int. J. Hydrogen Energy 32 (2007) 67–79.
[9] F.-X. Chiron, G.S. Patience, Fuel (2011), doi:10.1016/j.fuel.2011.02.029.
[10] P. Pimenidou, G. Rickett, V. Dupont, M.V. Twigg, Bioresour. Technol. 101 (2010) 6389–6397.
[11] P. Pimenidou, G. Rickett, V. Dupont, M.V. Twigg, Bioresour. Technol. 101 (2010) 9279–9286.
[12] A. Lima da Silva, I.L. Muller, Int. J. Hydrogen Energy 36 (2011) 2057–2075.
[13] N. Hildebrand, J. Readman, I.M. Dahl, R. Blom, Appl. Catal. A: Gen. 303 (2006) 131–137.
[14] R.V. Kumar, J.A. Cole, R.K. Lyon, Preprints of Symposia, 218th ACS National Meeting, vol. 44, no. 4, August 22–16, New Orleans, LA, 1999, pp. 894–898.
[15] O. Knacke, O. Kubaschewski, K. Hesselmann, Thermochemical Properties of Inorganic Substances, second ed., Springer-Verlag, Berlin, 1991.
[16] A. Lima da Silva, C.F. Malfatti, I.L. Muller, Int. J. Hydrogen Energy 34 (2009) 4321–4330.
[17] A. Lima da Silva, I.L. Muller, J. Power Sources 195 (2010) 5637–5644.
[18] B. Dou, V. Dupont, G. Rickett, N. Blakeman, P.T. Williams, H. Chen, Y. Ding, M. Ghadiri, Bioresour. Technol. 100 (2009) 3540–3547.

4.1.6. Performance of a PEMFC system integrated with a biogas chemical looping reforming processor: a theoretical analysis and comparison with other fuel processors (steam reforming, partial oxidation and auto-thermal reforming)

(Desempenho de um sistema composto por uma célula a combustível do tipo PEMFC integrado a um reformador não convencional de biogás, baseado na tecnologia de 'chemical looping': uma análise teórica e comparação com outros processadores de combustível (reforma a vapor, oxidação parcial e reforma auto-térmica))

Principais Resultados:

- Demonstração da possibilidade de obtenção de um processo eficiente, à pressão atmosférica, quando um processador de combustível baseado na tecnologia de *chemical looping* é integrado a um *stack* de células PEMFC; a literatura, até então, somente considerava a geração de eletricidade por *chemical looping* quando pressões elevadas eram empregadas, o que permitia o acoplamento com uma turbina a gás;
- H_2 pode ser eficientemente produzido a partir do processo de *chemical looping* usando biogás como combustível;
- Em comparação com os diversos tipos de reformadores, processadores de combustível que empregam a tecnologia de *chemical looping* e reforma a vapor permitem que maiores valores de voltagem sejam alcançados;
- A eficiência global alcançada por processadores de combustível baseados em *chemical looping* é similar àquela que pode ser alcançada por processadores baseados em reforma a vapor, auto-térmica e oxidação parcial;

INTERNATIONAL JOURNAL OF HYDROGEN ENERGY 37 (2012) 6580–6600

Available online at www.sciencedirect.com

SciVerse ScienceDirect

journal homepage: www.elsevier.com/locate/he

Performance of a PEMFC system integrated with a biogas chemical looping reforming processor: A theoretical analysis and comparison with other fuel processors (steam reforming, partial oxidation and auto-thermal reforming)

Aline Lima da Silva, Luís Frederico P. Dick, Iduvirges Lourdes Müller*

Program of Postgraduate Studies in Mining, Metals and Materials Engineering (PPGE3M), Federal University of Rio Grande do Sul – UFRGS, Campus do Vale, Setor 4, Av. Bento Gonçalves 9500, CEP 91501-970, Porto Alegre, RS, Brazil

ARTICLE INFO

Article history:
Received 10 November 2011
Received in revised form
30 December 2011
Accepted 8 January 2012
Available online 9 February 2012

Keywords:
Biogas
Reforming process
Chemical looping
Thermodynamic analysis
Material and energy balance
PEMFC system

ABSTRACT

In this work, the performance of a PEMFC (proton exchange membrane fuel cell) system integrated with a biogas chemical looping reforming processor is analyzed. The global efficiency is investigated by means of a thermodynamic study and the application of a generalized steady-state electrochemical model. The theoretical analysis is carried out for the commercial fuel cell BCS 500W stack. From literature, chemical looping reforming (CLR) is described as an attractive process only if the system operates at high pressure. However, the present research shows that advantages of the CLR process can be obtained at atmospheric pressure if this technology is integrated with a PEMFC system. The performance of a complete fuel cell system employing a fuel processor based on CLR technology is compared with those achieved when conventional fuel processors (steam reforming (SR), partial oxidation (PO) and auto-thermal reforming (ATR)) are used. In the first part of this paper, the Gibbs energy minimization method is applied to the unit comprising the fuel- and air-reactors in CLR or to the reformer (SR, PO, ATR). The goal is to investigate the characteristics of these different types of reforming process to generate hydrogen from clean model biogas and identify the optimized operating conditions for each process. Then, in the second part of this research, material and energy balances are solved for the complete fuel cell system processing biogas, taking into account the optimized conditions found in the first part. The overall efficiency of the PEMFC stack integrated with the fuel processor is found to be dependent on the required power demand. At low loads, efficiency is around 45%, whereas, at higher power demands, efficiencies around 25% are calculated for all the fuel processors. Simulation results show that, to generate the same molar flow-rate of H_2 to operate the PEMFC stack at a given current, the global process involving SR reactor is by far much more energy demanding than the other technologies. In this case, biogas is burnt in a catalytic combustor to supply the energy required, and there is a concern with respect to CO_2 emissions. The use of fuel processors based on CLR, PO or ATR results in an auto-thermal global process. If CLR based fuel processor is employed, CO_2 can be easily recovered, since air is not mixed with the reformate. In addition, the highest values of voltage and power are achieved when the PEMFC stack is fed on the stream coming from SR and CLR fuel processors. When a H_2 mixture is produced by reforming biogas through PO and ATR technologies, the relative

* *Corresponding author*. Tel.: +55 51 3308 9404.
E-mail address: adasilva26@gmail.com (A. Lima da Silva).
0360-3199/$ – see front matter Copyright © 2012, Hydrogen Energy Publications, LLC. Published by Elsevier Ltd. All rights reserved.
doi:10.1016/j.ijhydene.2012.01.031

anode overpotential of a single cell is about 55 mV, whereas, with the use of CLR and SR processes, this value is reduced to ~37 and 24 mV, respectively. In this way, CLR can be seen as an advantageous reforming technology, since it allows that the global process can be operated under auto-thermal conditions and, at the same time, it allows the PEMFC stack to achieve values of voltage and power closer to those obtained when SR fuel processors are used. Thus, efforts on the development of fuel processors based on CLR technology operating at atmospheric pressure can be considered by future researchers. In the case of biogas, the CO_2 captured can produce additional economical benefits in a 'carbon market'.

Copyright © 2012, Hydrogen Energy Publications, LLC. Published by Elsevier Ltd. All rights reserved.

Nomenclature

G	Total Gibbs energy of the system
G_i^0	Gibbs energy of species i at its standard state
n_i	Number of moles of species i
x_i	Mole fraction of species i
R	Gas Constant
T	Temperature of the system
P	Total pressure of the system
M, N	Total number of components and species, respectively
α_{ik}	Number of atoms of kth component present in each molecule of species i
b_k	Total number of atomic masses of kth component in the system
ΔH	change in enthalpy
$\Delta H_{(RX)}^{T_{FR}}$	variation of enthalpy of a certain reaction at a temperature T
$react._i$, $prod._i$	reactant and product species, respectively
H_i^T	enthalpy of species i at a temperature T
C_P	heat capacity of species i
F_S	oxygen-carrier flow-rate, g s^{-1} mol CH_4^{-1}
$\dot{n}_i$	molar flow-rate of species i, mol s^{-1}
M_i	molar mass of species i
$X_{NiO\rightarrow Ni}$	conversion of NiO to Ni in fuel reactor
n_{cells}	number of fuel cells in stack
i	fuel cell current density, A cm^{-2}
I	fuel cell current, A
$x_{H_2O}^{Sat.}$	molar fraction of water at saturation
$x_{inert}^{channel}$	molar fraction of inert species ($N_2 + CO_2 + CH_4$) at the anode interface
x_{inert}^{dry}	molar fraction of inert species at the product gas of biogas processor
$x_{N_2}^{channel}$	molar fraction of nitrogen at the cathode interface
$x_{in}^{hum.}$	molar fraction of inert species after humidification of the product gas of biogas processor
$x_{out}^{hum.}$	molar fraction of inert species at the exit gas of the anode
$x_{H_2O}^{dry}$	molar fraction of water at the product gas of biogas processor
$x_{H_2}^{dry}$	molar fraction of hydrogen at the product gas of biogas processor
$C_{O_2}^{interface}$	Concentration of oxygen gas at the surface of the catalyst at the cathode
$C_{H_2}^{interface}$	Concentration of hydrogen gas at the surface of the catalyst at the anode
F	Faraday Constant, 96,485 C mol^{-1}
W_{stack}	Power ouput of fuel cell stack, W
ψ	empirical parameter that describes membrane conditions
R_{elec}	ohmic electronic overvoltage resistance, Ω cm^{-2}
R_{prot}	ohmic protonic overvoltage resistance, Ω cm^{-2}
in	inlet
out	outlet

1. Introduction

Biogas is an attractive renewable energy source which is produced by anaerobic digestion of the organic matter [1]. It can be generated from municipal solid waste, wastewater, animal manure and agricultural wastes. Typically, biogas has a composition of 60–80% CH_4, 40–20% CO_2, 1% H_2O, 1–3% H_2S as well as traces of NH_3 [2]. Actually, its composition depends significantly on characteristics of the substrate digested and operation conditions of its source [3]. Therefore, the use of biogas as an energy source reduces the chance of possible emission of two greenhouse gases, CH_4 and CO_2, into the atmosphere at the same time. According to Komiyama et al. [4], there are two ways of using biogas as an energy source: (1) as a natural gas substitute, to burn it in a boiler or in a stove to obtain heat or to supply it to a gas engine for power generation, and (2) to reform it, to obtain hydrogen for fuel cell power generation. The latter way that involves a reforming process of biogas to generate hydrogen for fuel cell application can increase its energy conversion efficiency and reduce its NOx emissions to the atmosphere [5]. The merit of steam reforming of biogas to produce H_2, instead of simply using it as a natural gas substitute, lies in its additional freedom to be employed as a renewable energy source [6]. Indeed, biogas reforming for fuel cell application has been recently investigated through several experimental works [2,6–9]. It is worth mentioning that a reforming system to produce hydrogen from biogas requires a desulphurization unit as

a pretreatment process. The high sulfur content can deactivate severely the catalysts used in reforming and shift reactors, especially in the case of low catalyst operation temperature. Interestingly, the sulfur level achieved after desulphurization of biogas is comparable or even better than common natural gas or petroleum-based fuels. At this level, steam reforming of biogas should be a fairly simple and easy task, leading to power generation through fuel cells [4].

The technologies which can be applied for biogas reforming are the same than that used for natural gas reforming: steam reforming (SR), partial oxidation (PO) and auto-thermal reforming (ATR) [1]. Most of the studies focus on steam reforming, whereas only few publications deal with partial oxidation and auto-thermal reforming of biogas [9–12]. However, since the SR is an endothermic process and, therefore, energy demanding, the operational cost can be enlarged. Catalytic PO is a promising technology, which consists of sub-stoichiometric oxidation of methane. It is an exothermic process, which allows fast ignition of reactants and the use of a smaller reactor. However, hot spots usually occur along the reactor [13]. Partial oxidation operation is achieved by using air as an oxygen-carrier, since pure oxygen is not economical. Particularly, the capital costs of an oxygen plant can be remarkable. Up to 40% of the expenses of a reforming plant based on PO can be related to oxygen plant [14]. In this way, a major drawback of any partial oxidation operation or air addition is the nitrogen dilution of the hydrogen containing effluent [15]. Auto-thermal reforming (ATR) is very similar to the PO operation. The main difference is that PO does not require steam in the feedstock, whereas, in the ATR process, steam is added to the feed stream along with air [16]. In this way, at stoichiometric amounts of O_2, at which CH_4 is converted by partial oxidation with O_2 in air (R5), H_2 production in the ATR reactor can be increased, because of the effect of steam on the water–gas shift reaction (R8). Nevertheless, nitrogen dilution due to the use of air as oxygen-carrier is again the main drawback of this technology. Recently, chemical looping reforming (CLR) has been considered as an alternative process of catalytic steam reforming [17,18]. As can be seen in Fig. 1, a CLR system is made of two interconnected fluidized bed reactors, designated as air and fuel reactors. In the fuel reactor (FR), the oxygen-carrier (usually a metal oxide

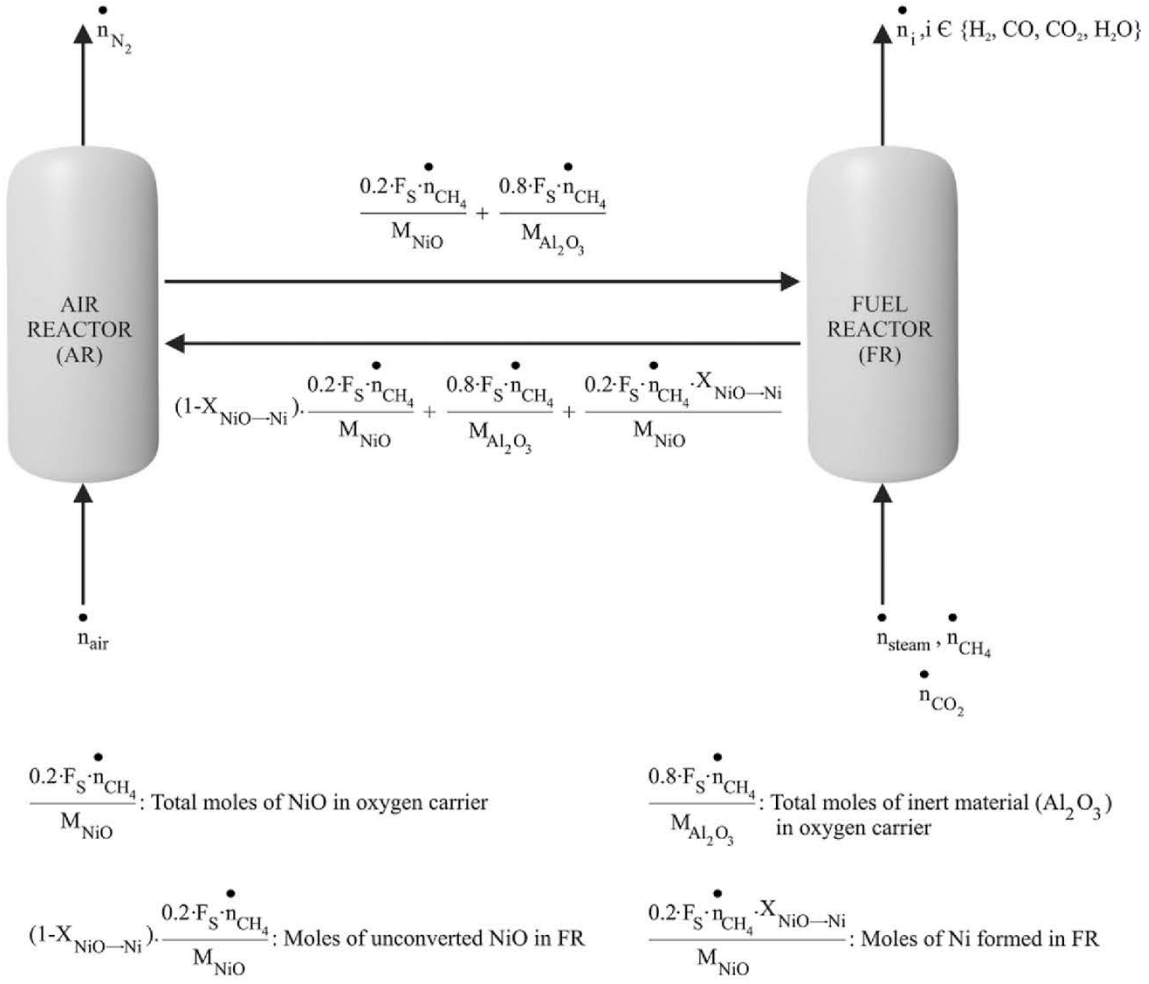

Fig. 1 – Chemical Looping Reforming process, with fuel reactor fed on methane (or clean model biogas) and steam. Material flux between the air and fuel reactors is also indicated.

(MeO)) is reduced to a metal (Me), with oxygen being transferred from the metal oxide to the fuel. In CLR technology, the desired product is H_2-rich reformate. In this way, the oxygen-to-fuel ratio is kept low to prevent the complete oxidation of the fuel to CO_2 and H_2O. The reduced metal is further transferred into the air reactor (AR) where it is oxidized with air, and the material regenerated is ready to start a new cycle. The oxidation reaction of the metal in the air reactor is very exothermic, whereas the reduction reactions and steam reforming in the fuel reactor are endothermic. So, the heat for the endothermic reactions is provided by circulating solids coming from the air reactor at higher temperature. The heat generated in the air reactor must be high enough to fulfill the heat balance in the system [18]. The flue gas leaving the air reactor contains mainly N_2 and non-reacted O_2, whereas the exit gas from the fuel reactor contains H_2, CO, H_2O and CO_2. Therefore, the major advantage of CLR technology is that the heat needed for converting the fuel into H_2 is supplied without costly oxygen production and without nitrogen dilution of the hydrogen containing effluent. In this way, CLR process could be an alternative technology to the conventional ATR. CLR has been extensively investigated using methane or natural gas as a fuel in a system as indicated in Fig. 1 [17,19–21]. However, to the best of our knowledge, a detailed study, experimental or theoretical, dealing with the CLR of biogas, has not yet been published. CLR can have additional benefits if CO_2 capture is considered. If biogas is used, the CO_2 captured could produce additional economical benefits in a 'carbon market'. Preliminary results from an experimental research [3] show the possibility of H_2 production from CLR using biogas with a CH_4/CO_2 molar ratio of 1.5 (46%vol CH_4, 31%vol CO_2) in a fluidized bed reactor. It is worth mentioning that, in reference [3], steam was added to the feedstock. However, for methane CLR, Ortiz et al. [18] showed that H_2O should be avoided in the fuel reactor in order to increase the energetic efficiency of the process and H_2 yield. Steam is considered only to prevent carbon formation in the fuel reactor. Nevertheless, carbon formation was not observed during continuous operation using Ni-based oxygen-carriers even when H_2O was not present in the feed stream [17]. Therefore, addition of steam should not be necessary in the fuel reactor.

Qi et al. [22] has reviewed the integrated fuel processors for PEMFC applications. Different reactor and heat exchanger configurations have been proposed for stationary systems operating on natural gas feed stream [23–26] and portable systems using methanol or ethanol [27,28]. More recently, Northrop et al. [29] evaluated a thermally integrated fuel processor design for fuel cell applications using methane as a fuel. However, it is important to emphasize that there is no previous study focused on the analysis of the global efficiency of CLR fuel processor integrated with a PEMFC stack. Therefore, this work is the first one to present optimized conditions of H_2 production through CLR of biogas working with Ni-based oxygen-carrier and to investigate the integration of CLR technology with a fuel cell system. In this way, it is expected that the results from this research can be used as a start point in experimental investigations. From literature [30], CLR is described as an attractive process only if the system operates at high pressure (1–2 MPa). In this case, a gas turbine is considered to produce energy. The present research aims to show that advantages of the CLR process can be obtained at atmospheric pressure if this technology is integrated with a PEMFC system. The performance of a complete fuel cell system employing a fuel processor based on CLR technology is compared with those achieved when conventional fuel processors (steam reforming (SR), partial oxidation (PO) and auto-thermal reforming (ATR)) are used. In the first part of this paper, the Gibbs energy minimization method is applied to the unit comprising the fuel- and air-reactors in CLR or to the reformer (SR, PO, ATR). The goal is to investigate the characteristics of these different types of reforming process to generate hydrogen from clean model biogas with a constant molar ratio of $CH_4/CO_2 = 1.5$ and identify the optimized operating conditions for each process. Then, in the second part of this research, material and energy balances are solved for the complete fuel cell system processing biogas, taking into account the optimized conditions found in the first part. The pretreatment unit (desulphurization) is not considered in the present analysis. With respect to the literature dealing with optimization of hydrogen production through CLR, it is worth mentioning the theoretical analysis performed by Ortiz et al. [18]. These authors carried out a thermodynamic analysis for methane CLR and identified the optimized conditions for auto-thermal operation with high H_2 yield.

2. Simulation methodology

The simulations were entirely performed using the Microsoft Excel spreadsheet package. Mass and energy balances, as well as the electrochemical model, can be easily implemented and solved using spreadsheets. The equilibrium compositions were computed by the Solver function, as described in the next section.

2.1. *Equilibrium composition in reformer (SR, PO, ATR) and FR–AR unit (CLR)*

For a system in which many simultaneous reactions take place, equilibrium calculations are performed through the Gibbs energy minimization method (non-stoichiometric approach). The total free energy of the system, composed of an ideal gas phase and pure condensed phases, may be expressed as

$$\frac{G}{RT} = \left(\sum_{i=1}^{N} n_i \left[\frac{G_i^0}{RT} + \ln(x_i P) \right] \right)_{gas} + \frac{1}{RT} \left(\sum_{i=1}^{N} n_i G_i^0 \right)_{condensed} \quad (1)$$

The problem consists in finding the different values of n_i which minimize the objective function given by Eq. (1), subject to the constraints of elemental mass balance

$$\sum_{i=1}^{N} n_i \alpha_{ik} = b_k \quad k = 1 \ldots M \quad (2)$$

In the non-stoichiometric approach, the species coexisting in the system at equilibrium must first be defined. The following species were considered: H_2, H_2O, CO, CO_2, CH_4 (ideal gas phase) and C (graphite, pure solid phase). In the case of CLR system, Ni and NiO are also included in the compound

basis set. The thermodynamic data necessary for describing the Gibbs energy of the species were obtained from Ref. [31].

The non-linear programming model comprising the objective function to be minimized and the constraints is solved by the Solver function contained in the Microsoft Excel spreadsheet package. In previous works [32,33], the Solver function was shown to be a robust tool, able to solve convex non-linear optimization problems. A detailed explanation concerning the Generalized Reduced Gradient (GRG) algorithm and the use of the Solver function in equilibrium calculations can be seen in [33].

In the case of SR process, the equilibrium composition was determined at different temperatures and inlet H_2O/CH_4 molar ratios. The temperature of the SR reactor is an input parameter, hence, the preheat temperature of reactants affects only the heat duty that is transferred to the SR reactor, and not the equilibrium composition. On the other hand, as PO and ATR reactors are modeled as adiabatic reactors, the preheat temperature of reactants affects the adiabatic temperature of the reactor and, hence, the equilibrium composition of the reactor. Under adiabatic conditions, ΔH is nearly zero in Eq. (3):

$$\Delta H = H_{\text{Products}}^{T_{\text{adiabatic}}} - H_{\text{Reactants}}^{T_{\text{preheat}}} \tag{3}$$

Where:

$$H_{\text{Reactants}}^{T_{\text{preheat}}} = \sum_{i=1}^{N} \text{react.}_i H_i^{T_{\text{preheat}}} \tag{4}$$

$$H_{\text{Products}}^{T_{\text{adiabatic}}} = \sum_{i=1}^{N} \text{prod.}_i H_i^{T_{\text{adiabatic}}} \tag{5}$$

and

$$H_i^T = H_i^{298} + \int_{T=298\ \text{K}}^{T} C_P dT \tag{6}$$

An important parameter to be considered in the analysis of PO, ATR and CLR is the air/CH_4 molar ratio:

$$\text{air}/CH_4 = \frac{\dot{n}_{O_2}}{2 \cdot \dot{n}_{CH_4}} \tag{7}$$

with O_2 fed to AR (CLR) or to reformer (PO and ATR), and CH_4 fed to FR (CLR) or to reformer (PO and ATR).

2.2. Main chemical reactions

Although the methodology of the present study is based on a non-stoichiometric approach and, hence, there is no need of considering chemical reactions in order to compute equilibrium compositions, the main reactions involved in the system CH_4–CO_2–H_2O–O_2–Ni are presented in Table 1. These reactions can be useful to understand the main trends of the species.

2.3. FR–AR unit (CLR)

In a CLR system, the main operating parameters are: oxygen-carrier circulation flow-rate (F_S), air/CH_4 and H_2O/CH_4 molar ratios, and oxygen-carrier conversion. The simulations were carried out assuming a NiO based carrier consisting of 20 wt % NiO and 80 wt% Al_2O_3. It is also considered that Ni particles leaving FR are totally oxidized in the air reactor, forming NiO again to be reduced in FR in a new cycle. Thus, all the oxygen in the air is consumed by the reaction (R17). According to Ortiz et al. [18], the heat balance in a CLR unit

Table 1 – Main chemical reactions involved in SR, ATR, PO and CLR of clean model biogas.

Reaction n°	Reaction	Reaction type	$\Delta H^0_{298\ \text{K}}$ J mol^{-1}
(R1)	Steam reforming	$CH_4 + H_2O \rightarrow CO{+}3H_2$	205,800
(R2)	Steam reforming	$CH_4 + 2H_2O \rightarrow CO_2 + 4H_2$	164,600
(R3)	Dry reforming	$CH_4 + CO_2 \rightarrow 2CO + 2H_2$	247,000
(R4)	Combustion	$CH_4 + 2O_2 \rightarrow CO_2 + 2H_2O$	−802,600
(R5)	Partial oxidation	$CH_4 + 0.5O_2 \rightarrow CO + 2H_2$	−36,000
(R6)	CO oxidation	$CO + 0.5O_2 \rightarrow CO_2$	−282,993
(R7)	H_2 oxidation	$H_2 + 0.5O_2 \rightarrow H_2O$	−241,856
(R8)	Water–gas shift	$CO + H_2O \rightarrow CO_2{+}H_2$	−41,200
(R9)	Methanation	$CO + 3H_2 \rightarrow CH_4 + H_2O$	−205,800
(R10)	Methanation	$CO_2 + 4H_2 \rightarrow CH_4 + 2H_2O$	−164,600
(R11)	Methanation	$2CO + 2H_2 \rightarrow CH_4 + CO_2$	−247,000
(R12)	Reverse water–gas shift	$CO_2 + H_2 \rightarrow CO + H_2O$	41,200
(R13)	Methane decomposition	$CH_4 \rightarrow C + 2H_2$	74,500
(R14)	Boudouard	$2CO \rightarrow CO_2 + C$	−172,500
(R15)	Reverse coal-gas	$CO_2 + 2H_2 \rightarrow 2H_2O + C$	−90,191
(R16)	Carbon gasification	$C + H_2O \rightarrow CO + H_2$	131,328
(R17)	Oxidation oxygen-carrier	$Ni + 0.5O_2 + 1.881N_2 \rightarrow NiO + 1.881N_2$	−239,000
(R18)	Oxygen-carrier reduction with CO	$CO + NiO \rightarrow CO_2 + Ni$	−44,000
(R19)	Oxygen-carrier reduction with H_2	$H_2 + NiO \rightarrow H_2O + Ni$	−2000
(R20)	Oxygen-carrier reduction with Ni	$NiO + C \rightarrow CO + Ni$	129,217
(R21)	Oxygen-carrier reduction with CH_4	$CH_4 + 4NiO \rightarrow CO_2 + 2H_2O + 4Ni$	156,000
(R22)	Global CLR reaction of biogas	$NiO + CH_4 + CO_2 + H_2O \rightarrow Ni + (C, CO, CO_2, H_2O) + H_2$	Endothermic

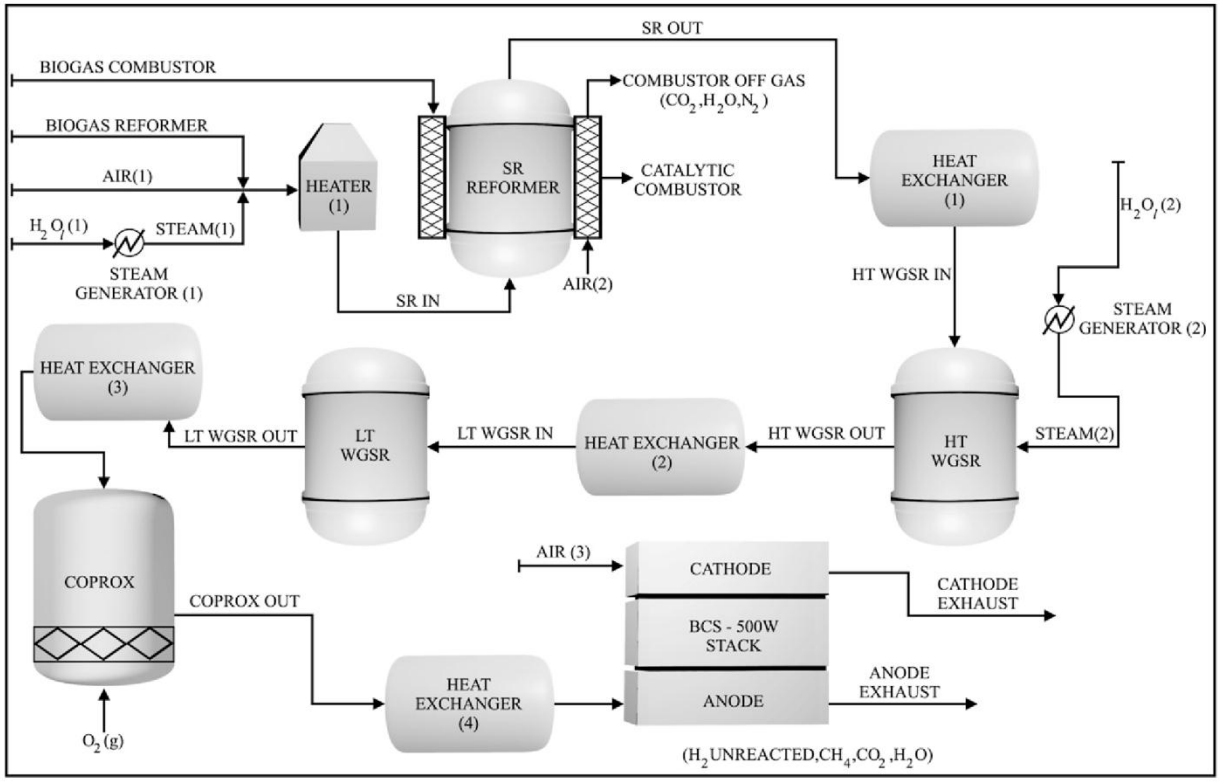

Fig. 2 – PEMFC stack integrated with the SR fuel processor unit.

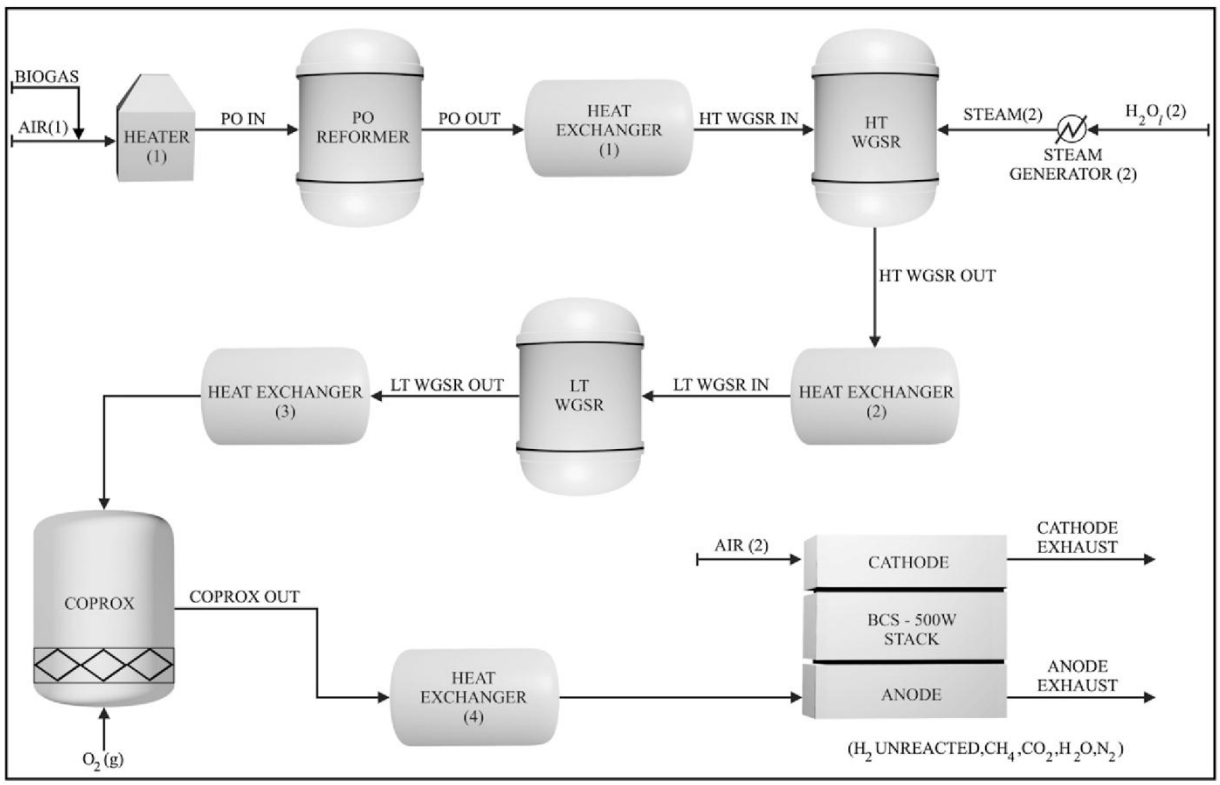

Fig. 3 – PEMFC stack integrated with the PO fuel processor unit.

can be done considering that the oxygen-to-fuel molar ratio can be controlled by two ways: (case 1) limiting the oxygen introduced to the air reactor by the air flow, i.e., varying the global air-to-fuel ratio, or (case 2) restricting the oxygen supplied to the fuel reactor by the oxygen-carrier circulation flow-rate. In the present work, the 'case 1' was considered. A lower excess of air was needed in the 'case 1', as demonstrated in [18].

In order to determine the auto-thermal conditions in the FR–AR unit in CLR system, the FR temperature is fixed (1073 K), and the energy in the air reactor is balanced, in such a way that the adiabatic temperature in air reactor ($T_{adiabatic,AR}$) is computed. The adiabatic temperature reached in the air reactor is determined by solving Eq. (8), which refers to material and heat balance in the air reactor:

Material and heat balance in the air reactor (AR)

$$\frac{0.2\cdot F_S\cdot \dot{n}_{CH_4}}{M_{NiO}}\left(H_{NiO}^{T_{adiabatic,AR}}-H_{NiO}^{T_M}\right)+\frac{0.8\cdot F_S\cdot \dot{n}_{CH_4}}{M_{Al_2O_3}}\left(H_{Al_2O_3}^{T_{adiabatic,AR}}-H_{Al_2O_3}^{T_M}\right)+0.5\cdot\left(\frac{0.2\cdot F_S\cdot \dot{n}_{CH_4}\cdot X_{NiO\rightarrow Ni}}{M_{NiO}}\right)\cdot\frac{0.7905}{0.2095}\left(H_{N_2}^{T_{adiabatic,AR}}-H_{N_2}^{T_M}\right)=\frac{0.2\cdot F_S\cdot \dot{n}_{CH_4}\cdot X_{NiO\rightarrow Ni}}{M_{NiO}}\cdot\Delta H_{(R17)}^{T_M} \quad (8)$$

When air at 673 K enters in contact with the oxygen-carrier (Ni + unconverted NiO + Al_2O_3 support), which is at the temperature of the fuel reactor (T_{FR}), it is assumed that an intermediate temperature (T_M) is achieved in the air reactor. T_M can be easily calculated assuming that the heat released due to the cooling of the oxygen-carrier from T_{FR} to T_M is used to heat up air from 673 K to T_M. The auto-thermal condition is achieved when the energy demand in FR, calculated by ΔH in Eq. (9), is equal to zero:

Material and heat balance in the fuel reactor (FR)

$$\Delta H=\frac{0.2\cdot F_S\cdot \dot{n}_{CH_4}}{M_{NiO}}\left(H_{NiO}^{T_{FR}}-H_{NiO}^{T_{adiabatic,AR}}\right)+\frac{0.8\cdot F_S\cdot \dot{n}_{CH_4}}{M_{Al_2O_3}}\times\left(H_{Al_2O_3}^{T_{FR}}-H_{Al_2O_3}^{T_{adiabatic,AR}}\right)\dot{n}_{steam}\left(H_{steam}^{T_{FR}}-H_{steam}^{T=673\ K}\right)+\dot{n}_{CH_4}\left(H_{CH_4}^{T_{FR}}-H_{CH_4}^{T=673\ K}\right)+\dot{n}_{CO_2}\left(H_{CO_2}^{T_{FR}}-H_{CO_2}^{T=673\ K}\right)+\Delta H_{(R22)}^{T_{FR}} \quad (9)$$

In order to determine the equilibrium composition in the fuel reactor at a given value of NiO conversion ($X_{NiO\rightarrow Ni}$), it is necessary to consider the $NiO_{reacted}/CH_4$ molar ratio as an input parameter in the Gibbs energy minimization method. This value can be calculated as follows:

$$(NiO_{reacted}/CH_4)=\frac{X_{NiO\rightarrow Ni}}{\dot{n}_{CH_4}}\cdot\left(\frac{0.2\cdot F_S\cdot \dot{n}_{CH_4}}{M_{NiO}}\right) \quad (10)$$

2.4. Fuel processor integrated with the PEMFC stack

Once the optimized operating conditions for the unit comprising the fuel- and air-reactors (CLR) and the reformer (SR, PO and ATR) are determined, a global heat balance of the whole fuel processor, integrating the FR–AR unit or the reformer with heaters, steam-generators, heat exchangers,

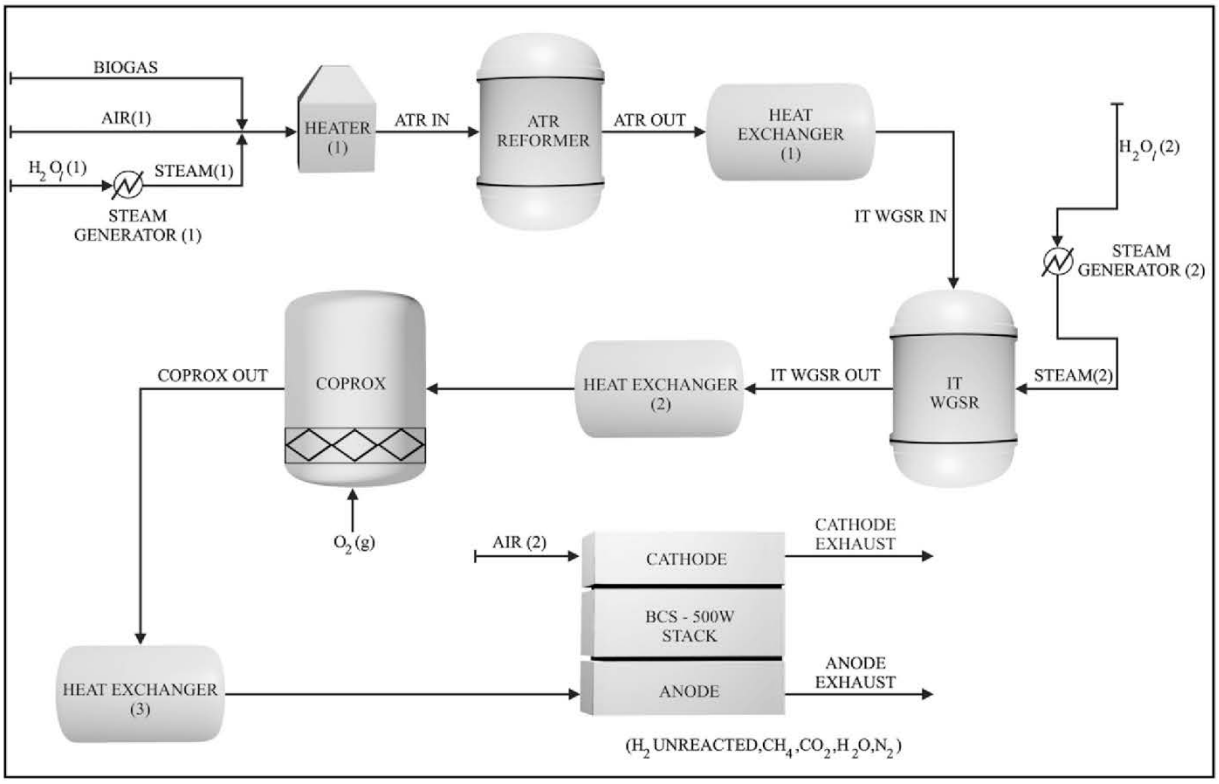

Fig. 4 – PEMFC stack integrated with the ATR fuel processor unit.

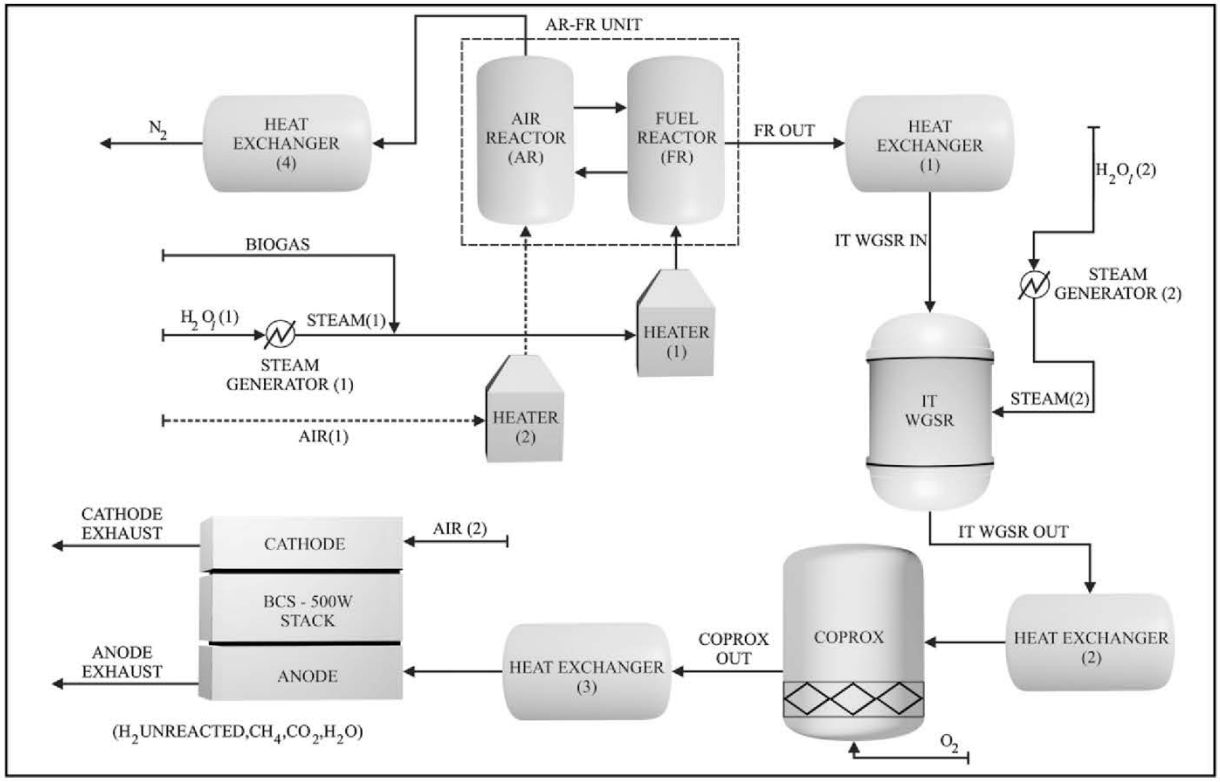

Fig. 5 – PEMFC stack integrated with a CLR unit comprising the air and fuel reactors.

water–gas shift reactors (WGSR) and CO preferential oxidation reactor (COPROX), as illustrated in Figs. (2)–(5), is carried out. The following assumptions were made in the present work:

* Biogas, steam and air are preheated in the heaters at 673 K.
* SR and PO fuel processors possess two water–gas shift reactors: a high temperature water–gas shift reactor (HT-WGSR), which operates at 703 K, and a low temperature water–gas shift reactor (LT-WGSR), which operates at 503 K.
* ATR and CLR fuel processors are characterized by one stage of water–gas shift. An intermediate temperature water–gas shift reactor (IT-WGSR), operating at 573 K, is employed.
* COPROX reactor works at 393 K for all the fuel processors.
* In CLR case, the air reactor output gas, which is assumed to be composed solely of N_2, is cooled down to 333 K in the heat exchanger (4) (see Fig. 5).
* In the WGSR, H_2 production is increased through the reaction (R8). The equilibrium composition in the WGSR is determined by the Gibbs energy minimization method (see section 2.1). However, only the species CO, CO_2, H_2O and H_2 are considered in the calculations. If CH_4 were introduced in the set of species, there would be a sensible consumption of H_2, due to methanation reactions (R9, R10, R11), which is not seen in real applications [34]. CH_4 is considered as an inert species.
* Among the different techniques used for hydrogen purification, the preferential oxidation of CO reaction (R6) is the most simple, efficient and economical way to reduce the concentration of CO to a level of ppm [35]. The preferential oxidation of CO, which occurs in the COPROX reactor, involves the oxidation of CO, in a reformate stream, to CO_2 on a suitable catalyst [36]. This is necessary because CO poisons the Pt anode catalyst of the PEMFC [37]. Due to the high concentration of H_2 in the feed gas, hydrogen can be consumed through reaction (R7). Generally, air is used during the operation. However, since the benefit of CO_2 capture is considered in CLR, the COPROX reactor should operate with oxygen instead of air. Note that, in all the cases, the COPROX reactor is operated with O_2, because the performance of the CLR fuel processor is compared with those achieved by other fuel processors and the consistency during the analysis should be kept. It is assumed that CO oxidation in the COPROX reactor occurs with a selectivity of 0.5, which is in agreement with typical catalysts [38]. The selectivity of CO oxidation in the COPROX reactor is defined as the ratio of oxygen consumed for CO oxidation to the total consumption of oxygen for oxidation of CO and H_2. The COPROX reactor is modeled taking into account the selectivity values and the stoichiometry of reactions (R6) and (R7).
* The CO-free hydrogen rich stream is fed to the anode of the PEMFC stack. In this work, a commercial 500W PEMFC stack, manufactured by the American company BCS Technologies [39], is considered.

2.5. *PEMFC stack model*

The PEMFC stack model implemented in this work, known as the generalized steady-state electrochemical model (GSSEM),

is based on the research of Amphlett et al. [40,41] and Mann et al. [42,43]. This model is zero-dimensional, semi-empirical, isothermal and static in nature. In this way, the parameters of the equations are experimentally determined to provide the time-independent polarization curves and system efficiencies at various operating conditions [44].

The output voltage of a single cell (V_{cell}) is calculated from the reversible voltage, which is decreased by the irreversible losses (Eq. (11)) [44,45]:

$$V_{cell} = E_{Nernst} - \varphi_{act} - \varphi_{ohm} - \varphi_{conc} \quad (11)$$

where E_{Nernst} is the thermodynamic potential of the cell; φ_{act} is the activation overvoltage, which corresponds to the amount of voltage used to drive the reaction; φ_{ohm} is the ohmic overvoltage, which corresponds to the amount of voltage lost due to the resistances of ionic conduction through the solid electrolyte and the resistance to electron flow in the electrodes; φ_{conc} is the concentration overvoltage, which represents the voltage drop due to the reduction of concentration of reactant at the electrode or, alternatively, due to the transport of mass of oxygen and hydrogen. There is another voltage drop associated to the internal currents and/or the fuel crossover [46]. This voltage drop is considered in the model, using a fixed current density even at 'no-load' operation ($i_{no\text{-}load}$).

The voltage of a stack (V_{stack}) of n_{cells} connected in series is calculated by:

$$V_{Stack} = n_{cell} V_{cell} \quad (12)$$

The equilibrium potential (E_{Nernst}), indicated in Eq. (11), is given by [43]:

$$E_{Nernst} = 1.229 - 0.8 \times 10^{-3}(T_{cell} - 298.15) + 4.3085 \times 10^{-5} T_{cell}\left(\ln\left(p_{H_2}^{interface}\right) + 0.5\ln\left(p_{O_2}^{interface}\right)\right) \quad (13)$$

T_{cell} is the stack temperature, and $p_{H_2}^{interface}$ and $p_{O_2}^{interface}$ are the hydrogen and oxygen partial pressures at the surface of the catalyst at the anode and cathode, respectively, and are given by [40,47]:

$$p_{H_2}^{interface} = P_{cell}\left[1 - 0.5x_{H_2O}^{Sat.} - x_{inert}^{channel}\exp\left(0.183i/T_{cell}^{0.832}\right)\right] \quad (14)$$

and

$$p_{O_2}^{interface} = P_{cell}\left[1 - x_{H_2O}^{Sat.} - x_{N_2}^{channel}\exp\left(0.291i/T_{cell}^{0.832}\right)\right] \quad (15)$$

The derivation of Eqs. (14) and (15) is based on the Stefan–Maxwell equations and kinetic theory. The deduction of these equations is found in Ref. [40]. Note that it is assumed that the cell operates with water-saturated cathode inlet stream and a half-saturated anode inlet stream.$x_{H_2O}^{Sat.}$ is the molar fraction of water in a gas stream at saturation for a given temperature, i is the current density (A cm^{-2}), P_{cell} is the cell operating pressure, $x_{inert}^{channel}$ is the arithmetic mean average mole fraction of inert species ($N_2 + CO_2 + CH_4$) at the interface of the anode, calculated by the following expression [38]:

$$x_{inert}^{channel} = \frac{x_{out}^{hum.} + x_{in}^{hum.}}{2} \quad (16)$$

where

$$x_{in}^{hum} = x_{inert}^{dry}\left(1 - \frac{0.5p_{H_2O}^{Sat.} - x_{H_2O}^{dry}P_{cell}}{P_{cell}}\right) \quad (17)$$

$$x_{out}^{hum} = \frac{x_{inert}^{dry}}{(1 - 1/\lambda_{H_2})x_{H_2}^{dry} + x_{inert}^{dry}} \times \left(1 - \frac{0.5p_{H_2O}^{Sat.} - x_{H_2O}^{dry}P_{cell}}{P_{cell}}\right) \quad (18)$$

where x_{inert}^{dry} is the sum of the molar fractions of inert species ($x_{CO_2} + x_{CH_4} + x_{N_2}$), $x_{H_2}^{dry}$ and $x_{H_2O}^{dry}$ are the molar fractions of hydrogen and water, respectively, in the product gas stream coming from COPROX reactor brought into the anode of the PEMFC stack. Note that CO_2 is considered as an inert species. Thus, the possibility of reverse water–gas shift reaction (R12), with some production of CO, is not assumed to occur at the anode. This same assumption has been made in other works [38,48]. The superscripts denoted as 'hum' refer to molar fractions after humidification of the gas stream. The saturation pressure of water vapor ($p_{H_2O}^{Sat.}$) is calculated by the following empirical equation [49]:

$$\ln\left(p_{H_2O}^{Sat.}\right) = 70.434643 - \frac{7362.6981}{T_{cell}} + 0.006952085T_{cell} - 9.0000\ln T_{cell} \quad (19)$$

and the molar fraction of water in a gas stream at saturation for a given temperature is calculated by:

$$x_{H_2O}^{Sat.} = \frac{p_{H_2O}^{Sat.}}{P_{cell}} \quad (20)$$

$x_{N_2}^{channel}$ is the log mean average mole fraction of nitrogen in the humidified gas at the interface of the cathode [40,44]:

$$x_{N_2}^{channel} = \frac{x_{N_2}^{in,hum} - x_{N2}^{out,hum}}{\ln\left(x_{N_2}^{in,hum}/x_{N_2}^{out,hum}\right)} \quad (21)$$

where

$$x_{N_2}^{in,hum} = \left(1 - x_{H_2O}^{Sat.}\right) \times 0.7905 \quad (22)$$

and

$$x_{N_2}^{out,hum} = \frac{1 - x_{H_2O}^{Sat.}}{1 + (\lambda_{air} - 1/\lambda_{air})(0.2095/0.7905)} \quad (23)$$

The activation overvoltage (φ_{act}), indicated in Eq. (11), is calculated from the semi-empirical expression proposed by Mann et al. [43]

$$\varphi_{act} = -\left(\xi_1 + \xi_2 T_{cell} + \xi_3 T_{cell}\left[\ln\left(C_{O_2}^{interface}\right)\right] + \xi_4 T_{cell}\ln(I + I_{no\text{-}load})\right) \quad (24)$$

where

$$C_{O_2}^{interface} = \frac{p_{O_2}^{interface}}{5.08 \times 10^6 \exp(-498/T_{cell})} \quad (25)$$

and the ξ coefficients of Eq. (24) are empirically determined for each individual fuel cell stack.

The ohmic overpotential (φ_{ohm}) is calculated by the Ohm's Law equation [50]:

$$\varphi_{ohm} = (I + I_{no\text{-}load})(R_{prot} + R_{elec}) = (I + I_{no\text{-}load})\left(\frac{r_m \ell}{A_{cell}} + R_{elec}\right) \quad (26)$$

where ℓ is the thickness of membrane (cm), A_{cell} is the cell active area (cm^2) and r_m is the specific resistivity of the membrane for the electron flow (Ω cm). The following numeric expression for the resistivity of the Nafion membranes is used [43]:

$$r_m = \frac{181.6\left[1 + 0.03(i + i_{no\text{-}load}) + 0.062(T_{cell}/303)^2(i + i_{no\text{-}load})^{2.5}\right]}{[\psi - 0.634 - 3(i + i_{no\text{-}load})]\exp(4.18(T_{cell} - 303)/T_{cell})} \quad (27)$$

The concentration overvoltage (φ_{conc}) can be determined by:

$$\varphi_{con} = -B \times \ln(1 - (i + i_{no\text{-}load})/i_{max}) \quad (28)$$

where B(V) is a parametric coefficient, which depends on the cell and its operation state, and i_{max} is the maximum current density, defined under which the fuel is being used at the maximum supply rate [51].

The output of the fuel cell system depends on the amount of reactants in the system. The relationship between the molar mass flow-rate of H_2 and cell current is given by [44]:

$$\dot{n}_{H_2}(\text{mol s}^{-1}) = \frac{I\lambda_{H_2} n_{cell}}{2F} \quad (29)$$

where λ_{H_2} is the stoichiometry of the hydrogen gas and F is Faraday's constant.

The stack power (W_{stack}) is given by:

$$W_{stack} = V_{stack} I \quad (30)$$

The global efficiency of the fuel processor integrated with a PEMFC stack is defined as:

$$\eta^{LHV}_{global} = \frac{W_{Stack}}{\dot{n}_{biogas}(LHV)_{biogas}} \quad (31)$$

where $\dot{n}_{biogas}$ is the total molar flow-rate of biogas for reforming and burning. The lower heating value of biogas (CH_4/CO_2 molar ratio of 1.5) is 481,349 J per mol of biogas.

The model parameters values used to evaluate the BCS 500W stack performance are shown in Table 2. These parameters were compiled from the work of Corrêa et al. [50]. In the present study, it is assumed that λ_{H_2} and λ_{air} are 1.25 and 2, respectively, which corresponds to a hydrogen utilization of 80% and oxygen utilization of 50%. The H_2 that does not react electrochemically is released in the anode exhaust along with the other reformate species (see Figs. 2–5). Besides, it is considered that $T_{cell} = 333$ K and $P_{cell} = 1$ atm.

Table 2 – BCS 500W stack parameters.

Parameter	Value
n_{cell}	32
A_{cell} (cm^2)	64
B (V)	0.016
$R_{elec.}$ (Ω)	0.0003
ξ_1	−0.948
ξ_2	[a]
ξ_3	7.6×10^{-5}
ξ_4	-1.93×10^{-4}
ψ	23
i_{max} (A cm^{-2})	0.469
$i_{no\text{-}load}$ (A cm^{-2})	0.003
I_{max} (A)	30

a $\xi_2 = 0.00286 + 0.0002\ln A_{cell} + 4.3 \times 10^{-5}\ln C^{interface}_{H_2}$, with $C^{interface}_{H_2} = p^{interface}_{H_2}/1.09 \times 10^6 \exp(77/T_{cell})$ [40].

3. Results and discussion

In the next sections (3.1–3.4), the theoretical analysis is focused on the FR–AR unit or the reformer (SR, ATR and PO), and the equilibrium compositions are computed as a function of different operating parameters. The equilibrium conversion of a reactant i is calculated by:

$$\text{Conversion}(\%) = 100 \times \frac{(n_{i,in} - n_{i,out})}{n_{i,in}} \quad (32)$$

In all the cases, atmospheric pressure was considered during calculations. From a previous study [30], CLR is described as an attractive process only if the system operates at high pressure (1–2 MPa). In this case, a gas turbine is considered to produce energy. The present research aims to show that advantages of the CLR process can be obtained at atmospheric pressure if this technology is integrated with a PEMFC system. In this way, atmospheric pressure was considered for CLR and the other technologies, since a comparison between these different processes is carried out. In addition, experimental studies show that high fuel conversion and high H_2 yield are obtained at atmospheric pressure during SR, ATR and PO of biogas [1,6,9,11,12].

3.1. FR–AR unit (CLR)

Fig. 6 (a) shows the effect of oxygen-carrier circulation flow-rate on the air reactor temperature and the oxygen-carrier conversion ($X_{Ni\rightarrow Ni}$) in the fuel reactor for auto-thermal operating conditions in FR–AR unit. As can be seen, the higher the oxygen-carrier circulation flow-rate is, the lower the air reactor temperature. From Fig. 6 (b), one can see that the air reactor temperature increases as $NiO_{reacted}/CH_4$ molar ratio increases, which results in a decrease of H_2 production. This trend is in agreement with that reported by Ortiz et al. [18] for CLR of pure methane. As suggested by these authors, an increase in temperature in air reactor diminishes the hydrogen production because more energy is required to raise the temperature in the air reactor, which is supplied by increasing the oxidation reactions (R18) and (R19). Thus, a higher $NiO_{reacted}/CH_4$ molar ratio is needed to reach auto-thermal operating conditions in FR–AR unit, and more H_2O and CO_2 are produced at expenses of H_2 and CO. In this way, H_2 production is maximized when the air reactor temperature is kept as low as possible. From Fig. 6 (a), one can observe that the air reactor temperature diminishes when the FR–AR unit operates with higher oxygen-carrier circulation flow-rates. Therefore, the air reactor temperature will be limited by the oxygen-carrier circulation flow-rate, which, according to Ortiz et al. [18], will depend on the characteristics of the oxygen-carrier (reactivity, particle size, etc), operation conditions and the configuration of the riser of the CLR installation.

Fig. 7 (a) and (c) depict the yield of species and the variation of enthalpy in FR as a function of air/CH_4 molar ratio (and

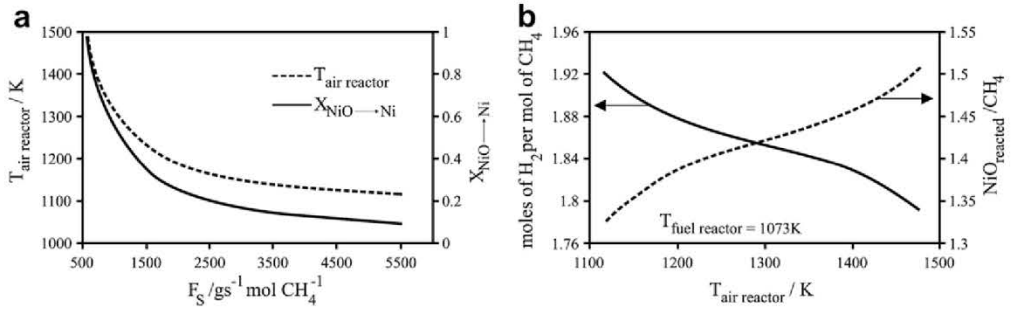

Fig. 6 – (a) Air reactor temperature and oxygen-carrier conversion in fuel reactor for auto-thermal operation in FR–AR unit as a function of oxygen-carrier circulation flow-rate. (b) Effect of air reactor temperature on H_2 production and $NiO_{reacted}/CH_4$ molar ratio. H_2O/CH_4 = 2 in fuel reactor, T_{FR} = 1073 K, auto-thermal operating conditions.

$NiO_{reacted}/CH_4$ molar ratio, see superior axis). The more CO and H_2 appear in the fuel reactor exhaust gas, the more endothermic becomes the overall reaction in the fuel reactor. However, the FR–AR unit is intended to operate under auto-thermal conditions. In this way, for an inlet H_2O/CH_4 molar ratio of 2 in the fuel reactor, the air/CH_4 molar ratio should be increased from 0.1 to 0.35 so that the FR–AR unit can operate auto-thermally (see Fig. 7(a)). Note that H_2 production is reduced from 2.6 to approximately 1.9 (mol per mol of CH_4). When air/CH_4 molar ratio is further increased, the overall reaction in the fuel reactor becomes increasingly exothermic, and the FR exhaust gas becomes more and more enriched in H_2O and CO_2, indicating the occurrence of the reactions (R18) and (R19). In absence of steam in the feedstock, H_2 production under auto-thermal conditions is reduced (~1.5 mol per mol of CH_4) with a CO yield (1.2 mol per mol of CH_4) greater than that obtained when steam is fed to FR (0.73 mol per mol of CH_4), as can be seen by comparing Fig. 7(a) and (c). Consistently, the CO_2 content obtained when no steam is added to FR, see Fig. 7(c) (0.47 mol per mol of CH_4), is lower than that shown in Fig. 7(a) (0.94 mol per mol of CH_4), which clearly suggests that, under auto-thermal conditions, the H_2O introduced in the fuel reactor only affects the equilibrium by the water–gas shift reaction (R8). Despite of the increase in the H_2 content in the fuel reactor when steam is added to the biogas in the feedstock, it will be demonstrated later that H_2 production is maximized when all the steam is fed to the WGS reactor, and the fuel reactor is operated without H_2O in the feed stream. From Fig. 7(b) and (d), one can see the FR gas composition along with the air reactor temperature. As stated before, the highest H_2 concentration is achieved at the lowest air reactor temperature. However, in order to work under auto-thermal conditions, H_2 concentration should be reduced to 53 (Fig. 7)(b) and 47 mol% (Fig. 7)(d), whereas the air reactor temperature should be increased to 1231 (Fig. 7(b)) and 1222 K (Fig. 7)(d). Fig. 7(e) shows the number of moles of carbon formed per mol of CH_4 in the fuel reactor as a function of air/CH_4 molar ratio, at different temperatures and at H_2O/CH_4 molar ratio of zero. The amount of carbon decreases as the air/CH_4 molar ratio increases. For air/CH_4 molar ratios greater than 0.2, carbon formation is completely inhibited. In this way, even in absence of steam, carbon deposition can be prevented if a suitable air-to-fuel ratio is used during the operation. This is in agreement with the experimental observations of Pröll et al. [21]. By controlling the air/CH_4 molar ratio, these authors avoided carbon deposition in the fuel reactor even when no steam was added to the natural gas feedstock. In this way, no carbon species were detected in the air reactor exhaust gas. In absence of steam in the feedstock, deposited carbon possibly reacts with NiO to form CO by the solid–solid reaction (R20) [52]. Note that, when steam is not added to the feedstock in fuel reactor (Fig. 7)(c), auto-thermal operation is achieved at an air/CH_4 molar ratio of 0.328. Thus, based on the results shown in Fig. 7(e), auto-thermal operation without carbon deposition can be reached even when steam is not added to the fuel reactor.

Fig. 8 shows the equilibrium compositions computed in the present study for methane and clean model biogas along with the experimental values obtained from Pröll et al. [21] for methane. By comparing methane vs. clean model biogas, one can see that the use of clean model biogas instead of methane in CLR operation results in lower H_2 concentrations, because, in the case of clean model biogas, the fuel reactor exhaust gas is richer in CO and CO_2. In addition, it is also possible to observe that, in the case of clean model biogas, the air/CH_4 molar ratio required to work under auto-thermal conditions is higher than that needed when methane is fed to FR, because there are more inert gases to be heated up to the reactor temperature in the case of biogas. From Fig. 8, one can see that experimental values approach thermodynamic predictions in the case of methane. This means that FR exhaust gas is in thermodynamic equilibrium. Thus, thermodynamic analysis is suitable to make predictions of the composition of fuel reactor exhaust gas. It is worth pointing out that the possibility of reaching thermodynamic equilibrium in a CLR system is also supported by the results reported by de Diego et al. [17]. In this way, the theoretical results from the present research for clean model biogas can be used as a guideline in experimental investigation. Fig. 9 shows that, in absence of steam, CO_2 conversion is positive for low values of air/CH_4 molar ratio. It is possible that, at sub-stoichiometric amounts of oxygen and in absence of steam in the feedstock, CH_4 can be converted through dry reforming reaction (R3), because dry reforming is slower than steam reforming. On the other hand, by working with higher inlet H_2O/CH_4 molar ratios in the fuel reactor, CO_2 possibly only affects the equilibrium through the

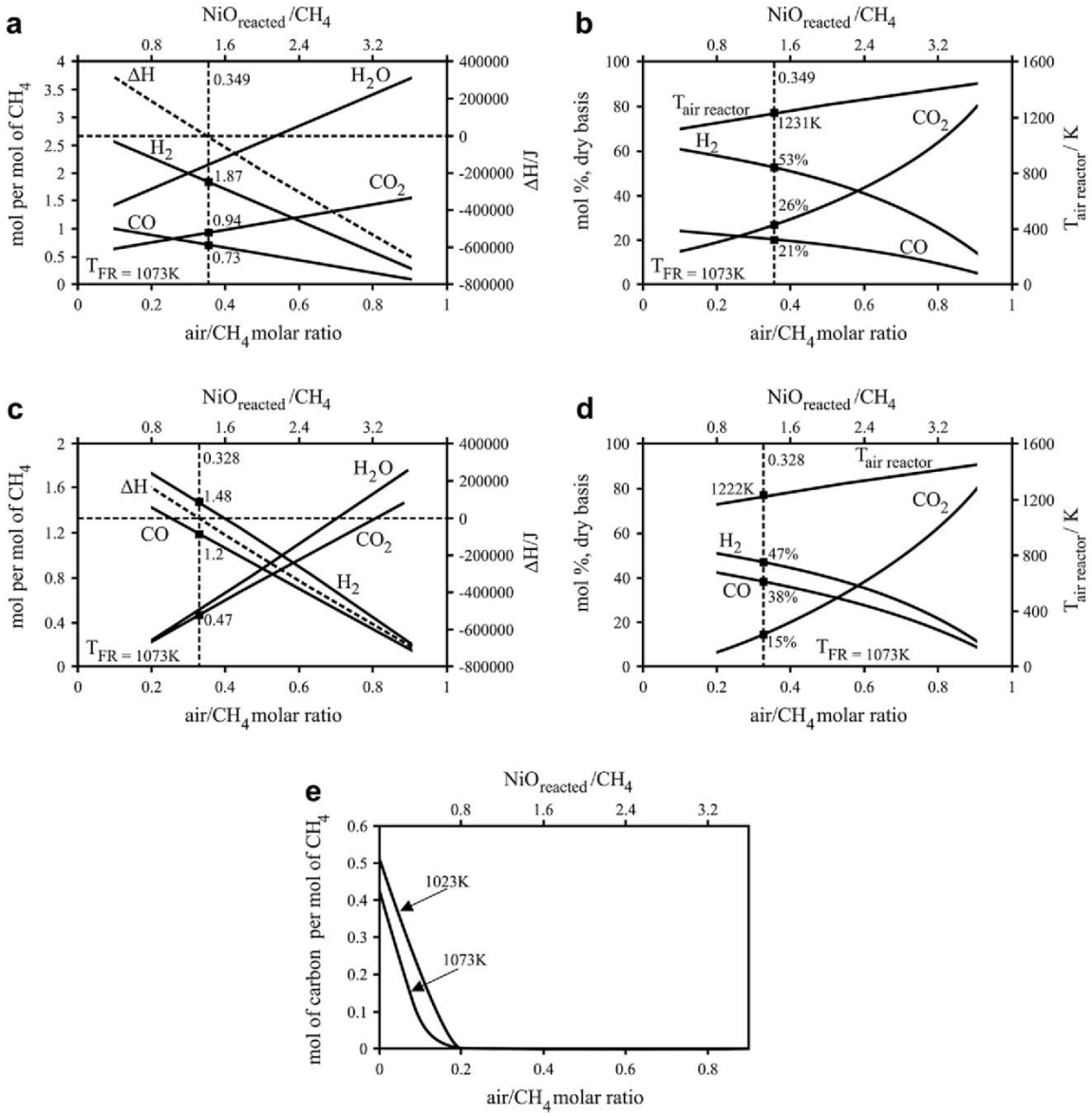

Fig. 7 – (a), (c) Equilibrium composition (mol per mol of CH_4) and enthalpy change in FR as a function of air/CH_4 molar ratio (or $NiO_{reacted}/CH_4$ molar ratio). (b), (d) Equilibrium composition (mol%, dry basis) and air reactor temperature as a function of air/CH_4 molar ratio. (e) Amount of carbon formed in FR as a function of air/CH_4 molar ratio. Inlet H_2O/CH_4 molar ratio = 2 in (a) and (b); Inlet H_2O/CH_4 molar ratio = 0 in (c), (d) and (e).

water–gas shift reaction (R8). Note that CH_4 conversion is over 99%, independently of the amounts of steam and air at $T_{FR} = 1073$ K.

Fig. 10 shows the number of moles of H_2 produced per mol of CH_4 after the water–gas shift reactor. As can be seen, the production of H_2 is maximized when the inlet H_2O/CH_4 molar ratio in the fuel reactor is equal to zero. The inferior line shows the H_2 production when total H_2O/CH_4 molar ratio (fuel reactor + WGSR) is equal to 2. Note that, in this case, the total net energy calculated for the overall process (see the complete fuel processor shown in Fig. 5) is in the range of −114 to −134 kJ mol CH_4^{-1}, indicating that there is a surplus of energy, which could be used to produce steam. In this way, as can be seen in the upper line, the inlet H_2O/CH_4 molar ratio in the IT-WGSR is increased, resulting in a higher production of H_2 during an auto-thermal global operation. These findings are in satisfactory agreement with those reported by Ortiz et al. [18]. Therefore, in the second part of this work, the performance of a PEMFC system integrated with a CLR fuel processor is evaluated considering the inlet H_2O/CH_4 molar ratio in the fuel reactor equal to zero. All the steam is fed to the water–gas shift reactor.

3.2. *ATR reactor*

The ATR reactor was modeled as an adiabatic reactor. In this way, for a fixed inlet H_2O/CH_4, air/CH_4 molar ratio and reactant preheat temperature (673 K), the equilibrium composition

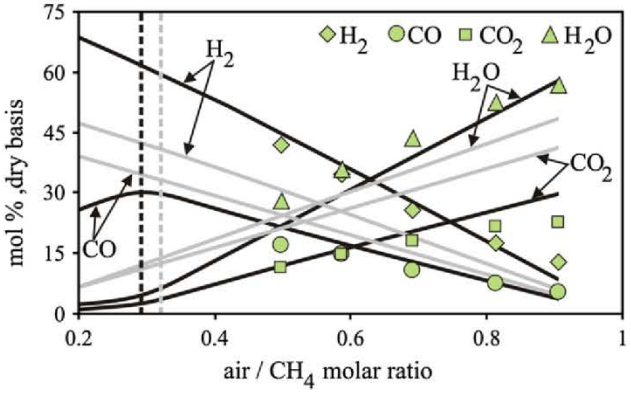

Fig. 8 – Gas compositions from fuel reactor at 1073 K, with fuel reactor fed on pure methane or clean model biogas (CH_4/CO_2 molar ratio of 1.5). Solid lines refer to thermodynamic equilibrium compositions. Vertical dashed lines refer to air/CH_4 molar ratio for auto-thermal operation of FR–AR unit. Black lines: pure methane; Gray lines: clean model biogas. The markers correspond to experimental points obtained from Ref. [21] for pure methane: △ (H_2O), ◇ (H_2), □ (CO_2) and ○ (CO). Inlet H_2O/CH_4 = 0; reactants preheat temperature: 673 K.

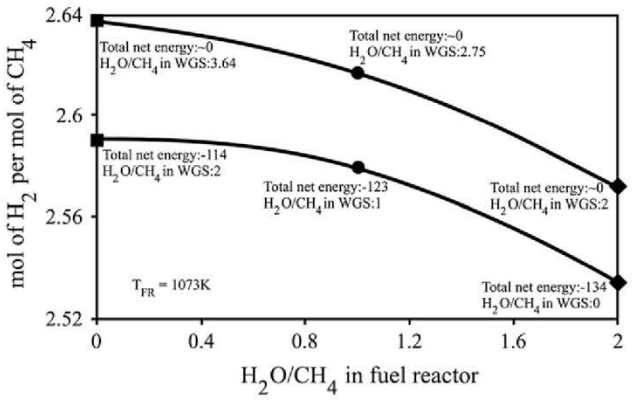

Fig. 10 – Moles of H_2 per mol of CH_4 produced after water–gas shift reactor as a function of H_2O/CH_4 in fuel reactor at different H_2O/CH_4 molar ratios in water–gas shift reactor. The inferior line shows the H_2 production when total H_2O/CH_4 molar ratio (FR + WGSR) is equal to 2. Total net energy, in kJ mol $CH4^{-1}$, is indicated. The markers show the air/CH_4 molar ratio for auto-thermal operation in FR: ■0.328, ●0.336, ◆0.349.

is computed at a certain temperature (adiabatic temperature) which satisfies the requirement of $\Delta H \sim 0$ in Eq. (3). Fig. 11 shows the influence of the inlet H_2O/CH_4 and air/CH_4 molar ratios on CH_4 conversion (a) and the adiabatic temperature reached in the reformer (b). As can be seen, the adiabatic temperature increases as air/CH_4 molar ratio increases. For air/CH_4 molar ratios greater than 0.25, the adiabatic temperature increases more steeply, and CH_4 conversion is ~100%. Interestingly, Araki et al. [11], who experimentally studied the auto-thermal reforming of biogas over a monolithic catalyst, also verified that CH_4 conversion increased with increasing air/CH_4 molar ratio. Additionally, they found that CH_4 conversion reached about 100% at an air/CH_4 molar ratio of 0.28. Note that, for air/CH_4 molar ratios greater than 0.25, the adiabatic temperature decreases as the inlet H_2O/CH_4 molar ratio increases. However, under these conditions, the oxidation reactions of methane (R4 and R5) dominate the equilibrium, and endothermic steam reforming reaction has no influence on the energy balance. The reason for the decrease in the adiabatic temperature is that more steam should be heated up to the reactor temperature. At sub-stoichiometric amounts of oxygen (air/CH_4 molar ratios <0.25), H_2O could have influence on the CH_4 conversion through endothermic SR reactions (R1) and (R2). Under these conditions, the adiabatic temperature can be as low as 600 K, depending on the amount of air and steam fed to the ATR reformer. Besides, at low values of air/CH_4 and H_2O/CH_4 molar ratios, CO_2 could be converted through reaction (R3). In fact, at an inlet H_2O/CH_4 molar ratio of 0.5 and air/CH_4 molar ratios lower than 0.1, a CO_2 conversion of 50% was calculated.

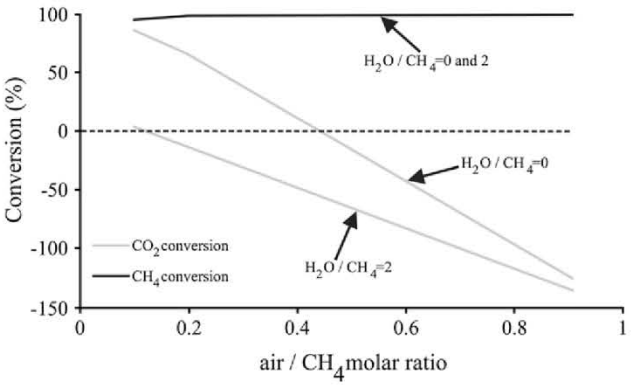

Fig. 9 – Methane and carbon dioxide conversion (%) as a function of air/CH_4 molar ratio for different amounts of steam in the feedstock at T_{FR} = 1073 K.

Fig. 12(a) shows that H_2 gradually increases with air/CH_4 molar ratio, reaching the maximum production at air/CH_4 molar ratios around 0.25. Under these conditions, CH_4 is converted through partial oxidation (R5). However, for air/CH_4 molar ratios >0.35, hydrogen production decreases, because H_2 is combusted to steam (R7). It is worth mentioning that Araki et al. [11] experimentally verified that the highest H_2 concentration occurs at air/CH_4 molar ratios in the range of 0.23–0.28. Interestingly, the maximum production of CO_2 also occurs at air/CH_4 molar ratios in the range of 0.15–0.35, as shown in Fig. 12(c). Note that the production of H_2 and CO_2 increases and CO production (see Fig. 12)(b) decreases with increasing inlet H_2O/CH_4 molar ratio. Thus, H_2O introduced in the ATR affects the gas composition through the water–gas shift reaction (R8).

3.3. *PO reactor*

The PO reactor was also modeled as an adiabatic reactor. The procedure adopted to compute the equilibrium composition

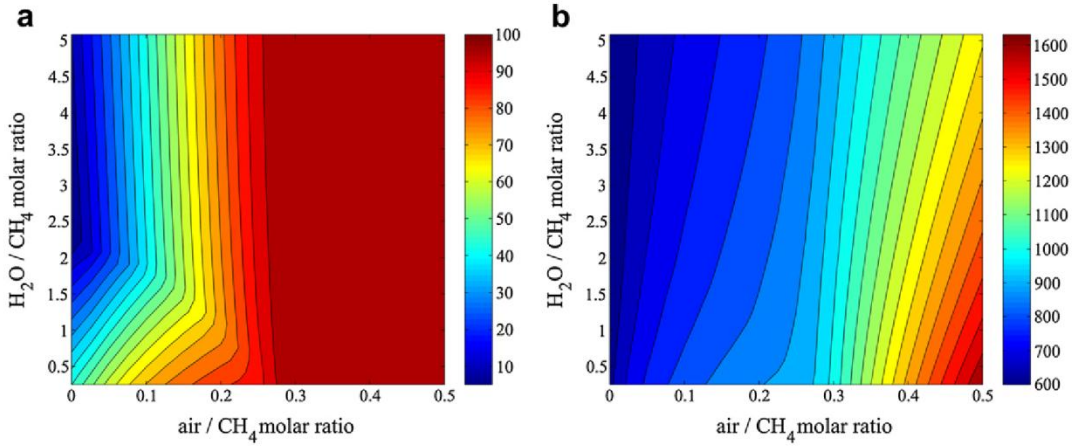

Fig. 11 – Effect of inlet air/CH_4 and H_2O/CH_4 molar ratios on: (a) CH_4 conversion (%) and (b) adiabatic temperature (K).

and adiabatic temperature was the same as that used for the ATR reactor. Fig. 13 depicts the effect of the reactants preheat temperature and air/CH_4 molar ratio on CH_4 conversion (a) and the adiabatic temperature reached in the reformer (b). The adiabatic temperature increases with the air/CH_4 molar ratio. Note, however, that it increases much more steeply in the region where carbon deposition is inhibited (air/CH_4 molar ratios $\geq$0.3). By increasing the air/CH_4 molar ratio, methane oxidation reactions (R4) and (R5) become more and more favored, with the exothermic combustion reaction (R4) prevailing at the highest air/CH_4 molar ratios. As a consequence, the adiabatic temperature can surpass 1800 K at an air/CH_4 molar ratio of 0.6. In fact, from Fig. 13 (a), one can see that methane conversion is ~100% for air/CH_4 molar ratios $\geq$0.3. On the other hand, at lower air/CH_4 molar ratios, methane conversion approaches 50%, which means that there is

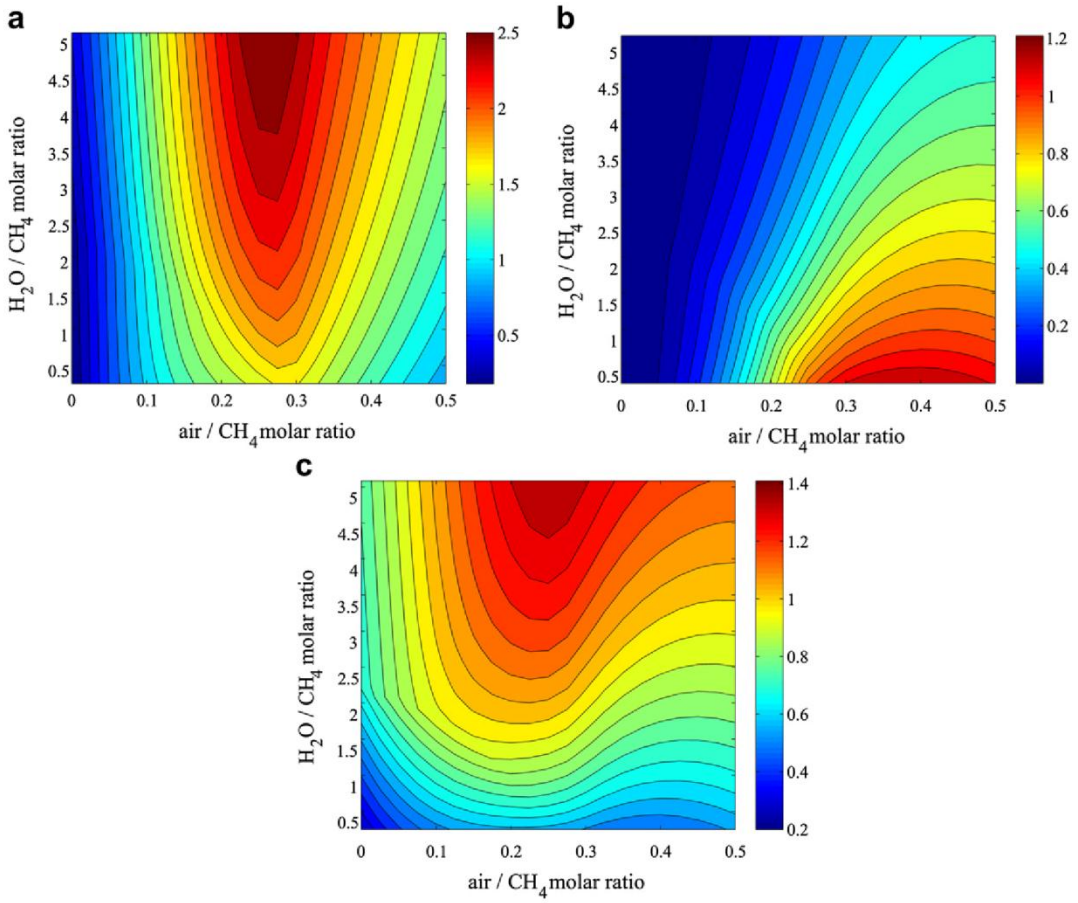

Fig. 12 – Effect of inlet air/CH_4 and H_2O/CH_4 molar ratios on the number of moles per mol of methane: H_2 (a), CO (b) and CO_2 (c).

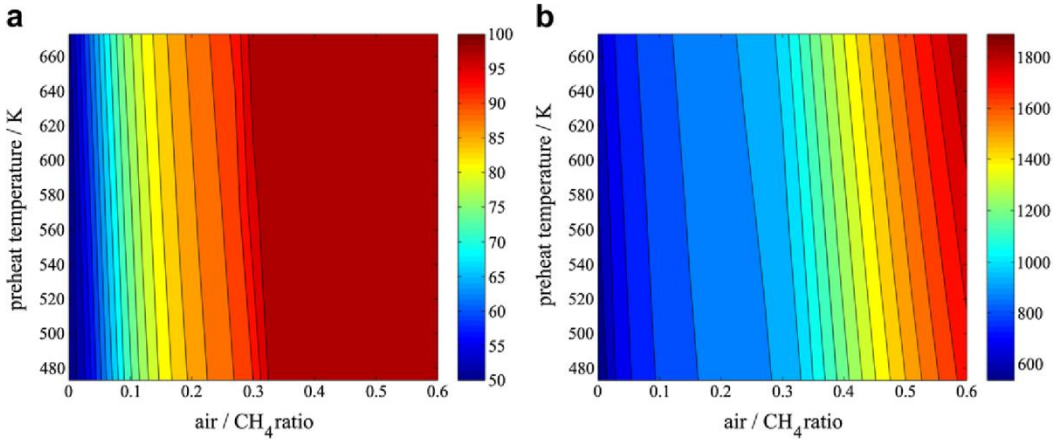

Fig. 13 – Effect of air/CH_4 molar ratio and reactants preheat temperature on: (a) CH_4 conversion (%) and (b) adiabatic temperature (K).

a significant amount of unconverted methane in the reformate. It should be pointed out that, at air/CH_4 molar ratios lower than 0.1, CO_2 conversion can be as high as 70%, which could be attributed to dry reforming reaction (R3). However, at air/CH_4 ratio around 0.3, where the reaction (R5) predominantly occurs, CO_2 affects the equilibrium composition by WGS reaction (R8).

Fig. 14 (a)-(b) shows that H_2 and CO are maximized when air/CH_4 molar ratio is in the range of 0.3–0.4. Under these conditions, the maximum H_2 production is ~1.6 mol per mol of CH_4. The use of air/CH_4 molar ratios greater than 0.4 results in a decrease of H_2 and CO, accompanied by an increase in H_2O and CO_2. Note, however, that the rate of decrease of CO is lower than that of H_2. In this way, at higher air/CH_4 molar ratios, the combustion reaction (R4) becomes more favorable than the other reforming reactions. CO production remains relatively high even at air/CH_4 molar ratios >0.3. It is worth mentioning that the theoretical results from the present research show similar trends as those from the experimental study of Rafiq et al. [12] for the catalytic partial oxidation of clean model biogas. These authors verified that the maximum hydrogen and carbon monoxide production occurs at an air/CH_4 molar ratio of 0.33, at ~20 and 18 mol%, dry basis, respectively, without reactants preheating. In the present work, the hydrogen and carbon monoxide content is ~25 and 21 mol%, dry basis, respectively, with reactants preheat temperature of 673 K. Note that the amount of H_2 produced in the PO reactor is lower than that produced in the ATR reactor, because the use of steam in the ATR enhances the water–gas shift reaction (R8). However, as it will be shown later, if the steam is added to the water–gas shift reactor, both PO and ATR based fuel processors are able to produce approximately the same amount of H_2.

3.4. *SR reformer*

Fig. 15 shows the effect of temperature and H_2O/CH_4 molar ratio on the conversion of CH_4 (a) and CO_2 (b). As can be seen, CH_4 conversion increases with temperature, reaching values of ~100%, which can be attributed to the endothermic SR (R1 and R2) and dry reforming (R3) reactions. CO_2 conversion can reach ~100% only at $T > 1050$ K and inlet H_2O/CH_4 molar ratios

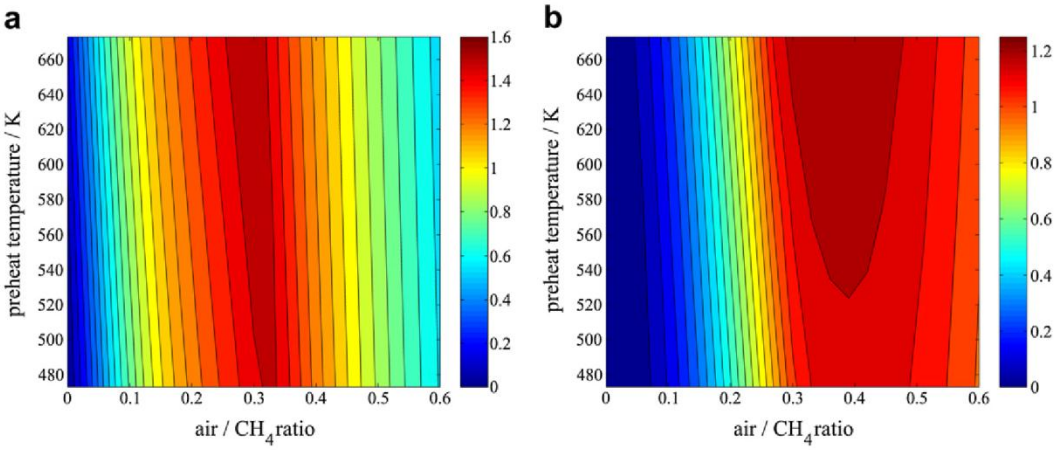

Fig. 14 – Effect of air/CH_4 molar ratio and reactants preheat temperature on the number of moles per mol of methane: (a) H_2, (b) CO.

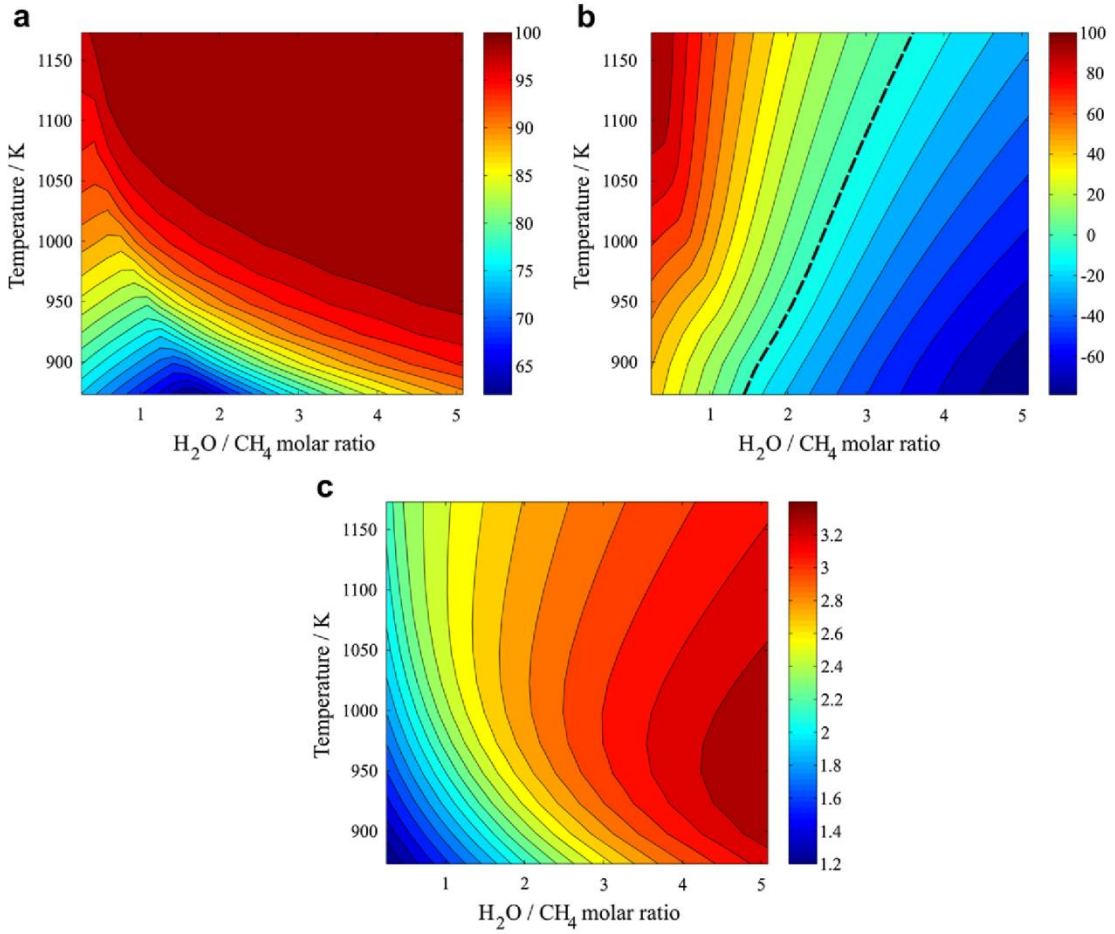

Fig. 15 – Effect of H_2O/CH_4 molar ratio and reformer temperature on (a) CH_4 conversion (%), (b) CO_2 conversion (%) and (c) moles of H_2 produced per mol of methane.

lower than 1. At a fixed temperature, for H_2O/CH_4 molar ratios that lie to the right of dashed line, CO_2 conversion is <0, which means that, for high values of inlet H_2O/CH_4 molar ratio, CO_2 present in the clean model biogas behaves as an inert species. It should be pointed out that the decrease of the CO_2 conversion is related not only to the lack of CH_4, which is consumed by reactions (R1) and (R2), enhanced in the presence of large amounts of steam, but also to the CO_2 produced by the SR reactions. In some experimental researches [53,54], it has been reported that CO_2 conversion decreases as the amount of steam added to the feedstock increases. Fig. 15(c) shows that the production of H_2 is maximized at high inlet H_2O/CH_4 molar ratios in the temperature range of 900-1050 K. The maximum H_2 production is approximately 3.3 moles per mol of methane under these conditions, which suggests the occurrence of reaction (R2), a combination of the reactions (R1) and (R8). Even though high inlet H_2O/CH_4 molar ratios favor H_2 production, the energy demand in the reformer should be taken into account. As can be seen in Fig. 16 (a), the energy demand in the reformer greatly increases with inlet H_2O/CH_4 molar ratio, reaching great values at high temperatures, such as ~350 J mol CH_4^{-1} at an inlet H_2O/CH_4 molar ratio of 5 at 1150 K. To generate this energy, biogas is burnt in a catalytic combustor, as indicated in Fig. 2. Fig. 16 (b) shows the number of moles of H_2 produced per total mol of methane, including not only the biogas used in the reformer, but also the biogas sent to the combustor to generate the energy. By comparing Fig. 15(c) *vs.* Fig. 16(b), it is possible to see that the production of H_2 per mol of CH_4 is reduced. The maximum H_2 production is ~2.3, similar or even lower than the maximum H_2 produced by an ATR reformer.

3.5. *Analysis of the complete fuel cell system processing clean model biogas*

Table 3 summarizes the optimized operating conditions for H_2 production from clean model biogas through different reforming technologies. Under these conditions, H_2 production per mol of methane is high, carbon deposition is unfeasible, and CH_4 conversion is greater than 99%. Actually, the operating conditions indicated in Table 3 were chosen in such a way that CH_4 conversion of each reforming technology was kept at exactly the same level, i.e, 99.7%. Taking into account the optimized conditions indicated in Table 3 for each reforming process (SR, PO, ATR and CLR), material and energy balance of the whole fuel processor unit integrated with a PEMFC stack was carried out. In the present work, the same heat-transfer efficiency of 0.8 is assumed for all units. Similar

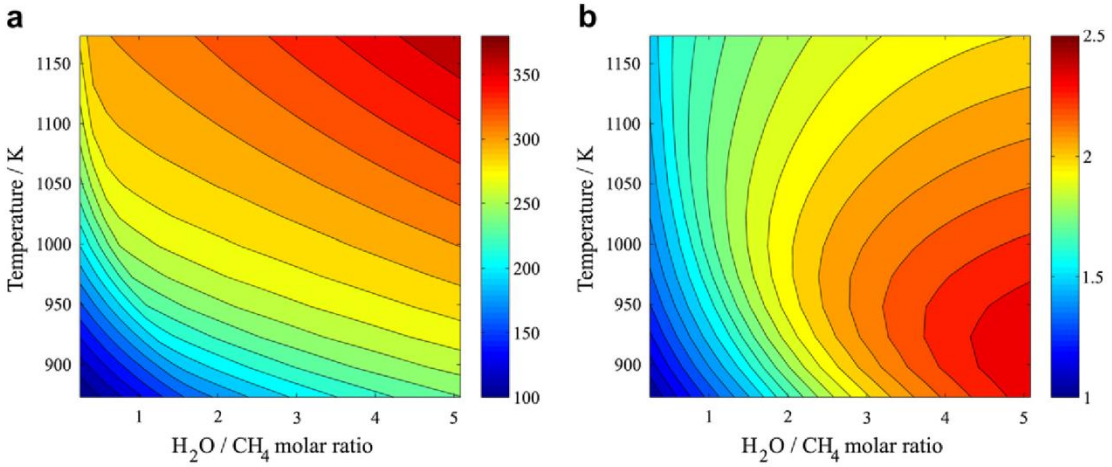

Fig. 16 – (a) Effect of H_2O/CH_4 molar ratio and reformer temperature on the energy demand in the reformer ($\times 10^3$ Jmol CH_4^{-1}) and (b) moles of H_2 produced per mol of methane (reformer + combustor).

assumption was made in the work of Seo et al. [55] for pure methane. Table 4 shows that, in order to produce the same molar flow-rate of H_2 (2.851×10^{-3} mol^{-1}), and, hence, the same current (13.75 A), SR is by far much more energy demanding than the other technologies, requiring approximately 280 W, which corresponds to the energy demanded in the reformer, considering a heat-transfer efficiency of 0.8. In this case, biogas is burnt in a catalytic combustor to supply the energy required. As can be seen from Fig. 2, air is fed to catalytic combustor, and the effluent contains CO_2, which is undesirable, due to greenhouse gas emissions. In this way, CO_2 should be captured. CO_2, however, is mixed with N_2 in the catalytic combustor effluent. Thus, an additional investment in a CO_2 separation step is needed. The use of fuel processors based on CLR, PO or ATR results in an auto-thermal global process, as shown in Table 4. If CLR fuel processor is employed, CO_2 can be easily recovered from the cell anode exhaust, since N_2 is not mixed with the reformate. The anode exhaust contains CO_2 mixed with unreacted H_2, residual CH_4 and steam. After combustion of unreacted H_2 and residual CH_4 with pure O_2 and steam condensation, CO_2 can be readily captured. A similar approach for CO_2 recovery from the cell anode exhaust gas has been investigated by Campanari et al. [56] for molten carbonate fuel cells. Note that neither the heat released due to the post-combustion nor the energy demanded for the production of pure O_2 was taken into account in the present analysis. In the case of PO and ATR fuel processors, the anode exhaust also contains N_2, which means additional costs in a CO_2 separation step. Thus, CLR represents the possibility of auto-thermal operation, high H_2 yield (2.60 mol per mol of CH_4), with the benefit of CO_2 capture. In the case of biogas, as stated before, the CO_2 captured can produce additional economical benefits in a 'carbon market'. Interestingly, as shown in Table 4, the highest values of voltage (and, thus, of the stack power) are achieved when SR and CLR fuel processors are employed. This can be attributed to the lower molar fraction of inert species at the product gas of biogas processor (x_{inert}^{dry}). In fact, the SR and CLR anodic stream does not contain N_2. The use of pure O_2 instead of air as feedstock in PO and ATR reformers could minimize the anode overpotential due to N_2 concentration. However, as mentioned in several works, an air separation unit to produce great amounts of O_2 would highly increase the plant costs and energy demand [14]. In this way, CLR can be seen as an advantageous reforming technology, since it allows auto-thermal conversion of biogas without mixing air with the

Table 3 – Optimized operating conditions for hydrogen production from clean model biogas via different reforming technologies.

	SR	PO	ATR	CLR
H_2O/CH_4 molar ratio in reformer (SR, PO, ATR) or Fuel reactor (CLR)	3.200	–	1.125	0
Air/fuel ratio	–	0.310	0.300	0.328
$NiO_{reacted}/CH_4$ molar ratio	–	–	–	1.31
Reformer (SR, PO, ATR) or Fuel reactor temperature (CLR)/K	1048	1050	1005	1073
Air reactor temperature (CLR)/K	–	–	–	1222
Preheat temperature of reactants (biogas, steam, air)/K	673	673	673	673
NiO conversion in Fuel Reactor (%)	–	–	–	32.70
Oxygen-carrier circulation flow-rate (Fs)/g s^{-1} mol CH_4^{-1}	–	–	–	1500
CH_4 conversion (%)	99.7	99.7	99.7	99.7

Table 4 – Comparison of material and energy balances, PEMFC performance and global system efficiency of different reforming technologies (SR, PO, ATR and CLR).

	SR	PO	ATR	CLR
Operation temperature/K				
Reformer(SR, PO, ATR)/Fuel Reactor(CLR)	1048	1050	1005	1073
HT-WGSR	703	703	–	–
IT-WGSR	–	–	573	573
LT-WGSR	503	503	–	–
COPROX reactor	393	393	393	393
BCS 500W stack	333	333	333	333
Material Balance				
Reformer/Fuel reactor input/mol s^{-1}				
CH_4	7.270×10^{-4}	1.050×10^{-3}	1.056×10^{-3}	1.095×10^{-3}
CO_2	4.847×10^{-4}	7.000×10^{-4}	7.040×10^{-4}	7.300×10^{-4}
H_2O	2.326×10^{-3}	–	1.188×10^{-3}	–
N_2	–	2.450×10^{-3}	2.384×10^{-3}	–
O_2	–	6.510×10^{-4}	6.336×10^{-4}	–
$NiO_{reacted}$	–	–	–	1.438×10^{-3}
H_2O input to WGSR/mol s^{-1}	1.818×10^{-4}	3.203×10^{-3}	2.165×10^{-3}	3.986×10^{-3}
O2 input to COPROX/mol s^{-1}	2.425×10^{-5}	1.573×10^{-5}	4.700×10^{-5}	3.813×10^{-5}
Anodic stream coming from COPROX reactor/mol s^{-1}				
H_2	2.851×10^{-3}	2.851×10^{-3}	2.851×10^{-3}	2.851×10^{-3}
CO	–	–	–	–
CO_2	1.210×10^{-3}	1.746×10^{-3}	1.757×10^{-3}	1.821×10^{-3}
CH_4	2.121×10^{-6}	3.805×10^{-6}	3.024×10^{-6}	3.494×10^{-6}
H_2O	1.107×10^{-3}	2.444×10^{-3}	2.608×10^{-3}	3.318×10^{-3}
N_2	–	2.450×10^{-3}	2.384×10^{-3}	–
$x_{H_2}^{dry}$	0.551	0.300	0.297	0.357
x_{inert}^{dry}	0.234	0.442	0.432	0.228
$x_{H_2O}^{dry}$	0.214	0.257	0.272	0.415
PEMFC stack-output				
Current/A	13.75	13.75	13.75	13.75
Voltage/V	20.48	19.51	19.49	20.07
Stack Power/W	281.77	268.3	267.98	275.96
Energy Balance				
Process/W				
Reformer (SR, PO, ATR) or AR–FR unit (CLR)	223.65	0.00	0.00	0.00
Heater (1)	45.46	65.64	77.44	31.37
Heater (2)	–	–	–	39.28
Steam generator (1)	108.61	–	55.46	0.00
Steam generator (2)	8.49	149.51	101.07	186.08
Heat exchanger (1)	−61.64	−74.04	−111.86	−69.89
Heat exchanger (2)	−36.17	−66.68	−59.34	−51.07
Heat exchanger (3)	−19.35	−35.36	−18.88	−16.28
Heat exchanger (4)	−10.22	−18.91	–	−76.50
HT-WGSR	−14.18	−3.71		
IT-WGSR	–	–	−18.95	−21.85
LT-WGSR	−7.84	−6.36		
COPROX reactor	−12.84	−8.23	−24.60	−20.00
Total net energy (Heat-transfer efficiency of 0.8)	279.96	~0	~0	~0
Biogas fed to fuel processor/mol s^{-1}				
Biogas fed to catalytic combustor	5.820×10^{-4}	–	–	–
Total biogas (reformer + combustor)	1.79×10^{-3}	1.75×10^{-3}	1.76×10^{-3}	1.83×10^{-3}
H_2 to total methane molar ratio	2.65	2.71	2.70	2.60
Total steam (WGSR + reformer or FR) to methane ratio	3.45	3.05	3.18	3.64
Global efficiency of the process (%)	32.64	31.85	31.64	31.40

reformate. At the current of 13.75 A, the global efficiency obtained for fuel processors based on CLR is 31.40%, which is close to those achieved for conventional fuel processors based on ATR, PO and SR (31.64, 31.85 and 32.64%, respectively).

Fig. 17 (a) depicts the polarization curves for the BCS 500W stack considering that the anode is fed on the output stream from SR, ATR, PO or CLR fuel processors, taking into account the optimized conditions of Table 3. In addition, the polarization curve for the anode fed on pure hydrogen is shown along with the experimental data from the manufacturer [39]. As can be seen, at a given current, the highest voltage and stack power are obtained for pure hydrogen, since, in the other cases, H_2 is diluted by the reformate components, which decreases the Nernst potential (see Eq. (13)) and increases the activation overpotential (see Eq. (24) and Table 2). The polarization curve simulated for the

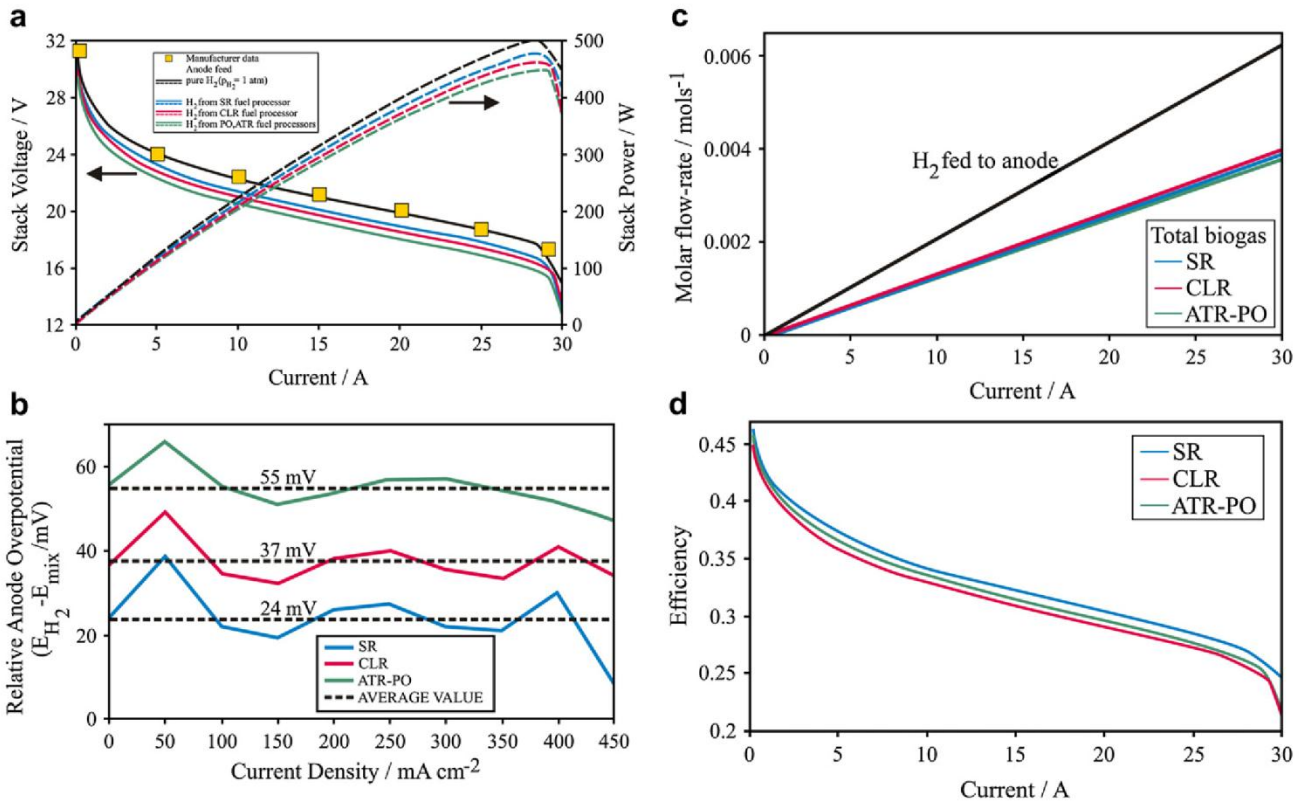

Fig. 17 – (a) Polarization curve and stack power of the BCS 500W fuel cell model, for the PEMFC stack integrated with different fuel processors (CLR, ATR, PO or SR). (b) Relative anode overpotential at different current densities for a single cell in the stack. The subscript 'mix' refers to H_2 mixed with other reformate components (CO_2, H_2O, N_2). (c) Molar flow-rate of H_2 fed to anode and total molar flow-rate of biogas as a function of the stack current. (d) Global efficiency as a function of current for different fuel processors (CLR, ATR, PO or SR).

PEMFC stack operating on H_2 produced by SR based fuel processor is the closest one to the polarization curve simulated taking into account pure hydrogen. In other words, the relative anode overpotential $(E_{H_2} - E_{mix})$ of a single cell computed for the PEMFC stack running on H_2 produced by SR fuel processor is the lowest one (an average value of 24 mV), as can be seen in Fig. 17(b). The use of ATR and PO fuel processors results in the highest values of relative anode overpotential (an average value of 55 mV), due to N_2 dilution of H_2 stream. One can see that, by replacing ATR and PO by CLR, it is possible to bring the values of relative anode potential closer to those calculated for SR fuel processors. Gu et al. [57] experimentally investigated the effect of reformate components on PEMFC performance and monitored the voltage loss due to N_2 dilution. For current densities in the range of 0–500 mA cm^{-2}, the relative anode overpotential varied from 10 to 60 mV, and it was approximately proportional to N_2 mole fraction. Fig. 17 (c) shows the molar flow-rate of H_2 fed to anode at each stack current. Besides, the total molar flow-rate of biogas to produce a certain molar flow-rate of H_2 and generate a given stack current is also shown. Fig. 17(d) depicts the global efficiency as a function of current for the different fuel processors. The overall efficiency of the PEMFC stack integrated with the fuel processor is found to be dependent on the current, and, consequently, on the power demand, which is in agreement with the findings of Francesconi et al. [45]. These authors investigated the performance of a PEMFC system integrated with a SR fuel processor operating on ethanol. Fig. 17(d) shows that, at low loads (thus, low values of current), efficiency is around 45%, whereas, at higher power demands (high current values), efficiencies around 25% are calculated for all the fuel processors. Francesconi et al. [45] also obtained, for an integrated ethanol processor, efficiency values less than 30% at high power demands. The global efficiency of CLR is ~0.4% lower than that of ATR and PO fuel processors and ~1% lower than that of SR fuel processors.

4. Conclusions

The performance of a PEMFC system integrated with a biogas chemical looping reforming processor was analyzed. It was found that the use of fuel processors based on CLR results in an auto-thermal global process, with high hydrogen yield (2.6 mol per mol of CH_4). If the CLR fuel processor is employed, CO_2 can be easily recovered, since air is not mixed with the reformate. Thus, in the case of biogas, the CO_2 captured could produce additional economical benefits in a 'carbon market'. The performance of a complete fuel cell system employing a fuel processor based on CLR technology was compared with

those achieved when conventional fuel processors (SR, PO and ATR) are used. It was found that the highest values of voltage and power are achieved when the PEMFC stack is fed on the stream coming from SR and CLR fuel processors, because, in these cases, the anodic stream does not contain N_2. When a H_2 mixture is produced by reforming biogas through PO and ATR technologies, the relative anode overpotential of a single cell is about 55 mV, whereas, with the use of CLR and SR fuel processors, this value is reduced to ~37 and 24 mV, respectively. In the case of PO and ATR, an auto-thermal global process is also reached. However, the CO_2 in the anode exhaust is mixed with N_2, which represents additional costs in a CO_2 separation step. With respect to SR fuel processor, it was found that, to generate the same molar flow-rate of H_2 to operate the PEMFC stack at a given current, the global process is by far much more energy demanding than PO, ATR and CLR. In this case, biogas is burnt in a catalytic combustor to supply the energy required, and there is a concern with respect to CO_2 emissions. Since air is fed to catalytic combustor, CO_2 is mixed with N_2 in the effluent, requiring, thus, additional investment for CO_2 separation.

The overall efficiency of the PEMFC stack integrated with the fuel processor is found to be dependent on the required power demand. At low loads, efficiency is around 45%, whereas, at higher power demands (high current values), efficiencies around 25% are calculated for all the fuel processors. The global efficiency obtained for fuel processors based on CLR technology is close to those achieved by conventional fuel processors (~0.4% lower than that of ATR and PO and ~1% lower than that of SR).

The optimized operating conditions were chosen in such a way that CH_4 conversion of each reforming technology is kept at exactly the same level (99.7%). For CLR, it was found that H_2 yield is maximized when steam is totally fed to the water–gas shift reactor, and fuel reactor operates in absence of steam. Even without the addition of steam to the fuel reactor, carbon deposition is avoided under auto-thermal conditions. The optimum air/CH_4 molar ratio for CLR operation is 0.328, which corresponds to a $NiO_{reacted}/CH_4$ molar ratio in fuel reactor of 1.31. These optimized operating conditions can be achieved by working with an oxygen-carrier circulation flow-rate of 1500 g s^{-1} mol CH_4^{-1} and oxygen-carrier conversion in air- and fuel-reactor equal to 100 and 32.70%, respectively. The optimized conditions are found for fuel- and air-reactors operating at 1073 and 1222 K, respectively. In the case of ATR reactor, the optimum inlet air/CH_4 and H_2O/CH_4 molar ratios are 0.300 and 1.125, respectively. Under these conditions, the adiabatic temperature in the ATR reactor is 1005 K. For the PO reactor, the adiabatic temperature is 1050 K. In this case, the optimum air/CH_4 molar ratio is of 0.310. The optimum temperature and inlet H_2O/CH_4 molar ratio in the SR reactor is 1048 K and 3.200, respectively.

Acknowledgments

The authors would like to acknowledge the CNPq-Brazil for financial support. Special thanks to Mr. José Walter Farfan Valverde for his contribution in this work.

REFERENCES

[1] Damyanova S, Pawelec B, Arishtirova K, Fierro JLG. Int J Hydrogen Energy 2011;36:10635–47.
[2] Effendi A, Hellgardt K, Zhang ZG, Yoshida T. Fuel 2005;84:869–74.
[3] Hoteit A, Chandel MK, Durécu S, Delebarre A. Int J Greenhouse Gas Contr 2009;3:561–7.
[4] Komiyama M, Misonou T, Takeuchi S, Umetsu K, Takahashi J. Int Congress Ser 2006;1293:234–7.
[5] Xuan J, Leung MKH, Leung DYC, Ni M. Renew Sust Energy Rev 2009;13:1301–13.
[6] Benito M, García S, Ferreira-Aparicio P, Serrano LG, Daza L. J Power Sources 2007;169:177–83.
[7] Zhang ZG, Xu G, Chen X, Honda K, Yoshida T. Fuel Process Technol 2004;85:1213–29.
[8] Xu G, Chen X, Honda K, Zhang ZG. AIChE J 2004;50:2467–80.
[9] Araki S, Hino N, Mori T, Hikazudani S. Int J Hydrogen Energy 2009;34:4727–34.
[10] Lau CS, Tsolakis A, Wyszynski ML. Int J Hydrogen Energy 2011;36:397–404.
[11] Araki S, Hino N, Mori T, Hikazudani S. J Natur Gas Chem 2010;19:477–81.
[12] Rafiq MH, Hustad JE. Renew Energ 2011;36:2878–87.
[13] Jing QS, Zheng XM. Energy 2006;31:2184–92.
[14] Aasberg-Petersen K, Bak Hansen JH, Christensen TS, Dybkjaer I, Seier Christensen P, Stub Nielsen C, et al. Appl Catal A Gen 2001;221:379–87.
[15] Rabenstein G, Hacker V. J Power Sources 2008;185:1293–304.
[16] de Ávila CN, Hori CE, de Assis AJ. Energy 2011;36:4385–95.
[17] de Diego LF, Ortiz M, García-Labiano F, Adánez J, Abad A, Gayán P. J Power Sources 2009;192:27–34.
[18] Ortiz M, Abad A, de Diego LF, García-Labiano F, Gayán P, Adánez J. Int J Hydrogen Energy 2011;36:9663–72.
[19] Rydén M, Lyngfelt A, Mattisson T. Fuel 2006;85:1631–41.
[20] Rydén M, Johansson M, Lyngfelt A, Mattisson T. Energ Environ Sci 2009;2:970–81.
[21] Pröll T, Bolhar-Nordenkampf J, Kolbitsch P, Hofbauer H. Fuel 2010;89:1249–56.
[22] Qi A, Peppley B, Karan K. Fuel Process Technol 2007;88:3–22.
[23] Adachi H, Ahmed S, Lee SHD, Papadias D, Ahluwalia RK, Bendert JC, et al. J Power Sources 2009;188:244–55.
[24] Di Bona D, Jannelli E, Minutillo M, Perna A. Int J Hydrogen Energy; 2011. doi:10.1016/y.ijhydene.2011.01.110.
[25] Lee SHD, Applegate DV, Ahmed S, Calderone SG, Harvey TL. Int J Hydrogen Energy 2005;30:829–42.
[26] Lee D, Lee HC, Lee KH, Kim SA. J Power Sources 2007;165:337–41.
[27] Aicher T, Full J, Schaadt A. Int J Hydrogen Energy 2009;34:8006–15.
[28] Besser RS. Int J Hydrogen Energy 2011;36:276–83.
[29] Northrop WF, Choi SO, Thompson LT. Int J Hydrogen Energy; 2012. doi:10.1016/j.ijhydene.2011.11.034.
[30] Ryden M, Lyngfelt A. Proceeding from the 7th Int. Conf. Greenhouse Gas Technologies, Vancouver (2004). http://uregina.ca/ghgt7/PDF/papers/peer/258.pdf.
[31] Knacke O, Kubaschewski O, Hesselmann K. Thermochemical properties of inorganic substances. 2nd ed. Berlin: Springer-Verlag; 1991.
[32] Lima da Silva A, Muller IL. J Power Sources 2010;195:5637–44.
[33] Lima da Silva A, Malfatti CF, Muller IL. Int J Hydrogen Energy 2009;34:4321–30.
[34] Dalle Nogare D, Baggio P, Tomasi C, Mutri L, Canu P. Chem Eng Sci 2007;62:5418–24.
[35] Monyanon S, Luengnaruemitchai A, Pongstabodee S. Int J Hydrogen Energy 2010;35:3234–42.

[36] Fonseca JSL, Ferreira HS, Bion N, P-Roy L, Rangel MC, Duprez D, et al. Catal Today 2012;180:34–41.
[37] Nilekar AU, Alayoglu S, Eichhorn B, Mavrikakis M. J Am Chem Soc 2010;132:7418–28.
[38] Ioannides T, Neophytides S. J Power Sources 2000;91: 150–6.
[39] Data sheet of a 500W fuel cell stack. Englewood, CO: BCS Technologies; 2001.
[40] Amphlett JC, Baumert RM, Harris TJ, Mann RF, Peppley BA, Roberge PR. J Electrochem Soc 1995;142:1–8.
[41] Amphlett JC, Baumert RM, Harris TJ, Mann RF, Peppley BA, Roberge PR. J Electrochem Soc 1995;142:9–15.
[42] Mann RF, Amphlett JC, Peppley BA, Thurgood CP. J Power Sources 2006;161:768–74.
[43] Mann RF, Amphlett JC, Hooper MAI, Jensen HM, Peppley BA, Roberge PR. J Power Sources 2000;86:173–80.
[44] Wishart J, Dong Z, Secanell M. J Power Sources 2006;161: 1041–55.
[45] Francesconi JA, Mussati MC, Aguirre PA. Int J Hydrogen Energy 2010;35:5940–6.
[46] Larminie J, Dicks A. Fuel cell systems explained. New York: Wiley; 2000.
[47] Xue D, Dong Z. J Power Sources 1998;76:69–80.
[48] Perna A. Int J Hydrogen Energy 2007;32:1811–9.
[49] Buchi FN, Scherer GG. J Electroanal Chem 1996;404:37–43.
[50] Corrêa JM, Farret FA, Canha LN, Simoes MG. IEEE Trans Ind Electron 2004;51:1103–12.
[51] Amphlett JC, Mann RF, Peppley BA, Roberge PR, Rodrigues A. J Power Sources 1996;61:183–8.
[52] Mattisson T, Johansson M, Lyngfelt A. Fuel 2006;85:736–47.
[53] Kolbitsch P, Pfeifer C, Hofbauer H. Fuel 2008;87:701–6.
[54] Soria MA, Mateos-Pedrero C, Guerrero-Ruiz A, Rodríguez-Ramos I. Int J Hydrogen Energy; 2011. doi:10.1016/j.ijhydene.2011.08.117.
[55] Seo YS, Shirley A, Kolaczkowski ST. J Power Sources 2002; 108:213–25.
[56] Campanari S, Chiesa P, Manzolini G. Int J Greenhouse Gas Contr 2010;4:441–51.
[57] Gu T, Lee WK, van Zee JW, Murthy M. J Electrochem Soc 2004; 151:A2100–5.

4.2. *Discussão integrando os resultados dos artigos*

Nesta seção, é feita uma breve discussão a respeito da relação que os artigos têm entre si. Todos os trabalhos têm um objetivo comum, que é a geração de eletricidade a partir de células a combustível. Enquanto alguns trabalhos estão focados essencialmente na produção de H_2 para posterior utilização no ânodo de uma célula PEMFC ou SOFC, outros trabalhos consideram que a conversão do combustível ocorra diretamente no ânodo de uma célula de alta temperatura (SOFC). A metodologia empregada na realização dos trabalhos é similar, baseando-se no método da minimização da energia de Gibbs. Esta Tese também mostra que diversas análises referentes à produção de H_2 e geração de eletricidade pertencem ao campo dos problemas convexos de otimização. De acordo com a aplicação, algumas modificações na metodologia são introduzidas, como o que ocorre nas restrições do balanço de massa elementar no caso em que se simula a conversão do combustível no ânodo da SOFC. Em outras situações, modelos eletroquímicos considerando irreversibilidades na operação da célula são acoplados ao modelo básico (minimização da energia de Gibbs) que é aplicado aos diferentes processadores de combustível. Além disso, conforme as particularidades do tipo de reator empregado, diversos parâmetros têm que ser incorporados dentro do modelo básico. Este é o caso de um reformador baseado na tecnologia de *chemical looping*. Para este tipo de sistema, a circulação das partículas entre os reatores deve ser considerada no modelo, e a minimização da energia de Gibbs deve estar acoplada às equações de balanço de massa e energia que estão envolvidas no reator de ar e de combustível. No caso da simulação do processo de reforma *unmixed*, em que não há circulação de partículas entre reatores, mas sim uma alternância entre sopros de combustível e de ar no mesmo reator, basicamente se inclui o parâmetro $NiO_{reagido}/CH_4$ na rotina de minimização. Outro aspecto que deve ser ressaltado é com respeito à evolução da

metodologia empregada e da ampliação dos resultados. Pode-se afirmar que os resultados dos diferentes trabalhos se complementam.

No artigo da seção 4.1.1, focou-se no desenvolvimento da ferramenta de cálculo que é empregada também em todos os demais trabalhos, além da análise de um sistema envolvendo puramente a fase gasosa. Neste trabalho, a tendência à deposição de carbono foi avaliada com base no valor da atividade, com referência na fase grafite, que é computada a partir da composição de equilíbrio da fase gasosa. Já no artigo da seção 4.1.2, fases condensadas foram introduzidas na descrição da energia de Gibbs, além de considerar-se um banco de dados muito maior, com o envolvimento de diversas espécies na fase gasosa (29 espécies). Neste mesmo artigo, a eficiência térmica do processo foi analisada para os diversos combustíveis; no artigo da seção 4.1.1, a eficiência não tinha sido considerada. O artigo da seção 4.1.2 pode ser considerado como uma evolução da análise realizada no artigo da seção 4.1.1. De acordo com a conclusão do artigo da seção 4.1.1, percebe-se que as condições otimizadas de produção de H_2 correspondem a altas temperaturas e valores relativamente altos para a razão de H_2O/etanol; nestas condições, a deposição de carbono poderia ser evitada e a concentração de CO poderia ser minimizada. No entanto, verifica-se, a partir desta análise, que a concentração de H_2 é em torno de 70% e que a concentração de CO ainda está muito acima da requerida para aplicação em células do tipo PEMFC. Para a obtenção de H_2 de alta pureza, necessita-se, portanto, de uma planta com maior complexidade, envolvendo reatores de purificação, como reatores WGS e reatores COPROX. Além disso, as elevadas temperaturas e altas razões de H_2O/etanol implicam em um balanço energético desfavorável no reformador, resultando em um processo muito endotérmico, baixando a eficiência térmica do processo. O artigo da seção 4.1.2 apresenta uma solução para este problema. Pela adição de CaO no reformador e com a

seleção adequada dos parâmetros de operação (pressão, temperatura e relação H_2O/combustível), demonstrou-se que é possível, usando-se diferentes combustíveis oxigenados, a obtenção de H_2 ultra-puro, com CO na faixa de 20ppm em um único passo, sem a necessidade de reatores WGS e COPROX. Além disso, devido à exotermicidade da reação de carbonatação, o processo de reforma passa a ter um balanço energético favorável, podendo aumentar a eficiência do processo. É preciso considerar, contudo, a energia que se demanda na regeneração do CaO. Além disso, o processo de decomposição do carbonato envolve um regenerador interconectado ao reformador. Seria interessante que o processo de reforma com captura *in situ* de CO_2 ocorresse no mesmo reator onde ocorre a regeneração. Isto é possível com a tecnologia de *unmixed reforming*, como demonstrado no artigo da seção 4.1.5. A termodinâmica demonstra que é possível obter, durante o sopro de combustível, um grande período de obtenção de H_2 de alta pureza, com favorecimento da reação de carbonatação tanto durante a redução de NiO como durante a reforma. O calor liberado devido à captura de CO_2 pode suprir a demanda energética durante o processo de produção de H_2. No período que corresponde ao sopro de ar, a oxidação do Ni libera calor suficiente para a regeneração do CaO. Os cálculos demonstram a possibilidade de um processo auto-térmico. Note que na seção 4.1.5 considerou-se metano como combustível. Isto foi feito simplesmente para poder fazer a validação com dados experimentais disponíveis na literatura. A mesma metodologia e análise são perfeitamente aplicáveis aos combustíveis oxigenados (etanol, glicerol, butanol, metanol).

Enquanto os artigos da seção 4.1.1, 4.1.2 e 4.1.5 têm suas análises focadas somente no reformador, o artigo da seção 4.1.6 investiga o desempenho de uma planta de conversão completa, considerando diferentes tipos de reformadores (reforma a vapor, autotérmica, oxidação parcial e *chemical looping*) integrados com as unidades de

purificação, aquecedores, trocadores de calor e o *stack* comercial da célula PEMFC, BCS 500W. A eficiência do processo global (não só a do reformador) é analisada. De fato, verifica-se que a eficiência global é função da corrente de operação do *stack*. Portanto, o artigo da seção 4.1.6 complementa os estudos das outras seções (4.1.1, 4.1.2 e 4.1.5), no sentido em que se considera uma planta e não somente um reator de conversão. Embora a planta tenha algumas simplificações, as quais são necessárias para poder fazer a análise empregando a ferramenta utilizada na presente Tese, os resultados são consistentes e de acordo com o esperado com base na literatura. Além disso, outro tipo de biocombustível –biogás – é analisado. Com a utilização da tecnologia de *chemical looping*, obtém-se um processo global eficiente, sem problemas de diluição do reformato pelo N_2 do ar, além da possibilidade de um processo inteiramente limpo, sem emissões de CO_2 para a atmosfera.

Os artigos das seções 4.1.3 e 4.1.4 estão focados na utilização direta de glicerol em ânodos de células SOFC. Enquanto o artigo da seção 4.1.3 investiga o efeito da densidade de corrente na composição da atmosfera do ânodo e na quantidade de carbono que pode ser depositada durante a operação, considerando-se somente o eletrólito condutor de íons O^{2-}, o artigo da seção 4.1.4 avalia o efeito da corrente de operação (ou utilização de combustível) quando o eletrólito é condutor de íons O^{2-} ou de íons H^+ (cerâmicas protônicas). Em ambos os artigos, avalia-se o potencial reversível da célula em função da densidade de corrente (ou utilização de combustível). Os diagramas resultantes deste tipo de análise são úteis na pesquisa experimental para determinação direta da eficiência da célula. Contudo, a abordagem do artigo da seção 4.1.4 é diferente da do artigo da seção 4.1.3. Na seção 4.1.4, o artigo considera que H_2 reaja eletroquimicamente de forma gradativa ao longo de um canal de comprimento L, o que corresponde ao modo de operação conhecido como *plug flow*. Além disso, é avaliada a

eficiência da SOFC quando diferentes eletrólitos são empregados, mostrando-se que células SOFC que empregam eletrólitos condutores de íons H^+ resultam em maior eficiência, mas também em maior tendência à deposição de carbono no ânodo. Na seção 4.1.3, não se considera que a reação eletroquímica ocorra de forma gradativa ao longo do canal, tendo diferentes valores de utilização de combustível conforme a posição no interior do canal. Considera-se, contudo, uma mistura perfeita no ânodo. Este é um modo de operação alternativo ao *plug flow*, conhecido como *perfect mixing*, sem gradiente espacial de composição.

Todos os trabalhos publicados estão baseados em simulações validadas, na medida do possível, por resultados experimentais da literatura. Durante o período de realização da presente Tese, verificou-se que muitos dos resultados teóricos foram utilizados na pesquisa experimental de outros pesquisadores, bem como a metodologia desenvolvida no presente trabalho, que serviu de base para o desenvolvimento de trabalhos teóricos de outros pesquisadores. De fato, uma característica comum aos artigos desta Tese, além da metodologia, é a elaboração de diagramas úteis para a pesquisa experimental. Seguem, então, as citações, em periódicos, referentes aos artigos publicados até o presente momento (agosto/2012):

g) **Artigo da seção 4.1.1** (*Thermodynamic analysis of ethanol steam reforming using Gibbs energy minimization method: A detailed study of the conditions of carbon deposition)*

- Vourliotakis e colaboradores [108]: trabalho teórico fazendo referência às condições otimizadas (H_2 em torno de 70% em altas temperaturas, T>1000K), condições de deposição de carbono e metodologia empregada;
- Cai e colaboradores [109]: trabalho experimental fazendo referência às condições calculadas para a completa conversão do etanol,

independentemente da quantidade de água adicionada à mistura de alimentação do reator; comparação dos resultados experimentais com os resultados teóricos da presente Tese para a conversão do etanol em H_2, CO, CO_2, CH_4;

- Balaji e colaboradores [110]: trabalho teórico fazendo referência à metodologia, ressaltando a característica do problema convexo, em que não há problema referente à escolha da estimativa inicial;
- Al-Hamamre e colaboradores [111]: trabalho teórico fazendo referência ao tipo de investigação teórica para processo de conversão com etanol;
- Wang e colaboradores [112]: trabalho teórico fazendo referência à metodologia (minimização da energia de Gibbs);
- Kale e colaboradores [113]: trabalho teórico fazendo referência à comparação realizada entre resultados termodinâmicos e experimentais, em que foram explicadas as discrepâncias;
- Chen e colaboradores [114]: trabalho experimental fazendo referência às condições calculadas para a máxima produção de H_2 em que a deposição de carbono é evitada (intervalo entre 823-1073K); referência às condições calculadas para a formação de CO;
- Wang e colaboradores [115]: trabalho teórico fazendo referência à metodologia (minimização da energia de Gibbs);
- Muhammad e colaboradores [116]: trabalho experimental fazendo referência à dependência da reação de reforma do etanol com a temperatura no intervalo analisado (500-1000ºC).

- Muhammad e Li [117]: trabalho experimental fazendo referência à dependência da reação de reforma do etanol com a temperatura no intervalo analisado (500-1000ºC).
- Li e colaboradores [118]: trabalho teórico fazendo referência ao método computacional empregado;
- Khaodee e colaboradores [119]: trabalho teórico fazendo referência à metodologia (minimização da energia de Gibbs);
- De Ávila e colaboradores [120]: trabalho teórico fazendo referência à condições ótimas de produção de H_2.
- Yenumala e Maity [121]: trabalho teórico fazendo referência ao estudo teórico aplicado à reforma do etanol;
- Gucciardi e colaboradores [122]: trabalho experimental fazendo referência às condições de deposição de carbono;
- Göll e colaboradores [123]: trabalho teórico fazendo referência à metodologia (minimização da energia de Gibbs);
- Nahar e Dupont [124]: trabalho de revisão, incluído resultados da análise do etanol;
- Trabold e colaboradores [125]: trabalho teórico-experimental em que foi empregada a metodologia da tese (ferramenta Solver e determinação da tendência à deposição de carbono para equação que relaciona os multiplicadores de Lagrange com a atividade termodinâmica);
- Wu e colaboradores [126]: trabalho teórico fazendo referência à metodologia e às condições otimizadas de produção de H_2;

- Rossetti e colaboradores [127]: trabalho experimental fazendo referência às condições de deposição de carbono e utilização de dados teóricos para explicação de tendências experimentais;
- Göll e colaboradores [128]: trabalho teórico fazendo referência à metodologia empregada (minimização da energia de Gibbs);
- Graschinsky e colaboradores [129]: trabalho teórico fazendo referência à metodologia, condições de deposição de carbono e aspectos térmicos mencionados no artigo;
- Shabbar e Janajreh [130]: trabalho teórico fazendo referência à metodologia (multiplicadores de Lagrange);
- Kale e colaboradores [131]: trabalho teórico fazendo referência ao estudo termodinâmico aplicado è reforma do etanol.

h) **Artigo da seção 4.1.2** (*Hydrogen production by sorption enhanced steam reforming of oxygenated hydrocarbons (ethanol, glycerol, n-butanol and methanol): Thermodynamic modeling)*

- Li e colaboradores [118]: trabalho teórico fazendo referência ao método computacional empregado;
- Yenumala e Maity [121]: trabalho teórico fazendo referência ao estudo teórico aplicado à reforma dos diferentes biocombustíveis;
- Roy e colaboradores [132]: trabalho experimental fazendo referência à análise aplicada ao *n*-butanol;
- Chanburanasiri e colaboradores [133]: trabalho experimental fazendo referência aos resultados da reforma com captura *in situ* de CO_2 de hidrocarbonetos oxigenados;

- Park e Yi [134]: trabalho experimental fazendo referência aos resultados da reforma com captura *in situ* de CO_2 de hidrocarbonetos oxigenados e à descrição do processo;
- Nahar e Dupont [124]: trabalho de revisão em que são incluídos resultados da análise do processo de reforma com captura *in situ* de CO_2 do etanol, glicerol e butanol.
- Wu e colaboradores [126]: trabalho teórico fazendo referência aos resultados obtidos para a reforma na presença de CaO; os resultados do artigo da seção 4.1.2 foram usados como *benchmark* para os autores validarem suas simulações; os autores compararam os resultados obtidos no artigo da seção 4.1.2, calculados para o CaO, com o resultados que eles obtiveram usando outros materiais, como hidrotalcitas e zirconato de lítio.

i) **Artigo da seção 4.1.3** (*Operation of solid oxide fuel cells on glycerol fuel: a thermodynamic analysis using the Gibbs free energy minimization approach)*

- Lo Faro e colaboradores [135]: trabalho experimental em que os autores fazem referência aos diagramas calculados de potencial reversível em função da densidade de corrente. Os valores são usados para estimar a eficiência real de sua célula a combustível operante com glicerol;
- Gao e colaboradores [136]: trabalho teórico-experimental em que os autores adotam a mesma metodologia de cálculo de equilíbrio do artigo da seção 4.1.3 para estimar a composição da atmosfera do ânodo e a quantidade possível de carbono que pode vir a se depositar em uma célula SOFC operante com metanol. Com respeito à deposição de carbono, os autores concluíram que os resultados experimentais e termodinâmicos coincidem.

- Qin e colaboradores [137]: Trabalho experimental em que os autores utilizaram dados teóricos do artigo da seção 4.1.3, referentes ao potencial de circuito aberto e valor da densidade de corrente limiar (aquela em que o carbono depositado no ânodo é completamente oxidado pelos íons O^{2-} que vêm do cátodo em direção ao ânodo), para comparar os dados obtidos experimentalmente para uma célula SOFC em operação com glicerol. Os autores verificam que os valores teóricos e experimentais são muito próximos.
- Siengchum e colaboradores [138]: Trabalho experimental em que os autores fazem referência à metodologia do artigo da seção 4.1.3 para cálculo de equilíbrio em um ânodo da célula SOFC. Os autores consideram uma célula operando diretamente com carbono sólido.
- Lo Faro e colaboradores [139]: Trabalho experimental em que os autores fazem referência à análise realizada para SOFCs operando com glicerol.

j) **<u>Artigo da seção 4.1.4</u>** (*Thermodynamic study on glycerol-fuelled intermediate-temperature solid oxide fuel cells (IT-SOFCs) with different electrolytes)*

- Li e colaboradores [140]: Trabalho teórico no qual os autores fazem referência às principais espécies que foram computadas nos cálculos de equilíbrio realizados no artigo da seção 4.1.4.
- Su e colaboradores [141]: Trabalho experimental em que os autores fazem referência à análise realizada para SOFCs operando com glicerol.
- Lo Faro e colaboradores [135]: Trabalho experimental em que os autores fazem referência à análise realizada para SOFCs operando com glicerol e aos resultados de eficiência teórica.

- Oulmi e colaboradores [142]: Trabalho teórico em que os autores mencionam a análise feita referente à reforma interna direta do glicerol em célula SOFC.
- Qin e colaboradores [137]: Trabalho experimental em que os autores fazem referência à análise realizada para SOFCs operando com glicerol, às reações químicas descritas no artigo e aos valores teóricos calculados referentes à operação da célula.
- Trabold e colaboradores [125]: Trabalho teórico-experimental em que os autores utilizaram resultados teóricos (temperatura em que a produção de H_2 é maximizada e em que a produção de H_2O passa por um mínimo) para explicar observações experimentais.
- Su e colaboradores [143]: Trabalho experimental em que os autores fazem referência à análise realizada para SOFCs operando com glicerol.

k) **Artigo da seção 4.1.5** (*Towards H_2-rich gas production from unmixed steam reforming of methane: Thermodynamic modeling)*

- Thursfield e colaboradores [144]: Trabalho de revisão no qual os autores mencionam a modelagem termodinâmica aplicada ao estágio correspondente ao sopro de combustível (metano) em que NiO foi empregado como carreador de oxigênio. Os autores também mencionam a validação da simulação com valores experimentais da literatura.

CAPÍTULO 5: CONCLUSÕES

Neste trabalho, desenvolveu-se uma metodologia que foi capaz de resolver diversos problemas de interesse na área de produção de hidrogênio e geração de eletricidade a partir de células a combustível de baixa temperatura (PEMFC) e alta temperatura (SOFC). Com a adequação da ferramenta *Solver* do Excel e a utilização de uma relação matemática que permite relacionar os multiplicadores de Lagrange com a atividade termodinâmica e, portanto, com a força motriz para a formação de uma fase, foi possível resolver, de forma robusta, sem dificuldades relacionadas com estimativas iniciais, diversos problemas convexos pertencentes ao ramo da otimização não-linear. Deste modo, este trabalho demonstra a possibilidade de utilização de uma ferramenta de fácil entendimento por parte do usuário, sem a necessidade de conhecimentos de programação, para realização de simulações termodinâmicas, desde que estas se enquadrem dentro do conjunto dos problemas convexos, o que garante que o mínimo local corresponda ao global. Para obtenção de bons resultados nas simulações, necessita-se também de fontes bibliográficas confiáveis para a descrição dos dados termodinâmicos. Devido à facilidade de utilização de planilhas do Excel, o presente trabalho ainda demonstra a viabilidade de simulação de uma planta de conversão de combustível, considerando-se os diversos reatores de purificação e outras unidades, além do reformador, com a possibilidade de realizar balanços de massa e energia em toda a planta. Além disso, há a facilidade na implementação de um modelo eletroquímico para descrição da curva de polarização de um *stack* de células PEMFC, integrando-o ao resto da planta. Deste modo, foi possível avaliar como o tipo de reformador e a escolha dos parâmetros de operação (temperatura, quantidade de água na

mistura, taxa de circulação de sólidos, corrente de operação do *stack*, etc) afetam a eficiência global do processo.

Diversas simulações puderam ser conduzidas contemplando diferentes rotas termoquímicas de produção de hidrogênio (reforma a vapor, autotérmica, oxidação parcial, reforma com captura *in situ* de CO_2, *unmixed reforming* e *chemical looping*) empregando-se diversos combustíveis (etanol, glicerol, metanol, *n*-butanol, biogás e metano). Além disso, foi analisada a utilização direta de combustível no ânodo de uma célula SOFC. Quatro objetivos gerais foram alcançados com a presente Tese:

- ✓ A partir de dados experimentais da literatura, foi possível propor explicações, com base na termodinâmica, capazes de justificar tais valores e tendências observados;
- ✓ Elaboração de diagramas práticos em que são mostradas as condições otimizadas para a realização de experimentos, o que é de utilidade para pesquisadores experimentalistas;
- ✓ Proposição de novas rotas eficientes para produção de H_2 e geração de eletricidade com o uso de células a combustível;
- ✓ Demonstração da aplicabilidade e robustez de uma ferramenta de fácil entendimento e acesso para o uso em simulações termodinâmicas;

CAPÍTULO 6: REFERÊNCIAS

[1] Aboudheir A, Akande A, Idem RO, Dalai A. Experimental studies and comprehensive reactor modeling of hydrogen production by the catalytic reforming of crude ethanol in a packed bed tubular reactor over a Ni/Al_2O_3 catalyst. *International Journal of Hydrogen Energy* 2006; 31:752-761.

[2] Navaro RM, Sanchez-Sanchez MC, Alvarez-Galvan MC, Fierro JLG, Al-Zaharani SM. H_2 production from renewables. In Robert H. Crabtree (Ed.). *Energy Production and Storage*: Inorganic Chemical Strategies for a Warming World. Wiley, 2010. p. 3-20.

[3] Decreto nº 5.163, de 30 de julho de 2004. www.ceb.com.br/CebNovo/arquivos/Pdf/decreto5163.pdf . Acesso em 27/07/2012.

[4] Haryanto A, Fernando S, Murali N, Adhikari S. Current Status of Hydrogen Production Techniques by Steam Reforming of Ethanol: A Review. *Energy & Fuels* 2005;19: 2098-2106.

[5] Profeti LPR, Ticianelli EA, Assaf EM. Production of hydrogen via steam reforming of biofuels on Ni/CeO_2-Al_2O_3 catalysts promoted by noble metals. *International Journal of Hydrogen Energy* 2009; 34: 5049-5060.

[6] Adhikari S, Fernando S, Gwaltney SR, Filip To SD, Mark Bricka R, Steele PH, Haryanto A. A thermodynamic analysis of hydrogen production by steam reforming of glycerol, *International Journal of Hydrogen Energy* 2007; 32: 2875-2880.

[7] Nahar GA, Madhani SS. Thermodynamics of hydrogen production by the steam reforming of butanol: analysis of inorganic gases and light hydrocarbons. *International Journal of Hydrogen Energy* 2010; 35: 98-109.

[8] Hipolito CN, Crabbe E, Badillo CM, Zarrabal OC, Morales Mora MA, Flores GP, et al. Bioconversion of industrial wastewater from palm oil processing to butanol by *Clostridium saccharoperbutylacetonicum* N1-4 (ATCC 13564). *Journal of Cleaner Production* 2008; 16: 632-638.

[9] Atsumi S, Hanai T, Liao JC. Non fermentative pathways for synthesis of branched-chain higher alcohols as biofuels. *Nature* 2008; 451: 86-89.

[10] Advanced Research projects Agency, US department of Energy. http://www.energy.gov/news/8207.htm. Acesso em 26 de outubro de 2009.

[11] Hohn KL, Lin YC. Catalytic partial oxidation of methanol and ethanol for hydrogen generation. *CheSusChem* 2009; 2: 927-940.

[12] ANEEL – Agência Nacional de Energia Elétrica, resolução normativa, nº 390, 15 de dezembro de 2009. www.aneel.gov.br/cedoc/ren2009390.pdf, acesso em 29/06/2012.

[13] Staniforth J, Kendall K. Biogas powering a small tubular solid oxide fuel cell. *Journal of Power Sources* 1998; 71: 275-277.

[14] Weiland P. Biogas production:current status and perspectives. *Appl. Microbiol*. *Biotechnol*, 2010; 85: 849-860.

[15] Wang J-H, Liu M. Computational study of sulphur-nickel interactions: A new S-Ni phase diagram. *Electrochemistry Communications* 2007; 9: 2212-2217.

[16] Laycock C J, Staniforth JZ, Ormerod RM. Biogas as a fuel for solid oxide fuel cell and synthesis gas production: effects of ceria doping and hydrogen sulfide on the performance of nickel-based anode materials. *Dalton Transactions* 2011; 40: 5494-5504.

[17] Laosiripojana N, Charojrochkul et al. Role and advantages of H_2S in catalytic steam reforming over nanoscale CeO_2-based catalysts. *Journal of Catalysis* 2010; 276: 6-15.

[18] Ball M, Weindorf W, Bunger U. Hydrogen production. In M Ball e M Wietschel (Eds.). *The Hydrogen Economy*. Cambridge: Cambridge University press, 2009, p.277.

[19] IEA (International Energy Association), *Hydrogen production and Distribution*, OECD/IEA, Paris, 2007.

[20] Zanfir M, Gavriilidis A. Catalytic combustion assisted methane steam reforming in a catalytic plate reactor. *Chemical engineering science* 2003; 58: 3947-3960.

[21] Aasberg-Petersen K, Bak Hansen JH, Christensen TS, Dybkjaer I, Seier Christensen P, Stub Nielsen C, Winter Madsen SEL, Rostrup-Nielsen JR. Technologies for large-scale gas conversion. *Applied Catalysis A: General* 2001; 221: 379-387.

[22] Fan L-S. Chemical looping systems for fossil energy conversions. Hoboken, NJ : Wiley-AIChE, 2010, 420p.

[23] Rabenstein G, Hacker V. Hydrogen for fuel cells from ethanol by steam-reforming, partial-oxidation and combined auto-thermal reforming: A thermodynamic analysis. *Journal of Power Sources* 2008; 185: 1293-1304.

[24] Gu T, Lee WK, van Zee JW, Murthy M. The effect of reformate components on PEMFC performance: dilution and reverse water gas shift reaction. *Journal of Electrochemical Society*; 2004; 151:A2100-A2105.

[25] Corbo P, Migliardini F. Hydrogen production by catalytic partial oxidation of methane and propane on Ni and Pt catalysts. *International Journal of Hydrogen Energy* 2007; 32: 55-66.

[26] Sandia's Hydrogen Program – short contact reactors. http://www.sandia.gov/hydrogen/research/production/shortContactReactors.html. Acesso em 28/07/2012.

[27] Neumann D., Kirchhoff M., Veser G. Towards an efficient process for small-scale, decentralized conversion of methane to synthesis gas: combined reactor engineering and catalyst synthesis. *Catalysis Today* 2004; 98: 565-574.

[28] Amirshaghaghi H. Zamanyan A., Ebrahimi H., Zarkesh M. Numerical simulation of methane partialoxidation in the burner and combustion chamber of autothermal reformer. *Applied Mathematical modeling* 2010; 34: 2312-2322.

[29] Wang W, Cao Y. Hydrogen production via sorption enhanced steam reforming of butanol: thermodynamic analysis. *International Journal of Hydrogen Energy* 2011; 36: 2887-2895.

[30] de Diego LF, Ortiz M, García-Labiano F, Adánez J, Abad A, Gayán P. Hydrogen production by chemical-looping reforming in a circulating fluidized bed reactor using Ni-based oxygen carriers. *Journal of Power Sources* 2009; 192: 27-34.

[31] Mattisson T, Johansson M, Lyngfelt A. The use of NiO as an oxygen carrier in chemical-looping combustion. *Fuel* 2005; 85: 736-747.

[32] Lyon RK, Cole JA. Unmixed combustion: an alternative to fire. *Combustion Flame* 2000; 121: 249-261.

[33] Dupont V, Ross AB, Knight E, Hanley I, Twigg MV. Production of hydrogen by unmixed steam reforming of methane. *Chemical Engineering Science* 2008; 63: 2966-2979.

[34]Dupont V, Ross AB, Hanley I, Twigg. Unmixed steam reforming of methane and sunflower oil: A single-reactor process for H_2-rich gas. *International Journal of Hydrogen Energy* 2007; 32: 67-79.

[35] Chiron F-X, Patience GS. Steam carbon gasification of a nickel based oxygen carrier. *Fuel* 2011; 90: 2461-2466.

[36]Pimenidou P, Rickett G, Dupont V, Twigg MV. Chemical looping reforming of waste cooking oil in packed bed reactor. *Bioresource Technology* 2010; 101: 6389-6397.

[37]Pimenidou P, Rickett G, Dupont V, Twigg MV. High purity H_2 by sorption-enhanced chemical looping reforming of waste cooking oil in a packed bed reactor. *Bioresource Technology* 2010; 101: 9279-9286.

[38] Kumar RV, Cole JA, Lyon RK. Preprints of Symposia, 218th ACS National Meeting, vol.44, nº4, August 22-16, new Orleans, LA, 1999,p. 894-898.

[39] Giannakeas N, Lea-Langton A, Dupont V, Twigg MV. Hydrogen from Scrap Tyre Oil via Steam Reforming and Chemical Looping in a Packed Bed Reactor. *Applied Catalysis B:Environmental*, In Press.

[40] Ishida M, Zheng D, Akehata T. Evaluation of a chemical-looping-combustion power-generation system by graphic exergy analysis. *Energy* 1987; 12: 147-154.

[41] Jin H, Ishida M. A new type of coal gas fueled chemical looping combustion. *Fuel* 2004; 83: 2411-2417.

[42] Mattison T, Lyngfelt A. Proceedings of the 2nd Nordic minisymposium on carbon dioxide capture and storage, Göteborg, Sweden, 2001.

[43] Adanez J, Abad A, Garcia-Labiano F, Gayan P, de Diego LF. Progress in Chemical-Looping Combustion and Reforming technologies. Progress in Energy and Combustion Science 2012; 38: 215-282.

[44] Ryden M, Lyngfelt A.Proceeding from the 7th Int. Conf. Greenhouse Gas technologies, Vancouver 2004.http://uregina.ca/ghgt7/PDF/papers/peer/258.pdf. Acesso em 28/07/2012.

[45] Zafar Q, Mattison T, Gevert B.Integrated hydrogen and power production with CO_2 capture using chemical-looping reforming-redox reactivity of particles of CuO, Mn_2O_3, NiO, and Fe_2O_3 using SiO_2 as a support. *Industrial & Engineering Chemistry Research* 2005, 44, 3485–3498.

[46] Zafar Q, Mattison T, Gevert B. Redox investigation of some oxides of transition-state metals Ni, Cu, Fe, and Mn supported on SiO_2 and $MgAl_2O_4$. *Energy & Fuels* 2006; 20: 34–44.

[47] Johansson M, Mattisson T, Lyngfelt A, Abad A. Using continuous and pulse experiments to compare two promising nickel-based oxygen-carriers for use in chemical-looping technologies. *Fuel* 2008; 87: 988–1001.

[48] de Diego L.F, Ortiz M, Adánez J, García-Labiano F, Abad A, Gayán P. Synthesis gas generation by chemical-looping reforming in a batch fluidized bed reactor using Ni-based oxygen-carriers. *Chemical Engineering Journal* 2008; 144: 289–298.

[49] Ortiz M, de Diego LF, Abad A, Garcıa-Labiano F, Gayan P, Adanez J. Hydrogen production by auto-thermal chemical looping reforming in a pressurized fluidized bed reactor

using Ni-based oxygen carriers. *International Journal of Hydrogen Energy* 2010; 35: 151-160.

[50] Ryden M, Lyngfelt A, Mattisson T. Synthesis gas generation by chemical-looping reforming in a continuously operating laboratory reactor. *Fuel* 2006; 85: 1631-1641.

[51] Ryden M, Johansson M, Lyngfelt A, Mattisson T. NiO supported on Mg-ZrO2 as oxygen-carrier for chemical looping combustion and chemical-looping reforming. *Energy and Environmental Science* 2009; 2: 970-981.

[52] Ryden M, Lyngfelt A, Mattisson T. Chemical-looping combustion and chemical-looping reforming in a circulating fluidized-bed reactor using Ni-based oxygen-carriers. *Energy &Fuels* 2008; 22: 2585-297.

[53] Proll T, Bolhar-Nordenkampf J, Kolbitsch P, Hofbauer H. Syngas and a separate nitrogen/argon stream via chemical looping reforming e a 140 kW pilot plant study. *Fuel* 2010; 89:1249-1256.

[54] de Andrade LM. Reforma a vapor e oxidativa de etanol para a produção de hidrogênio utilizando catalisadores de ródio suportados em γ-Al_2O_3, CeO_2, e CeO_2-γ-Al_2O_3. Dissertação de mestrado. São Carlos, 2007.

[55] Fatsikostas AN, Kondarides DI, Verykios XE. Production of hydrogen for fuel cells by reformation of biomass-derived ethanol. *Catalysis Today* 2002; 75: 145-155.

[56] Fatsikostas NA, Kondarides DI., Verykios XE. Steam reforming of biomass-derived ethanol for the production of hydrogen for fuel cell applications. *Chemical Communications* 2001; 851-852.

[57] Llorca J, Homs N, Sales J, de La Piscina PR. Efficient production of hydrogen over supported cobalt catalysts from ethanol steam reforming. *Journal of Catalysis* 2002; 209:306-317.

[58] Fierro V, Akdim O, Mirodatos C. On-board hydrogen production in a hybrid electric vehicle by bio-ethanol oxidative steam reforming over Ni and noble metal based catalysts. *Green Chemistry* 2003; 5:20-24

[59] Navarro RN, Alvarez-Galván MC, Sanchez-Sanchez MC, Rosa F, Fierro JLG. Production of hydrogen by oxidative reforming of ethanol over Pt catalysts supported on Al_2O_3 modified with Ce and La. *Applied catalysis B: Environmental* 2005; 55: 229-241.

[60] Gonçalves BRL, Perez L, Ângelo ACD. Glicerol: Uma inovadora fonte de energia proveniente da produção do biodiesel. International Workshop Advances in Cleaner Production, São Paulo SP, Brasil, 2009.

[61] Sakai S, Yagishita T. Microbial production of hydrogen and ethanol from glycerol-containing wastes discharged from a biodiesel fuel production plant in a bioelectrochemical reactor with thionine. *Biotechnol. Bioeng*. 2007; 8: 340-348.

[62] Da Costa, J B. Produção biotecnológica de hidrogênio, etanol e outros produtos a partir do glicerol da reação de formação do biodiesel. Dissertação de mestrado, 2010, Porto Alegre.

[63] Arechederra R.L, Treu B.L., Minteer S.D. Development of glycerol/O_2 biofuel cell. *Journal of Power Sources* 2007; 173: 156-161.

[64] Iriondo A, Barrio VL, Cambra JF, Arias PL, Guemez MB, Sanchez-Sanchez MC, et al. Glycerol steam reforming over Ni catalysts supported on ceria and ceria-promoted alumina. *International Journal of Hydrogen Energy* 2010; 35:11622-11633.

[65] Carvalho DL, de Avillez RR, Rodrigues MT, Borges LEP, Appel LG. Mg and Al mixed oxides and the synthesis of n-butanol from ethanol. *Applied Catalysis A: general* 2012; 415-416: 96-100.

[66] Roy B, Sullivan H, Leclerc CA. Aqueous-phase reforming of n-BuOH over Ni/Al_2O_3 and Ni/CeO_2 catalysts. *Journal of Power Sources* 2011; 196: 10652-10657.

[67] Cai W, Homs N, de la Piscina PR. Efficient hydrogen production from bio-butanol oxidative steam reforming over bimetallic Co–Ir/ZnO catalysts. *Green Chemistry* 2012; 14: 1035-1043.

[68] Staniforth J, Ormerod M. Clean destruction of waste ammonia with consummate production of electrical power within a solid oxide fuel cell system. *Green Chemistry* 2003; 5: 606-609.

[69] Atkinson A, Kilner J, Skinner S, Brandon NP, Brett DJL. Intermediate-Temperature Solid Oxide Fuel Cells. In Robert H. Crabtree (Ed.). *Energy Production and Storage*: Inorganic Chemical Strategies for a Warming World. Wiley, 2010. p. 173-189.

[70] Shao Z, Haile SM, Ahn J, Ronney PD, Zhan Z, Barnett SA. A thermally self sustained micro solid-oxide fuel-cell stack with high power density. *Nature* 2005; 435:795-798.

[71] Boder M, Dittmeyer R. Catalytic modification of conventional SOFC anodes with a view to reducing their activity for direct internal reforming of natural gas. *Journal of Power Sources* 2006; 155: 13-22.

[72] Development and characterisation of materials and compound structures for the Solid Oxide Fuel Cell (SOFC). Karlsruhe Institute of Technology. http://www.iwe.kit.edu/english/mitarbeiter_sofc.php. Acesso em 28/07/2012.

[73] Institute of Energy and Climate Research (IEK) – Jülich Forschungszentrum. http://www2.fz-juelich.de/ief/ief-1/index.php?index=61. Acesso em 28/07/2012.

[74] Steele BCH.Material science and engineering: The enabling technology for the commercialisation of fuel cell. *Journal of Materials Science* 2001; 36:1053-1068.

[75] Steele BCH. Materials for IT-SOFC stacks: 35 years R&D: the inevitability of gradualness?*Solid State Ionics* 2000; 134: 3-20.

[76] Guo Y, Lin Y, Ran R, Shao Z. Zirconium doping effect on the performance of proton-conducting $BaZr_yCe_{0.8-y}Y_{0.2}O_{3-\delta}$ ($0 \leq y \leq 0.8$) for fuel cell applications. *Journal of Power Sources* 2009; 193:400-407.

[77] Iwahara H, Esaka T, Uchida H e Maeda N. Proton conduction in sintered oxides and its application to steam electrolysis for hydrogen production. *Solid State Ionics* 1981; 3/4: 359-363.

[78] Coors, W. Grover; Readey, Dennis W. Proton conductivity measurements in yttrium barium cerate by impedance spectroscopy. *Journal of American Ceramic Society* 2002; 85: 2637-2640.

[79] Norby Truls, Widerøe Marius, Glöckner Ronny, Larring Yngve. Hydrogen in oxides. *Dalton Transactions* 2004:3012-3018.

[80] Haile, SM. Fuel cell materials and components. *Acta Materialia* 2003; 51:5981-6000.

[81] Hoogers, G. Fuel Cell Handbook, 2ª ed., CRC Press LLC, Trier University of Applied Sciences, Umwelt-Campus Birkenfeld, 2003.

[82] Horita, T.; Yamaji, K.; Kato, T.; Kishimoto, H.; Xiong, Y.; Sakai, N.; Brito, M.E.; Yokokawa, H. Imaging of CH4 Decomposition Around the Ni/YSZ Interfaces under Anodic Polarization. *Journal of Power Sources* 2005; 145: 133-138.

[83] Singhal, S.C. Solid Oxide Fuel Cells for Stationary, Mobile, and Military Applications. *Solid State Ionics* 2002; 152: 405-410.

[84] Clarke SH, Dicks AL, Poinon K, Smith TA, Swann A. Catalytic aspects of the steam reforming of hydrocarbons in internal reforming fuel cells. *Catalysis Today* 1997; 38: 411-423.

[85] Devanathan R. Proton Exchange Membranes for Fuel Cells. In Robert H. Crabtree (Ed.). *Energy Production and Storage*: Inorganic Chemical Strategies for a Warming World. Wiley, 2010. p.89-100.

[86] Sasikumar G, Ihm JW, Ryu H. Optimum Nafion content in PEM fuel cell eletrodes. *Electrochimica Acta* 2004; 50: 601-605.

[87] Zamel N, Litovsky E, Li X, Kleiman J. Measurement of the through plane thermal conductivity of carbon paper diffusion media for the temperature range from -50 to +120ºC. *International Journal of Hydrogen Energy* 2011; 36: 12618-12625.

[88] Nores Pondal F J, Vilella IMJ, Troiani H, Granada M, de Miguel SR, Scelza OA, Corti HR, Catalytic activity vs. size correlation in platinum catalysts of PEM fuel cells prepared on carbon black by different methods. *International Journal of Hydrogen Energy* 2009; 34: 8193-8203.

[89] Foulds, L.R. Optimization Techniques – an Introduction, Springer-Verlag, New York, 1981, p.2-9.

[90] Secchi, A.R. Otimização de Processos. Apostila da disciplina de Otimização de Processos/PPGEQ-UFRGS, p. 5, 7,16-19, 84-91, 96-105.

[91] Gramlich, G., Werner, W. Numerische Mathematik mit Matlab – Eine Einführung für Naturwissenschaft und Ingenieure, Heidelberg:dpunkt, 2000, p.128.

[92] Edgar, T F., Himmelblau, DM. Optimization of Chemical Processes, McGraw-Hill, p. 301-334, 1988.

[93] Rossi CCRS, Berezuk ME, Cardoso-Filho L, Guirardello R. Simultaneous calculation of chemical and phase equilibria using convexity analysis. *Computers and Chemical Engineering* 2011; 35: 1226-1237.

[94] Edgar TF, Himmelblau DM, Lasdon SL. Optimization of Chemical Processes (2^{nd} ed). New York: McGraw Hill.

[95] Rossi CCRS, Alonso CG, Antunes OAC, Guirardello R, Cardozo-Filho L. Thermodynamic analysis of steam reforming of ethanol and glycerine for hydrogen production. *International Journal of Hydrogen Energy* 2009; 34: 323-332.

[96] He L, Salamanca Parra JM, Blekkan EA, Chen D. Towards efficient hydrogen production from glycerol by sorption enhanced steam reforming. *Energy & Environmental Science* 2010; 3: 1046-1056.

[97] Cheng CK, Foo SY, Adesina AA. Thermodynamic analysis of glycerol-steam reforming in the presence of CO_2 or H_2 as carbon gasifying agent. *International Journal of Hydrogen Energy* 2012; 37: 10101-10110.

[98] Lohsoontorn P, Brett DJL, Brandon NP. Thermodynamic predictions of the impact of fuel composition on the propensity of sulphur to interact with Ni and ceria-based anodes for solid oxide fuel cells. *Journal of Power Sources* 2008; 175: 60-67.

[99] Lwin Y, Daud WRW, Mohamad AB, Yaakob Z. Hydrogen production from steam-methanol reforming: Thermodynamic analysis. *International Journal of Hydrogen Energy* 2000; 25: 47-53.

[100] Kelley, K.K., US Bur.Mines,Bull., n.476, 1949.

[101] Kubaschewski, O., Knacke, O., Hesselmann, K. Thermochemical Properties of Inorganic Substances, 1ª ed., Springer Verlag, New York, 1991, vol. 1,p. 264, 273, 307, 309, 803, 811.

[102] Sandler, S. Chemical and Engineering Thermodynamics, 3ªed., John Wiley & Sons, New York, 1999, p.745-747.

[103] Reid RC, Prausnitz JM, Poling BE. The properties of gases and liquids, 4ª edição, McGraw-Hill, Nova York, 1987.

[104] Fylstra D, Lasdon L, Watson J, Waren A. Design and use of the Microsoft Excel Solver. *Interfaces* 1998; 28: 29-55.

[105] Amphlett JC, Baumert RM, Mann RF, Peppley BA, Roberge, Harris TJ. Performance Modeling of the Ballard Mark IV solid polymer electrolyte fuel cell. I. Mechanistic Model Development. *Journal of the electrochemical society* 1995; 142:1-8.

[106] Amphlett JC, Baumert RM, Mann RF, Peppley BA, Roberge PR, Harris TJ. Performance modeling of the Ballard Mark IV. II Empirical Model Development. Journal of the electrochemical society 1995; 142:9-15.

[107] Mann RF, Amphlett JC, Hooper MAI, Jensen HM, Peppley BA, Roberge. Development and application of a generalized steady-state electrochemical model for a PEM fuel cell. Journal of Power Sources 2010; 86: 173-180.

[108]Vourliotakis G, Skevis G, Founti MA. Detailed kinetic modelling of non-catalytic ethanol reforming for SOFC applications. International Journal of Hydrogen Energy 2009; 34:7626-7637.

[109] Cai W, Wang F, van Veen A, Descorme C, Schuurman Y, Shen W, Mirodatos C. Hydrogen production from ethanol steam reforming in a micro-channel reactor. International Journal of Hydrogen Energy 2010; 35:1152-1159.

[110] Balaji S, Ilic J, Ydstie BE, Krogh BH. Control-Based Modeling and Simulation of the Chemical-Looping Combustion Process. Industrial & engineering chemistry research 2010; 49: 4566-4575.

[111] Al-Hamamre Z, Hararah MA. Hydrogen production by thermal partial oxidation of ethanol: Thermodynamics and kinetics study. International Journal of Hydrogen Energy 2010; 35: 5367-5377.

[112] Wang X, Li M, Li S, Wang H, Wang S, Ma X. Hydrogen production by glycerol steam reforming with/without calcium oxide sorbent: A comparative study of thermodynamic and experimental work. Fuel Processing Technology 2010; 91:1812-1818.

[113] Kale GR, Kulkarni BD. Thermoneutral point analysis of ethanol dry autothermal reforming. Chemical Engineering Journal 2010; 165: 864-873.

[114] Chen L, Choong CKS, Zhong Z, Huang L, Ang TP, Hong L, Lin J. Carbon monoxide-free hydrogen production via low-temperature steam reforming of ethanol over iron-promoted Rh catalyst. Journal of Catalysis 2010; 276: 197-200.

[115] Wang X, Wang N, Wang L. Hydrogen production by sorption enhanced steam reforming of propane: A thermodynamic investigation. International Journal of Hydrogen Energy 2011; 36: 466-472.

[116] Muhammad Y, Lu Y, Shen C, Li C. Dibenzothiophene hydrodesulfurization over Ru promoted alumina based catalysts using in situ generated hydrogen. Energy Conversion and Management 2011; 52: 1364-1370.

[117] Muhammad Y, Li C. Dibenzothiophene hydrodesulfurization using in situ generated hydrogen over Pd promoted alumina-based catalysts. Fuel Processing Technology 2011; 92: 624-630.

[118] Li J, Yu H, Yang G, Peng F, Xie D, Wang H, Yang J. Steam Reforming of Oxygenate Fuels for Hydrogen Production: A Thermodynamic Study. Energy & Fuels 2011; 25: 2643-2650.

[119] Khaodee W, Wongsakulphasath S, Kiatkittipong W, Arpornwichanop A, Laosiripojana N, Assabumrungrat S. Selection of appropriate primary fuel for hydrogen production for different fuel cell types: Comparison between decomposition and steam reforming. International Journal of Hydrogen Energy 2011; 36: 7696-7706.

[120] de Ávila CN, Hori CE, de Assis AJ. Thermodynamic assessment of hydrogen production and cobalt oxidation susceptibility under ethanol reforming conditions. Energy 2011; 36: 4385-4395.

[121] Yenumala SR, Maity SK. Reforming of vegetable oil for production of hydrogen: A thermodynamic analysis. International Journal of Hydrogen Energy 2011; 36: 11666-11675.

[122] Gucciardi E, Chiodo V, Freni S, Cavallaro S, Galvagno A, Bart JCJ. Ethanol and dimethyl ether steam reforming on Rh/Al_2O_3 catalysts for high-temperature fuel-cell feeds. Reaction kinetics, mechanisms and catalysis 2011; 104: 75-87.

[123] Göll S, Samsun RC, Peters R. Analysis and optimization of solid oxide fuel cell-based auxiliary power units using a generic zero-dimensional fuel cell model. Journal of Power Sources 2011; 196:9500-9509.

[124] Nahar G, Dupont V. Hydrogen via steam reforming of liquid biofeedstock. Biofuels 2012; 3: 167-191.

[125] Trabold TA, Lylac JS, Walluk MR, Lin JF, Troiani DR. Measurement and analysis of carbon formation during diesel reforming for solid oxide fuel cells. International Journal of Hydrogen Energy 2012; 37: 5190-5201.

[126] Wu YJ, Díaz-Alvarado F, Santos JC, Gracia F, Cunha AF, Rodrigues AE. Sorption-Enhanced Steam Reforming of Ethanol: Thermodynamic Comparison of CO_2 Sorbents. Chemical Engineering & Technology 2012; 35: 847-858.

[127] Rossetti I, Biffi C, Bianchi CL, Nichele V et al. Ni/SiO_2 and Ni/ZrO_2 catalysts for the steam reforming of ethanol. Applied Catalysis B: Environmental 2012; 117-118: 384-396.

[128] Göll S, Samsun RC, Peters R. Enhancing the Efficiency of SOFC-Based Auxiliary Power Units by Intermediate Methanation. Fuel Cells 2012; 12: 474-486.

[129] Graschinsky C, Giunta P, Amadeo N, Laborde M. Thermodynamic analysis of hydrogen production by autothermal reforming of ethanol. International Journal of Hydrogen Energy 2012; 37: 10118-10124.

[130] Shabbar S, Janajreh I. Thermodynamic equilibrium analysis of coal gasification using Gibbs energy minimization method. Energy and Conversion Management 2012; *In press*.

[131] Kale GR, Kulkarni BD, Bharadwaj. Chemical looping reforming of ethanol for syngas generation: A theoretical investigation. International Journal of Energy Research 2012; *In press*.

[132] Roy B, Sullivan H, Leclerc CA. Aqueous-phase reforming of n-BuOH over Ni/Al_2O_3 and Ni/CeO_2 catalysts. Journal of Power Sources 2011; 196: 10652–10657.

[133] Chanburanasiri N, Ribeiro AM, Rodrigues AE, Arpornwichanop A, Laosiripojana N, Praserthdam P, Assabumrungrat S. Hydrogen Production via Sorption Enhanced Steam Methane Reforming Process Using Ni/CaO Multifunctional Catalyst. Industrial & Engineering Chemistry Research 2011; 50: 13662–13671.

[134] Park J, Yi KB. Effects of preparation method on cyclic stability and CO_2 absorption capacity of synthetic CaO–MgO absorbent for sorption-enhanced hydrogen production. International Journal of Hydrogen Energy 2012; 37: 95-102.

[135] Lo Faro M, Minutoli M, Monforte G, Antonucci V, Aricò AS. Glycerol oxidation in solid oxide fuel cells based on a Ni-perovskite electrocatalyst. Biomass and Bioenergy 2011; 35: 1075-1084.

[136] Gao Z, Raza R, Zhu B, Mao Z, Wang C, Liu Z. Preparation and characterization of $Sm_{0.2}Ce_{0.8}O_{1.9}/Na_2CO_3$ nanocomposite electrolyte for low-temperature solid oxide fuel cells. International Journal of Hydrogen Energy 2011; 36: 3984-3988.

[137] Qin H, Zhu Z, Liu Q, Jing Y, Raza R, Imran S, Singh M, Abbas G, Zhu B. Direct biofuel low-temperature solid oxide fuel cells. Energy and Environmental Science 2011; 4: 1273-1276.

[138] Siengchum T, Guzman F, Chuang SSC. Analysis of gas products from direct utilization of carbon in a solid oxide fuel cell. Journal of Power Sources 2012; 213: 375-381.

[139] Lo Faro M, Antonucci V, Antonucci PL, Aricò AS. Fuel flexibility: A key challenge for SOFC technology. Fuel 2012. *In press*.

[140] Li Y, Wang W, Chen B, Cao Y. Thermodynamic analysis of hydrogen production via glycerol steam reforming with CO_2 adsorption. International Journal of Hydrogen Energy 2010; 35: 7768-7777.

[141] Su C, Ran R, Wang W, Shao Z. Coke formation and performance of an intermediate-temperature solid oxide fuel cell operating on dimethyl ether fuel. Journal of Power Sources 2011; 56: 1967-1974.

[142] Oulmi K, Zitouni B, Moussa HB, Abdenebi H, Andreadis GM. Total polarization effect on the location of maximum temperature value in planar SOFC. International Journal of Hydrogen Energy 2011; 36: 4236:4243.

[143] Su C, Wang W, Ran R, Zheng T, Shao Z. Further performance enhancement of a DME-fueled solid oxide fuel cell by applying anode functional catalyst. International Journal of Hydrogen Energy 2012; 37: 6844-6852.

[144] Thursfield A, Murugan A, Franca R, Metcalfe IS. Chemical looping and oxygen permeable ceramic membranes for hydrogen production – a review . Energy and Environmental Science 2012;5: 7421-7459.